

DISS. ETH NO. 26321

**Three-dimensional localization spectroscopy of
individual nuclear spins in diamond**

A thesis submitted to attain the degree of
DOCTOR OF SCIENCE of ETH ZURICH
(Dr. sc. ETH Zurich)

presented by

Jonathan Zopes

M.Sc. in Physics, University of Bonn

born on 26.01.1989

citizen of Germany

accepted on the recommendation of
Prof. Dr. Christian Degen, examiner
Prof. Dr. Andreas Vaterlaus, co-examiner

2019

“Never measure anything but frequency!”

Arthur Schawlow

Abstract

Well-controlled quantum systems, such as defects in the solid state, have emerged in recent years as candidates for novel precision sensors for magnetic or electric fields on nanoscopic length scales. This thesis reports on experiments with one such quantum sensor: the nitrogen-vacancy (NV) center in diamond. The NV center is a stable defect whose electron spin can be optically polarized and read out. Furthermore, coherent control of the spin state is possible even at room temperature. These unique properties allow us to use the NV center as a local sensor for magnetic fields.

The main focus of this work is addressing the detection of nuclear magnetic resonance (NMR) signals in the atomistic environment of the defect. The long-term goal of this research is the structure elucidation of individual molecules attached onto the diamond surface. In our experiments we detect NMR signals, arising from ^{13}C spins in the vicinity of the defect, using dynamical decoupling spectroscopy. Dynamical decoupling spectroscopy uses a set of equidistant refocusing pulses applied to the sensor to detect weak magnetic fields oscillating at a specific frequency. The detection frequency is controlled by the temporal separation between microwave pulses.

In a first set of experiments (in Chapter 5) we introduce a simple method, based on shaped microwave pulses, to enhance control over the temporal separation between the pulses. Thereby we significantly increase the frequency tunability of our spectroscopy sequences beyond the time resolution of our control hardware.

By detecting the position-dependent NMR frequencies of individual ^{13}C nuclei, their location relative to the defect can be determined. In previous NV-NMR experiments, however, only partial spatial information was available. The second project (Chapters 6 and 7) demonstrates the full three-dimensional imaging of individual nuclear spins by using the magnetic field vector of a custom-built planar radio-frequency coil as a spatial reference. Two different imaging strategies are presented, which are based on different NMR control sequences and produce consistent imaging results for nuclei at distances of up to $\sim 12 \text{ \AA}$ from the sensor.

Apart from the NMR experiments, which require the sensitive detection of harmonic signals, this thesis further explores the more general problem of how arbitrary magnetic waveforms can be detected with the NV center. We present a novel sensing protocol (Chapter 8), which is based on differential spin echo sequences. The method enables the reconstruction-free detection of waveforms with both high field sensitivity ($4 \mu\text{T}/\sqrt{\text{Hz}}$) and high time resolution (20 ns). This new measurement technique has potential applications for studying dynamics in nanoscale devices.

Zusammenfassung

Wohlkontrollierte Quantensysteme, wie beispielsweise Defektzentren in Festkörpern, wurden in den letzten Jahren als neuartige Präzisionssensoren für magnetische und elektrische Felder auf der Nanoskala indentifiziert. Die vorliegende Arbeit berichtet über Experimente mit einem solchen Quantensensor: dem Stickstoff-Fehlstellen-Zentrum (NV-Zentrum) in Diamant. Das NV-Zentrum ist ein stabiler Defekt, dessen Elektronenspin optisch polarisiert und ausgelesen werden kann. Desweiteren kann der Defekt bei Raumtemperatur kohärent kontrolliert werden. Diese einzigartigen Eigenschaften erlauben es das NV-Zentrum als Sensor für lokale magnetische Felder zu verwenden.

Der Hauptfokus dieser Arbeit liegt in der Detektion von Kernspinresonanz-Signalen (NMR-Signale) in der Umgebung des Defektzentrums. Das langfristige Ziel dieser Forschung liegt in der Strukturbestimmung von einzelnen Molekülen, welche dazu auf die Diamantoberfläche aufgebracht werden. In den hier diskutierten Experimenten detektieren wir die NMR-Signale von ^{13}C -Spins in der direkten Umgebung des Defekts mittels dynamischer Entkopplungsspektroskopie. Bei der dynamischen Entkopplungsspektroskopie werden equidistante Refokussierungspulse verwendet, um magnetische Felder bei einer wohldefinierten Frequenz zu detektieren. Die Detektionsfrequenz ist dabei durch den zeitlichen Abstand von Refokussierungspulse gegeben.

In einer ersten Studie (siehe Kapitel 5) führen wir eine einfache Methode ein, welche amplitudenmodulierte Pulse nutzt, um den zeitlichen Abstand zwischen Refokussierungspulsen sehr präzise einzustellen. Dadurch erhöht sich die Frequenzabstimmbarkeit der Spektroskopiesequenz signifikant und überschreitet das Limit welches durch die Zeitauflösung der Steuerungselektronik gegeben ist.

Durch die Detektion von positionsabhängigen Präzessionsfrequenzen von einzelnen ^{13}C -Spins lässt sich deren relativer Distanzvektor zum NV-Zentrum ermitteln. In bisherigen NV-NMR Experimenten konnten nur partielle Informationen über den Distanzvektor einzelner Kernspins ermittelt werden. Das zweite in dieser Arbeit beschriebene Projekt zeigt in den Kapiteln 6 und 7 wie der gesamte dreidimensionale Distanzvektor einzelner Kernspins bestimmt werden kann. Dazu wurde der lokale Feldvektor einer selbstgebauten, planaren Radiofrequenz-Spule als Ortsreferenz eingesetzt. Zwei konzeptionell unterschiedliche Positionierungsverfahren wurden entwickelt, welche auf unterschiedlichen NMR Sequenzen basieren. Die Methoden liefern konsistente Resultate und ermöglichen in den vorgestellten Versuchen die Positionsbestimmung von Kernspins mit einem Abstand von bis zu $\sim 12 \text{ \AA}$ zum Sensorspin.

Zusätzlich zu den NV-NMR Experimenten, welche die Detektion von harmonischen Signalen erfordern, wurde in Kapitel 8 ein Verfahren für die Vermessung von beliebigen Signalformen entwickelt. Dazu führen wir eine Sequenz ein, welche auf differentiellen Spin-Echos basiert. Die Methode ermöglicht eine rekonstruktionsfreie Detektion von Signalformen mit hoher Feld- ($4 \mu\text{T}/\sqrt{\text{Hz}}$) und Zeitauflösung (20 ns). Diese Methode kann für die Untersuchung von dynamischen Prozessen in nanoskaligen Proben genutzt werden.

Contents

Abstract	v
1 Introduction	1
1.1 Outline of this thesis	3
2 The nitrogen-vacancy center: A single-atom magnetometer	5
2.1 Introduction	5
2.2 Defect structure	6
2.3 Optical properties of the NV^- defect	7
2.4 Spin states of the NV^- electronic ground-state	8
2.4.1 Zero-field and Zeeman splitting	8
2.4.2 Optically detected magnetic resonance	9
2.4.3 Hyperfine structure due to the intrinsic nitrogen spin	9
2.5 Magnetometry with the NV center	10
2.5.1 Magnetic field sensing with the Ramsey method	11
Quadratic or variance detection	12
Linear magnetic field detection	13
2.5.2 Magnetic field sensitivity of Ramsey spectroscopy	13
Readout noise sources	13
2.5.3 Detection of ac signals	16
Hahn echo method	16
Sensitivity for Hahn echo detection	17
2.6 Coherence and lifetime properties of the m_S -states	17
Electron spin dephasing time T_2^*	19
Electron spin coherence time T_2^{echo}	19
Electron spin lifetime T_1	19
3 Detection, polarization and control of remote nuclear spins	21
3.1 Definition of the spin system	21
3.2 Hyperfine interaction to remote spins	22
3.3 Nuclear spin imaging	23
3.4 Detection of the presence of nuclear spins	24
3.4.1 Dynamical decoupling sequences	24
Experimental protocol	24
Sensor phase accumulation during the sensing sequence	26
Spectral weighting function of the sensing sequence	26
Detection of complex, multi-frequency signals	27
Frequency resolution of dynamical decoupling spectroscopy	27
3.4.2 NMR detection with dynamical decoupling spectroscopy	27
Spectroscopy on a bath of spins	27

	Spectroscopy on individual nuclear spins	29
3.5	Control of nuclei using dynamical decoupling	29
3.5.1	Rotating-frame transformation	29
3.5.2	Precession axes of nuclear spins	29
3.5.3	Two-level description of the NV center	30
3.5.4	Evolution of nuclear spins during decoupling	30
3.5.5	Dynamical decoupling signal of individual spins	31
3.6	Polarization transfer to individual nuclear spins	32
3.7	Nuclear spin state tomography	34
	Pulse sequence for nuclear state tomography	35
	Product-operator description of state tomography	35
	Detection of nuclear precession by state tomography	36
3.8	Correlation hyperfine spectroscopy	37
3.8.1	Spectroscopy of the parallel hyperfine coupling	37
	Product operator description	37
3.8.2	Spectroscopy of the perpendicular hyperfine coupling	40
3.8.3	Determination of hyperfine couplings from precession frequencies	41
3.8.4	Frequency-resolution of correlation spectroscopy	41
4	Experimental methods	43
4.1	Introduction	43
4.2	Diamond chips	43
4.3	Experimental setup	44
4.3.1	Confocal laser microscope	44
4.3.2	Control and readout electronics	46
	Microwave and radio-frequency signal generation	46
	Time-resolved photon counting	49
	Control of the confocal microscope	50
4.3.3	Calibration and alignment of static quantization fields B_0	50
	Field alignment at high magnetic field ($20 \text{ mT} < B_0 < 350 \text{ mT}$)	51
	Field alignment at low magnetic field ($B_0 < 20 \text{ mT}$)	51
	Stability of B_0	51
4.3.4	Planar radio-frequency coils for nuclear spin control	52
	Numerical optimization of the coil geometry	52
	Integration into the confocal microscope	53
4.3.5	In-situ characterization of the planar coils	53
	Heating effects due to DC current and current pulses	53
	Field magnitude measurement and vector magnetometry	54
	Step response of the coil circuit	56
	Nuclear radio-frequency pulses	56
	Development of an improved coil design	57
5	High-resolution quantum sensing with shaped control pulses	59
5.1	Introduction	59
5.1.1	The time-resolution limitations of multi-pulse sequences	60
5.1.2	Pulse shaping for high-resolution dynamical decoupling	60
5.2	Experimental realization	61
5.3	Theoretical description and analysis	62
5.4	Non-linear signal detection	64

5.5	Comparison of filter functions for dynamical decoupling sequences with different pulse shapes	64
5.6	Applications of dynamical decoupling with shaped pulses	64
5.7	Conclusion and outlook	65
6	Three-dimensional localization spectroscopy of individual nuclear spins with sub-Angstrom resolution	67
6.1	Introduction	67
6.2	Theoretical description of the method	68
6.3	Results	70
6.3.1	Mapping of r and θ	70
6.3.2	Mapping of ϕ	72
6.3.3	Fermi contact interaction	72
6.3.4	Extended electronic wave function	76
6.3.5	Conclusion	76
6.3.6	Outlook	76
7	Three-dimensional nuclear spin positioning using coherent radio-frequency control	79
7.1	Introduction	79
7.2	Theory	81
7.3	Experimental method	81
7.4	Results	82
7.4.1	Flip and evolve method	82
	Low-field measurements	82
	High-field measurements	85
7.4.2	Nuclear echo method	86
7.4.3	Density matrix simulations and estimation of ϕ	86
	Density matrix simulations of the spin system	86
	Extraction of the nuclear precession frequency	87
	Extraction of the azimuthal position	87
7.4.4	Effect of tilted magnetic bias fields on the accuracy in estimating $\vec{r} = (r, \theta, \phi)$	87
7.5	Conclusion	89
8	Reconstruction-free quantum sensing of arbitrary waveforms	91
8.1	Introduction	91
8.2	Waveform quantum sensing protocols	93
8.3	Experimental realization	94
8.4	Detection of a magnetic square waveform pulse	94
8.5	Time resolution of waveform sensing	96
8.6	Signal gain by repetitive acquisition	97
8.7	Detection of a complex test waveform	97
8.8	Limitations and possible remedies	98
8.9	Conclusion and Outlook	99
9	Conclusion and Outlook	101
	Nanoscale magnetic resonance imaging	101
	Detection of arbitrary magnetic signals	102
A	Product operator calculations	105

B Nuclear precession in tilted magnetic fields	107
B.0.1 Definition of Hamilton operators	107
B.0.2 Perturbation theory up to second order and for $D \gg B_z$	107
C Sensitivity and transfer function of the differential echo sequence	111
C.1 Transfer function and response time	111
C.2 Sensitivity Analysis	112
Bibliography	115
Danksagung	133

Physical Constants

Speed of Light	$c_0 = 2.997\,924\,58 \times 10^8 \text{ m s}^{-1}$ (exact)
Planck's constant	$h = 6.626\,070\,15 \times 10^{-34} \text{ J s}$ (exact)
Boltzmann's constant	$k_B = 1.380\,649 \times 10^{-23} \text{ J K}^{-1}$ (exact)
Elementary charge	$e = 1.602\,176\,634 \times 10^{-19} \text{ C}$ (exact)
Vacuum permeability	$\mu_0 = 1.256\,637\,062\,12 \times 10^{-7} \text{ H m}^{-1}$
Gyromagnetic ratio of the electron	$\gamma_e/(2\pi) = 28.024\,951\,64 \times 10^9 \text{ Hz T}^{-1}$
Gyromagnetic ratio of ^{13}C	$\gamma_n/(2\pi) = 10.7084 \times 10^6 \text{ Hz T}^{-1}$
Gyromagnetic ratio of ^{15}N	$\gamma_{^{15}\text{N}}/(2\pi) = -4.316 \times 10^6 \text{ Hz T}^{-1}$
Gyromagnetic ratio of ^{14}N	$\gamma_{^{14}\text{N}}/(2\pi) = 3.077 \times 10^6 \text{ Hz T}^{-1}$
Gyromagnetic ratio of ^1H	$\gamma_{^1\text{H}}/(2\pi) = 42.577\,478\,92 \times 10^6 \text{ Hz T}^{-1}$

— SI system as of May 20, 2019 —

List of Symbols

(x, y, z)	cartesian coordinates	(m,m,m)
(r, θ, ϕ)	spherical coordinates	(m,rad,rad)
r	(radial) distance	m
θ	polar position angle	rad
ϕ	azimuthal position angle	rad
E	energy	J
P	power	W (J s^{-1})
I	intensity	$\frac{\text{W}}{\text{m}^2}$ ($\text{J s}^{-1} \text{m}^{-2}$)
λ	wavelength	m
NA	numerical aperture	(-)
R_p	photon detection rate	(kCts/s)
T	Temperature	(K)
i	electrical current	A
R	electrical resistance	Ω
C	electrical capacitance	F
L	electrical inductance	H
f	ordinary frequency	Hz
ω	angular frequency	rad s^{-1}
Ω_R	Rabi frequency	rad s^{-1}
t_π	π pulse duration	s
τ	inter-pulse separation	s
f_{ac}	signal frequency	Hz
t	time	s
a_{iso}	contact hyperfine coupling	rad s^{-1}
a_{\parallel}	parallel hyperfine coupling	rad s^{-1}
a_{\perp}	perpendicular hyperfine coupling	rad s^{-1}

CHAPTER 1

Introduction

About a century after the discovery of quantum mechanics [1–5] modern technology enables physicists to fully control small quantum systems in a laboratory environment. Apart from using these pristine systems for tests of the fundamental laws of quantum theory [6–10], also the technological application of well-controlled quantum systems in computing [11–13], secure communication [14–16] and sensing or metrology [17–22] is nowadays of interest. This is because devices based on quantum systems can or are expected to perform certain tasks better than their classical implementation. This includes computational algorithms that leverage quantum mechanics to provide exponential speed-ups versus their classical counterpart [23], communication protocols that are information-theoretically secure [14] and quantum-enhanced sensors whose precision improves faster with the number of measurements than a classical counterpart [17, 18].

In quantum sensing a controllable quantum system is used to estimate an a-priori unknown parameter, e.g., the local magnetic or electric field at the location of the sensor system, by monitoring either energy splittings or the transition rate between energy levels [22]. From the fundamental viewpoint quantum-enhanced sensing requires an entangled set of sensing qubits to achieve a scaling advantage in measurement precision over classical systems [17, 18]. Nevertheless, in recent years, mainly individual sensing qubits or ensembles of uncorrelated quantum sensors have found rich applications, which merely exploit, for example, the nanoscale spatial extension of the sensor [20, 24–28]. Further, in frequency metrology, laser oscillators locked to narrow optical transitions of trapped ensembles of ultracold atoms [29, 30] or individual ions [31–33] are currently providing the most precise time standards. Here, the extremely high quality factor of optical transitions combined with the fact that all atoms or ions are identical in their physical properties is exploited.

In this thesis, we use an *artificial atom* [34], the nitrogen-vacancy center (NV center) in diamond, as a quantum sensor. The NV center consists of a substitutional nitrogen atom neighboring a vacancy in the diamond lattice [35, 36]. The defect occurs naturally in diamond crystals, but can also be created artificially for example by ion implantation of diamond with nitrogen [37]. Using a combination of optical transitions driven by laser pulses and magnetic transitions controlled with microwaves, the NV center can be used to detect the local temperature [38], pressure [39], electric [40] or magnetic field [20]. Throughout this thesis we will focus on the detection of magnetic fields and therefore use the NV center as a local magnetometer. For this purpose we monitor the splitting between energy levels associated with the spin of the defect, which depends on magnetic field via the Zeeman effect [41].

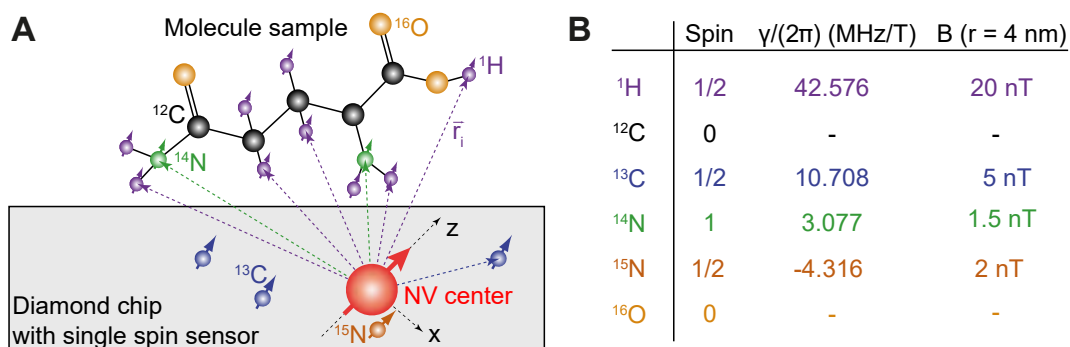


FIGURE 1.1: Long-term vision for nanoscale magnetic resonance imaging with a single NV sensor. (a) Sketch of the envisioned single-molecule imaging experiment with a spin sensor. The atomic structure of a single molecule, here exemplarily the amino acid glutamine, could potentially be directly imaged by measuring the distance vectors (dashed arrows) between the NV electron spin and the nuclei composing the molecule. In this approach the sensor spin has to be placed at most a few nanometers below the diamond surface to detect the faint NMR signals of the nuclei. Spatial positions of nuclei can be encoded into NMR frequencies by the dipolar hyperfine gradient of the sensor spin. In this thesis proof-of-principle imaging methods based on the hyperfine gradient are experimentally demonstrated on ^{13}C spins (blue) inside the diamond crystal. (b) Summary of different nuclear spin species, their spin quantum number, their gyromagnetic ratio γ and the generated magnetic field B at a distance of $r = 4$ nm to the sensor spin. In their most abundant isotope oxygen and carbon nuclear spins possess zero spin and are therefore not detectable with NMR methods.

As the NV center is localized to atomic dimensions it is susceptible to variations in magnetic field on the same length scale. Consequently, the NV center can be used for nanoscale magnetic imaging, for example, by scanning a diamond tip hosting a single NV center at its apex over a sample of interest. This was initially proposed in [25, 42, 43] and recently demonstrated in several experiments at room and low-temperature [28, 44–50]. In addition, a sample can be attached to the surface of the diamond chip and a shallow NV center can be used to detect the magnetic field generated by the sample to study its properties. Potential samples include solid-state systems [51, 52], biomolecules [53–55] or small microwave and radio-frequency circuits [56, 57].

Throughout the course of this thesis we will focus on magnetometry with individual, stationary NV centers residing in single-crystal diamonds. The long-term motivation behind our experiments is to map the structure of individual biomolecules that are attached to the surface of the diamond sensor chip. An illustration of such an envisioned imaging experiment is shown in Fig. 1.1 (a). Here, a single NV center serves as a sensor of the nuclear magnetic resonance (NMR) signals of the nuclei composing the molecule. The structure of the molecule can be determined by measuring the distance vectors between the sensor spin and the nuclei. In contrast to established structural imaging techniques like conventional NMR or cryogenic electron microscopy, which average over large numbers of target molecules, only a single copy of a molecule is required. Further, ensemble averages in conventional structure determination can conceal conformational differences between individual molecules, which could be unravelled using single-molecule NMR.

Heading for this challenging research goal this thesis reports on the measurement of three-dimensional distance vectors between the NV center and individual ^{13}C nuclei. In our experiments these nuclei are stochastically distributed (natural

abundance 1.1 %) in the nanometer-scale vicinity of the defect inside the diamond host (blue spins in Fig. 1.1 (a)). This nuclear spin system provides an ideal testbed for NV-based NMR imaging experiments, because no molecule deposition is required at this point and the nuclear spins are perfectly fixated inside the diamond. Further, due to the short distances to the nuclei (distances ~ 1 nm in this thesis), the magnetic interaction to the sensor is stronger when compared to the expected interaction strength with external spins (see Fig. 1.1 (b) for a summary of the expected magnetic interaction strength). This reduces the required sensor sensitivity to detect the spins and decreases the experimental averaging time. Two complementary methods for three-dimensional distance measurements will be presented in chapter 6 and 7.

A second set of experiments, presented in chapter 8, addresses a more general sensing task. Here, we present the design and implementation of a novel sensing sequence for the detection of arbitrary, time-dependent magnetic fields. This sequence enables us to operate the NV center in analogy to a conventional oscilloscope and enables the study of complex temporal dynamics in nanoscale systems.

1.1 Outline of this thesis

This thesis is structured as follows:

- In Chapter 2 the basic electronic, optical and magnetic properties of the NV center in diamond are described and the coherence times of the NV center at room temperature are discussed. Finally, the basic concepts of magnetic field sensing with the NV center are summarized.
- Chapter 3 introduces the basic pulse sequences used to detect, polarize, control and spectroscopically characterize nuclear spins in the vicinity of the NV center.
- Chapter 4 provides a description of the experimental methods used throughout this thesis.

Parts of the chapter are based on results from the publication: T. Unden, N. Tomek, T. Weggler, F. Frank, P. London, J. Zopes, C. L. Degen, N. Raatz, J. Meijer, H. Watanabe, K. M. Itoh, M. B. Plenio, B. Naydenov, and F. Jelezko, *Coherent control of solid state nuclear spin nano-ensembles*, npj Quantum Information **4**, 39 (2018).

- Chapter 5 discusses the application of shaped microwave pulses to high-resolution quantum sensing of NMR signals with the NV center.

The chapter is based on the publication: J. Zopes, K. Sasaki, K. S. Cujia, J. M. Boss, K. Chang, T. F. Segawa, K. M. Itoh, C. L. Degen, *High resolution quantum sensing with shaped control pulses*, Phys. Rev. Lett. **119**, 260501 (2017).

- Chapter 6 introduces a experimental technique to determine the location of individual nuclear spins relative to the NV center. In addition, the limitation in spatial resolution due to the finite extension of the electronic wave function of the NV center in the diamond lattice is discussed.

The chapter is based on the publication: J. Zopes, K. S. Cujia, K. Sasaki, J. M. Boss, K. M. Itoh, C. L. Degen, *Three-dimensional localization spectroscopy of individual nuclear spins with sub-Angstrom resolution*, Nature Communications **9**, 4678 (2018).

- In Chapter 7 a second method for three-dimensional localization spectroscopy of nuclear spins is introduced, which uses coherent radio-frequency pulses applied to nuclear spins.

The chapter is based on the publication: J. Zopes, K. Herb, K. S. Cujia, C. L. Degen, *Three-Dimensional Nuclear Spin Positioning Using Coherent Radio-Frequency Control*, Phys. Rev. Lett. **121**, 170801 (2018).

- Chapter 8 introduces a novel quantum sensing sequence based on differential spin echoes, that enables the detection of arbitrary magnetic field waveforms with a two-level quantum sensor.

The chapter is based on the publication J. Zopes and C. L. Degen, *Reconstruction-free quantum sensing of arbitrary waveforms*, arXiv:1906.09176 (2019).

- Chapter 9 provides a conclusion on the results presented in this thesis and gives an outlook on future opportunities and challenges.

The nitrogen-vacancy center: A single-atom magnetometer

Summary

This chapter introduces the nitrogen-vacancy (NV) center in diamond, a stable defect that we employ as a single-atom magnetometer throughout this thesis. In a first step we will summarize the most relevant physical properties of the defect for magnetometry applications. In a second step we will discuss how the electron spin associated with the defect can be leveraged as a sensor. Furthermore, we will introduce the basic magnetometry techniques and discuss their sensitivity to static and time-dependent magnetic fields.

2.1 Introduction

Historically, the strong potential of NV centers for quantum technologies was identified after the first optical detection of individual NV centers in 1997 [58]. Before that ensembles of NV centers were already investigated optically and with electron paramagnetic resonance (EPR) methods and the basic level structure of the defect was inferred by Loubser and van Wyk in the 1970s [59]. After the aforementioned optical detection of individual NV centers, initial experiments employed the NV center to realize basic protocols of quantum information processing, e.g. controlled single [60] and two-qubit gates [61]. Due to the large band gap of diamond the NV center also represents a very stable single photon source, which led to early applications in quantum optics leading e.g. to the realization of Wheeler's delayed choice Gedanken experiment [9] and more recently to loophole-free tests of Bell's inequality [10].

The optically-detected magnetic resonance (ODMR) effect resulting from spin-dependent fluorescence and optical polarizability founded the NV center's use as a local magnetic field sensor [62, 63], which has become a fast-growing research direction in the last decade. The description in this chapter will focus on the room-temperature properties of the defect and rationalizes the use of NV centers as single spin sensors. Potential applications include, e.g., nanoscale nuclear magnetic resonance (NMR) [64] electron paramagnetic resonance (EPR) spectroscopy [65] of individual biomolecules [53] or solid-state systems [52] at ambient conditions. In addition, NV centers are currently also explored at cryogenic temperature ($T < 10$ K)

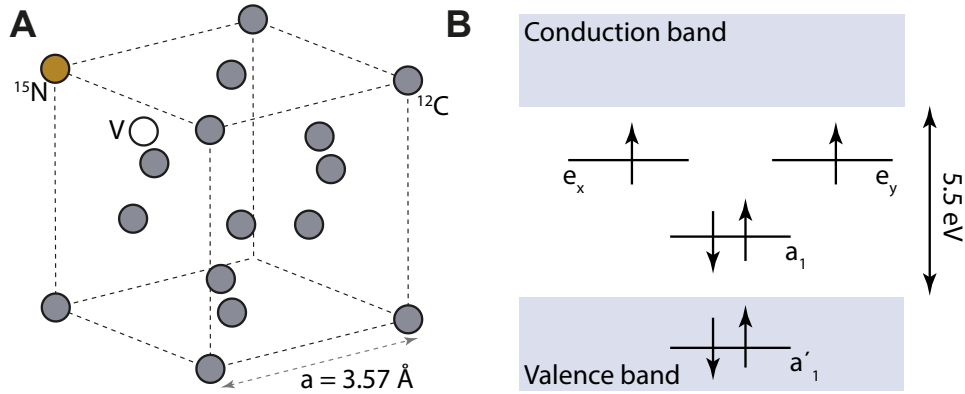


FIGURE 2.1: **Electronic structure of the NV center.** (a) Crystal structure of the NV center defect in the diamond host crystal. Dark grey points represent the carbon atoms of the diamond lattice. The defect consists of a vacancy (white point with label V) adjacent to a nitrogen atom (yellow point with label ^{15}N). The isotope of the nitrogen atom can be either ^{14}N (natural abundance: 99.6%) or ^{15}N (natural abundance 0.4%). Throughout this thesis we work with NV centers with nitrogen nuclei of the ^{15}N isotope, which are artificially generated by ion implantation (see section 4.2 in chapter 4). (b) Filling of the molecular orbitals of the NV^- defect in the ground-state with 6 electrons which comprise the valence shell and originate from the carbon dangling bonds (3 electrons), the nitrogen atom (2 electrons) and the lattice (1 electron). The lowest-lying energy level lies in the valence band of the host crystal. Under optical illumination the occupation of the levels in the band gap changes from the configuration $a_1^2 e^2$ to the configuration $a_1^1 e^3$.

where resonant optical transitions are resolved and enable spin-photon entanglement [66] with applications in quantum communication [15]. Apart from the basic description of the NV center in this chapter, with a focus on quantum sensing applications, extensive details on the NV center properties can be found in recent review articles [35, 36, 39].

2.2 Defect structure

In Fig. 2.1 (a) we show the basic atomic structure of the NV center inside the diamond crystal. It consists of a vacancy adjacent to a substitutional nitrogen atom. The distance between vacancy and nitrogen inside the lattice according to density functional theory (DFT) calculations is ~ 1.65 Angstrom, while the empirical diamond bond length between carbon atoms, at room-temperature, is 1.54 Angstrom.

The NV center exists in three different charge states, namely the NV^+ , NV^0 and NV^- state. The NV^0 and NV^- state are stable at room-temperature and can be distinguished optically via their optical zero phonon line (ZPL). The NV^+ has been discovered only recently [67] with additional external gate structures patterned onto the diamond substrate. Only the negatively-charged NV^- state provides an optical interface to the spin state via state-dependent fluorescence and optical spin polarization and is therefore of interest for quantum sensing applications. Therefore, we will in the following discussion exclusively focus on the negative charge state.

The axial C_{3v} symmetry of the defect defines the molecular orbitals, which transform according to the irreducible representations of the point group. The filling of the molecular orbitals of this NV^- defect in the ground-state with the 6 electrons which comprise the valence shell is shown in Fig. 2.1 (b). The electrons originate

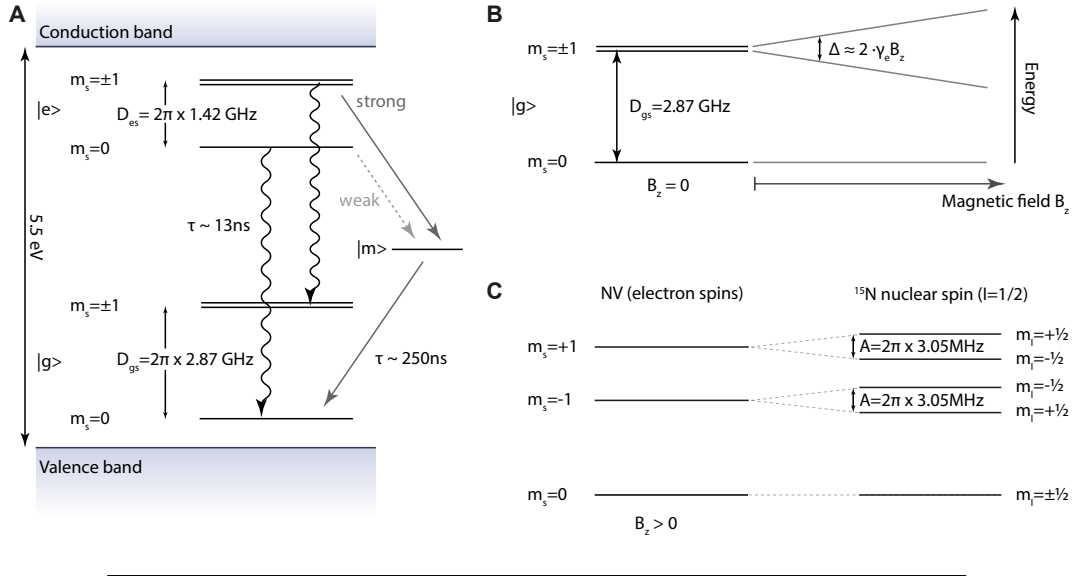


FIGURE 2.2: **Quantum states of the NV center.** (a) Electronic excited ($|e\rangle$) and ground-state ($|g\rangle$) of the NV center inside the bandgap of the diamond host crystal. Both electronic states comprise a spin-triplet ($S = 1$) sub-structure. A third meta-stable state ($|m\rangle$) is preferentially populated from the $m_S = \pm 1$ spin states of $|e\rangle$, which due to the slower and selective relaxation to $m_S = 0$ leads to spin read-out and optical spin polarization. (b) Magnetic states of the NV center in the orbital ground-state in an external magnetic field aligned along the z -axis. Here, the z -direction is defined by the symmetry axis of the defect, which points along the $\langle 111 \rangle$ direction of the diamond crystal. The energy of the spin states is described by the Hamiltonian $\hat{H}_{e,gs,\parallel}$ given in Eq. 2.4. (c) Hyperfine structure of the NV center magnetic spin states due to the intrinsic nitrogen nuclear spin, here of the ^{15}N isotope with spin $1/2$. The hyperfine splitting amounts to $a_{\parallel} = 2\pi \times 3.05 \text{ MHz}$.

from the carbon dangling bonds (3 electrons), the nitrogen atom (2 electrons) and the lattice (1 electron). The lowest-lying energy level lies in the valence band of the host crystal [68]. Under optical illumination the occupation of the levels changes from the configuration $a_1^2 e^2$ to the configuration $a_1^1 e^3$. The fact that these energy levels are located deep inside the large band gap of diamond (5.5 eV) explains the photo stability of the NV center.

2.3 Optical properties of the NV^- defect

We will now turn to the available optical transitions of the NV center, which are schematically represented in Fig. 2.2 (a). Both the electronic ground and excited states have a spin triplet and a spin singlet state. The energy difference between the ground and excited triplet state amounts to 1.945 eV, which defines the optical zero phonon line (ZPL) of $\lambda_{\text{ZPL}} = 637 \text{ nm}$. The energy levels of the singlet states have not been measured to date. For the description of the optical properties of the NV center these can be subsumed under a single level $|m\rangle$ in-between the triplet states (see Fig. 2.2 (a)). This simplification suffices to describe the relevant photo-physical processes. Furthermore, as also indicated in Fig. 2.2 (a), spin-orbit and spin-spin interaction split the m_S -states of both the ground and excited triplet states. These zero field splitting shifts are indicated and summarized in Tab. 2.1.

With the resulting level structure, we can describe the mechanism behind the

spin-state dependent fluorescence and the optical spin polarization once we introduce the allowed transitions between the levels. In general, we excite the NV center with laser radiation at a wavelength of $\lambda = 532$ nm. This prepares the defect into the phonon sideband above the excited state. After a fast non-radiative decay the NV center ends up in the excited state $|e\rangle$. From the excited state the NV center can decay either to the ground-state $|g\rangle$ by re-emission of a photon or to the singlet state $|m\rangle$, which has a long lifetime $\tau \sim 250$ ns. The latter process occurs preferentially from the $m_S = \pm 1$ states and leads to a spin-dependent fluorescence, which enables spin-state read-out. Furthermore, the decay from the singlet states preferentially populates the $m_S = 0$ state, which results in optically induced spin polarization under laser illumination and provides the basis for initialization of the electron spin. This is an important prerequisite for quantum sensing and information processing applications (see section 2.5). The spin polarization that can be achieved with this very simple method reaches up to 95% [39].

2.4 Spin states of the NV^- electronic ground-state

In the following, we want to describe, in further detail, the structure of magnetic states of the NV center in its electronic ground-state. We will consider the zero-field-splitting, due to spin-spin interaction, the Zeeman splitting and the related g-factor and finally turn to the hyperfine structure of the defect due to the intrinsic nitrogen nuclear spin.

2.4.1 Zero-field and Zeeman splitting

The electron spin eigenstates of the NV center in the orbital ground-state with $S = 1$ are defined by the Hamiltonian $H_{e,gs}$, which consists of a zero field splitting term (ZFS) due to spin-spin interaction and a Zeeman interaction term due to coupling to external magnetic fields \vec{B}_0 :

$$\hat{H}_{e,gs} = D_{gs} S_z^2 - \gamma_e \vec{B}_0 \vec{S}. \quad (2.1)$$

Here, we have neglected the effect of strain and higher order spin-orbit coupling and introduced the ZFS energy $D_{gs} = 2\pi \times 2.87$ GHz. The most precise measurement of the g-factor g_e of the NV center is given by [69]

$$g_e = -2.0029(2), \quad (2.2)$$

which differs only very slightly from the value of the free electron [70]

$$g_{\text{free}} = 2.00231930436256(35). \quad (2.3)$$

The anisotropy of the g-factor of the NV center is negligible. The gyromagnetic ratio $\gamma_e = g_e \mu_B / \hbar$ of the NV center thus coincides very well with the one of the free electron.

If no external magnetic field \vec{B}_0 is applied the eigenstates of the Hamiltonian are eigenstates of the S_z operator and the projections $m_S = \pm 1$ are degenerate. This degeneracy of the S_z eigenstates is lifted by the application of an external field. The field is in most experiments aligned along the z-direction, which simplifies the Hamiltonian to:

$$\hat{H}_{e,gs,\parallel} = D_{gs} S_z^2 - \gamma_e B_0 S_z. \quad (2.4)$$

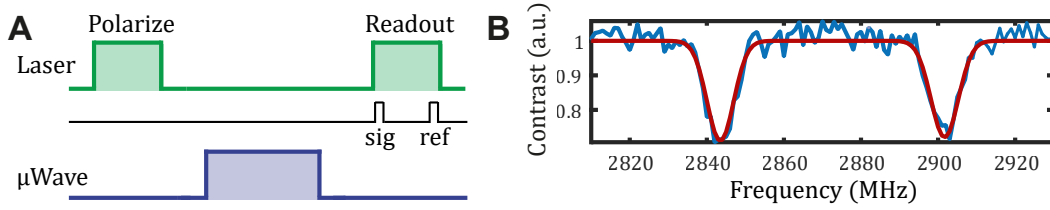


FIGURE 2.3: **Optically detected magnetic resonance.** (a) Experimental sequence for pulsed optically detected magnetic resonance. Initially, the NV center spin state is initialized with a short laser pulse (duration $\sim 2 \mu\text{s}$) and subsequently a microwave pulse with frequency f drives a transition to either the $m_S = +1$ or $m_S = -1$ state, if f matches one of the two magnetic transition frequencies. Finally, a second laser pulse detects the spin-state of the NV center. (b) Resulting measurement spectrum of the normalized photon count rate (averaged over many repetitions of the experiment) as a function of the microwave frequency f . Note that the photon count rate is integrated only for a short time window after the start of the second laser pulse. These integration windows are indicated in (a) as *sig* and *ref* for the sensor signal and a reference measurement, respectively. Details on the time-resolved photon integration follow in Chapter 4.

The z-direction is defined by the symmetry axis of the defect, which points along the $\langle 111 \rangle$ direction of the diamond crystal. The resulting energy diagram of the three magnetic states in the ground-state is shown in Fig. 2.2 (b).

2.4.2 Optically detected magnetic resonance

The combination of optically induced spin polarization, spin dependent fluorescence and the Zeeman splitting of the m_S states (eigenstates of S_z) provides the basis for the phenomenon of optically detected magnetic resonance (ODMR), which is the fundamental physical mechanism for using the NV center as a local magnetic field sensor. To explain the mechanism, we will consider the following experimental protocol which is schematically illustrated in Fig. 2.3 (a). Initially, we illuminate the NV center for a short duration (typically $2 \mu\text{s}$) with a laser pulse ($\lambda = 532 \text{ nm}$) to initialize it in the $m_S = 0$ state. Subsequently, we apply a microwave pulse with frequency f . Finally, we apply a second laser pulse and detect photons that are emitted by the NV center. After averaging this experiment over many iterations (typically $10^5 - 10^6$ repetitions), to build up sufficient photon statistics, we observe a signal trace as shown in Fig. 2.3 (b). We can identify a reduced number of average photon counts, if the microwave frequency f is tuned to a transition from the bright $m_S = 0$ state to either the $m_S = +1$ or $m_S = -1$ dark state. As this transition frequency between the m_S states depends on the applied external field via the Zeeman effect, the local magnetic field at the position of the NV center can be inferred by detecting the magnetic resonance effect optically. This basic magnetometry method will be extended to more sensitive, coherent methods in section 2.5 of this chapter.

2.4.3 Hyperfine structure due to the intrinsic nitrogen spin

Each NV center possesses the intrinsic nuclear spin of the nitrogen atom leading to a hyperfine splitting of the $m_S = \pm 1$ states. In principle the naturally most abundant nuclear spin is of ^{14}N isotope with spin $I = 1$. However, in all experiments reported in this thesis the nitrogen atom is of ^{15}N isotope with spin $I = 1/2$, due to the isotope choice during ion implantation which is employed for NV center generation (see chapter 4 for details). To describe the composite two spin system, we extend the

Hamiltonian $\hat{H}_{e,gs,\parallel}$ with a nuclear Zeeman term and the hyperfine interaction term:

$$\hat{H}_{en,gs,\parallel} = D_{gs}S_z^2 - \gamma_e B_0 S_z - \gamma_{^{15}\text{N}} B_0 I_z + \vec{S}\mathbf{A}\vec{I}. \quad (2.5)$$

Here, $\gamma_{^{15}\text{N}}/(2\pi) = -4.316 \text{ MHz/T}$ is the gyromagnetic ratio of the nitrogen nuclear spin and \mathbf{A} is the hyperfine tensor, which describes the coupling between the electron and the nuclear spin of the NV center. The hyperfine tensor in the principal axis system (PAS) can be written as:

$$\mathbf{A} = \begin{pmatrix} A_{11} & 0 & 0 \\ 0 & A_{22} & 0 \\ 0 & 0 & A_{33} \end{pmatrix}. \quad (2.6)$$

In the electronic ground-state the hyperfine tensor components are given by $a_{\perp} = A_{11} = A_{22} = 2\pi \times 3.65 \text{ MHz}$ and $a_{\parallel} = A_{33} = 2\pi \times 3.05 \text{ MHz}$ [68]. In the excited state only the A_{33} component has been characterized experimentally and exceeds $2\pi \times 60 \text{ MHz}$ [71]. Using the hyperfine tensor in the PAS, we rewrite the Hamiltonian of the composite electron-nuclear spin system and obtain:

$$\hat{H}_{en,gs,\parallel,PAS} = D_{gs}S_z^2 - \gamma_e B_0 S_z - \gamma_{^{15}\text{N}} B_0 I_z + a_{\parallel} S_z I_z + a_{\perp} (S_x I_x + S_y I_y). \quad (2.7)$$

Flip-flop transitions of the electronic and nuclear spin are strongly suppressed due to the large energy mismatch in our experiments. Therefore, we can usually neglect the last term in the previous Hamiltonian, thus finally arriving at the secular Hamiltonian $\hat{H}_{en,gs,\parallel,PAS,Sec}$:

$$\hat{H}_{en,gs,\parallel,PAS,Sec} = D_{gs}S_z^2 - \gamma_e B_0 S_z - \gamma_{^{15}\text{N}} B_0 I_z + a_{\parallel} S_z I_z. \quad (2.8)$$

The resulting energy states are indicated in Fig. 2.2 (c). We note, that the intrinsic nitrogen nuclear spin can be a useful additional resource for quantum sensing experiments, as it can serve as a nuclear quantum memory[72, 73] and enables repetitive read-out schemes[73, 74]. The splitting of the electron spin states $m_S = \pm 1$ into a doublet can experimentally be resolved by ESR spectroscopy and a typical hyperfine-resolved spectrum of a single NV center is shown in Fig. 2.5 (b).

2.5 Magnetometry with the NV center

In the following paragraphs we will describe how the room-temperature quantum coherence between the m_S states of the NV center can be leveraged for sensitive detection of local magnetic fields. We now assume that a static external bias field B_0 is aligned with the quantization axis of the NV center. This bias field enables us to selectively operate with the effective two-level system, defined by the $m_S = 0$ ($|0\rangle$) and $m_S = -1$ ($|-1\rangle$) states. The transition frequency between these two states is given by $\omega_{-1} = D_{gs} - \gamma_e B_0$. We pick these levels because the transition frequency can be covered with our measurement electronics over a large range of bias fields B_0 .

At the beginning of every sensing experiment performed during this thesis work, we use a short laser pulse to polarize the NV center in the $m_S = 0$ state. Subsequently, we apply a microwave pulse sequence which manipulates the spin state of the NV center. This pulse sequence actuates the spin such that it becomes susceptible to an a-priori unknown magnetic field $B(t)$ that we wish to detect. Finally, the

NV center is read out with a second laser pulse and the information on B is encoded in the probability p that the spin state has changed from the $m_S = 0$ state.

2.5.1 Magnetic field sensing with the Ramsey method

The interferometric Ramsey pulse sequence¹ provides the basis for most common quantum sensing sequences. The sequence is shown in Fig. 2.4 (a). Here, the NV spin is initially prepared in the superposition state $|\psi_i\rangle$ of the $m_S = 0$ and the $m_S = -1$ state by employing a $\pi/2$ rotation:

$$|\psi_i\rangle = \frac{1}{\sqrt{2}} (|0\rangle + |-1\rangle). \quad (2.9)$$

In the reference frame rotating with the transition frequency between the energy levels $\omega_{-1} = D_{gs} - \gamma_e B_0$ the phase relation for this superposition state of $m_S = 0$ and $m_S = -1$ remains constant over time. Thus, the quantum state after a evolution time τ is unchanged in this rotating reference frame. Hence a second, in-phase, $\pi/2$ rotation results in the final state $\psi_f = |-1\rangle$. This final state is experimentally detected with a second laser pulse. We thus conclude that if apart from the static bias field B_0 no additional Zeeman field interacts with the NV spin and the microwave frequency is properly calibrated to ω_{-1} , we find a probability of $p = 100\%$ that the NV center changes from $m_S = 0$ to $m_S = -1$ independent of the waiting time τ .

If, however, a second unknown magnetic field $B(t)$ acts on the sensor along the quantization axis, it will imprint a shift on the phase during the waiting time, given by:

$$\phi(\tau) = \int_0^\tau \gamma_e B(t') dt'. \quad (2.10)$$

The resulting quantum state $|\psi(\tau)\rangle$ after the waiting time is thus given by:

$$|\psi(\tau)\rangle = \frac{1}{\sqrt{2}} (|0\rangle + \exp(-i\phi(\tau)) |-1\rangle). \quad (2.11)$$

The phase shift is subsequently converted to a detectable change in the spin state populations by the second $\pi/2$ pulse, which results in the state $|\psi_f(\tau)\rangle$:

$$|\psi_f(\tau)\rangle = \frac{1}{2} (1 + \exp(-i\phi(\tau))) |0\rangle + \frac{1}{2} (1 - \exp(-i\phi(\tau))) |-1\rangle. \quad (2.12)$$

The final readout laser pulse detects the probability of finding the NV center in the $|0\rangle$ state. The transition probability of the NV center from the initial state is then given by:

$$p(\tau) = 1 - |\langle 0 | \psi_f(\tau) \rangle|^2. \quad (2.13)$$

As an example let us assume that the unknown magnetic field $B(t)$ is constant over time $B(t) = B_c$. In this case the phase shift amounts to $\phi(\tau) = \gamma_e B_c \tau$ and thus the state after the waiting time τ is given by:

$$|\psi_f(\tau)\rangle = \frac{1}{2} (1 + \exp(-i\gamma_e B_c \tau)) |0\rangle + \frac{1}{2} (1 - \exp(-i\gamma_e B_c \tau)) |-1\rangle. \quad (2.14)$$

¹Named after the American physicist Norman Ramsey (1915-2011).

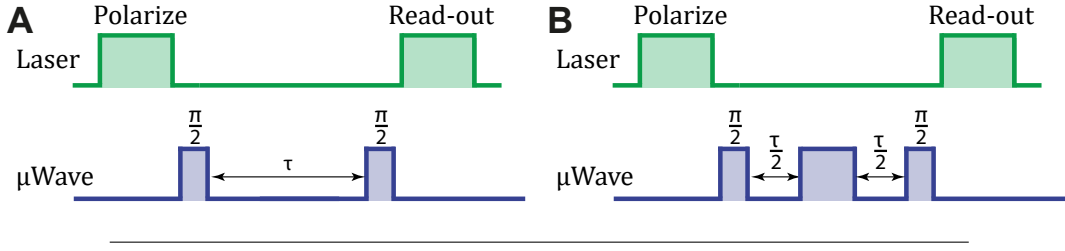


FIGURE 2.4: **Ramsey and Spin echo magnetometry sequences.** (a) Experimental Ramsey spectroscopy sequence applied to the NV center. Initially, the NV center is prepared in the $m_s = 0$ state with a Laser pulse. Subsequently, a microwave pulse with rotation angle $\pi/2$ prepares a coherent superposition state of the $m_s = 0$ and $m_s = -1$ manifold. The coherence precesses and acquires a phase that depends on the magnetic field acting on the NV center during the waiting time τ . The resulting phase, as given by Eq. 2.10, is converted into a detectable spin state population with the second $\pi/2$ pulse and readout with the final laser pulse. (b) Spin echo sequence for NV magnetometry. In comparison to the Ramsey sequence the pulse sequence is extended by a refocusing π -pulse, which is applied after half of the free precession time $\tau/2$. This enables the detection of ac signals, as discussed in further detail in the text.

Using equation 2.13 we infer the transition probability $p(\tau)$, which reads:

$$p(\tau) = \sin^2(\gamma_e B_c \tau) = \frac{1}{2} (1 - \cos(\gamma_e B_c \tau)). \quad (2.15)$$

Consequently, the unknown static field B_c can be detected by recording the transition probability of the NV center for varying τ . From equation 2.15 we can directly infer that if the static perturbation B_c is small, the waiting time τ needs to be long to ensure a detectable variation in p . This statement will be further clarified in the following paragraph.

Quadratic or variance detection

After deriving the sensor output $p(\tau)$, we can in a next step derive an approximate expression in the limit of small acquired sensor phases $\phi(\tau)$. In the following we will keep the assumption that the unknown magnetic field is constant over time $B(t) = B_c$. Further, we will assume that the magnetic field is small, so that in fact the sensor phase is small $\phi(\tau) = \gamma_e B_c \tau \ll 1$. In this case we can perform a Taylor expansion of the cosine function in Equation 2.15: $\cos(x) \approx 1 - 1/2x^2 + \mathcal{O}(x^4)$ for $x \ll 1$. Applying the expansion to Equation 2.15 we obtain:

$$p(\tau) \approx \frac{1}{2} (1 - 1 + 1/2(\gamma_e B_c \tau)^2) = \frac{1}{4} \gamma_e^2 B_c^2 \tau^2 = \frac{1}{4} \phi(\tau)^2. \quad (2.16)$$

We observe that the variation in the sensor output $p(\tau)$ depends quadratically on the acquired phase $\phi(\tau)$ for small $\phi \ll 1$. For this reason the detection sequence is also called quadratic or variance detection [22], because fluctuating magnetic fields with $\langle B(t) \rangle = 0$ can be detected as long as the variance does not vanish $\langle B^2(t) \rangle \neq 0$. This is particularly useful for the spectroscopy of noise processes as discussed in further detail in Chapter 3 and in [22, 75, 76].

Linear magnetic field detection

The Ramsey spectroscopy sequence is most sensitive to small signals when operated in the so-called linear detection regime. This measurement regime can be realized, e.g., by phase shifting the second $\pi/2$ -pulse by 90° relative to the first one. In this case the resulting transition probability of the sensor is given by:

$$p(\tau) = \frac{1}{2}(1 - \sin(\gamma_e B_c \tau)). \quad (2.17)$$

We can again perform a Taylor expansion of the transition probability $\sin(x) = x + \mathcal{O}(x^3)$ for $x \ll 1$ and obtain:

$$p(\tau) \approx \frac{1}{2}(1 - \gamma_e B_c \tau) = \frac{1}{2} - \frac{\gamma_e}{2} B_c \tau = \frac{1}{2} - \frac{1}{2} \phi(\tau). \quad (2.18)$$

The signal depends now linearly, instead of quadratically, on the small phase $\phi(\tau)$ and therefore more sensitive detection of magnetic fields with $\langle B(t) \rangle \neq 0$ is feasible.

2.5.2 Magnetic field sensitivity of Ramsey spectroscopy

At this point we can derive the magnetic field sensitivity of a spin-based quantum sensor when operated with Ramsey spectroscopy in the linear detection regime. Sensitivity in units of T/ $\sqrt{\text{Hz}}$ is defined as the minimum field that yields unit SNR for an total measurement duration of $T = 1$ s [22, 36]. The general expression for the SNR is given by:

$$\text{SNR} = \frac{\delta p}{\sigma_p}, \quad (2.19)$$

where δp is the variation in the sensor output $p(\tau)$ and σ_p is the readout uncertainty of the sensor variation. To derive sensitivity, we constrain the following derivation steps to the linear detection regime. Hence, the variation in the sensor output is given by $\delta p = 1/2 \gamma_e B_c \tau$, as derived in equation 2.18. The readout uncertainty is composed of several contributions that we will summarize now. The description follows in parts [36] and [22]:

Readout noise sources

- *Quantum projection noise:* A single readout of the quantum sensor in the state $|\psi\rangle = \alpha|0\rangle + \beta|-1\rangle$ yields a discrete outcome of detecting either the state $|0\rangle$ with probability $|\alpha|^2$ or the state $|-1\rangle$ with probability $|\beta|^2$. If we want to estimate, for example, $p = |\alpha|^2$ we have to perform a set of M measurements with M_0 outcomes of detecting the sensor in state $|0\rangle$ and M_1 realizations of detecting the state $|-1\rangle$. The estimate of p , is then given by: $p = \frac{M_0}{M}$. The associated uncertainty $\sigma_{p,qp}$ of this estimate is given by the variance of the binomial distribution $\sigma_{p,qp}^2 = \frac{1}{M} p(1-p)$. In the linear detection limit, we have $p \sim 0.5$ and thus the variance due to projection noise is given by

$$\sigma_{p=0.5,qp}^2 \approx \frac{1}{4M}. \quad (2.20)$$

- *Photon shot noise:* The readout of the NV center's spin state is realized by detecting fluorescence photons. The detection itself is a stochastic process due to

Quantity	Value	Reference
zero phonon line λ_{ZPL}	637 nm (1.945 eV)	[39]
number of valence electrons n_V	6	[35, 39]
ground-state electronic configuration	$a_1^2 e^2$	[39]
excited-state electronic configuration	$a_1^1 e^3$	[39]
ground-state zero field splitting D_{gs}	$2\pi \times 2.87$ GHz	[39]
excited-state zero field splitting D_{es}	$2\pi \times 1.42$ GHz	[39]
electronic g-factor g_e	2.0028	[39]
ground-state spin quantum number	$S = 1$	[39]
excited-state spin quantum number	$S = 1$	[39]
maximum ODMR contrast C	30 – 38 %	[35]
optical electron spin polarization	~ 95 %	[35]
ground-state parallel hyperfine coupling to ^{14}N	$-2\pi \times 2.16$ MHz	[39]
ground-state parallel hyperfine coupling to ^{15}N	$2\pi \times 3.05$ MHz	[77]
ground-state quadrupole shift from ^{14}N	$2\pi \times 5$ MHz	[77]
room-temperature spin lifetime T_1	$\sim 1 - 5$ ms	[77]
room-temperature dephasing time T_2^*	$\sim 1 - 2$ μs (1.1 % ^{13}C)	[20]
room-temperature dephasing time T_2^*	$\sim 10 - 20$ μs (<0.3 % ^{13}C)	[62]
room-temperature decoherence time T_2	up to $\sim T_1$ under decoupling	[78]
photon rate (bulk diamond, air objective)	~ 50 kCts/s	[79]
photon rate (patterned diamond, air objective)	~ 500 kCts/s	[74]

TABLE 2.1: **Data base of physical properties of the NV^- defect at room-temperature.** This table summarizes the most important electronic, optical and magnetic properties of the NV^- defect center in diamond. All parameters refer to the room-temperature value if not specified else wise.

the inherent shot noise. The associated variance of this Poissonian process is given by $\sigma^2 = c$, where c is the number of photon counts detected. The average number of detected photons for a single readout is given by the photon count rate $R_p \approx 50$ kCts/s (see Table 2.1, for bulk diamonds) multiplied with the readout duration $t_r \approx 500$ ns (see Section 4.3.2), which yields $R_p \times t_r \approx 0.03$. Consequently, we detect significantly less than one photon per readout on average. Therefore, it is clearly not possible to detect the spin state of the NV center with a single experimental realization and we can thus only detect the average spin state by performing the same experiment many times.

We will assume now that we have performed M repetitions of an sensing experiment and have recorded c photon counts from which we want to estimate the transition probability p . In addition, we have reference values for the number of detected photons for the same number of measurements for the bright state $m_S = 0$ indicated by c_0 and for the dark state $m_S = -1$ indicated by c_{-1} . In this case we can estimate the probability p by the following relation:

$$p = \frac{c - c_0}{c_{-1} - c_0}. \quad (2.21)$$

Now, we want to estimate the uncertainty in p , under the assumption that the measurement of c_p is limited by shot noise and that the reference values for c_0 and c_{-1} incur no statistical uncertainty. Due to the Poissonian character of shot noise the variance in c_p is given by $\sigma_c^2 = c_p$ as discussed above. Therefore the

variance in p is given by:

$$\sigma_{p,sn}^2 = \left(\frac{1}{c_{-1} - c_0} \right)^2 \sigma_c^2 = \left(\frac{1}{c_{-1} - c_0} \right)^2 c_p. \quad (2.22)$$

To express this uncertainty as function of the number of measurements, in analogy to the quantum projection noise described before, we have to express the number of collected photons as a function of the number of measurements. This relation is given by: $c_p = (1 - pC)MR_p t_r$, where R_p is the photon count rate (see Table 2.1), C is the ODMR contrast and t_r is the integration duration of the readout laser pulse (see Chapter 4). Inserting this expression into the relation for the shot noise relation, we obtain:

$$\sigma_{p,sn}^2 = \left(\frac{1}{(1 - C)MR_p t_r - MR_p t_r} \right)^2 (1 - pC)MR_p t_r = \frac{1 - pC}{C^2 MR_p t_r}. \quad (2.23)$$

The final expression can be further simplified at $p = 0.5$ to make comparison with the quantum projection noise more convenient:

$$\sigma_{p,sn}^2 = \frac{\alpha}{4M} = \alpha \times \sigma_{p=0.5,qp}^2. \quad (2.24)$$

Here the factor α expresses how strongly shot noise dominates over the projection noise. Under typical experimental conditions and for $p = 0.5$ the pre-factor α is given by: $\alpha = \frac{1 - C/2}{C^2 R_p t_r} \approx 400$. Shot noise is thus by $\sqrt{\alpha} = 20$ more significant than the quantum projection noise. Here, we have assumed a fluorescence count rate detected from the NV center of $R_p(m_S = 0) = 50$ kCts/s and a fluorescence contrast of $C = 30\%$.

- *Decoherence*: Decoherence of the quantum sensor during the waiting time τ originates either from spin flip processes of the sensor spin or dephasing due to low-frequency magnetic noise. In both cases the sensor variation δp is reduced and the reduction can be very generally modeled by a phenomenological decoherence function $\Xi(\tau) \propto (\Gamma\tau)^\beta$ in the form $\delta p_d(\tau) = \delta p(\tau) \exp(-\Xi(\tau))$ [22]. Here, Γ is the decoherence rate and $\beta \in [1, 3]$ depends on the underlying decoherence mechanism.

After we have derived the different noise sources limiting the performance of the sensor, we can compute the signal to noise ratio $\text{SNR} = \frac{\delta p}{\sigma_p}$. For the signal variation δp_d , we will use the model including decoherence:

$$\delta p_d = \delta p \times (\tau) \exp(-\Xi(\tau)). \quad (2.25)$$

Furthermore, we include an exponential dephasing term

$$\exp(-\Xi(\tau)) = \exp(-\tau/T_2^*), \quad (2.26)$$

with dephasing time T_2^* . For the noise term σ_p , we constrain ourselves to the shot noise contribution as the quantum projection noise term is orders of magnitude smaller for $p = 0.5$. Further, we can approximate $\frac{1 - C/2}{C^2} \approx 1/C^2$. Hence, we find for the SNR:

$$\text{SNR}(\tau, M) = \delta p \exp(-\Xi(\tau)) C \sqrt{MR_p t_r} = \gamma_e B_c \tau \exp(-\tau/T_2^*) 2C \sqrt{MR_p t_r}. \quad (2.27)$$

Finally, we compute the sensitivity, which is the minimum detectable field B_c for a total integration time $T = 1$ s for which a $\text{SNR} = 1$ is reached. Setting $\text{SNR}(\tau, M) = 1$ and solving for $B_c = B_{\min}$, we obtain:

$$B_{\min}(\tau, M) = \frac{\exp(\tau/T_2^*)}{2C\gamma_e\tau\sqrt{MR_p t_r}} \quad (2.28)$$

The total duration of a single experiment is given by $\tau + t_r + t_i$, where t_i is the duration of sensor initialization. This corresponds to the duration of the laser pulse in our experiments. Consequently, the total duration of M experiments is given by $T(M) = M \times (\tau + t_r + t_i)$. Setting $T(M) = 1$ s and solving for M we find the number of experiments that can be performed in 1 s: $M = \frac{1}{\tau + t_r + t_i}$. Inserting this expression for M into Equation 2.28 we obtain the Ramsey sensitivity $\eta_R(\tau)$:

$$\eta_R(\tau) = B_{\min}(T = 1 \text{ s}) = \frac{\exp(\tau/T_2^*)\sqrt{\tau + t_r + t_i}}{2C\gamma_e\tau\sqrt{R_p t_r}}. \quad (2.29)$$

If we assume that the evolution time is significantly longer than readout and initialization durations, $\tau \gg t_r + t_i$, which is fulfilled for isotopically purified samples with long electron spin dephasing times, the optimum evolution/sensing time is given by $\tau = T_2^*/2$ [22]. In this case we find for the optimum sensitivity:

$$\eta_{R,\text{opt}} = \frac{\sqrt{2e}}{\gamma_e C \sqrt{T_2^*} \sqrt{R_p t_r}} \quad (2.30)$$

To finally compute the optimum Ramsey sensitivity for the experimental parameters typical in our experiments, we insert $R_p = 50$ kCts/s, $C = 0.3$, $T_2^* = 5$ μ s and $t_r = 500$ ns and obtain: $\eta_{R,\text{opt}} = 125$ nT/ $\sqrt{\text{Hz}}$.

2.5.3 Detection of ac signals

At the heart of this thesis is the detection of nuclear spins with the NV center. To detect these precessing spins we require a method that detects the resulting time-dependent signal. In principle also the static field of the nuclei could be detected [80], but ac sensing tends to be more sensitive. According to equation 2.10 the phase ϕ accumulated during the Ramsey sequence is proportional to the integral of the magnetic field $B(t)$. Thus for a rapidly oscillating magnetic field the phase accumulation is averaged out over the waiting time:

$$\phi(\tau) = \gamma_e \langle B_c(t) \rangle \rightarrow 0. \quad (2.31)$$

In fact, the Ramsey sequence is not sensitive to signals that vary faster than a low-frequency cut-off [22]. Thus we require a different pulse sequence to gain sensitivity to alternating signals.

Hahn echo method

The most common approach to detect ac signals is based on the well-known Hahn echo method, which is shown in Fig. 2.4 (b). In the Hahn echo sequence a third microwave pulse with a π rotation angle is inserted in the middle of the waiting time. This π pulse inverts the sign of the phase accumulation, such that the acquired

phase after the total waiting time 2τ amounts to:

$$\phi(2\tau) = \int_0^\tau \gamma_e B_c(t') dt' - \int_\tau^{2\tau} \gamma_e B_c(t') dt'. \quad (2.32)$$

The Hahn echo sequence thus rectifies a sinusoidal signal whose period exactly fits into the waiting duration 2τ and whose phase is matched with the sensing sequence. Hence the refocusing pulse leads to a phase build-up that would be exactly cancelled in the Ramsey sequence. In other words, the Hahn echo sequence can be tuned into resonance with ac signals at frequency $f_c = 1/(2\tau)$ by varying the waiting time τ before and after the π pulse. In fact, as discussed in detail in Chapter 3, the Hahn echo sequence effectively acts as a filter with center frequency f_c and filter bandwidth given by the total waiting time 2τ .

Further, the Hahn echo sequence can be extended by adding additional π -pulses in the waiting time to further prolong sensor coherence and design more complex filter characteristics. Details on the detection of ac signals using these so-called multi-pulse dynamical decoupling sequences will follow in Chapter 3 and 5. In addition, in Chapter 8, we will present a novel detection method based on the differential application of two refocusing pulses that enables the more general task of reconstruction-free detection of arbitrary magnetic waveforms $B(t)$.

Sensitivity for Hahn echo detection

The optimal sensitivity of the Hahn echo sequence to time-dependent signals $B(t)$ can be derived in analogy to the Ramsey sequence and the enhancement due to the prolonged coherence time $T_2^{\text{echo}} > T_2^*$ results in the echo sensitivity η_E :

$$\eta_E = \sqrt{\frac{T_2^*}{T_2^{\text{echo}}}} \eta_R. \quad (2.33)$$

As the coherence time T_2^{echo} is typically one order of magnitude larger than T_2^* the optimum sensitivity is approximately improved by a factor of $\times 3$ for the detection of ac signals using the echo method with potential further improvement with multi-pulse sequences.

2.6 Coherence and lifetime properties of the m_S -states

As discussed in the previous section 2.5, the sensitivity of the NV quantum sensor and thereby its ability to detect remote nuclear spins or other faint sources of magnetic signals is limited by the coherence time of the sensor spin. In this context, we now report on the typical coherence times that we observe for shallow NV centers in two different electronic-grade samples from ElementSix.

In recent years, the influence of a surface and the bulk bath of electronic spins [82, 83], surface-modified phononic coupling [84], fluctuating electric charges [85] and the nuclear spin bath of ^{13}C spins inside the diamond [86] and ^1H spins [75, 76] at the surface has been identified as sources of NV decoherence. In particular a depth-calibrated study [83] revealed, that NV coherence starts to significantly deteriorate at distances from the surface smaller than $d = 25$ nm.

The experiments reported in this work were performed on NV centers at a depth of $d \sim 8$ nm. This depth can be controlled by the energy of the ions during the implantation procedure, which we fixed to 5 keV. The estimated depth can be obtained

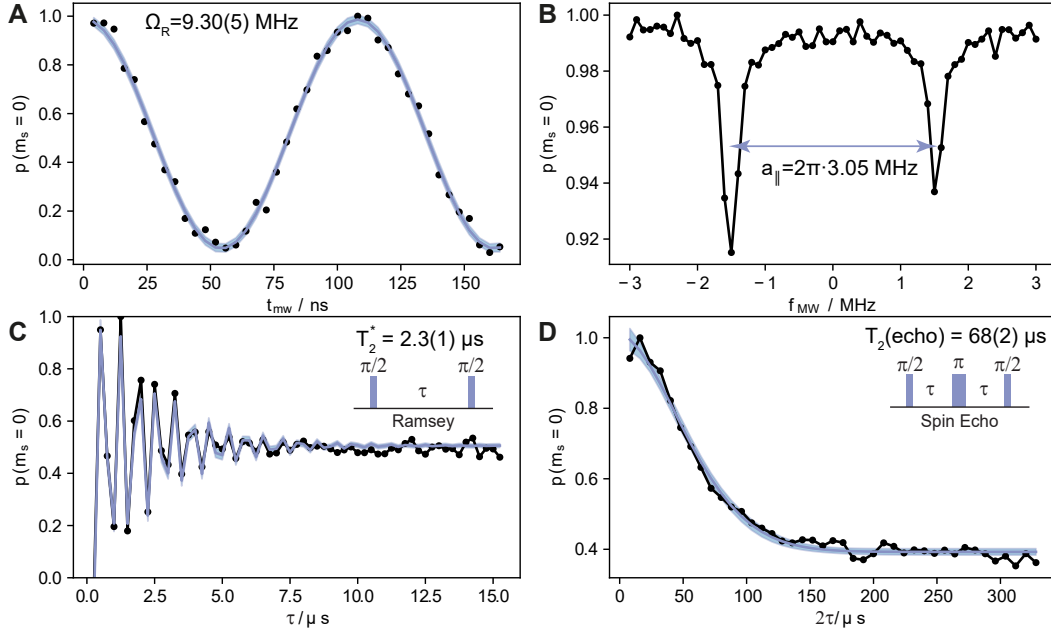


FIGURE 2.5: **Coherent control of the m_S states of the NV center.** (a) Microwave-driven Rabi oscillation between the $m_S = 0$ initial state and the $m_S = -1$ state. The probability of detecting the NV center in the $m_S = 0$ state after a resonant MW pulse (angular frequency $\omega_{\text{mw}} = D_{\text{gs}} - \gamma_e B_0$) of length t_{mw} is shown. The Rabi frequency amounts here to $\omega_R = 2\pi \times 9.30(5)$ MHz. In our experiments Rabi frequencies of up to $\omega_R \geq 2\pi \times 30$ MHz can be realized with a coplanar waveguide structure described in Chapter 4, which is positioned in the vicinity of the NV center. (b) Hyperfine-resolved spectroscopy of the transition between $m_S = 0$ and $m_S = -1$. The duration of the microwave pulse is fixed at $\sim 3 \mu\text{s}$ and the frequency of the pulse is swept across the resonance. Two resonances are detected due to the hyperfine splitting caused by the intrinsic nuclear spin of isotope ^{15}N . The energy levels of the spin system are described by the Hamiltonian given in Eq. 2.8. The asymmetry in the transition probability between the states is caused by the dynamical nuclear polarization effect during optical excitation of the NV center [81]. (c) Ramsey spectroscopy performed by the pulse sequence shown as an inset. The waiting time τ between the two $\pi/2$ pulses is swept to record the decay of Ramsey fringes due to dephasing. The modulation of the signal is due to a small detuning of the microwave frequency to the transition frequency. The dephasing time amounts to $T_2^* = 2.3(1) \mu\text{s}$. (d) Hahn-echo decay of the coherence between $m_S = 0$ and $m_S = -1$. The employed microwave pulse sequence is again shown as an inset. The total free-precession time 2τ is swept to detect the decay of coherence, which is described by the model $\exp(-(t_{\text{free}}/T_2)^n)$ with $t_{\text{free}} = 2\tau$. For the particular defect center we obtain $T_2(\text{echo}) = 68(2) \mu\text{s}$ and $n \approx 1.7$. All measurements shown in this figure were performed on the same NV center on sample E1303 described in Chapter 4. This sample is partially purified from ^{13}C spins and thus no ^{13}C revivals are found in the spin echo measurement.

by computer simulations using the SRIM software package². For our particular implantation energy the average depth is 8 nm with a straggle of 3 nm. When performing experiments with individual NV centers we initially characterize the dephasing time T_2^* and the Hahn echo decay time T_2^{echo} using the Ramsey and Hahn echo experiments discussed in the previous section. This is because NV centers show large variation in coherence times, as discussed below.

²Stopping Range of Ions in Matter.

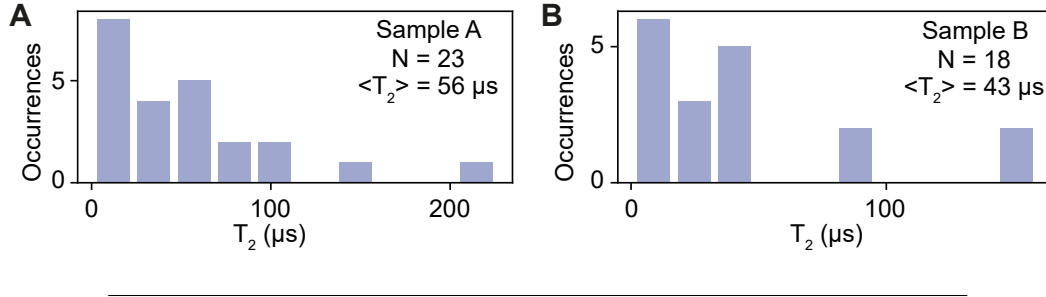


FIGURE 2.6: **Distribution of coherence times for shallow NV centers.** (a) Coherence time of NV centers (sample size $N = 23$) detected on the electronic-grade sample E1303 (see Chapter 4 for further details). We find an average coherence time of $\langle T_2 \rangle = 56 \mu\text{s}$. The NV centers were generated by ion implantation with an energy of 5 keV, which leads to a depth of $\sim 8 \text{ nm}$ below the diamond surface. The coherence time was measured with the Hahn Echo sequence. (b) Distribution of coherence times on a second sample with identifier: *Berta*, which is overgrown with a $50 \mu\text{m}$ layer of spin-free ^{12}C (concentration 99.999 %). NV centers were again generated with the same implantation energy. In addition, the sample is again of electronic-grade quality. We find a average coherence time of $\langle T_2 \rangle = 43 \mu\text{s}$ for a sample size of 18 NV centers.

Electron spin dephasing time T_2^*

In Fig. 2.5 (c), we show a representative measurement of the Ramsey coherence decay for a single NV center. The decay of the Ramsey contrast is caused by slow fluctuations of the local magnetic field, which is due to ^{13}C spins in the vicinity of the NV center, drifts in the static quantization field and due to spin flips in the electron spin bath at the surface and inside the diamond. The decay time $T_2^* = 2.3 \mu\text{s}$ represents a typical value for shallow NV centers with a natural abundance of ^{13}C nuclei in the sensor environment. The signal modulation is caused by a small detuning of the microwave oscillator to the electron spin transition. For NV defects which reside far from the surface inside the diamond crystal, which is additionally isotopically purified to reduce the concentration of ^{13}C spins the dephasing time can be prolonged by approximately an order of magnitude $T_2^* \sim 10 - 20 \mu\text{s}$ [62] at room-temperature.

Electron spin coherence time T_2^{echo}

In Fig. 2.5 (d), we show a representative measurement of the Hahn echo decay time T_2^{echo} performed on the same NV center. The microwave pulse sequence for this measurement is shown as an inset of the figure. The decay time of $T_2^{\text{echo}} = 68(2) \mu\text{s}$ again represents a typical result for NV centers at a depth of $d \sim 8 \text{ nm}$. The refocusing pulse consequently increases the sensor coherence by a factor of $\times 30$, which significantly increases the sensitivity to time-dependent magnetic fields.

In Fig. 2.6, we provide a more systematic study of the coherence time of shallow NV centers. We show two histograms of the coherence times acquired on shallow NV centers (implantation energy 5 keV) on two different electronic-grade samples. On both samples around 20 NV centers were investigated and the average coherence time is approximately $50 \mu\text{s}$.

Electron spin lifetime T_1

The lifetime of the electron spin T_1 specifies the time until the electron spin stochastically flips to a different m_S state. Spin flips at room-temperature are resulting

from thermally-activated, two-phonon Raman or Orbach-type processes [87] and from cross-relaxation of the NV center with nearby impurity spins. Impurity spins comprise nitrogen defects in the lattice (called P1 centers) originating, e.g., from the implantation procedure, dangling bonds at the surface and potentially distant NV centers. The typical spin lifetime of the electron spin of the NV center at room-temperature amounts to a few milliseconds, which is also correlated with the distance from the surface [82]. We note that at low temperatures ($T < 10$ K) the spin lifetime of the NV center can exceed hundreds of seconds [88].

Detection, polarization and control of remote nuclear spins

Summary

This chapter introduces the basic pulse sequences that enable the NMR experiments presented in Chapters 5,6 and 7 of this thesis. First, we will give a short description of the underlying spin system, which includes the NV electron spin surrounded by an ensemble of ^{13}C nuclei. In this context we will describe the Hamiltonian that governs the dynamics of the spin system. Further, we discuss how the presence of nuclear spins in the vicinity of the NV sensor can be detected and how nuclei can be polarized, spectroscopically characterized and controlled merely by periodically flipping the NV center between the $m_S = 0$ and $m_S = -1$ states. The pulse sequences discussed in this chapter have recently been established by various groups in the NV center research community and can be found in the selected references [77, 86, 89, 90].

3.1 Definition of the spin system

We consider in the following a spin system comprising the central electron spin of the NV center, which is coupled by the hyperfine interaction to N remote nuclear spins of the ^{13}C isotope with gyromagnetic ratio $\gamma_n = 2\pi \times 10.7084 \text{ MHz/T}$ (see Fig. 3.1 (a)). We assume that a magnetic bias field is applied to the system and aligned with the crystallographic quantization axis of the NV center (z -direction). Here, we neglect inter-spin coupling between the nuclei as the density of ^{13}C spins inside the diamond host at natural abundance is sufficiently low (1.1%). In addition, we also neglect the hyperfine splitting of the m_S states due to the intrinsic nitrogen spin (see Chapter 2 for details). The resulting Hamiltonian of the system can then be written as (operators S refer to the NV center and operators I refer to nuclear spins):

$$\hat{H}_{\text{SI}} = D_{\text{gs}} \hat{S}_z^2 - \gamma_e B_0 \hat{S}_z - \sum_{i=1}^N \gamma_n B_0 \hat{I}_{z,i} + \sum_{i=1}^N \vec{S} \mathbf{A}_i(\vec{r}_i) \vec{I}_i. \quad (3.1)$$

The coupling between each individual nuclear spin, described by the spin operators $\vec{I}_i = (\hat{I}_{x,i}, \hat{I}_{y,i}, \hat{I}_{z,i})$, to the central spin is given by the hyperfine tensor $\mathbf{A}_i(\vec{r}_i)$ and the

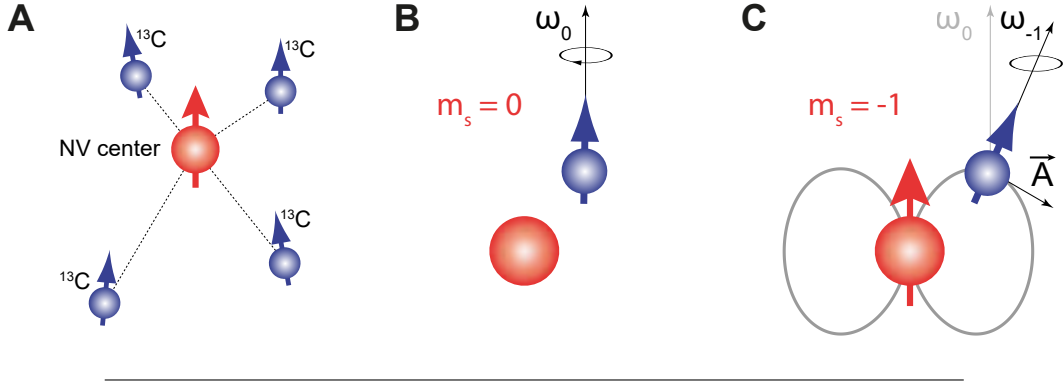


FIGURE 3.1: **Coupling of the NV center to ^{13}C nuclear spins in the diamond host.** (a) Schematic illustration of four ^{13}C nuclear spins coupled to the NV center via the hyperfine interaction. (b) Precession axis and frequency of a single ^{13}C spin if the NV center is in the $m_s = 0$ state. In this case the nuclear spin solely precesses along the external bias field B_0 and the precession frequency is given by $\omega_0 = \gamma_n B_0$. (c) If the NV center is prepared in the $m_s = -1$ state the additional hyperfine field of the NV center tilts the precession axis and leads to a variation of the precession frequency. The precession axis in this case is given by $\omega_{-1} = -\gamma_n B_0 \mathbf{e}_z - \mathbf{A}_z(\vec{r})$. The secular hyperfine vector $\mathbf{A}_z(\vec{r})$ contains information about the distance vector between NV and nuclear spin. The frequency of the precession is given by the magnitude of the precession axis vector, which is $\omega_{-1} = \sqrt{(\gamma_n B_0 + a_{\parallel})^2 + a_{\perp}^2}$. In the limit that the hyperfine interaction is weak compared to the Zeeman field: $\gamma_n B_0 \gg a_{\perp}, a_{\parallel}$, the precession frequency can be simplified to $\omega_{-1} = \gamma_n B_0 + a_{\parallel}$.

elements of the tensor depend on the distance vector $\vec{r}_i = (r_i, \theta_i, \phi_i)$ from the electron spin to the nucleus (details follow in the rest of this paragraph). Nuclear spins are called weakly coupled, if the hyperfine splitting is not resolved in ESR experiments, which means that the line width of the ESR transition exceeds the hyperfine splitting $1/(\pi T_2^*) \gg \|\mathbf{A}_i\|$. In the following, we will focus on the detection and control of these weakly coupled nuclear spins using dynamical decoupling techniques. To simplify the description, we will focus in the following on the composite spin system of the NV center and just a single nuclear spin.

3.2 Hyperfine interaction to remote spins

The hyperfine interaction for such a sufficiently distant nuclear spins is of dipolar character and in analogy to the interaction of two classical magnetic moments at distance $\vec{r} = (r, \theta, \phi)$ the energy can be written as [91]:

$$\hat{H}_{\text{HF}} = \frac{\mu_0 \gamma_e \gamma_i \hbar}{4\pi r^3} \left(\vec{S} \vec{I} - \frac{3(\vec{S} \cdot \vec{r})(\vec{I} \cdot \vec{r})}{r^2} \right). \quad (3.2)$$

In contrast, if nuclei are in close vicinity of the central spin an additional Fermi contact energy shift and the extent of the electron spin wavefunction have to be taken into account [68, 92]. As this will be discussed in detail in chapter 6, we constrain ourselves to the simplified discussion and assume that the electron spin generates the field of a point-dipole at the position of the nuclear spin, therefore Eq. 3.2 is exact.

With the exception of the experiments discussed in chapter 6 the bias magnetic field B_0 is very well aligned along the z -axis and therefore all terms of \hat{H}_{HF} that

do not commute with \hat{S}_z in Eq. 3.2 can be neglected. This simplifies the hyperfine interaction to the secular form:

$$\hat{H}_{\text{HF}} = \frac{\mu_0 \gamma_e \gamma_i \hbar}{4\pi r^3} \left((3 \cos^2 \theta - 1) \hat{S}_z \hat{I}_z + (3 \sin \theta \cos \theta) (\cos^2 \phi \hat{S}_z \hat{I}_x + \sin^2 \phi \hat{S}_z \hat{I}_y) \right). \quad (3.3)$$

To further simplify the discussion, we will now assume that the distance vector of the particular nuclear spin we consider lies in the xz -plane, i.e., $\phi = 0$. In Chapters 6 and 7 this simplification will be reconsidered, when the three-dimensional imaging of nuclear spins is demonstrated and ϕ is a critical observable. However, at this point the physics of the composite spin system is independent of ϕ . Using $\phi = 0$ in Eq. 3.3 allows us to write the hyperfine interaction in the form:

$$\hat{H}_{\text{HF}} = a_{\parallel} \hat{S}_z \hat{I}_z + a_{\perp} \hat{S}_z \hat{I}_x, \quad (3.4)$$

with the parallel and perpendicular hyperfine interaction parameters a_{\parallel} and a_{\perp} , respectively, given by:

$$a_{\parallel} = \frac{\mu_0 \gamma_e \gamma_n \hbar}{4\pi r^3} (3 \cos^2 \theta - 1), \quad (3.5)$$

$$a_{\perp} = \frac{\mu_0 \gamma_e \gamma_n \hbar}{4\pi r^3} 3 \sin \theta \cos \theta. \quad (3.6)$$

To finalize the derivation of spin system's Hamiltonian, we incorporate the just derived hyperfine coupling constants into equation 3.3:

$$\hat{H}_{\text{SI}} = D_{\text{gs}} \hat{S}_z^2 - \gamma_e B_0 \hat{S}_z - \gamma_i B_0 \hat{I}_z + a_{\parallel} \hat{S}_z \hat{I}_z + a_{\perp} \hat{S}_z \hat{I}_x. \quad (3.7)$$

3.3 Nuclear spin imaging

The coupling between the central electron spin and a specific nuclear spin can thus be characterized by two hyperfine coupling constants. These coupling constants contain information about the relative position of the nuclei from the electron spin. By inverting equation 3.5 and 3.6, we can directly estimate the radial distance and the polar angle of the distance vector from the hyperfine coupling constants:

$$\theta = \arctan \left\{ \frac{1}{2} \left(-3 \frac{a_{\parallel}}{a_{\perp}} + \sqrt{9 \frac{a_{\parallel}^2}{a_{\perp}^2} + 8} \right) \right\}, \quad (3.8)$$

$$r = \left\{ \frac{\mu_0 \gamma_e \gamma_n \hbar (3 \cos^2 \theta - 1)}{4\pi a_{\parallel}} \right\}^{1/3}. \quad (3.9)$$

Therefore, hyperfine spectroscopy of the parallel and perpendicular components provides spatial information about nuclear spins in the vicinity of the NV center and is a highly relevant set of parameters for nanoscale magnetic resonance imaging. Here, we exploit the gradient of the dipole field generated by the NV center for encoding nuclear positions into hyperfine frequencies.

In the remainder of this chapter we will introduce several spectroscopy methods that allow us to measure $(a_{\parallel}, a_{\perp})$ (for a summary see table 3.1). All methods are based on temporally controlling the hyperfine interaction between the NV center and nuclear spins. Thereby also coherent control and polarization transfer to the nuclei can be realized. In fact, all techniques can be efficiently realized merely using the method of dynamic decoupling applied to the NV center. Combined with the

Method	Observables	Spectral resolution	Reference
DD spectroscopy	$(\omega_0, a_{\parallel}, a_{\perp})$	$\sim 1/T_2$	Ch. 5, 6, 7
Spin state tomography	$(\omega_0, a_{\parallel}^a, a_{\perp}^a, \phi)$	$\sim 1/T_{2,\text{nuc}}^*$	Ch. 7
Correlation spectroscopy	$(\omega_0, a_{\parallel}, a_{\perp}, \phi^b)$	$\sim 1/T_1$	Ch. 6, 7
Polarization transfer	-	-	Ch. 7

TABLE 3.1: **Summary of measurement methods used in this work** This table summarizes the most important experimental sequences used for NMR imaging experiments with references to the corresponding chapter in which it is used. In this chapter we derive the accessible observables of all listed spectroscopy methods using the product operator method. ^aThe detection of $(a_{\parallel}, a_{\perp})$ using spin state tomography is not explicitly demonstrated in this work. ^bCorrelation spectroscopy gives access to the azimuthal position ϕ of nuclei in tilted magnetic quantization fields. For details, see chapter 6.

novel methods presented in chapters 6 and 7, which also gives access to the third component ϕ of the distance vector $\vec{r} = (r, \theta, \phi)$, we are then able to fully reconstruct the three-dimensional distance vector of individual spins.

3.4 Detection of the presence of nuclear spins

After deriving the coupling Hamiltonian between the NV center and a single nuclear spin, we now introduce the method of dynamical decoupling (DD), which enables the sensitive detection of weakly-coupled nuclei (as defined in section 3.1). Dynamical decoupling is a coherent control method, which protects the sensor from unwanted decoherence in a similar fashion as the well-known Hahn echo method. However, instead of a single refocusing pulse many pulses are applied to the sensor spin with inter-pulse delay τ . In fact, the number of pulses N in our system approaches 10^4 in particular applications demonstrated in Chapter 5 and enables much longer coherent evolution than the echo decay time T_2^{echo} .

3.4.1 Dynamical decoupling sequences

Experimental protocol

A particular implementation of multi-pulse dynamical decoupling that is almost exclusively used in our experiments is shown in Fig. 3.2 (a). The NV center is initially polarized in the $m_S = 0$ state with a laser pulse and subsequently prepared in a superposition of $m_S = 0$ and $m_S = -1$ with a $\pi/2$ -rotation around the x -axis using a microwave pulse. The resulting state can be written as:

$$|-Y\rangle = \frac{1}{\sqrt{2}}(|0\rangle - i|-1\rangle). \quad (3.10)$$

Subsequently, we apply a sequence of N equidistant π -pulses (inter-pulse spacing τ), known as the Carr-Purcell-Meiboom-Gill (CPMG) sequence [93]. We vary the rotation axes of the π -pulses in sub-blocks of 8 pulses according to the scheme X - Y - X - Y - X - Y - X - Y - X to minimize the influence of pulse error accumulation. As such this sequence is identified as the $XY8 - k$ pulse sequence where k denotes the number of repetitions of the fundamental building block and $N = 8k$ is the total number of microwave pulses excluding the $\pi/2$ rotations.

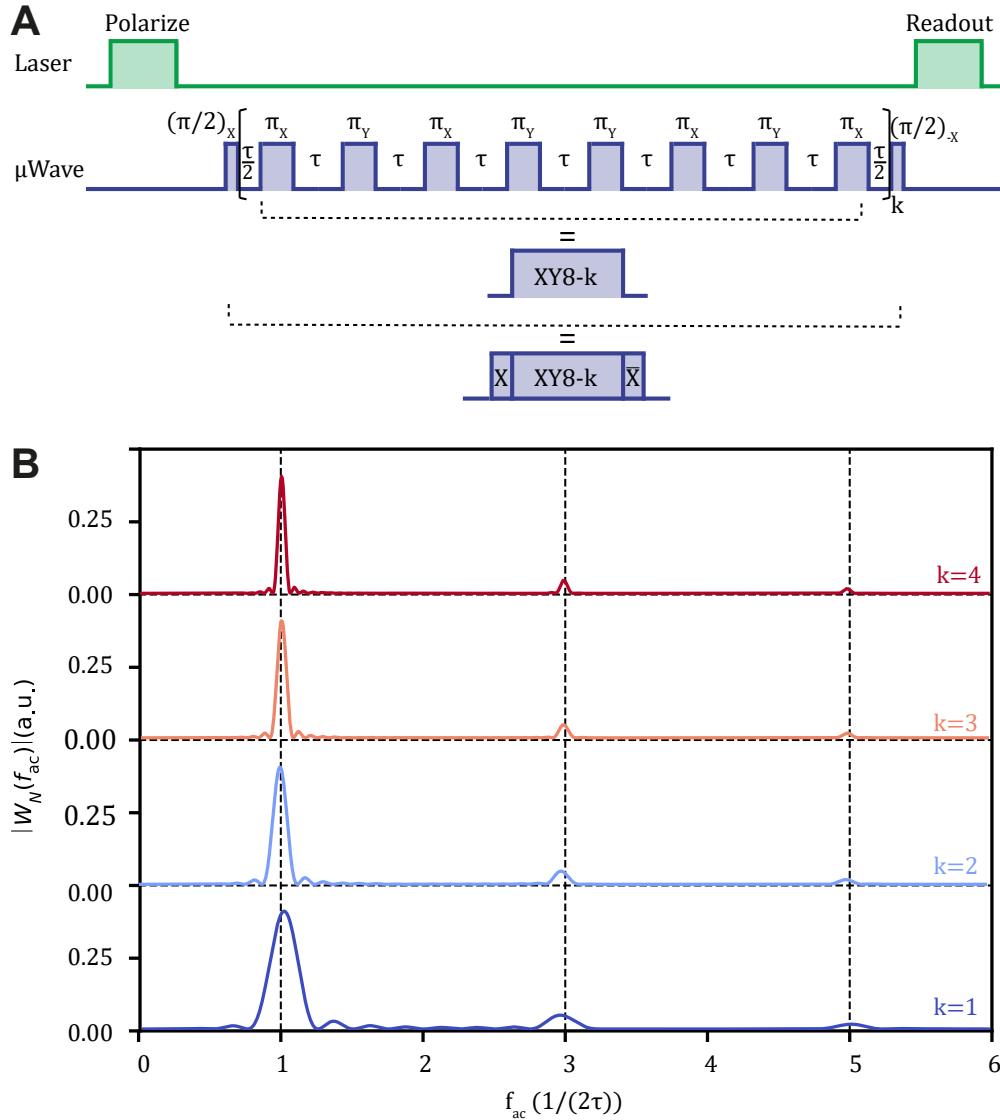


FIGURE 3.2: **Dynamical decoupling sequence with XY8 phase cycling.** (a) Experimental implementation: After polarizing the NV center with a short laser pulse (duration $\sim 2 \mu\text{s}$), we apply a sequence of in total $8k + 2$ microwave pulses ($8k$ up to 10.000 in Chapter 5). Initially, a coherent superposition is prepared with a $\pi/2$ rotation. Subsequently, we apply k repetitions of 8 π -pulses with the phase cycling scheme X-Y-X-Y-X-Y-X. The purpose of the phase alteration is to cancel pulse imperfections. The duration of π -pulses typically amounts to 20 – 40 ns and the pulses are shaped with a \cos^2 -envelope as discussed in Chapter 5. Finally, a second $\pi/2$ -pulse converts the phase Φ acquired during the refocusing pulses into a measurable polarization, which is subsequently readout with a second laser pulse. (b) Spectral weighting or frequency filter function $W_{N,\tau}(f_{ac})$ associated with spectroscopy sequence for $k = \{1, 2, 3, 4\}$. As described in the main text the dynamical decoupling sequence effectively acts as a filter with center frequency $f_c = 1/(2\tau)$ and with the filter bandwidth given by the total duration of the pulse sequence $\Delta f = 1/T = 1/(N\tau) = 1/(8k\tau)$. This method enables the sensitive detection of magnetic signals in a specific frequency window: By varying the inter-pulse delay τ , the sequence can be tuned into resonance with AC signals. Further, the back-action of the sensor spin during the sensing protocol on nuclear spins leads to the ability of controlled rotations of the latter.

Sensor phase accumulation during the sensing sequence

During the decoupling sequence a phase Φ accumulates between the states $m_S = 0$ and $m_S = -1$, in analogy to the Ramsey or Spin echo sequence described in Chapter 2. In the case of the multi-pulse decoupling sequence this phase is given by:

$$\Phi = \int_0^{N\tau} \gamma_e B(t') M(t') dt', \quad (3.11)$$

where $B(t)$ is the local magnetic field projected onto the quantization axis of the sensor spin and $M(t) = \pm 1$ is the modulation function of the pulse sequence, which changes sign whenever a π -pulse is applied to the sensor [22]. The quantum state after the multi-pulse sequence can be written as:

$$|\Phi\rangle = \frac{1}{\sqrt{2}}(|0\rangle - ie^{-i\Phi}|-1\rangle). \quad (3.12)$$

The final $\pi/2$ -pulse along the $-x$ -axis results in the final state

$$|\Psi\rangle = \cos(\Phi)|0\rangle + \sin(\Phi)|-1\rangle, \quad (3.13)$$

which is subsequently readout in the \hat{S}_z basis with a laser pulse. Consequently, we will detect the NV center in the bright state $|0\rangle$, if no phase Φ has been acquired during the sensing sequence. In the other extreme case, if the phase acquired during detection sequence corresponds to $\Phi = \pi/2$, we will detect the NV center in the dark state $|-1\rangle$.

Spectral weighting function of the sensing sequence

To get an intuitive understanding of phase accumulation during the multi-pulse sequence it is beneficial to consider the response of the sensor to a harmonic signal $B(t)$ of the form:

$$B(t) = B \cos(2\pi f_{ac} t + \alpha) \quad (3.14)$$

with amplitude B , frequency f_{ac} and phase α . In this case the acquired sensor phase Φ is given by [22]:

$$\Phi = \frac{\gamma_e B}{2\pi f_{ac}} \left[\sin(\alpha) - (-1)^N \sin(2\pi f_{ac} t + \alpha) + 2 \sum_{j=1}^N (-1)^j \sin(2\pi f_{ac} t_j + \alpha) \right] \quad (3.15)$$

$$= \gamma_e B t \times W_{N,\tau}(f_{ac}, \alpha), \quad (3.16)$$

where $0 < t_j < N\tau$ are the times at which the π -pulse with index j is applied. Here, we assume that the π -rotations are infinitely short. The limitations of this assumption are described in a recent study of our group [94]. In the second line of equation 3.16 we introduced, the spectral weighting function $W_N(f_{ac}, \alpha)$, which quantifies the sensitivity of the sensor under the dynamical decoupling sequence to a signal at frequency f_{ac} . The spectral weighting function for the CPMG-sequence shown in Fig. 3.2 (a) is given by [22]:

$$W_{N,\tau}(f_{ac}) = \left| \frac{\sin(\pi f_{ac} N\tau)}{\pi f_{ac} N\tau} [1 - \sec(\pi f_{ac} \tau)] \cos(\alpha + \pi f_{ac} N\tau) \right|, \quad (3.17)$$

In Fig. 3.2, we show this spectral weighting or filter function $W_{N,\tau}(f_{ac})$ for fixed inter-pulse spacing τ and variable number of pulses $N = \{8, 16, 24, 32\}$. Here, we

fixed the relative phase of the harmonic signal to the sensing sequence to $\alpha = 0$. Clearly, the sinc-term of the weighting function leads to a filter behavior with resonances, which become increasingly narrow for an growing number of pulses N . Consequently, the $XY8 - k$ sequence acts as a filter with center frequency given by $f_c = 1/(2\tau)$ and filter-bandwidth $\Delta f = 1/(N\tau)$. Therefore for large N the sensor is effectively decoupled from signals that are not resonant with the center filter frequencies defined by $f_c = q/(2\tau)$. Here, $q = \{1, 3, 5, \dots\}$ is the harmonic order of the filter. From Fig. 3.2 (b) we deduce that higher harmonic orders show reduced spectral weights, thus leading to a reduced sensor response. Therefore, we typically use the first order harmonic $q = 1$ for sensitive detection of ac-signals.

Detection of complex, multi-frequency signals

Finally, if the detected magnetic field is composed of several frequency components with amplitudes B_i the accumulated total phase Φ after the sensing sequence is given by the sum of the frequency amplitudes B_i multiplied with the spectral weighting function at the corresponding frequency. However, for the most general application of sensing an arbitrary magnetic field $B(t)$ the sensor phase is non-trivially connected to sensor phase. Nevertheless, in this case the magnetic field can also be detected using the NV center with adapted sensing methods, as demonstrated in Chapter 8. The frequency response of the $XY8 - k$ multi-pulse sequence will be further explored experimentally in Chapter 5 and we will show that the expression in Equation 3.17 can be experimentally verified over a wide range of parameters.

Frequency resolution of dynamical decoupling spectroscopy

As described in the previous paragraph, the filter-bandwidth of the multi-pulse spectroscopy sequence depends on the total duration of the sequence $N\tau = 8k\tau$. In experiments the maximum duration of the spectroscopy sequence is limited by the coherence time of the NV center T_2 under the decoupling sequence. Consequently, the frequency resolution is limited by $\sim 1/T_2$ for this spectroscopy technique. In the following paragraphs of this Chapter we will introduce spectroscopy techniques (see Section 3.8) that are instead limited by the spin lifetime T_1 of the NV electron spin, which is typically much longer (see Chapter 2). Further, the spectroscopic resolution can be enhanced to the spin lifetime $T_{1,n}$ of an auxiliary, nuclear quantum memory [72, 73], which again is typically longer than the T_1 time of the NV electron spin. Finally, recently developed methods have been introduced that are not limited by the coherence or lifetime of the sensor spin [74, 95].

3.4.2 NMR detection with dynamical decoupling spectroscopy

Spectroscopy on a bath of spins

Following the considerations in the previous paragraph, we can detect the presence of nuclear spins in the vicinity of the NV center by tuning the center frequency of the $XY8 - k$ sequence $f_c = 1/(2\tau)$ into resonance with the Larmor frequency of nuclear spins. This in turn leads to the accumulation of a sizable sensor phase due to the oscillating AC field generated by the nuclei, which can subsequently be detected by the optical readout of the sensor. In Fig. 3.3 (c) we show the population p of an individual NV center in the $m_S = 0$ state after applying the $XY8 - k$ protocol with $k = 32$ or $N = 256$ for varying filter center frequencies $1/(2\tau)$. The external bias field was here set to $B_0 = 186$ mT and we therefore expect ^{13}C nuclei hosted inside the diamond

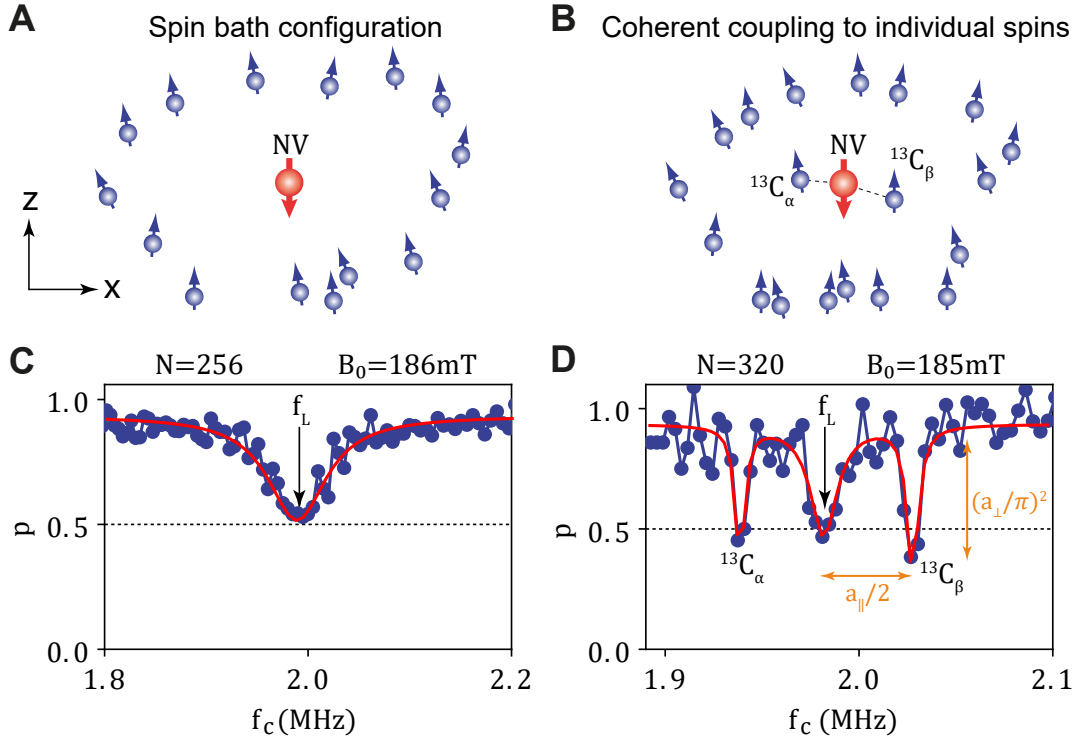


FIGURE 3.3: **Detection of NMR signals with dynamical decoupling spectroscopy.** Spectroscopy measurements with the $XY8 - k$ sequence on two different NV centers in the same diamond sample (E1303) are shown. In (a) the spectrum of a bath of ^{13}C spins is shown, which precess at a Larmor frequency f_L close to 2 MHz due to the applied external bias field of $B_0 = 186 \text{ mT}$. In this particular experiment the total number of pulses amounted to $N = 256$ and hence $k = 32$. The measurement signal never exceeds the threshold of $p < 0.5$, which would indicate coherent coupling to individual or a small number of spins [96]. The red line is a numerical fit with a single Lorentzian function. The spectrum in (b) reveals a richer structure due to two nearby nuclei, indicated in the spectrum as $^{13}\text{C}_\alpha$ and $^{13}\text{C}_\beta$, which are spectrally shifted from the bath peak due the hyperfine interaction with the NV center, as given by the Hamiltonian in equation 3.4. In this measurement $N = 320$ and thus $k = 40$. The red line is a fit which includes three independent Lorentzians.

to precess at a frequency of $f_L = \| -\gamma_n B_0 \| = 2\pi \times 1991 \text{ kHz}$. The measurement clearly shows that the NV center population is only changed if the center frequency of the DD sequence is tuned into resonance with the ^{13}C precession frequency¹. This is consistent with the dependence of the NV center population on the acquired sensor phase as given by Equation 3.13. The width of the resonance observed in Fig. 3.3 (a) is determined by the filter-bandwidth $\Delta f = 1/(N\tau)$, which depends on the total duration of the dynamical decoupling sequence. In this experiment the NMR signal arises from a bath of many weakly coupled ^{13}C spins in the vicinity of the NV center. Individual nuclei can not be spectroscopically distinguished with the given frequency resolution. This is schematically sketched with the spin environment in Fig. 3.3 (a).

¹In principle also for uneven subharmonics of f_c and for spurious higher harmonics at $2f_c, 4f_c, 8f_c$ as well as their odd subharmonics $2f_c/q, 4f_c/q, 8f_c/q$ [94].

Spectroscopy on individual nuclear spins

In Fig. 3.3 (d), we show a complementary NMR spectrum acquired on a different NV center. In this case we applied the XY8 – k protocol with $k = 40$ under a similar magnetic field of $B_0 = 185$ mT. Again we observe a spectral feature at the expected Larmor frequency of the nuclei, which is highlighted by f_L . In addition, we observe two satellite peaks at slightly higher and slightly lower frequency. These arise from two ^{13}C nuclei, which are sufficiently strongly coupled to the NV center via the hyperfine interaction such that we can spectrally distinguish them from the bath nuclei. The spectral separation arises from the fact that during the multi-pulse sequence the ^{13}C nuclei precess with an average frequency that is given by the external bias field B_0 and by the hyperfine field of the NV center. Further details will be described in Section 3.5.4. In Fig. 3.3 (b), we again schematically represent the local nuclear environment of the specific NV center.

3.5 Control of nuclei using dynamical decoupling

In this section, we aim to discuss how a particular nuclear spin can be detected, coherently controlled and polarized using the NV center via dynamical decoupling control. This forms the basis for all spectroscopy experiments performed in this thesis. Parts of the description have been to a large part inspired by the original research papers [77, 86, 89].

In a first step we will transform the Hamiltonian from Eq. 3.7 into the rotating frame of the NV center. Subsequently we will describe the nuclear spin evolution conditional on the state of the NV center, while working in the reduced two-level system of the $m_S = 0$ and $m_S = -1$ -state. Finally, we will show that conditional rotations of the nuclear spin can be realized with the NV center and will describe how this can be leveraged in spectroscopy and for polarization of nuclei.

3.5.1 Rotating-frame transformation

Transforming into the rotating-frame of the NV center simplifies the Hamiltonian derived in Eq. 3.7 and enables us to focus on the nuclear spin evolution during dynamical decoupling. Following the description in Ref. [77], we apply the transformation $e^{-i\omega_{01}\hat{S}_z t}$ with $\omega_{01} = D_{\text{gs}} - \gamma_e B_0$ being the precession frequency between the $m_S = 0$ and the $m_S = -1$ state and obtain:

$$\hat{H}_{\text{SI,rF}} = D_{\text{gs}}(\hat{S}_z^2 + \hat{S}_z) - \gamma_n B_0 \hat{I}_z + a_{\parallel} \hat{S}_z \hat{I}_z + a_{\perp} \hat{S}_z \hat{I}_x. \quad (3.18)$$

If the $m_S = 1$ state is not populated in experiments the first term in Eq. 3.18 can be neglected and we obtain the Hamiltonian describing the nuclear spin dynamics, conditional on the electron spin state:

$$\hat{H}_{\text{nuc}} = -\gamma_n B_0 \hat{I}_z + a_{\parallel} \hat{S}_z \hat{I}_z + a_{\perp} \hat{S}_z \hat{I}_x. \quad (3.19)$$

3.5.2 Precession axes of nuclear spins

From Eq. 3.19 we deduce that the nuclear spin evolution is conditional on the m_S projection of the electron spin. The Hamiltonian governing the dynamics if the NV

center is held in the $m_S = 0$ or $m_S = -1$ state is then given by:

$$\hat{H}_0 = -\gamma_n B_0 \hat{I}_z \quad (3.20)$$

$$\hat{H}_{-1} = -\gamma_n B_0 \hat{I}_z - a_{\parallel} \hat{I}_z - a_{\perp} \hat{I}_x. \quad (3.21)$$

From these Hamiltonians we can directly deduce the precession axes of the nuclear spin conditional on the m_S state of the NV center. These precession axes are sketched in Fig. 3.1 (b) and (c), respectively. In the NV center is held in the $m_S = 0$ state, the nuclear spin precesses around the axis $\boldsymbol{\omega}_0$:

$$\boldsymbol{\omega}_0 = -\gamma_n B_0 \mathbf{e}_z, \quad (3.22)$$

with \mathbf{e}_z the unit vector along the symmetry axis of the NV center. In the case of the NV center held in the $m_S = -1$ -state, the nuclear spin precesses around the axis $\boldsymbol{\omega}_{-1}$:

$$\boldsymbol{\omega}_{-1} = -\gamma_n B_0 \mathbf{e}_z + \mathbf{A}_z, \quad (3.23)$$

where $\mathbf{A}_z = (a_{\perp}, 0, a_{\parallel})$ is the secular hyperfine vector field under the assumption that the internuclear vector has $\phi = 0$, as discussed before.

3.5.3 Two-level description of the NV center

In the following paragraphs we want to describe NV-NMR sequences based on the dynamical decoupling sequence. A simple, yet rigorous, formalism to compute the unitary evolution of the spin system during the pulse sequences is the product operator formalism. As the standard product operator formalism uses spin-1/2 operators it is at this point advantageous to reduce the spin operators S associated to the NV center to spin-1/2 by reducing the Hilbert space to the manifold between $m_S = 0$ and $m_S = -1$. In the remainder of this chapter the spin operators hence always refer to spin-1/2 representation. Consequently, the secular Hamiltonian in Eq. 3.19, describing the interaction between NV center and a single nuclear spin, becomes:

$$H_f = -\omega_L S_e \otimes \hat{I}_z + a_{\parallel} (\hat{S}_z - \hat{S}_e/2) \otimes \hat{I}_z + a_{\perp} (\hat{S}_z - \hat{S}_e/2) \otimes \hat{I}_x. \quad (3.24)$$

3.5.4 Evolution of nuclear spins during decoupling

We now want to describe the time evolution of a nuclear spin during a dynamical decoupling sequence applied to the NV electron spin. For simplicity we constrain ourselves to a description of the effective Hamiltonian acting during the sequence, if it is tuned into resonance with the target nuclear spin. A general, rigorous treatment of the evolution of the spin-system during the dynamical decoupling sequence can be found in [97, 98]. In the limit $\omega_0 \gg a_{\parallel}, a_{\perp}$ the dynamical decoupling sequence is resonant with the target nuclear spin, if the interpulse spacing is tuned to [89]:

$$\tau = \frac{q\pi}{\omega_0 + a_{\parallel}/2}. \quad (3.25)$$

Here, q is the harmonic order of the filter function, as introduced in section 3.4.1. Based on this expression, we again confirm that the frequency shift of the nuclear spins in the NMR spectrum in Fig. 3.3 (d) corresponds to $\Delta f = a_{\parallel}/(4\pi)$.

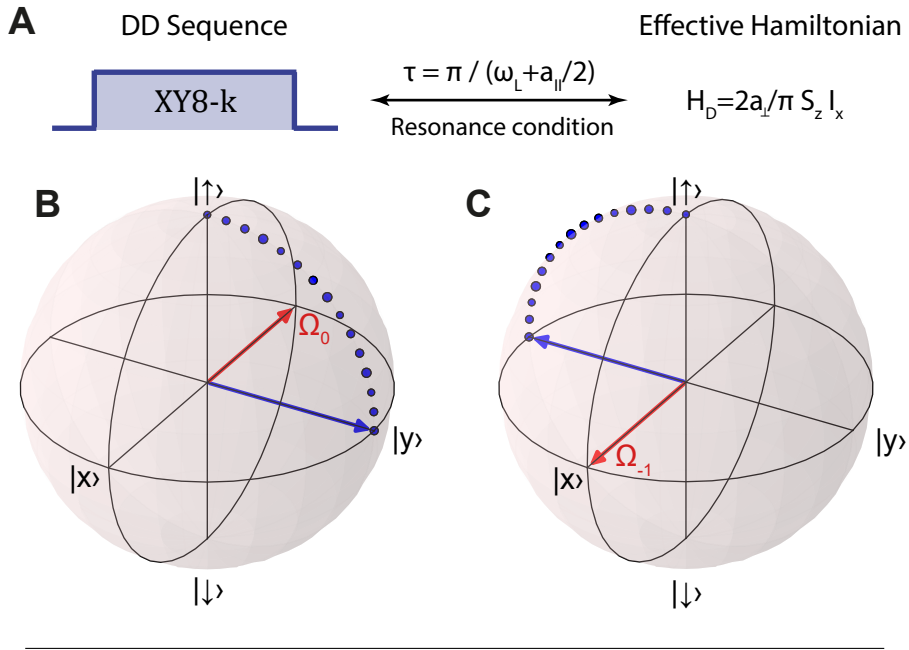


FIGURE 3.4: **Nuclear spin evolution during dynamical decoupling.** (a) Under resonant dynamical decoupling with $\tau = \pi / (\omega_L + a_{\parallel}/2)$ the composite spin system of NV center and nuclear spin evolves under the Hamiltonian $H_d = 2a_{\perp} / \pi \hat{S}_z \otimes \hat{I}_x$. (b) Thus, if the NV center is initially in the $m_S = 0$ state, the nuclear spin rotates around the $-x$ axis by an angle given by $\alpha = 2a_{\perp} / \pi t$, where t is the duration of the dynamical decoupling block. (c) If the NV center is initially prepared in the $m_S = -1$ state the nuclear spin instead rotates around the x axis.

For odd harmonic orders $q = 1, 3, 5, \dots$ and resonant interpulse separation τ the effective Hamiltonian acting on the two-spin system during the dynamical decoupling sequence is given by [86, 89, 97]:

$$\hat{H}_d = 2a_{\perp} / \pi \hat{S}_z \otimes \hat{I}_x. \quad (3.26)$$

The effect of this Hamiltonian on the nuclear spin is a rotation around the x -axis, which is conditional on the state of the NV center at the beginning of the dynamical decoupling sequence. In Fig. 3.4 (b) and (c), we show the resulting nuclear spin evolution for both the $m_S = 0$ and $m_S = -1$ initial state of the NV center. We note that for even harmonic orders of the resonance condition the dynamical decoupling sequence realizes an unconditional rotation of the nuclear spin along x . We will show in the following sections, that conditional or controlled rotations of the nuclear spin permit state tomography and polarization transfer protocols.

3.5.5 Dynamical decoupling signal of individual spins

At this point, we can derive the spectroscopy signal of a single nuclear spin using the product operator formalism (see appendix A) and the effective Hamiltonian of the decoupling sequence. Thereby we can explain the properties of the satellite peaks in the NMR spectrum in Fig. 3.3 (d). We will assume, that the interpulse spacing τ is resonant with a single nuclear spin, such that the decoupling sequence realizes the effective Hamiltonian given in Eq. 3.26.

The initial density matrix after the laser pulse in Fig. 3.2 (a) is given by:

$$\rho_{\text{init}} = (\hat{S}_z + \hat{S}_e/2) \otimes \hat{I}_e/2. \quad (3.27)$$

This density matrix comprises a polarized NV center and an unpolarized nuclear spin. After the initial $\pi/2$ pulse along the x -axis the density matrix transforms to ρ_α :

$$\rho_\alpha = (-\hat{S}_y + \hat{S}_e/2) \otimes \hat{I}_e/2. \quad (3.28)$$

Subsequent to the $\pi/2$ pulse we apply the dynamical decoupling sequence. As described in the previous sections, the XY8 – k dynamical decoupling sequence with resonant τ leads to the evolution of the spin-system under the Hamiltonian $H_d = \frac{2a_\perp}{\pi} \hat{S}_z \hat{I}_x$, for a duration $t = 8k\tau$. The propagator for the decoupling sequence is thus given by $U_d = e^{-iH_d t}$. The resulting density matrix $\rho_\beta = U_d \rho_\alpha U_d^\dagger$, derived using Eq. A.5, reads:

$$\rho_\beta = \cos(\alpha/2)(-\hat{S}_y) \otimes \hat{I}_e/2 + \sin(\alpha/2)\hat{S}_x \otimes \hat{I}_x + \frac{1}{4}\hat{S}_e \otimes \hat{I}_e. \quad (3.29)$$

After the final microwave $\pi/2$ -rotation along the $-x$ -axis we obtain the final density matrix ρ_γ :

$$\rho_\gamma = \cos(\alpha/2)\hat{S}_z \otimes \hat{I}_e/2 + \sin(\alpha/2)\hat{S}_x \otimes \hat{I}_x + \frac{1}{4}\hat{S}_e \otimes \hat{I}_e. \quad (3.30)$$

The readout with the final laser pulse produces the observable p , which is the probability that the initial state of the NV center ($m_S = 0$) is varied:

$$p = \frac{1}{2} - \text{Tr}[\rho_\gamma \hat{S}_z] = \frac{1}{2}(1 - \cos(\alpha/2)). \quad (3.31)$$

The change in the initial state of the NV center thus depends on the perpendicular hyperfine coupling a_\perp :

$$p(t) = \frac{1}{2}(1 - \cos(a_\perp / \pi t)). \quad (3.32)$$

For small α , we can expand the cosine function and find that the variation in p at resonance is given by:

$$p(t) \approx a_\perp^2 t^2 / (4\pi^2). \quad (3.33)$$

Therefore, we can estimate the perpendicular hyperfine coupling by recording the peak depth in the spectrum as function of the number of pulses in the sequence. This is shown in Fig. 3.3 (d), where we indicate how the parallel and perpendicular hyperfine influence position and modulation depth of the spectral feature associated with $^{13}\text{C}_\beta$.

3.6 Polarization transfer to individual nuclear spins

The next sequence that we describe, again via the product operator method, allows us to selectively transfer polarization from the NV center to a nuclear spin. The pulse sequence for this experiment is shown in Fig. 3.5 (b) and has been introduced to the field of NV-NMR in reference [86]. Effectively the sequence realizes a swap operation of the quantum states of the NV center and the target nuclear spin. Further,

the sequence is a central building block of the three-dimensional nuclear localization experiment with coherent radio-frequency pulses discussed and introduced in Chapter 7.

The density matrix of the spin system after the first laser pulse (see Fig. 3.5 (b)) is again given by a polarized NV center (operator S) and a nuclear spin in a fully mixed state (operator I):

$$\rho_{\text{init}} = \rho(t_\alpha) = (\hat{S}_z + \frac{1}{2}\hat{S}_e) \otimes \frac{1}{2}\hat{I}_e. \quad (3.34)$$

In this paragraph we compute the density matrix at the times indicated below the schematic of the pulse sequence in Fig. 3.5 (b). The first $\pi/2$ -rotation with a microwave pulse around the y -axis prepares the state:

$$\rho(t_\beta) = (\hat{S}_x + \frac{1}{2}\hat{S}_e) \otimes \frac{1}{2}\hat{I}_e = \frac{1}{2}\hat{S}_x \otimes \hat{I}_e + \frac{1}{4}\hat{S}_e \otimes \hat{I}_e. \quad (3.35)$$

Subsequently, the $XY8 - k$ decoupling sequence transforms the density matrix with the unitary transformation $U_d = e^{-i\hat{H}_d t}$ with \hat{H}_d given in Eq. 3.26. This is in analogy to the previous discussion of the $XY8 - k$ spectroscopy signal. However, here $t = 8k\tau$ is fixed to produce an evolution of $\pi\hat{S}_z \otimes \hat{I}_x$. Thus the density matrix ρ_x transforms into:

$$\rho(t_\gamma) = \frac{1}{4}\hat{S}_e \otimes \hat{I}_e + \hat{S}_y \otimes \hat{I}_x. \quad (3.36)$$

Subsequently, again a $\pi/2$ rotation around the x -axis is applied to the NV center with an additional microwave pulse:

$$\rho(t_\delta) = \frac{1}{4}\hat{S}_e \otimes \hat{I}_e + \hat{S}_z \otimes \hat{I}_x, \quad (3.37)$$

and directly followed by free precession of the nuclear spin for an angle $\pi/2$ around the z -axis:

$$\rho(t_\epsilon) = \frac{1}{4}\hat{S}_e \otimes \hat{I}_e + \hat{S}_z \otimes \hat{I}_y. \quad (3.38)$$

This rotation around the z -axis is realized by simply waiting for a time $\tau/2$. Finally, the second conditional rotation again given by $\pi\hat{S}_z \otimes \hat{I}_x$ is applied to the spin system with a second $XY8 - k$ sequence, resulting in the final density matrix:

$$\rho(t_\zeta) = \frac{1}{4}\hat{S}_e \otimes \hat{I}_e + \frac{1}{2}\hat{S}_e \otimes \hat{I}_z = \frac{1}{2}\hat{S}_e \otimes (\hat{I}_z \otimes \frac{1}{2}\hat{I}_e). \quad (3.39)$$

Clearly, the population of the electron spin and the nuclear spin have been interchanged and thus the initial polarization on the NV center has been transferred to the nucleus. The final laser pulse shown in Fig. 3.5 (b) repolarizes the NV center in the $m_S = 0$ state and concludes the initialization of the spin system. We note, that due to the limited fidelity of all parts of the entire sequence the resulting polarization of the nuclear spin is typically not larger than 50 % in our experiments.

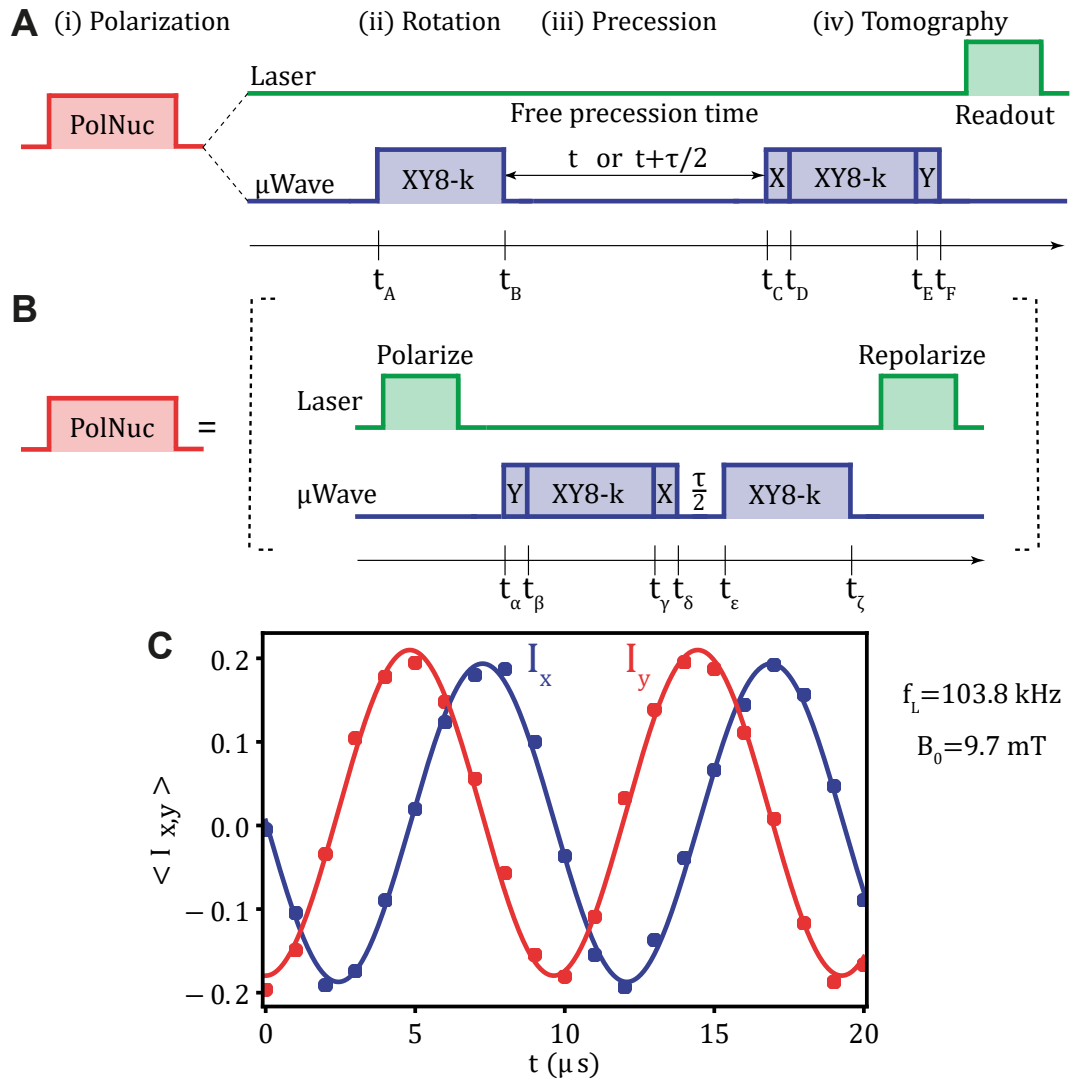


FIGURE 3.5: **Polarization and state tomography of individual nuclear spins.** (a) Laser and microwave pulse sequence used to first polarize (indicated as (i)), then rotate by $\theta = \pi/2$ (ii) and finally after a precession time t (iii) readout a single spin's $\langle I_x \rangle$ or $\langle I_y \rangle$ expectation value (iv). The polarization protocol is shown in detail in (b) and consists of two conditional rotations of the nuclear spin mediated via the hyperfine interaction. The rotation of the nuclear spin after the polarization and the tomography is based on a resonant XY8 – k dynamical decoupling sequence with $\tau \approx [2(f_0 + f_1)]^{-1}$, with f_0 and f_1 defined in Fig. 3.1. This sequence is the central building block of the three-dimensional imaging protocol with coherent radio-frequency pulses as described in Chapter 7. (c) Measurement of the $\langle I_x \rangle$ and $\langle I_y \rangle$ components of a single ^{13}C nuclear spin. The applied magnetic bias field amounts to $B_0 = 9.7$ mT which results in a precession frequency of $f_L = 104$ kHz. The quadrature $\langle I_y \rangle$ is detected by converting it into a $\langle I_x \rangle$ component with a static waiting time $\tau/2$ as shown in (a).

3.7 Nuclear spin state tomography

The third sequence that we describe via the product operator formalism allows us to probe the nuclear spin state with the NV center. We will refer to it as the nuclear spin state tomography sequence as, in principle, all three nuclear spin projections $\langle I_x \rangle$, $\langle I_y \rangle$ and $\langle I_z \rangle$ can be measured via this sequence. Nevertheless we will restrict

ourselves here to a detailed description of the sequence probing the $\langle I_x \rangle$ component. The detection of the $\langle I_y \rangle$ projection can be simply realized by waiting for a quarter of the precession period of the nuclear spins prior to readout, as this converts the $\langle I_x \rangle$ component into the $\langle I_y \rangle$ component. The detection of the $\langle I_z \rangle$ instead requires a second additional rotation around the x -axis, which initially converts $\langle I_z \rangle$ into the $\langle I_y \rangle$ component. Further details on extensions of the sequence to the detection of the $\langle I_y \rangle$ and $\langle I_z \rangle$ component can be found in reference [86].

Pulse sequence for nuclear state tomography

In the following, we will consider the composite pulse sequence shown in Fig. 3.5 (a). The first part of the sequence, which is labelled *polarization*, is the previously discussed sequence that enables the polarization of both the target nuclear spin and the NV center. The detailed subsequence is shown in Fig. 3.5 (b). In principle also a different polarization transfer mechanism could be employed here, for example using the Hartmann-Hahn method [99]. In the second part of the main sequence (labelled *rotation*), we apply a $XY8 - k$ sequence which is tuned into resonance with the pre-polarized nuclear spin. The rotation angle is set to $\theta = \pi/2$ by the proper choice of k . Consequently, we start out with a nuclear spin state prepared in the xy -plane of the Bloch sphere. Subsequently, in the sequence element labelled *precession*, we let the nuclear spin precess in the equatorial plane. The resulting nuclear spin density operator after the precession can be written as:

$$\rho_p = \zeta \hat{I}_x + \chi \hat{I}_y, \quad (3.40)$$

with $|\zeta|^2 + |\chi|^2 = 1$. Here, the amplitudes ζ and χ are defined by the precession time and the Larmor frequency of the target nuclear spin. The final part of the pulse sequence under the block labelled *tomography* in Fig. 3.5 (a) represents the tomography part of the sequence that we wish to describe in detail in the following. We will again use the product operator method to show that this tomography sequence probes the $\langle I_x \rangle$ component of the nuclear spin and thus the amplitude ζ .

Product-operator description of state tomography

Now, we will compute the effect of the $\langle I_x \rangle$ tomography sequence on the precessing nuclear spin, described by the density matrix $\rho_p = \rho(t_C)$. The NV center is initially prepared in the polarized state \hat{S}_z (by the repolarization pulse in Fig. 3.5(b)) and thus the density matrix of the full spin system, omitting terms proportional to \hat{S}_e , can be written as:

$$\rho(t_C) = \hat{S}_z \otimes (\zeta \hat{I}_x + \chi \hat{I}_y). \quad (3.41)$$

The time axis of the sequence is again indicated below the sketch of the sequence in Fig. 3.5 (a). Application of the initial microwave pulse by $\pi/2$ to the NV center along the x -axis leaves us with:

$$\rho(t_D) = -\hat{S}_y \otimes (\zeta \hat{I}_x + \chi \hat{I}_y) = -\hat{S}_y \otimes \zeta \hat{I}_x + -\hat{S}_y \otimes \chi \hat{I}_y = \rho_x(t_D) + \rho_y(t_D) \quad (3.42)$$

In the last step we have separated the density matrix into two product operators $\rho_x(t_D) = -\hat{S}_y \otimes \zeta \hat{I}_x$ and $\rho_y(t_D) = -\hat{S}_y \otimes \chi \hat{I}_y$ and we will consider the effect of the rest of the sequences separately.

As discussed in section 3.5.4 the subsequent $XY8 - k$ dynamical decoupling sequence realizes a conditional rotation of the nuclear spin around the x -axis as described by $\pi\hat{S}_z \otimes \hat{I}_x$, which, according to Equation A.5, produces the density matrix:

$$\rho_x(t_E) = -\frac{\tilde{\zeta}}{2} (\hat{S}_y \otimes \hat{I}_x + 4i(\hat{S}_y\hat{S}_z) \otimes (\hat{I}_x\hat{I}_x) - 4i(\hat{S}_z\hat{S}_y) \otimes (\hat{I}_x\hat{I}_x) + 16(\hat{S}_z\hat{S}_y\hat{S}_z) \otimes (\hat{I}_x\hat{I}_x\hat{I}_x)) \quad (3.43)$$

$$= -\frac{\tilde{\zeta}}{2} (\hat{S}_y \otimes \hat{I}_x - \hat{S}_y \otimes \hat{I}_x - \hat{S}_x \otimes \hat{I}_e - \hat{S}_x \otimes \hat{I}_e) \quad (3.44)$$

$$= \tilde{\zeta}\hat{S}_x \otimes \hat{I}_e. \quad (3.45)$$

The final $\pi/2$ pulse on the electron spin along the y -axis results in the density matrix:

$$\rho_x(t_F) = \zeta\hat{S}_z \otimes \hat{I}_e. \quad (3.46)$$

Thus the sequence converts the $\langle I_x \rangle$ population into a measurable $\langle S_z \rangle$ polarization. Further, it is possible to show that the second product state in the density matrix ρ_y produces no observable $\langle S_z \rangle$ polarization after application of the tomography sequence. As already mentioned before, it is possible to detect the $\langle I_y \rangle$ amplitude χ by inserting an extra waiting time $\tau/2$ before the tomography sequence, which converts this population into a $\langle I_x \rangle$ population, and vice versa. This is also indicated in Fig. 3.5 (b).

Detection of nuclear precession by state tomography

In Fig. 3.5 (c) we show a measurement of the $\langle I_x \rangle$ and $\langle I_y \rangle$ components of a single nuclear spin after a variable precession time t . The applied magnetic quantization field amounted to $B_0 = 9.7$ mT, which results in a nuclear precession frequency of approximately $f_L = 104$ kHz. As expected both measurement traces are 90° out of phase. The inferred nuclear projection onto $\langle I_x \rangle$ and $\langle I_y \rangle$ does not reach the maximum excursion of $\pm 1/2$ due to non-ideal initial polarization and non-ideal nuclear rotations.

As the NV center is kept in the $m_S = 0$ state during this free precession, the spin precesses at the bare Larmor frequency given by the quantization field $f_L = \gamma_n/(2\pi)B_0$. Thus, nuclear tomography provides an efficient method to determine the nuclear precession frequency with high-resolution, especially as no coherence on the NV center needs to be preserved during the precession time. This is in contrast to the basic dynamical decoupling spectroscopy discussed before. Thus the frequency resolution of this spectroscopy method is not limited by T_2 of the NV center but merely by the spin lifetime T_1 , as spin flips on the NV center lead to stochastic switching of the hyperfine interaction. This frequency resolution can be further increased up to the dephasing time of the nuclear spin [100]. Note that we can in principle also measure the hyperfine shift of the NV center onto the nuclear spin by preparing the NV center in the $m_S = -1$ state prior to the free precession period. However, spectroscopy of hyperfine shifts was performed mainly using the correlation spectroscopy technique, which is in detail discussed in the following section. In chapter 7, we use the nuclear spin state tomography to detect the nuclear precession phase after rotating the nuclear spin with a radio-frequency pulse applied to the planar coil. This gives access to the azimuthal component ϕ of the distance vector between NV center and nuclear spin.

3.8 Correlation hyperfine spectroscopy

We now describe how the hyperfine couplings a_{\parallel} and a_{\perp} can be determined with high precision using multi-pulse dynamical decoupling without the need to polarize the nuclear spins. These methods are extensively used in chapter 5,6 and 7 for the positioning of nuclear spins.

In the following we assume that the nuclear Zeeman frequency $\omega_L = \gamma_n B_0$ is much larger than $(a_{\parallel}, a_{\perp})$ and that the inter-pulse delay τ is fixed to $\tau = \pi/(\omega_L + a_{\parallel}/2)$ such that the expression for the action of the dynamical decoupling sequence derived in equation 3.26 is exact. In some experiments in Chapters 6 and 7 the approximation $\omega_L \gg a_{\parallel}, a_{\perp}$ is not fulfilled and a full description of the spin dynamics requires numerical simulations based on the density matrix formalism (see chapter 7 for details). Nonetheless the methods described here can still be applied when extra care is taken during data analysis of $(a_{\parallel}, a_{\perp})$ [77]. This is further discussed in section 3.8.3.

3.8.1 Spectroscopy of the parallel hyperfine coupling

The basic pulse protocol for high-resolution correlation spectroscopy is shown in Fig. 3.6 (a) and consists of two dynamical decoupling blocks sandwiched in between two $\pi/2$ pulses each and separated by a variable waiting or precession time t_1 . We will now show that this sequence enables us to detect the nuclear free induction decay (FID). In addition, the sensing duration, which determines the frequency resolution of the spectroscopy method is limited by T_1 of the NV center electron spin, instead of T_2 in the case of dynamical decoupling spectroscopy.

Product operator description

In a first step we derive the effect of the basic correlation spectroscopy protocol using the product operator approach and we show that the Larmor frequency ω_L and the parallel hyperfine coupling a_{\parallel} can be measured with this protocol. Later we will also discuss variations of the basic pulse sequence which enables the measurement of the transverse hyperfine coupling a_{\perp} .

The initial density matrix at the beginning of the experiment is given by (the time axis is indicated below the pulse sequence in Fig. 3.6 (a), (i)):

$$\rho_{\text{init}} = \rho(t_{\alpha}) = (\hat{S}_z + \hat{S}_e/2) \otimes (\hat{I}_e/2), \quad (3.47)$$

and after the initial $\pi/2$ rotation around the x -axis we obtain the density matrix:

$$\rho(t_{\beta}) = (\hat{S}_e/2 - \hat{S}_y) \otimes (\hat{I}_e/2). \quad (3.48)$$

The density matrix after the decoupling sequence then reads $\rho = \hat{U}_d \rho \hat{U}_d^{\dagger}$ which according to equation A.5 can be written as:

$$\begin{aligned} \rho(t_{\gamma}) = & \cos^2(\alpha/4)(-\hat{S}_y) \otimes \hat{I}_e/2 - \sin^2(\alpha/4)(-\hat{S}_y) \otimes (\hat{I}_e/2) \\ & + 2 \sin(\alpha/4) \cos(\alpha/4) \hat{S}_x \otimes \hat{I}_x, \end{aligned} \quad (3.49)$$

with $\alpha = 2a_{\perp}/\pi N\tau$. Now we use the trigonometric identities $\cos^2(x) - \sin^2(x) = \cos(2x)$ and $2 \cos(x) \sin(x) = \sin(2x)$ to simplify the expressions above and thereby

obtain:

$$\rho(t_\gamma) = \cos(\alpha/2)(-\hat{S}_y) \otimes \hat{I}_e/2 + \sin(\alpha/2)\hat{S}_x \otimes \hat{I}_x. \quad (3.50)$$

After the second $\pi/2$ pulse around the y -axis the density matrix reads:

$$\rho(t_\delta) = \cos(\alpha/2)(-\hat{S}_y) \otimes \hat{I}_e/2 + \sin(\alpha/2)\hat{S}_z \otimes \hat{I}_x. \quad (3.51)$$

After this pulse the spin system evolves freely for a duration t_1 . The Hamiltonian during the free evolution, again under the assumption $\omega_L \gg a_{||}, a_{\perp}$, is given by:

$$H_f = -\omega_L \hat{S}_e \otimes \hat{I}_z + a_{||}(\hat{S}_z - \hat{S}_e/2) \otimes \hat{I}_z. \quad (3.52)$$

In the following we will neglect the electron coherence, i.e. the term scaling with \hat{S}_y , because the free precession time t_1 is in experiments always chosen much longer than the dephasing time T_2^* of the electron spin and hence the coherence term \hat{S}_y decays during t_1 . Consequently, we only continue the computation with the density operator:

$$\rho_I(t_\delta) = \sin(\alpha/2)\hat{S}_z \otimes \hat{I}_x. \quad (3.53)$$

Again, we use Equation A.5, to compute the effect of H_f on the spin system's density matrix. After simplifying the resulting expressions, we obtain the following density operator:

$$\begin{aligned} \rho_I(t_\epsilon) = & \zeta \cos(a_{||}/2t_1)\hat{S}_z \otimes [\cos(-(\omega_l + a_{||}/2)t_1)\hat{I}_x + \sin(-(\omega_l + a_{||}/2)t_1)\hat{I}_y] \\ & + \zeta \sin(a_{||}/2t_1)\hat{S}_e/2 \otimes [\cos(-(\omega_l + a_{||}/2)t_1)\hat{I}_y - \sin(-(\omega_l + a_{||}/2)t_1)\hat{I}_x], \end{aligned} \quad (3.54)$$

with $\zeta = \sin(\alpha/2)$. After multiplying out the terms in the previous expression and using the trigonometric product-to-sum identities, we obtain the density matrix after the free-precession time :

$$\begin{aligned} \rho_I(t_\epsilon) = & \frac{\zeta}{2}(\cos(-\omega' t_1)(\hat{S}_z - \hat{S}_e/2) \otimes \hat{I}_x + \cos(-\omega_l t_1)(\hat{S}_z + \hat{S}_e/2) \otimes \hat{I}_x \\ & + \sin(-\omega' t_1)(\hat{S}_z - \hat{S}_e/2) \otimes \hat{I}_y + \sin(-\omega_l t_1)(\hat{S}_z + \hat{S}_e/2) \otimes \hat{I}_y). \end{aligned} \quad (3.55)$$

Here, we introduced the precession frequency $\omega' = \omega_L + a_{||}$.

We proceed with the $\pi/2$ -pulse around the y -axis, which results in the density matrix:

$$\begin{aligned} \rho_I(t_\zeta) = & \frac{\zeta}{2}(\cos(-\omega' t_1)(\hat{S}_x - \hat{S}_e/2) \otimes \hat{I}_x + \cos(-\omega_l t_1)(\hat{S}_x + \hat{S}_e/2) \otimes \hat{I}_x \\ & + \sin(-\omega' t_1)(\hat{S}_x - \hat{S}_e/2) \otimes \hat{I}_y + \sin(-\omega_l t_1)(\hat{S}_x + \hat{S}_e/2) \otimes \hat{I}_y). \end{aligned} \quad (3.56)$$

Afterwards, we apply a second decoupling sequence to the spin system, which is followed by a final $\pi/2$ pulse along the x -axis and the laser readout. To keep expressions concise, we now only consider elements of the density matrix which result in a detectable variation in \hat{S}_z at readout. A short computation shows that this requires us to only keep terms proportional to $\hat{S}_x \otimes \hat{I}_x$, which results density matrix prior to

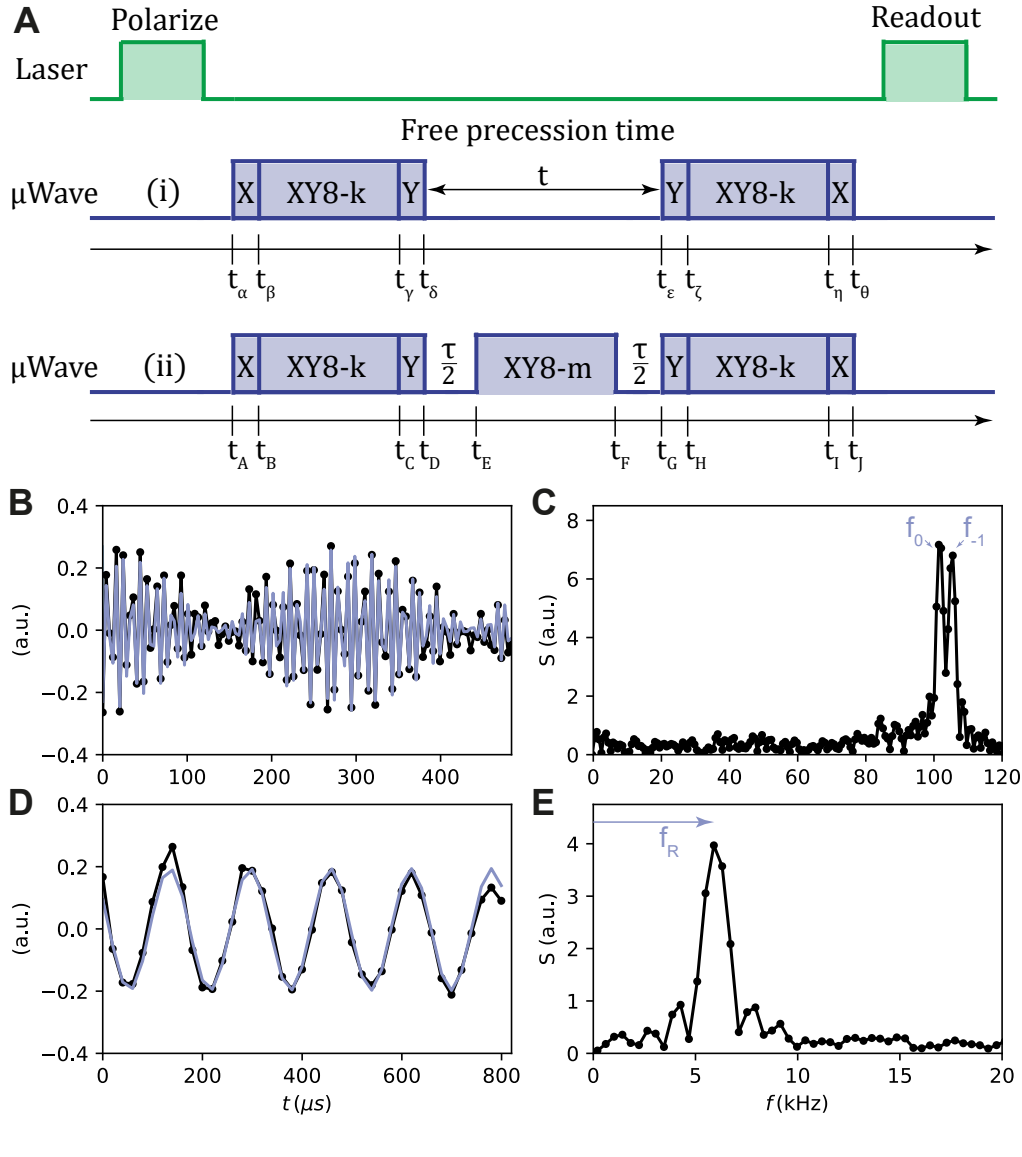


FIGURE 3.6: **Correlation spectroscopy applied to a single nuclear spin.** Correlation-type sequences are extensively used throughout this thesis to detect nuclear spins and to precisely determine their hyperfine coupling to the NV center. The first sequence, indicated as (i) in (a), consists of two nuclear phase measurements with the NV center, which are correlated and enable the detection of the free induction decay (FID) of the nuclear spins by scanning the free precession time t . The second correlation spectroscopy sequence, indicated as (ii) in (a), is used to measure the perpendicular hyperfine coupling a_{\perp} . (b) Free precession signal recorded on a single nuclear spin using the sequence displayed in Fig. 3.6 (a), (i). (c) Power spectrum of the measurement trace shown in (a). The two Fourier components (f_0, f_{-1}) represent the nuclear Larmor frequency $f_0 = \gamma_n B_0$ and the hyperfine shifted precession frequency $f_{-1} \approx \gamma_n B_0 + a_{\parallel}$. (d) Measurement of the perpendicular hyperfine coupling using the correlation spectroscopy sequence shown in Fig. 3.6 (a), (ii). (e) Power spectrum of the measurement data in (d). The single Fourier component f_R is proportional to the transverse hyperfine coupling component, according to $f_R = a_{\perp} / (2\pi^2)$. The external magnetic bias field B_0 in both measurements amounted to 9.6 mT, aligned to the quantization axis of the NV center. The interpulse delay of the dynamical XY8 - k decoupling sequence was set to $\tau = 4.762 \mu\text{s}$. In (b,c) the number of pulses was fixed to $N = 8$ pulses and in (d,e) it was swept up to $N = 168$.

readout:

$$\rho_I(t_\theta) = \frac{\xi^2}{4} \cos(\omega_I t_1) \hat{S}_z \otimes \hat{I}_e + \frac{\xi^2}{4} \cos(\omega' t_1) \hat{S}_z \otimes \hat{I}_e. \quad (3.57)$$

As the readout probes the expectation value of the \hat{S}_z operator, we obtain for the signal $p(t_1)$ of the correlation spectroscopy sequence:

$$p(t_1) = \frac{1}{2} - \text{Tr}[\rho_I(t_\theta) \hat{S}_z] = \frac{1}{2} \left[1 - \frac{\xi^2}{2} \cos(\omega_I t_1) - \frac{\xi^2}{2} \cos(\omega' t_1) \right]. \quad (3.58)$$

The signal thus contains two frequencies, the bare Larmor frequency ω_I and the Larmor frequency shifted by the parallel hyperfine parameter of the targeted nuclear spin $\omega' = \omega_I + a_{\parallel}$.

In Fig. 3.6 (b) we show a representative correlation spectroscopy signal $p(t_1)$ for a single nuclear spin. The measurement was performed at a magnetic field of 9.6 mT. From the power spectrum of the time trace, which is shown in Fig. 3.6 (c), we clearly identify the two frequency components $(\omega_I, \omega') = (2\pi \times 104(1), 2\pi \times 107(1))$ kHz. Hence, the correlation sequence enables the measurement of the Larmor frequency and the parallel hyperfine coupling of an individual nuclear spin.

3.8.2 Spectroscopy of the perpendicular hyperfine coupling

In this paragraph we describe a second correlation-based spectroscopy sequence to detect the perpendicular hyperfine coupling a_{\perp} between the NV center and a target nuclear spin. The experimental pulse sequence is depicted in Fig. 3.6 (a), (ii). Clearly, the sequence is analogous to the previous sequence until the time $t_\delta = t_D$, indicated below the sequence protocols in Fig. 3.6 (a). In addition, the electron coherence can again be neglected and we can thus write the density matrix at t_D as:

$$\rho_I(t_D) = \xi \hat{S}_z \otimes \hat{I}_x, \quad (3.59)$$

with $\xi = \sin(\alpha/2)$, as defined in the previous section. The waiting time $\tau/2$, from t_D to t_E , converts the nuclear projection from \hat{I}_x to \hat{I}_y :

$$\rho_I(t_E) = \xi \hat{S}_z \otimes \hat{I}_y. \quad (3.60)$$

Subsequently we apply a decoupling sequence with $8m$ pulses, where m is a free parameter that we sweep to record a time trace. In the example measurement shown in Fig. 3.6 (d) we varied m from 1 to 21. Note that by increasing m the duration of the decoupling sequence, corresponding to $t = t_F - t_E$ on the x-axis in Fig. 3.6 (d), increases as well. The effect of the decoupling sequence is again given by the unitary transformation $\hat{U}_d = \exp(i2a_{\perp}/\pi 8m\tau \hat{S}_z \otimes \hat{I}_x)$, which results in the density matrix:

$$\rho_I(t_F) = \xi \cos(\Theta/2) \hat{S}_z \otimes \hat{I}_y + \xi \sin(\Theta/2) \hat{S}_e/2 \otimes \hat{I}_z, \quad (3.61)$$

with $\Theta = 2a_{\perp}/\pi 8m\tau$. After the waiting time $\tau/2$ the density matrix is given by:

$$\rho_I(t_G) = -\xi \cos(\Theta/2) \hat{S}_z \otimes \hat{I}_x + \xi \sin(\Theta/2) \hat{S}_e/2 \otimes \hat{I}_z. \quad (3.62)$$

Further, after the microwave rotation by $\pi/2$ around the y -axis we find:

$$\rho_I(t_H) = -\xi \cos(\Theta/2) \hat{S}_x \otimes \hat{I}_x + \xi \sin(\Theta/2) \hat{S}_e/2 \otimes \hat{I}_z. \quad (3.63)$$

Here we recall that, as discussed in the previous section, only the term proportional to $\hat{S}_x \otimes \hat{I}_x$ produces a observable variation in the sensor projection \hat{S}_z at the end of the sequence. The resulting density matrix prior to readout is thus given by:

$$\rho_I(t_J) = -\zeta \cos(\Theta/2) \hat{S}_z \otimes \hat{I}_e. \quad (3.64)$$

The laser readout probes the \hat{S}_z component of the NV center and the measurement signal is therefore:

$$p(t_J) = \frac{1}{2} - \text{Tr} [\rho_I(t_J) \hat{S}_z] = \frac{1}{2} (1 + \zeta \cos(\Theta/2)) = \frac{1}{2} (1 + \zeta \cos(a_\perp / \pi 8m\tau)) \quad (3.65)$$

Consequently, we expect to observe a Rabi-like oscillation with Rabi frequency $\omega_R = a_\perp / \pi$ and contrast $\zeta \in [0, 1]$ after applying the sequence for varying $t = 8m\tau$.

A measurement realizing this sequence on a single nuclear spin is shown in Fig. 3.6 (d). In addition, in Fig. 3.6 (e) we show the Fourier spectrum of the time trace, which clearly shows a single component corresponding to $f_R = a_\perp / (2\pi^2)$. Here, we observe a Rabi frequency of $\omega_R = 2\pi \times 6(1)$ kHz, which results from a perpendicular hyperfine coupling of $a_\perp = 2\pi \times 18(1)$ kHz.

3.8.3 Determination of hyperfine couplings from precession frequencies

The hyperfine couplings a_\parallel and a_\perp in the limit $2\pi f_0 \gg a_\parallel, a_\perp$ are given by:

$$a_\parallel / (2\pi) = f_{-1} - f_0, \quad (3.66)$$

$$a_\perp / (2\pi) = \pi f_R. \quad (3.67)$$

Here, (f_0, f_{-1}, f_R) are the frequencies detected in the correlation spectroscopy protocol (as indicated in Fig. 3.6 (c) and (e)). In some of our experiments in chapter 6 and 7 the hyperfine couplings and the nuclear Larmor frequency f_0 were of similar magnitude, and we used the following transformations, derived analytically in [77], to obtain the hyperfine couplings:

$$a_\parallel = 2\pi f_{-1} \left(\frac{\cos(2\pi f_{-1} \frac{\tau}{2}) \cos(2\pi f_0 \frac{\tau}{2}) - \cos(\pi - 2\pi f_R \tau)}{\sin(2\pi f_{-1} \frac{\tau}{2}) \sin(2\pi f_0 \frac{\tau}{2})} \right) - 2\pi f_0 \quad (3.68)$$

$$a_\perp = \sqrt{(2\pi f_{-1})^2 - (2\pi f_0 + a_\parallel)^2} \quad (3.69)$$

Alternatively, the hyperfine couplings can be obtained by fitting numerical simulations to the measurement traces. This is discussed in further detail in chapter 7.

3.8.4 Frequency-resolution of correlation spectroscopy

The frequency resolution Δf of the dynamical decoupling spectroscopy protocol introduced in the previous sections is limited by the coherence time $\Delta f = 1/T_2$. The frequency resolution of the correlation spectroscopy sequence is determined by the waiting time between the two phase measurements of the nuclear spin. As the phase detected in the first measurement is stored in the population of the NV center, the waiting time can be extended up to the spin lifetime T_1 of the electron spin. Consequently, the frequency resolution of the correlation spectroscopy sequence is limited by the inverse of this time-scale. As the spin lifetime of the electron spin is typically

much longer than the coherence time, correlation spectroscopy enables higher resolution and therefore also higher precision measurements of the nuclear precession frequencies.

Experimental methods

Summary

This chapter covers a technical description of the diamond chips and the experimental setup used for the experiments described in this thesis. In a first step the properties of the employed single-crystal diamonds and their generation with ion implantation and subsequent high temperature annealing will be described. Subsequently, we will briefly describe all components of the experimental setup for optical, microwave and radio-frequency control of the NV center and nearby nuclear spins. This includes the description of a novel planar, radio-frequency coil for nuclear spin manipulations.

4.1 Introduction

The previous chapter summarized the basic physical properties of the NV^- center in diamond. We have seen that the defect shows quantum coherence under ambient conditions, which makes it a promising system for sensing applications, e.g. of biological systems with NMR methods. This chapter will provide a concise summary of the experimental setup that enables NV-NMR and the more general quantum sensing experiments described in Chapters 5, 6, 7 and 8 of this thesis. In addition, the employed bulk diamond chips and the preparation of NV centers using ion implantation and annealing will be discussed at the beginning of this chapter. Further details on the experimental setup can be found in the following PhD theses from our research group [79, 97, 101].

4.2 Diamond chips

The experiments described in this thesis were performed on bulk, electronic-grade diamond crystals from ElementSix with typical dimensions $2\text{ mm} \times 2\text{ mm} \times 0.5\text{ mm}$ with $\langle 110 \rangle$ edges and a $\langle 100 \rangle$ front facet. After receiving the samples, NV centers were generated by ion implantation of ^{15}N with an energy of 5 keV, corresponding to a depth d of $\sim 5 - 10\text{ nm}$. This implantation depth is a compromise between the deteriorated coherence properties of very shallow NV centers ($d < 5\text{ nm}$) and the distance of the sensor to target molecules that we plan to embed into a matrix layer on top of the diamond chip for future experiments. First experiments describing the preparation of surface matrix layers with spin-coating techniques are described in

the Master's thesis of N. Hauff [102]. The implantation process itself was carried out by collaborators at the University of Leipzig¹ or alternatively by an industrial partner². Prior to the implantation process we attached a metallic mask with a grid of $\sim 100 \mu\text{m}$ -wide holes on top of the front facet of the diamond to define a implantation pattern. After implantation, we anneal the samples in-house with a custom-built, evacuated tube furnace (Carbolite MTF) at a background pressure lower than 10^{-8} mbar for 60 – 120 min at $T = 880^\circ\text{C}$. During the annealing step vacancies, that are generated during the implantation process, mobilize and combine with the nitrogen atoms to form NV centers. The conversion efficiency of implanted nitrogen to NV centers at the given implantation energy amounts to approximately 0.5% [103]. The temperature of the tube furnace is ramped up slowly to the desired set temperature to preserve high-vacuum during the entire process. Further details on the recent development of diamond processing can be found in the Master's thesis of N. Hauff [102].

The diamond chip used for most experiments in Chapters 5, 6, 7 and 8 with the internal identifier *E1303* was overgrown, prior to implantation, with a layer structure of 20 nm enriched ^{12}C (99.99%), 1 nm enriched ^{13}C (estimated in-grown concentration $\sim 5 - 10\%$) and a 5 nm cap layer of again enriched ^{12}C (99.99%). The overgrowth was performed by H. Watanabe at AIST, Japan. The resulting isotope structure is shown in Fig. 4.1, where the estimated distribution of NV centers relative to the isotope layers is indicated. After annealing this particular sample, we had to slightly etch the surface (at 580°C in pure O_2) to remove persistent surface fluorescence. Further characterizations and details on the sample can be found in a recently published study (sample B in Ref. [104]). In general the sample shows on the one hand NV centers with long dephasing times ($T_2^* \sim 5 - 15 \mu\text{s}$), which are most likely located beneath the enriched ^{13}C layer in a spin-free environment. On the other hand also strongly coupled nuclear spins can be observed on defects which are most likely located close to the enriched layer and which show shorter dephasing times. Finally, a very high charge stability of most NV centers studied during the course of this thesis was observed.

4.3 Experimental setup

The experimental setup for sensing experiments with NV centers operates at room-temperature and fits onto a small optical table, with further miniaturization possible and under way. The setup can be divided into four main components, which will be described in the following in further detail: a confocal laser microscope for the optical initialization and read-out of the NV center, a microwave line to control the electron spin of the NV center, a planar microcoil to control nuclear spins and finally a moveable permanent magnet to apply magnetic bias fields.

4.3.1 Confocal laser microscope

The experimental setup is centered around a custom-built confocal microscope, which is optimized for the optical excitation and emission spectrum of the NV center. A simplified schematic of the microscope is shown in Fig. 4.2 (a). We excite the NV center with a diode-pumped solid-state laser (DPSSL) with a wavelength of $\lambda = 532 \text{ nm}$. For fast optical pulses we switch the laser on and off with an acousto-optic modulator (AOM, GH AOMO 3200-125) that has a typical rise time of 10 nanoseconds

¹By the group of Prof. Jan Meijer at the Felix-Bloch-Institute.

²Cutting Edge Ions, CA, USA.

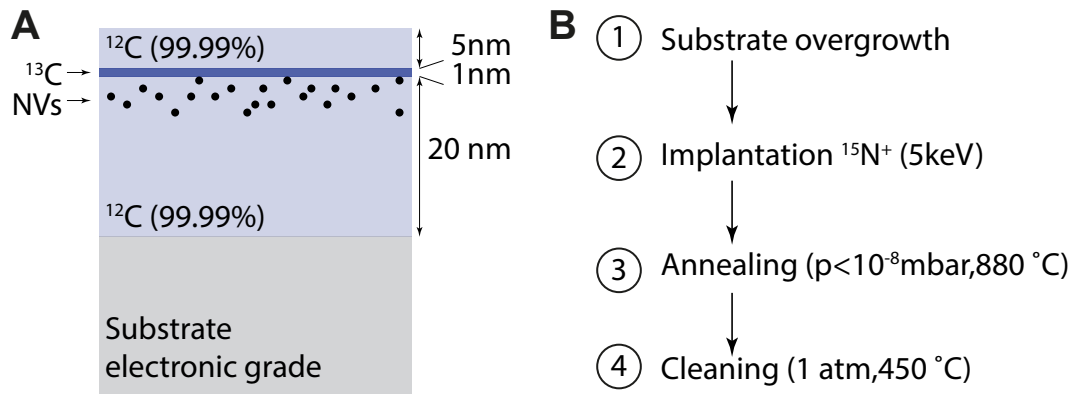


FIGURE 4.1: **Layer structure of isotopically-purified diamond samples hosting NV centers.** (a) Layer structure of an isotopically-purified diamond sample, that was employed for most experiments in Chapters 5, 6 and 7. The substrate is a bulk, electronic-grade diamond from ElementSix, which was overgrown with a layer structure of 20 nm enriched ^{12}C (99.99%), 1 nm enriched ^{13}C (estimated in-grown concentration $\sim 5 - 10\%$) and a 5 nm cap layer of again enriched ^{12}C (99.99%) at the AIST, Japan. (b) After overgrowth Nitrogen-vacancy (NV) centers were generated by ion-implantation of ^{15}N with an energy of 5 keV and subsequent annealing in a custom-built tube furnace at 880 °C under high vacuum. The NV centers were formed at a depth of $\sim 5 - 10$ nm according to Stopping Range of Ions in Matter (SRIM) simulations. The final cleaning step, again performed in the tube furnace, but under ambient pressure, is performed to remove fluorescent graphite on the diamond surface that forms during annealing.

and an extinction ratio in double-pass configuration that is better than 50 dB. Recently, our group has also developed a new laser source [102] that does not require an acousto-optic modulator and is based on directly switching the current applied to a high-bandwidth (> 150 MHz) laser diode. This approach considerably simplifies the optical setup, increases the extinction ratio and is further not prone to misalignment due to mechanical drift. Nevertheless, all experiments in this thesis were performed with the AOM-based laser system. For bulk diamond samples we typically require optical powers in the range of 5 – 10 mW to saturate the NV center. After passing the AOM the laser beam is coupled to a single-mode fiber in order to clean the transverse mode profile and to deliver the beam to the main setup (see Fig. 4.2 (a)).

The green excitation beam is subsequently transmitted through a dichroic mirror and via a dual-axis, galvanometric mirror system (GM, Thorlabs, GVS212) steered into a high-resolution microscope objective with a numerical aperture of $\text{NA} = 0.95$, which is compensating for chromatic aberrations. The objective focuses the excitation beam onto the diamond sample and collects the emitted, red-shifted photons. For axial focusing we employ a piezo-based objective scanner (Piezo Systems Jena MIPOS-100) with a travelling range of 90 μm . The red-shifted photons, emitted by the NV center, propagate through the optical path in opposite direction and are separated from the excitation photons on the dichroic mirror where they are reflected. After passing a pin-hole (PH, 30 μm diameter) photons are focused on an avalanche photodiode (APD). From individual NV centers in a bulk sample we typically detect 40 – 50 kCts/s with a background fluorescence of 2 – 5 kCts/s, which results in ODMR contrasts of up to 40%. The collection efficiency is mainly limited by total internal reflection of the emitted photons at the diamond-air surface due to the high refractive index of diamond $n = 2.41$ [105] and can be increased, by more than one

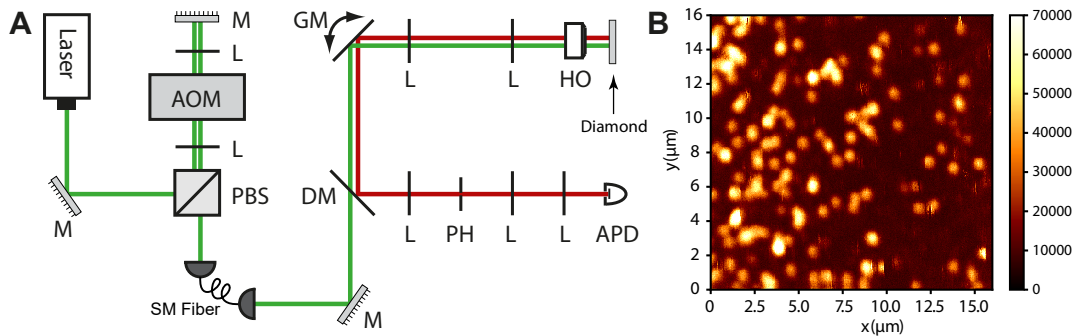


FIGURE 4.2: **Confocal microscopy of individual NV centers.** (a) Schematic of the custom-built confocal microscope used in all experiments reported in this thesis. A diode-pumped solid-state laser (DPSSL) with wavelength $\lambda = 532 \text{ nm}$ is switched on and off using an acousto-optic modulator (AOM) in double-pass configuration and transferred to the confocal microscope via a single-mode (SM) fiber. The laser beam is steered over the sample in the lateral, xy - directions by means of a galvanometric pair of mirrors (GM), which varies the entrance angle into a high numerical-aperture (NA=0.95) objective (HO), which focuses the beam onto the diamond surface. A high-precision, piezo-electric actuator is employed for focusing in the z -direction. The emitted, red-shifted photons are collected with the objective, separated from the excitation photons using a dichroic mirror (DM), filtered by a pin-hole (diameter $\sim 20 \mu\text{m}$) and finally detected with an avalanche-photodiode (APD). Mirrors (M) and lenses (L) are included in the schematic and indicated by the respective capital letters. (b) Confocal scan ($15 \mu\text{m} \times 15 \mu\text{m}$) of a bulk diamond sample. From individual NV centers we typically detect 40 – 50 kCts/s with a background fluorescence of 5 kCts/s.

order of magnitude, by etching photonic structures into the diamond chip [106].

4.3.2 Control and readout electronics

The electronic signals required to steer the experimental setup are controlled by two arbitrary waveform generators (AWG-1 and AWG-2) and a multi-channel data acquisition board. A schematic of the control electronics is shown in Fig. 4.3. All devices are operated with a control software implemented in Labview, which is further described in [79].

Microwave and radio-frequency signal generation

The first AWG (AWG-1, Tektronix AWG5002C) acts as the master device, which triggers the execution of signal generation and acquisition on the other devices (see Fig. 4.3 (b)). In addition, the internal reference clock of AWG-1 is distributed to all other devices to ensure proper synchronization of all sub-systems (see Fig. 4.3 (c)).

AWG-1 has two analog output channels with a resolution of 14 bits and a maximum sampling rate of 600 MS/s and controls the microwave pulses that we use to manipulate the electron spin of the NV center. For this purpose we up-convert the output of the AWG-1, which is set to a carrier frequency of 100 MHz. For up-conversion we employ an IQ-mixer (Marki IQ1545) in the single sideband regime and a low phase noise local oscillator (Phasematrix, Quicksyn FSW-0020). The resulting signal at frequency 1 – 4 GHz is subsequently amplified and transmitted to an impedance-matched coplanar waveguide (CPW) and dissipated in an attenuator rated for high powers of up to 100 W. Details on the microwave CPW can be found

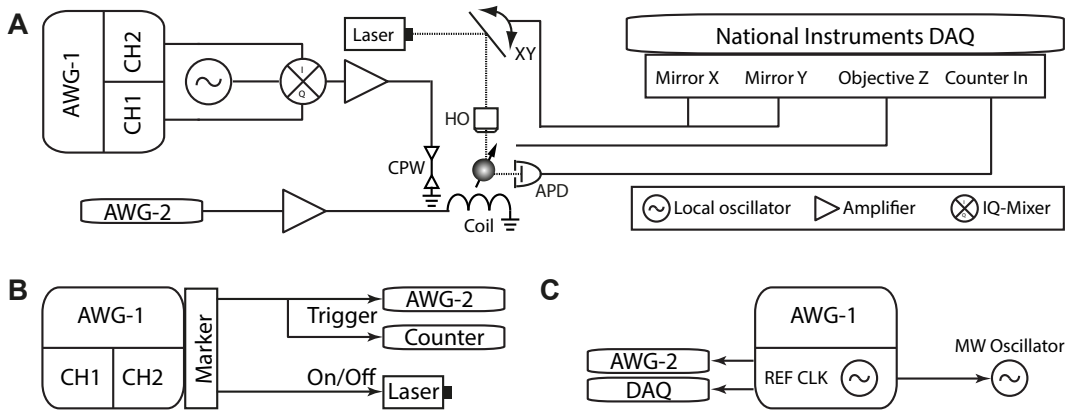


FIGURE 4.3: **Control electronics of the experimental setup.** (a) Two arbitrary waveform generators (AWG-1,AWG-2) generate the microwave and radio-frequency pulses. AWG-1 (Tektronix AWG5002C) has two analog output channels with a resolution of 14 bits and a maximum sampling rate of 600 MS/s and drives the I and Q channels of a IQ-Mixer (Marki IQ1545), which is operated in the single sideband regime to up-convert the AWG carrier frequency of 100 MHz with a high-frequency tone at 1 – 4 GHz with a low phase noise local oscillator. The resulting microwave pulses are amplified with a waveform amplifier (Accel Instruments TS-200) that drives the radio-frequency coil. The scanning mirrors (Thorlabs GVS212) and a z-focusing piezo attached to the microscope objective (HO) are steered by analog control signal from a DAQ card (National Instruments PCIe-6363). Photons emitted by the NV center are detected with an avalanche photodiode (APD) and time tagged with the integrated counter of the DAQ card with a temporal resolution of 10 ns. (b) The master device AWG-1 provides the start trigger for the execution of waveforms on AWG-2 and for the counter clock. Furthermore, the laser is switched with a digital output of AWG-1. (c) Timing synchronization of all devices is ensured by distributing the integrated 10 MHz reference clock of AWG-1 to AWG-2, the DAQ and the microwave oscillator.

in [101]. Apart from the two analog output channels AWG-1 also includes four digital marker output channels, which we use to trigger the slave devices and to switch the laser.

The second AWG (AWG-2, National Instruments, PCI-5421) controls the radio-frequency pulses for nuclear spin control. The device provides a single analog output channel with a resolution of 16 bit and a maximum sampling rate of 100 MS/s. The generated voltage signals are subsequently amplified with a waveform amplifier (Accel Instruments TS-200) that drives the radio-frequency coil. The waveform amplifier has a limited bandwidth of ~ 1 MHz. In most NMR experiment performed at low magnetic bias field this bandwidth is sufficient. At higher magnetic bias field and thus higher nuclear precession frequencies, we switch to a conventional radio-frequency amplifier (Mini Circuits LZY-22+ 200 MHz bandwidth).

At the beginning of each experiment the corresponding pulse sequences including all trigger and marker signals are compiled from a script file (see [79] for example pulse files and details of the script syntax) that contains a chronological set of instructions that are executed during the sequence. Subsequent to the compilation the resulting waveforms are uploaded to the waveform generators and signal generation starts upon a trigger signal.

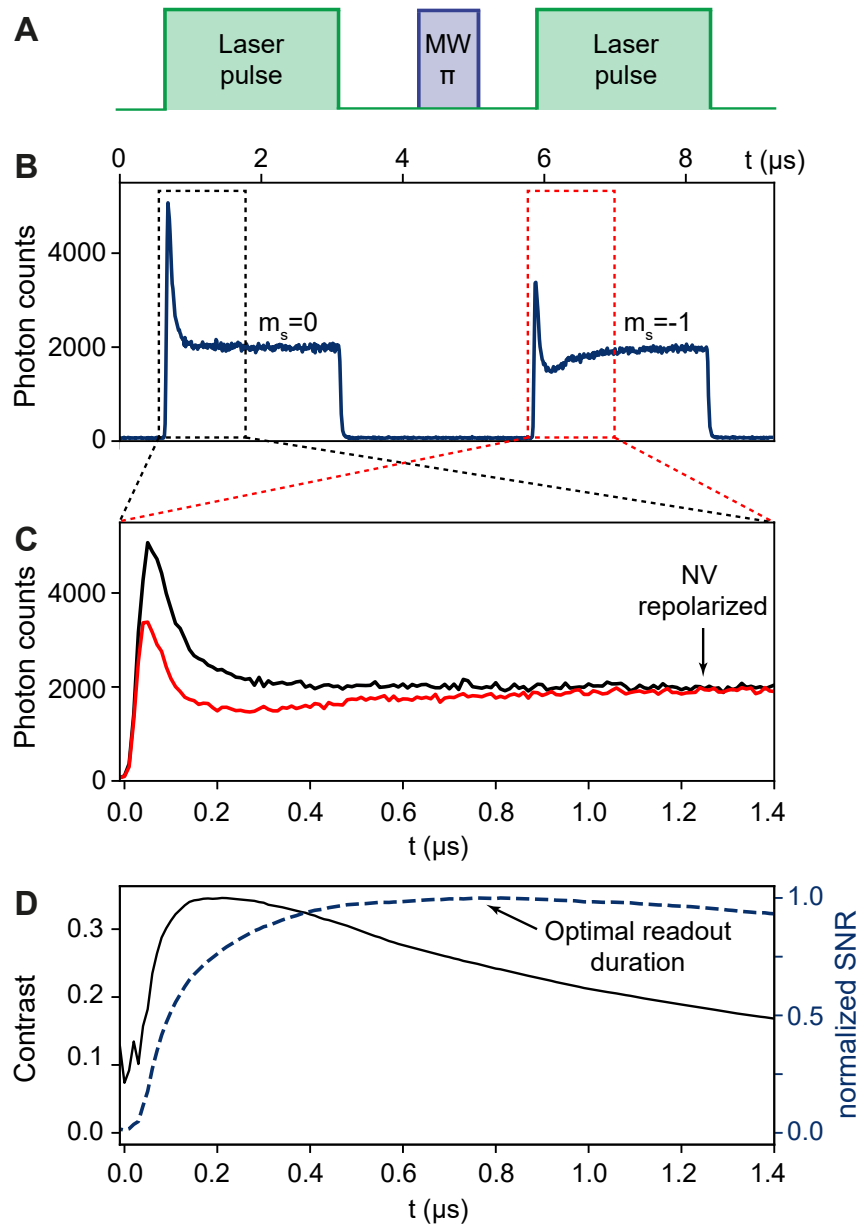


FIGURE 4.4: **Time-resolved photon counting.** (a) Experimental sequence used to probe the time-dependent fluorescence rate of the NV center prepared either in the $m_s = 0$ (first laser pulse in the sequence) or $m_s = -1$ state (second and final laser pulse in the sequence). The sequence is repeated $10^5 - 10^6$ to acquire sufficient photon statistics. (b) Histogram of photon counts for the experimental sequence shown in (a). The first burst of photons results from readout of the NV center prepared in the $m_s = 0$ state and the second photon burst results from readout of the NV center after a π -pulse has been applied to prepare the NV center in the $m_s = -1$ state. (c) Overlay of the two photon bursts shown in (b) according to the timing table generated from the pulse file corresponding to the sequence shown in (a). (d) ODMR contrast (black line) and normalized read-out SNR (blue dashed line) as function of the integration window of the time-dependent photon rate. The maximum contrast for individual NV centers in well aligned magnetic fields (tilt of the external bias field to the quantization axis smaller than 1°) is 30 – 40 %.

Time-resolved photon counting

The integrated counter of a multi-channel data acquisition board (National Instruments PCIe-6363) time stamps the photons, that are detected by the APD, relative to the start trigger with a time resolution of 10 ns. The resulting time stamps are binned into a histogram in software. Based on the pulse file, discussed in the previous paragraph, the software further generates an integration table, which defines the integration intervals of the histogram. This integration table is later used for the analysis of the measurements as described below.

A very basic example of an experiment, which merely records the photon count rate of the NV center in the $m_s = 0$ and the $m_s = -1$ state is shown in Fig. 4.4 (a): Two laser pulses with duration $t_p = 2 \mu\text{s}$ are applied to the NV center. The second laser pulse is preceded by a microwave π -pulse, which prepares the NV center in the dark $m_s = -1$ state. Fig. 4.4 (b) shows the resulting histogram of photon counts, obtained from the time tags of the counter. Clearly, two time intervals with photon bursts can be identified. In the remaining time intervals the photon count-rate corresponds to the dark count rate of the detector because in this time interval the laser is turned off (typical dark count rate $\sim 40 - 100$ Cts/s). Furthermore, the initial count rate of the first photon burst is significantly stronger than that of the second photon burst. This is also shown in Fig. 4.4 (c) where both bursts are overlaid. We also note that the photon count rates converge to a common steady state value approximately after $t = 1.2 \mu\text{s}$, which implies that the NV center is repolarized into the $m_s = 0$ state.

To optimize the efficiency of spin-state readout photon counts have to be integrated in an integration window that maximizes the read-out SNR. In the measurement software both starting position of the integration and length of the integration window are selected to ensure optimal readout. In Fig. 4.4 (d) we show the ODMR contrast on a single NV center, obtained from the measurements shown in Fig. 4.4 (b) as function of the integration duration. The black line in Fig. 4.4 (d) shows the ODMR contrast, that is the relative change in fluorescence rate between $m_s = 0$ and $m_s = -1$, as function of the integration window width. The integration duration for optimal ODMR contrast is obtained for an integration duration of approximately 200 ns. Optimal integration duration is, however, not only determined by the ODMR contrast C but also by the number of photons N collected. In Fig. 4.4 (d) we therefore also show the normalized signal to noise ratio of the NV readout (as discussed in Chapter 2) as function of the integration (blue dashed line):

$$\text{SNR} \propto C\sqrt{N}. \quad (4.1)$$

Here, optimal readout SNR is achieved for an integration duration of approximately 700 ns where a reduction in ODMR contrast is compensated by higher absolute photon counts, which reduces the photon shot noise.

The ideal starting position of the integration may shift over time as the dead time of the acousto-optic modulator changes if the position of the laser beam entering the modulator varies. Further, the optimal window of the integration generally changes with the laser intensity. Therefore, the integration settings have to be controlled regularly and adjusted correctly. Complementary details on the readout procedure are additionally described in [79]. Finally, we note that the typical peak ODMR contrast is between $C \sim 30 - 40\%$ on diamond chips with low background fluorescence and under the condition that the external magnetic bias field is properly aligned.

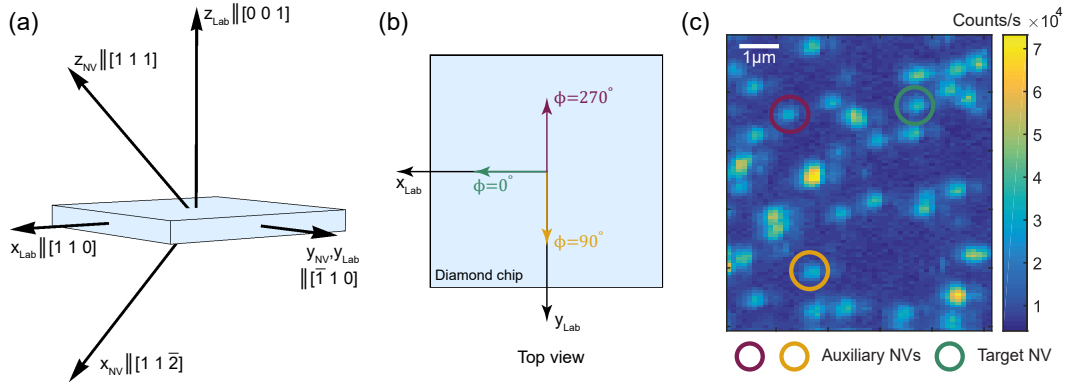


FIGURE 4.5: **Definition of the laboratory and NV center coordinate systems.** (a) Definition of the laboratory and NV center coordinate systems. The diamond chip with $\langle 110 \rangle$ edges and a $\langle 001 \rangle$ front facet is indicated in light blue. The origins of the coordinate systems coincide with the position of the vacancy in the lattice. (b) (Top view) NV centers with laboratory, azimuthal orientation $\phi = 0^\circ$ (green) are used for NMR spectroscopy or quantum sensing experiments. NV centers with azimuthal orientations $\phi_{a,1} = 90^\circ$ (yellow) and $\phi_{a,2} = 270^\circ$ (purple) are employed as auxiliary field sensors for the calibration of vector magnetic fields. (c) Confocal scan of a segment of the diamond chip. A green circle indicates the sensing NV with $\phi = 0^\circ$ and yellow and purple circles highlight the auxiliary NV centers used for field calibrations.

Control of the confocal microscope

In addition to photon integration, the multi-channel data acquisition board (National Instruments, PCIe-6363) controls the scanning mirrors and the focusing piezo attached to the microscope objective with three analog control signals. The focusing piezo has a traveling range of $90\ \mu\text{m}$ and the scanning mirrors enable access over a field of view of at least $150\ \mu\text{m} \times 150\ \mu\text{m}$. During experiments the spatial focusing position of the target NV center shifts, mainly due to the heating effects resulting from dissipation of microwave power in the coplanar waveguide. To continuously correct for this shift the scanning mirrors setting and the focus position are re-optimized for maximum fluorescence rate 10 – 20 times per hour. Further details on the fluorescence rate optimization procedure can be found in the thesis of T. Rosskopf [79].

4.3.3 Calibration and alignment of static quantization fields B_0

We apply static quantization fields with a cylindrical, NdFeB magnet, which is attached to a three-axis, precision translation stage. By varying the distance between sample and magnet the magnitude of the bias field can be altered between $\sim 5\ \text{mT}$ to $\sim 350\ \text{mT}$. The orientation of the bias field can be changed and aligned to the crystallographically defined z -axis of the NV center by moving the magnet relative to the sample.

Precise alignment of the external bias field to the quantization axis of the NV center (z -axis) is critical to ensure long coherence times and high contrast of the ODMR effect [107]. Further, very precise alignment of the external quantization field is very important for azimuthal localization measurements reported in Chapter 6 and 7, because residual transverse fields of \vec{B}_0 introduce systematic uncertainty in the nuclear position vector inferred from spectroscopy experiments.

Field alignment at high magnetic field ($20 \text{ mT} < B_0 < 350 \text{ mT}$)

To align the vector magnet field in the limit of high magnetic fields ($20 \text{ mT} < B_0 < 350 \text{ mT}$), we first move the magnet to several spatial (x, y, z) -positions (typical 4 – 5 positions) above the sample and record the ODMR resonance frequencies of a particular NV center to which we aim to align the permanent magnet's field. Subsequently, we determine the orientation and spatial position of the NV center, in the coordinate system of the xyz -stage moving the magnet. This is achieved by fitting a numerical model of the field map generated by the permanent magnet to the recorded ODMR frequencies, which encode the vector field experienced by the NV center. Once the orientation and position of the NV center in the coordinate system of the permanent magnet is known, the model allows us to predict where to move the permanent magnet to generate an aligned magnetic field with desired magnitude B_0 at the position of the NV center. This procedure enables us to align the vector field of the permanent magnet with a residual tilt of a few degrees to the z -axis of the NV center.

Field alignment at low magnetic field ($B_0 < 20 \text{ mT}$)

At low magnetic fields ($B_0 < 20 \text{ mT}$) the field of the magnet can be aligned to the symmetry axis of the NV center with a different technique, which typically results in more precise alignment. The coarse alignment of the magnet and a rough adjustment of the magnitude of the field is again achieved by recording ODMR spectra of the target NV center for different (x, y, z) -positions of the magnet and by fitting procedure described above. Afterwards, we iteratively optimize the alignment of the magnet. In each iteration, we reconstructed the vector field \vec{B}_0 using the method used for the calibration of the coil field $\Delta\vec{B}$ as described in section 4.3.5. Subsequently, we move the magnet in the lateral (x, y) -plane of the laboratory frame. The direction and step size is determined from a field map of the permanent magnet and the residual transverse components of the field \vec{B}_0 . We terminate this iterative process when the residual transverse field components are smaller than $50 \mu\text{T}$. Thus we achieve residual tilts to the quantization axis of the NV center which are significantly smaller than 1° . At high magnetic field this procedure can not be used because the significant magnitude of transverse fields acting on the auxiliary NV centers eliminates the ODMR contrast due to state mixing [107].

Stability of B_0

For NV-NMR experiments the stability of the external bias field is crucial, because temporal drifts of B_0 lead to a variation of the Larmor frequency of nuclear spins which over long integration times leads to broadened spectra [73] and non-resonant multi-pulse dynamical decoupling sequences. Most experiments reported in this thesis have been performed at low magnetic bias fields of $\sim 10 \text{ mT}$. At this magnitude of B_0 we have calibrated the magnetic field stability by tracking the EPR frequency of the NV center over several hours. A resulting trace of the EPR frequency is shown in Fig. 4.6 (b), for a measurement duration of $\sim 35 \text{ hrs}$. The standard deviation of the EPR frequency amounts to 33 kHz , which corresponds to a magnetic field stability of $\sim 1.2 \mu\text{T}$. The variation in the magnetic field is most likely resulting from temperature fluctuations in the laboratory, which lead to a change in the magnetization of the permanent magnet. At higher magnetic field, we find that the relative fluctuations in the magnetization with temperature remain similar. However, the absolute shifts in frequency are consequently significantly larger. For

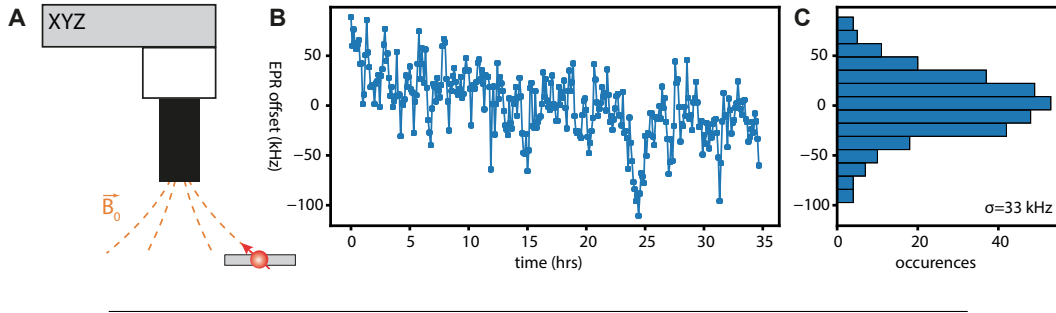


FIGURE 4.6: **Magnetic bias field source and field stability.** (a) A cylindrical NdFeB permanent magnet attached to a high-precision translation stage *Newport M-462-XYZ-M* (resolution in xyz : $1\ \mu\text{m}$, travel range in xyz : $25\ \text{mm}$) provides the magnetic bias field. By moving the magnet relative to the sample vector fields with magnitude between $\sim 5\ \text{mT}$ and $\sim 350\ \text{mT}$ can be applied and aligned to the quantization direction of the NV center. (b) Stability of the EPR frequency over the course of a long experiment ($> 30\ \text{hrs}$ integration time) at $B_0 \approx 10\ \text{mT}$. The fluctuations in the magnetic field are predominantly caused by temperature-induced variations of the magnetization of the permanent magnet. (c) Histogram of the EPR shifts generated from the time trace in (b). The distribution of EPR shifts shows a standard deviation of $\sigma = 33\ \text{kHz}$, which corresponds to a fluctuation of the magnetic field of $1.2\ \mu\text{T}$.

example, at a magnetic field of $200\ \text{mT}$ the typical fluctuations of the EPR transition are in the range of several MHz, translating into a magnetic field stability in the range of $\sim 20 - 30\ \mu\text{T}$.

4.3.4 Planar radio-frequency coils for nuclear spin control

The NV-NMR experiments in this thesis require active control of both the sensor electron spin of the NV center and of target nuclear spins. In principle both the microwave pulses for the sensor and the radio-frequency pulses for the nuclei can be transmitted through the coplanar waveguide, however, a planar micro-coil directly placed above the sample achieve significantly higher nuclear Rabi frequencies: In fact, we typically achieve Rabi frequencies of $\Omega_R \sim 2\pi \times 30\ \text{MHz}$ on the electron spin of the NV center, which correspond to a driving fields of $B_1 = \sqrt{2}\Omega_R/\gamma_e \sim 0.76\ \text{mT}$. In contrast we have, based on numerical simulations (see section 4.3.4), estimated that driving fields of $B_1 \sim 5 - 10\ \text{mT}$ are feasible with a small planar coil. This represents an increase of one order of magnitude in the driving field and permits much faster control of nuclear spins. We note that an alternative approach to achieve high nuclear Rabi frequencies would be to directly pattern a small conductor onto the diamond as was demonstrated in [108]. In this case, however, the conducting material on the diamond surface might deteriorate the coherence properties of shallow NV centers [109] and further complicates sample deposition on the diamond chip.

Numerical optimization of the coil geometry

We have performed a simple numerical optimization of the coil geometry with the target of maximizing the coil B_1 field, while constraining the inductance of the coils to $2.5\ \mu\text{H}$ to maintain sufficient bandwidth. The coil geometry was parameterized by its inner diameter d_i , the number of windings N_1 and the number of layers N_2 . We constrained ourselves to circular windings and wire diameters of $120\ \mu\text{m}$ (including the isolation layers). Further, only a small set of possible inner diameters, provided

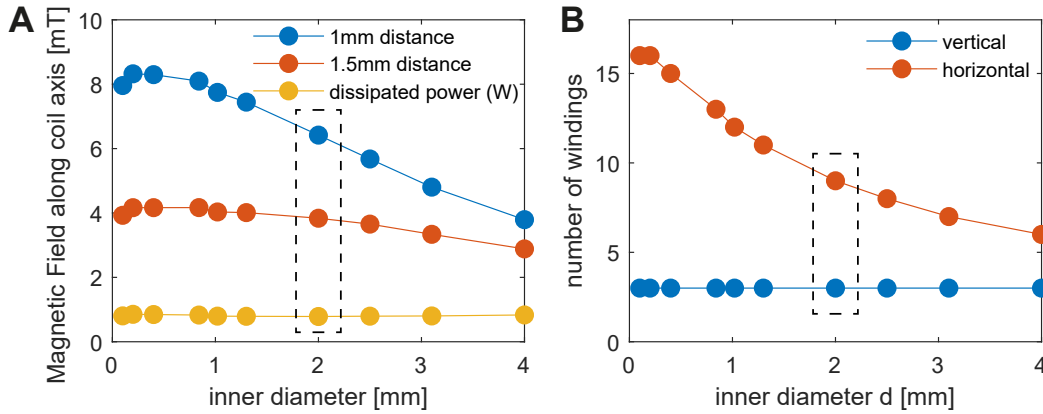


FIGURE 4.7: **Numerical optimization of the coil geometry.** (a) Optimized coil magnetic field magnitude for various inner diameters d_i of the coil. For the optimization the number of vertical and horizontal windings has been varied under the constraint that the inductance remains below $2.5 \mu\text{H}$. The magnetic field was computed using the Biot-Savart law and the inductance of the coil was estimated from empirical analytical models [110]. (b) Optimized number of vertical and horizontal windings for the same inner diameters as in (a). In this thesis experiments were performed with a coil with inner diameter $d_i = 2 \text{ mm}$ (highlighted with a dashed box).

by the manufacturer (Sibatron AG) was evaluated to keep the production cost low. The magnetic field B_1 produced by the coils described by (d_i, N_1, N_2) , at a stand-off distance of 1 mm was computed using the Biot-Savart law. This vertical offset of the coil from the NV centers results from the thickness of the diamond ($500 \mu\text{m}$), the thickness of the microscope glass slide used to mount the diamond ($200 \mu\text{m}$) and possible air gaps. The resulting optimized parameter sets (N_1, N_2) for all d_i are shown in Fig. 4.7 (b).

Integration into the confocal microscope

A schematic of the mechanical holder structure used to integrate the planar coil into the existing confocal microscope is shown in Fig. 4.8. Apart from minimizing the stand-off distance of the coil to the NV centers, an efficient thermal contact of the coil to the metallic holder structure is highly desirable to minimize heating due to the Joule effect. Therefore, we glued the coil with silver glue to a small copper plate, which itself was attached with the same glue to a holder frame made of aluminium (see Fig. 4.8). This heat sink structure was later replaced with a diamond plate and attached with non-conductive glue to reduce eddy currents, which limit the coils bandwidth (see description of an improved coil design at the end of this chapter). Using the holder structure the coil can be placed directly on top of the microscopy glass slide holding the diamond. We estimated the final stand-off distance of the vertical center of the coil to the NV center to be $\sim 925 - 1125 \mu\text{m}$.

4.3.5 In-situ characterization of the planar coils

Heating effects due to DC current and current pulses

After installation of the coil into the setup, we carefully tested heating effect while applying DC current with a 100% duty cycle. We used a handheld infrared thermometer to measure the temperature of the coil for varying input currents. In Fig.

geometry		v 1.0 (this work)	v 2.0 [98]
magnetic fields	no. of windings (lateral)	9	10
	no. of layers (vertical)	3	2
	wire diameter (inc. isolation)	120 μm	120 μm
	inner diameter	2 mm	1.02 mm
	outer diameter	4.2 mm	2.22 mm
	vertical height	360 μm	240 μm
	vertical stand-off to NV center	$\sim 1000 \mu\text{m}$	$\sim 1000 \mu\text{m}$
electrical	B (~ 1 mm stand-off, simulated)	~ 6.4 mT/A	~ 4.5 mT/A
	B (~ 1 mm stand-off, measured)	~ 5.6 mT/A	-
	self-inductance	$\sim 2.5 \mu\text{H}$	$\sim 0.9 \mu\text{H}$
	intrinsic resistance (at DC)	$\sim 0.5 \Omega$	$\sim 0.5 \Omega$
	termination resistance	4.7 Ω	50 Ω
	bandwidth (-3dB criterion)	~ 100 kHz	~ 20 MHz
	max. current (100% duty cycle)	0.6 A	~ 2 A
	max. current (10% duty cycle)	2 A	> 2 A

TABLE 4.1: **Geometry, magnetic and electrical design properties of the planar coil.** This table summarizes the design properties of the planar micro-coils that have recently been developed in our group. The properties of the initially developed, first version (v 1.0) is highlighted in Fig. 4.7 (a) and (b). The coil was manufactured by Sibatron AG and used for all low field NMR experiments reported in Chapters 6 and 7. A coil with lower inductance, higher bandwidth and more efficient thermal management (v 2.0) was used for the high-field NMR measurements ($B_0 > 200$ mT). This coil was also manufactured by Sibatron AG. The development of this coil is described in detail in [98].

4.9 (a), we show the measured temperature of two different coils with a total number of windings of 15 and 27, respectively. Both measurements show a quadratic dependence of the temperature onto the injected current. For current higher than 1 A, we observe temperatures exceeding 40 °C, which also led to thermal drifts detected in the confocal microscope, prohibiting higher current. Nonetheless higher currents can be applied in pulsed operation with reduced duty cycles. Temperature measurements have shown that at a duty cycle of 10% square current pulses with 2 A can be applied without exceeding 40 °C. At these peak currents B_1 fields of up to 10 mT can be realized, which is approximately one order of magnitude higher than the fields produced by the microwave stripline.

Field magnitude measurement and vector magnetometry

We calibrated the vector field generated by the coil $\Delta\vec{B}$ using the target NV, coupled to nuclear spins of interest, and two auxiliary NV centers with different crystallographic orientation. All three NV centers were located in close proximity to each other, with a distance of typically $\leq 5 \mu\text{m}$ (see Fig. 4.5 (c)). Over this separation the magnetic field of the coil can be assumed to be homogeneous. We determined the orientation of the symmetry axis of many NV centers by moving the permanent magnet over the sample and observing the ODMR splitting. The azimuthal orientation of the target NVs defines the x-axis in the laboratory and NV frame ($\phi = 0$). This orientation was the same for all target NV centers investigated in this work. The auxiliary NV centers were selected to be oriented along $\phi_{a_1} = 90^\circ$ and $\phi_{a_2} = 270^\circ$.

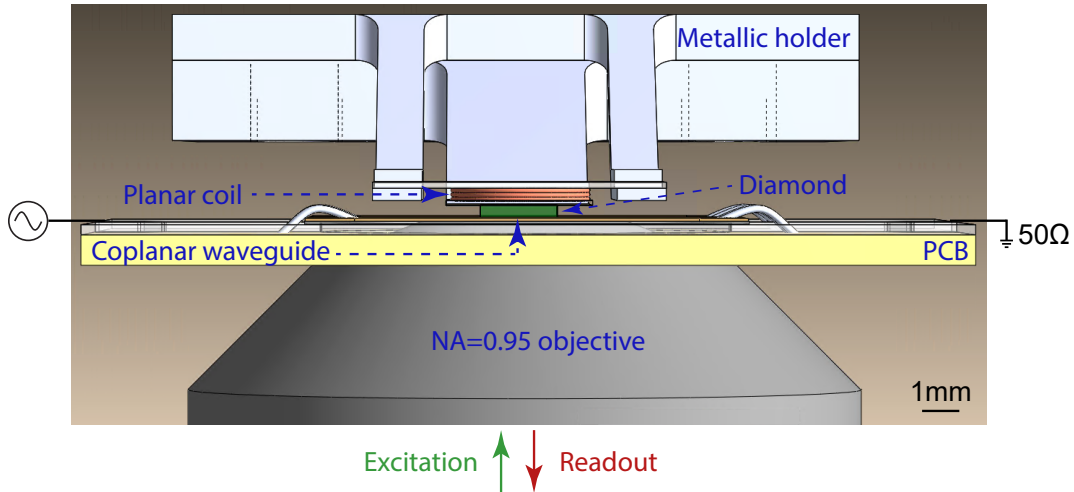


FIGURE 4.8: **Schematic of the central part of the experimental setup used in this work.** Microwaves for spin control are transmitted through a coplanar waveguide, which has been lithographically defined on a quartz slide. The quartz slide is glued onto a PCB board and contacted to SMA connectors using wire bonds. A bulk diamond chip is placed on top of a quartz slide and NV centers are excited and detected with a high-resolution (NA=0.95) objective, which is installed below the quartz slide. For focusing the microscope objective can be translated in the vertical direction using a piezo scanner. The planar coil is located directly on top of the diamond chip and glued to a copper plate, which itself is mounted on metallic holder.

To calibrate the coil field, we removed the permanent magnet and recorded ODMR spectra for the target NV center and both auxiliary NV centers with the field of the coil activated. In this way we record in total 6 ODMR lines, with 2 lines per NV center.

A numerical, nonlinear optimization method was used to determine the magnetic field $\Delta\vec{B}$ from these ODMR resonances. For each of the three NV centers we simultaneously minimized the difference between the measured ODMR lines and the eigenvalues of the ground-state Hamiltonian:

$$H_i = DS_z^2 + \gamma_e(\Delta\vec{B})_i \cdot \vec{S}. \quad (4.2)$$

Here, the magnetic field $(\Delta\vec{B})_i$ acting onto the specific NV center is obtained by a proper rotation of $\Delta\vec{B}$ into the respective reference frame. It is important to note that for certain orientations of the coil field the determination of the field from the six ODMR resonances is not unique due to the symmetry of the diamond crystal. Nevertheless, a single solution could always be identified by invoking that the coil field is oriented approximately along the z-direction of the laboratory system.

All calibration measurements of the produced magnetic field were performed with a coil with parameters ($d_i = 2$ mm, $N_1 = 9$, $N_2 = 3$). These calibrations were performed with an injected current of ~ 0.5 A and the magnitude of the calibrated magnetic field vector was ~ 2.5 mT, which corresponds to a normalized produced B_1 field of 5 mT/A. This normalized field is slightly smaller than the theoretical expectation from the idealized simulation in Fig. 4.7 from which we expect a normalized field of ~ 6 mT/A at a stand-off distance of 1 mm.

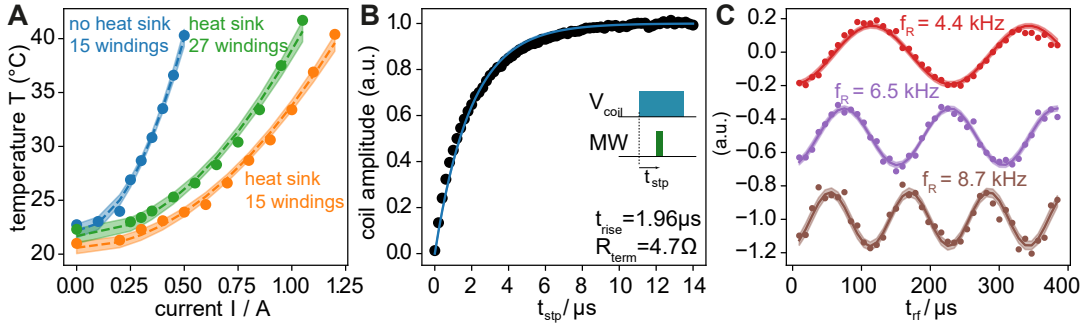


FIGURE 4.9: **Characterization of the planar, radio-frequency coil.** (a) Temperature of the planar coil as a function of injected DC current (100% duty-cycle). The temperature was detected with an optical temperature sensor. A coil with 15 windings was tested with (orange) and without (blue) heat sink / holder made out of copper. Clearly, the heat sink enables much higher operation currents. In addition, we tested a coil with 27 windings, which was ultimately used for most measurements in this work and whose properties are summarized in detail in Table 4.1. The shaded areas represent the confidence intervals of a quadratic fit to the measured data points. (b) Step-response of the coil circuit detected by the NV center. The data points (black) show the normalized shift of the NV’s EPR transition frequency due to the coil’s magnetic field. The rise-time of the coil circuit amounts to $1.96 \mu\text{s}$ with an ohmic termination of 4.7Ω . The shift of the EPR frequency was detected with time-resolved ODMR spectroscopy (experimental sequence indicated as an inset), which is explained in detail in Chapter 7. In addition, the time-resolved detection of the magnetic field could be realized by the protocol developed in Chapter 8. The rise time of the coil can be reduced by using a higher impedance termination. (c) Rabi-oscillations of a single ^{13}C nuclear spin driven by the planar coil for increasing peak currents (top to bottom). The injected currents are $I = \{0.2, 0.3, 0.4\}$ A which is significantly below the threshold current with 100% duty cycle of $I \sim 1.2$ A. The external bias field amounted to ~ 9.81 mT and the frequency of the coil pulse (square envelope) was fixed to the nuclear precession frequency $f_L = 105$ kHz. The Rabi frequency in these experiments varied between 4.4 kHz to 8.7 kHz. Using the planar coil Rabi frequencies up to 25 kHz have been realized.

Step response of the coil circuit

To calibrate the dynamic response of the coil, we perform in situ measurements of the step-response using time-resolved ODMR spectroscopy (see Fig. 4.9(b)). In brief, we acquired ODMR spectra in snapshots of 200 ns after applying a step to the AWG controlling the coil circuit, and determine the temporal magnetic field profile by fitting the peak positions of the resonance curves (see inset of Fig. 4.9 (b) for the pulse sequence). Full details on time-resolved ODMR techniques are provided in Chapter 7 and 8. The microwave pulses applied to the NV center had a duration of 100 ns to provide sufficient time-resolution. In this measurement we terminated the coil circuit with a small high-power resistor ($R=4.7 \Omega$). All measurements reported in Chapter 6 and the low field measurements in Chapter 7 were conducted in this configuration. We deduce a rise-time of the coil circuit of $t_{\text{rise}} = 1.96 \mu\text{s}$. This corresponds to a bandwidth of ~ 77 kHz. The bandwidth can be increased by employing a higher ohmic termination (e.g. 50Ω), because the time constant of the RL circuit is given by $\tau = L/R$.

Nuclear radio-frequency pulses

As discussed in the beginning of this section, the main purpose of the planar coil is to apply radio-frequency pulses for active control of nuclear spins. In Fig. 4.9

(c), we show exemplary Rabi oscillation measurements on a ^{13}C single nuclear spin. The measurements were performed at a magnetic bias field of $B_0 = 9.81$ mT. Hence, the nuclear Larmor frequency amounted to 105 kHz. Resonant coil pulses with frequency fixed to the Larmor frequency and with a square pulse-shape were generated with AWG-2 and amplified with a waveform amplifier. Details of the coil electronics are described in the previous section 4.3.2. The nuclear spin was polarized prior to the application of the radio-frequency pulse using a polarization transfer method [111], which is in more detail described in Chapters 3 and 7. We detect the $\langle I_z \rangle$ expectation value of the nuclear spin, after application of a rf-pulse with length t_{rf} , using AC magnetometry with the NV center, as described in full detail in Chapter 7. We observe Rabi oscillations with increasing Rabi frequencies $\Omega_R = 2\pi \times \{4.4, 6.5, 8.7\}$ kHz for moderate injected currents $I \sim \{0.2, 0.3, 0.4\}$ A. The maximum Rabi frequencies that were achieved in experiments on ^{13}C amounted to $\Omega_R = 2\pi \times 25$ kHz for injected peak currents of 1.2 A.

Development of an improved coil design

The first version of the planar micro coil, described in the previous sections, has recently been replaced by an improved design. This design was developed in the course of the Master's thesis of K. Herb [98]. The new design resulted in higher bandwidth as well as better thermal heat management and thus stronger generated magnetic radio-frequency fields. The design properties are summarized in table 4.1 and key changes are summarized in the following.

- **Increased bandwidth:** Most NMR experiments in this thesis were performed at low magnetic field ($B_0 = 10$ mT) on ^{13}C spins. For these magnetic fields the bandwidth of the first generation coil (~ 100 kHz) was sufficient. At higher magnetic fields nuclei precess at higher frequency and hence radio-frequency pulses with higher frequency are required. Therefore three measures have been taken to increase the coil circuits bandwidth. First, the termination resistance of the circuit was adapted to 50Ω . This increases the time constant of the coil circuit, which is given by $\tau = L/R$. In addition, the coil was attached with a non-conductive glue to a heat sink made of non-conducting diamond. This ensures that no eddy currents are excited, which would otherwise limit the bandwidth. Finally, a smaller coil with lower inductance $L = 0.9 \mu\text{H}$ was installed to increase the resulting bandwidth to ~ 20 MHz. This upgrade will enable NMR pulses on both ^{13}C and ^1H at magnetic fields of up to ~ 0.5 T.
- **Improved thermal heat management:** In the new coil design the coil is glued to a thin diamond plate. Due to the very high thermal conductivity of diamond, which exceeds that of copper, higher threshold currents can be applied to the coil (2 A at 100% duty cycle). The thermal management of the metallic holder structure was also improved by using thicker structures made of copper, which remove heat more efficiently from the coil.
- **Better positioning capabilities:** The smaller size of the new coil requires a more precise positioning relative to the diamond sample. Hence, the new coil holder is equipped with three translation stages, which permit precise adjustments of the coil's position relative to the diamond chip.

High-resolution quantum sensing with shaped control pulses

Summary

In this chapter we investigate the application of amplitude-shaped control pulses for enhancing the time and frequency resolution of multipulse quantum sensing sequences. Using the electronic spin of the nitrogen vacancy center in diamond and up to 10,000 coherent microwave pulses with a cosine square envelope, we demonstrate 0.6 ps timing resolution for the interpulse delay. This represents a refinement by over 3 orders of magnitude compared to the 2 ns hardware sampling. We apply the method for the detection of external AC magnetic fields and nuclear magnetic resonance signals of ^{13}C spins with high spectral resolution. Our method is simple to implement and especially useful for quantum applications that require fast phase gates, many control pulses, and high fidelity.

This chapter has been previously published as:

J. Zopes, K. Sasaki, K. S. Cujia, J. M. Boss, K. Chang, T. F. Segawa, K. M. Itoh, C. L. Degen, *High resolution quantum sensing with shaped control pulses*, Phys. Rev. Lett. **119**, 260501 (2017)

5.1 Introduction

Pulse shaping is a well-established method in many areas of physics including magnetic resonance [112–114], trapped ion physics [115, 116] and superconducting electronics [117] for improving the coherent response of quantum systems. Introduced to the field of nuclear magnetic resonance (NMR) spectroscopy in the 1980s, shaped pulses enable selective excitation of nuclear spins with uniform response over the desired bandwidth, which led to more selective and more sensitive measurement techniques. More recently, with the advent of fast arbitrary waveform generators (AWG), pulse shaping techniques also entered the field of electron paramagnetic resonance (EPR), thereby improving spectrometer performance via chirped pulses for broadband excitation [118, 119]. In quantum information processing applications, shaped microwave pulses are utilized to optimize the fidelity and stability of gate operations against environmental perturbations that cause detuning of transition frequencies or fluctuations in the driving frequency [120, 121].

5.1.1 The time-resolution limitations of multi-pulse sequences

In this chapter we investigate the application of pulse shaping to enhance the timing resolution in the emerging field of dynamical decoupling spectroscopy [122, 123]. Dynamical decoupling is a quantum control method developed to protect a quantum system against dephasing by environmental noise [124]. More recently dynamical decoupling sequences have also been applied to map out noise spectra and to detect time-varying signals with high signal-to-noise ratio [123, 125–127]. In their simplest implementation, dynamical decoupling sequences consist of a periodic series of π pulses with repetition time τ [93] (see Figure 5.1(a)). For large numbers of pulses N , the spectral response of these sequences resembles that of a narrowband frequency filter, with center frequency $1/(2\tau)$ and bandwidth $1/(N\tau)$, that rejects noise at all frequencies except for those commensurate with the repetition time τ . By tuning τ into resonance with a signal at a particular frequency $f_{ac} \approx 1/(2\tau)$, the sensitivity to the signal can be enhanced while suppressing the influence of noise, thereby resembling the properties of a classical lock-in amplifier in the quantum regime [125].

When using many control pulses, the filter bandwidth becomes very narrow and the repetition time τ must be precisely tuned to the signal frequency $f_{ac} \approx 1/(2\tau)$. On any controller hardware, however, τ can only be adjusted in increments of the sampling time t_s . This limits in practice the frequency resolution of the technique [128]. Specifically, when detecting a signal with frequency f_{ac} , the minimum frequency increment is given by

$$\delta f = \frac{1}{2\tau} - \frac{1}{2\tau + 2t_s} \approx 2t_s f_{ac}^2. \quad (5.1)$$

Arbitrary waveform generators (AWGs) employed for the control of superconducting and spin qubits have sampling rates of typically 1 GS/s, corresponding to a time resolution of $t_s = 1$ ns. When operating at high frequencies f_{ac} this timing resolution quickly becomes prohibitive. For example, at a signal frequency of $f_{ac} = 5$ MHz, the minimum frequency increment is $\delta f = 50$ kHz, which precludes the detection of weak signals with sharply defined spectra. Although pulse generators with faster sampling rates exist, they are either extremely costly or require dedicated hardware development [129, 130] yet barely reach adequate timing resolution. Hardware sampling therefore is a severe limitation for dynamical decoupling spectroscopy.

5.1.2 Pulse shaping for high-resolution dynamical decoupling

Recently, an elaborate experimental scheme termed *quantum interpolation* has been devised and demonstrated to overcome this issue [131]. It enables a frequency sampling beyond the hardware limit of the control electronics by varying the interpulse delay between subblocks of the sensing sequence. This leads to an interpolation of the spin evolution at a more precisely controlled interpulse delay.

Here, we study the complementary and conceptually simpler approach of utilizing shaped control pulses to interpolate the pulse timing. The concept of our method is illustrated in Figure 5.1. Instead of modulating the high frequency control field by the common square pulse profile (Fig. 5.1(b)), we shape the envelope of the pulses by a smooth function. In this study we use a cosine-square profile (Fig. 5.1(c)) which is very simple to implement, although any other smooth profile could be applied [132, 133]. It is also possible to implement optimized control pulses that are more robust against pulse imperfections [134]. Because the AWG has a high vertical resolution,

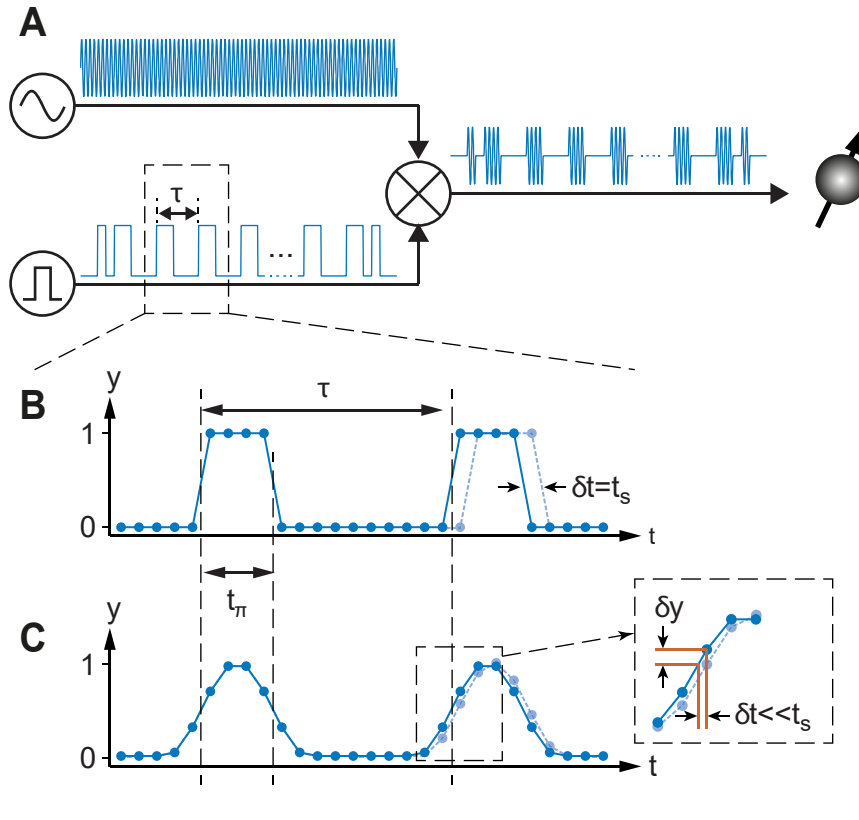


FIGURE 5.1: **Pulse shaping for dynamical decoupling spectroscopy.** (a) Dynamical decoupling spectroscopy is based on a periodic pulse modulation of the qubit control field with a precisely timed pulse repetition time τ . (b) Modulation of the microwave signal with square pulses limits the time resolution to multiples of the sampling time t_s of the pulse generator hardware. Solid and faint profiles show original and time-shifted pulses. (c) Shaped pulses, here with a cosine-square amplitude profile, enable much finer variations of the pulse timing at the same hardware sampling rate. The minimum interpolated δt is set by the slope of the pulse envelope and the vertical resolution of the pulse generator (inset). t_π is the duration of the π pulse defined by the full width at half maximum of the pulse envelope. In our experiments, the qubit is the solid-state spin of a single nitrogen-vacancy center in diamond.

we can interpolate the center position of a pulse with a timing resolution δt that is far better than sampling time t_s . The interpolated timing resolution δt is approximately given by the slope of the pulse envelope, $\delta t = (\partial y / \partial t)^{-1} \delta y \sim t_\pi \delta y$, where t_π is the duration of the pulse and δy the minimum amplitude increment. Specifically, for a cosine-square shaped pulse of duration $t_\pi = 25$ ns implemented on an AWG with 14 bits of vertical resolution ($\delta y = 2^{-14}$), an interpolated timing resolution of $\delta t \sim 1$ ps can be expected.

5.2 Experimental realization

To experimentally demonstrate the shaped-pulse interpolation method we study the coherent response of the electronic spin associated with a single nitrogen-vacancy (NV) center in a diamond single crystal [135]. Control pulses are generated on an AWG operating at 500 MS/s with 14 bits of vertical resolution (Tektronix AWG5002C), and upconverted to the ~ 2.2 GHz qubit resonance by frequency mixing with a local oscillator (Fig. 5.1(a)). Additional amplification is used to reach Rabi frequencies of

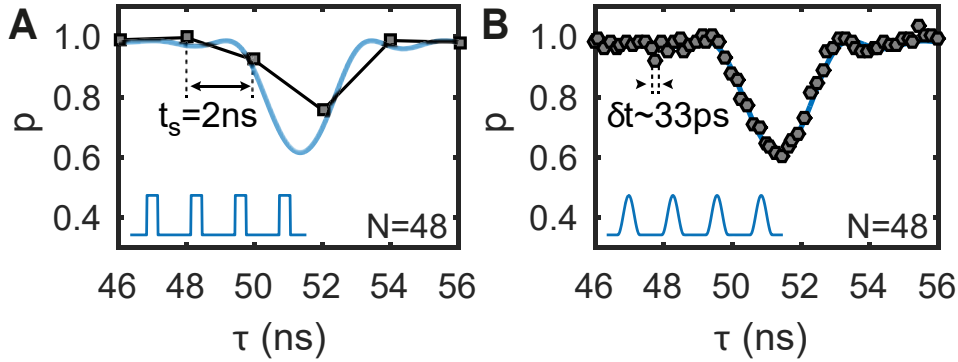


FIGURE 5.2: **Demonstration of high time-resolution with shaped pulses.** Experimental sampling resolution for a sensing sequence with (a) square control pulses and (b) cosine-square control pulses. t_s is the hardware sampling time and δt the interpolated sampling time enabled by the pulse shaping. N is the number of control pulses. p is the probability that the qubit sensor maintains its coherence for different values of the pulse repetition time τ . Solid lines show the theoretical response given by Eq. (2) and (3) with B_{ac} as the only free parameter, squares and hexagons show the experimental data, and sketches show pulse shapes.

~ 20 MHz corresponding to pulse durations of $t_\pi \sim 25$ ns. Microwave pulses are applied to the NV center by a coplanar waveguide structure, and the NV spin state is initialized and read out by optical means [136]. All experiments are performed under ambient conditions.

Figure 5.2 shows a first set of measurements, in which we directly compare the timing resolution of dynamical decoupling sequences with and without shaped pulses. For this purpose we combine the control field with a sinusoidal AC test signal ($f_{ac} = 9.746969$ MHz, $B_{ac} = 7.15$ T) before delivering it to the coplanar waveguide. In this case the sensing sequence becomes resonant with the AC field for a pulse repetition time of $\tau = 51.298$ ns. When utilizing square pulses, the repetition time can only be stepped in increments of $t_s = 2$ ns and the sampling of the AC signal spectrum is very coarse (Fig. 5.2(a)). In stark contrast, we can finely sample the spectrum using shaped control pulses and clearly augment the hardware-limited time resolution (Fig. 5.2(b)).

5.3 Theoretical description and analysis

We have compared the experimental data to the expected spectral response for the dynamical decoupling sequence. Because the phase of the AC magnetic field is not synchronized to the measurement sequence, we can describe the probability that the sensor qubit maintains its original state by [22]

$$p(t, \tau) = \frac{1}{2} [1 + J_0(W_{N,\tau} \gamma B_{ac} t)]. \quad (5.2)$$

Here, $\gamma = 2\pi \times 28$ GHz/T is the gyromagnetic ratio of the electronic sensor spin, $t = N\tau$ is the total duration of the phase acquisition, and J_0 is the zeroth-order Bessel function of the first kind. Further, $W_{N,\tau}(f_{ac})$ is the spectral weighting or filter

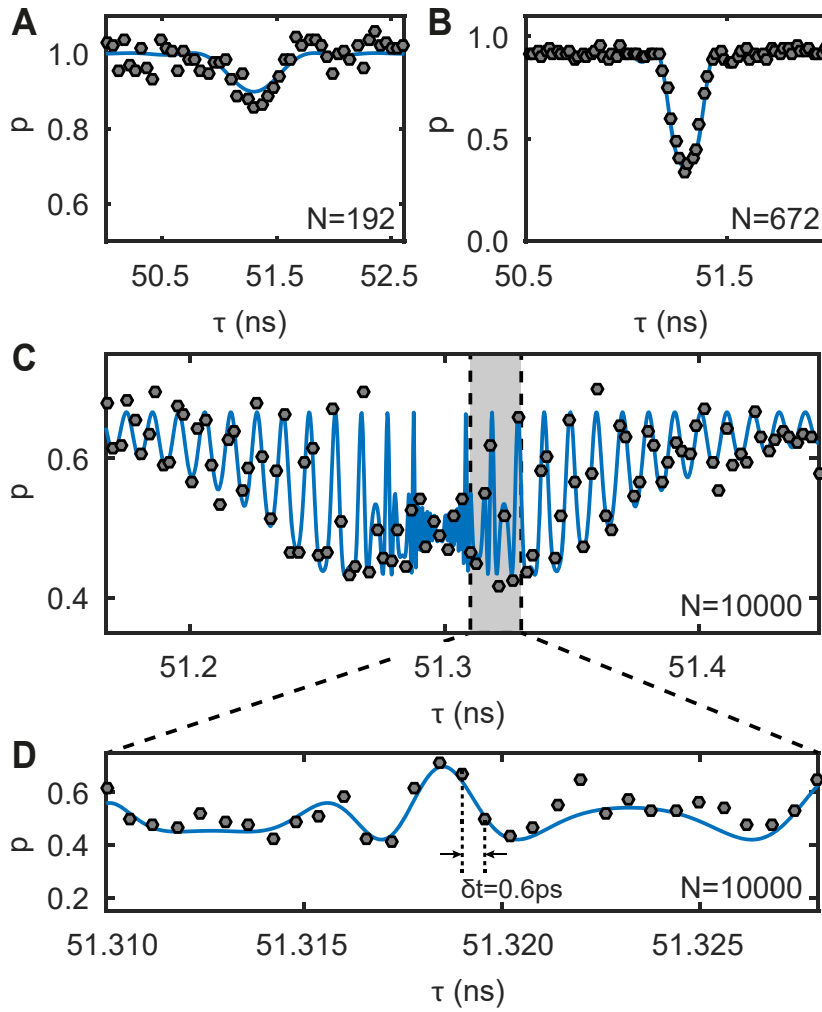


FIGURE 5.3: **Sensor response for increasing number of shaped pulses.** Sensor response to a dynamical decoupling sequence with (a) $N = 192$, (b) $N = 672$ and (c) $N = 10,000$ shaped control pulses. The frequency and amplitude of the AC test signal is $f_{ac} = 9.746969$ MHz and $B_{ac} = 0.84$ T for all measurements, respectively. (d) High-resolution plot of the $N = 10,000$ dynamical decoupling sequence showing a timing resolution of $\delta t = 0.6$ ps. Solid lines reflect the theoretical model multiplied by an overall decoherence factor $\exp(-(t/T_2)^2)$ with $T_2 = 535$ us.

function of the sequence [22],

$$W_{N,\tau}(f_{ac}) = \left| \frac{\sin(\pi f_{ac} N \tau)}{\pi f_{ac} N \tau} [1 - \sec(\pi f_{ac} \tau)] \right|, \quad (5.3)$$

which has a maximum response of $W = 2/\pi$ when $f_{ac} = 1/(2\tau)$. We find excellent agreement between the experimental spectra and the analytical filter profile of the dynamical decoupling sequence, but only the interpolated sequence provides the required fine frequency sampling. We have verified that the filter profile does not depend on whether square or shaped control pulses are used.

In a second set of experiments, shown in Figure 5.3, we analyze the sensor response under the action of an increasing number of shaped microwave pulses. Here, we keep the frequency of the test signal unchanged but reduce its amplitude. We

first record the response to a sequence with $N = 192$ and 672 shaped pulses to calibrate the amplitude of the AC signal. In both cases the sensor is operated in the small signal regime where the argument of the Bessel function is small ($W_{N,\tau}\gamma B_{ac}t \leq 2\gamma B_{ac}t/\pi \ll \pi$).

5.4 Non-linear signal detection

Subsequently, we tune the sensor into the strongly non-linear regime by increasing N up to 10,000 (Fig. 5.3(c)). For this large number of pulses, the argument of the Bessel function in Eq. 5.2 is no longer a small quantity because the total duration of the sequence $t = N\tau$ becomes very long. The non-linear regime has recently been explored with trapped ions [137] and it has been found that this regime gives rise to spectral features far below the Fourier limit. Here, we exploit these features to precisely characterize and test the frequency response of the sensor. Figure 5.3(d) shows a zoom into the center region of spectrum (c) that is acquired with a time increment of $\delta t = 0.6$ ps. We observe that even for this fine time resolution the observed response of the sensor spin agrees well with the model expressed by Eq. 5.2. The time increment of 0.6 ps corresponds to a frequency sampling of 114 Hz, which is an improvement by over three orders of magnitude compared to the frequency sampling of 380 kHz possible without pulse shaping.

5.5 Comparison of filter functions for dynamical decoupling sequences with different pulse shapes

To investigate whether the type of control pulse used has an influence on the filter function of a dynamical decoupling sequence, we simulated the response of the sequence to a single ^{13}C nucleus using the density matrix method [77, 94]. For this example, we used the same parameters as for the ^{13}C in Fig. 4(b) of the main manuscript. The π pulse duration was $t_\pi = 25$ ns, the ^{13}C Zeeman frequency was 1.975 MHz, and the detuning of the NV electronic spin due to the ^{15}N nuclear was taken into account.

We simulated the responses of sequences using four different control pulses: ideal, square, cosine-square-shaped, and cosine-square-shaped rounded to 14 bits. Figure 5.4(a) shows the response for the sequence with ideal (infinitely short and exact) π rotations. Figure 5.4(b) plots the difference to the ideal response when using square pulses (blue curve) and when using cosine-square-shaped pulses (red curve). We find that there is a difference to the ideal response, but that the difference between the square and cosine-square control pulses is small. The differences are mainly due to the rather low Rabi frequency (~ 20 MHz) which results in comparably long pulses and different phase pickup between ideal, square and cosine-square sequences. We have also simulated the response to cosine-square pulses with a discrete amplitude, reflecting the 14 bits of vertical resolution of the AWG; here, the difference in p is $< 10^{-6}$ (not shown).

5.6 Applications of dynamical decoupling with shaped pulses

To demonstrate the ability of the interpolated dynamical decoupling sequence to spectrally resolve nearby signals, we expose the sensor to a two-tone AC magnetic field composed of two slightly different frequencies. We select equal amplitudes

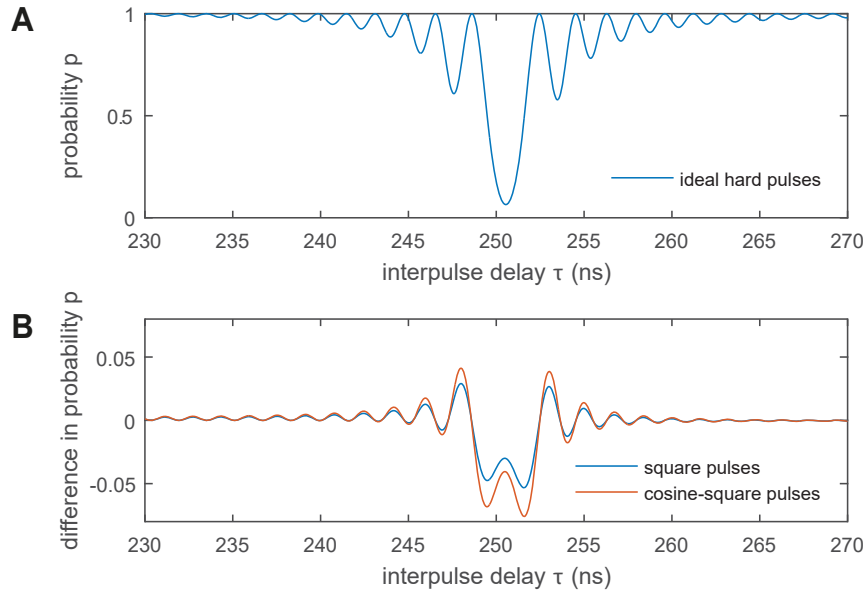


FIGURE 5.4: **Numerical comparison between ideal and non-ideal as well as shaped and non-shaped control pulses.** Simulated response of a dynamical decoupling sequence with $N = 320$ pulses to a single ^{13}C nuclear spin. (a) Response of a sequence with ideal π pulses. (b) Response of the sequences with square and cosine-square-shaped π pulses, respectively. Shown is the difference to the ideal response.

for both frequency components and operated the sensor in the linear regime. As shown in Figure 5.5(a) both frequency components can be clearly distinguished in the resulting spectrum even though the frequencies are only 3 kHz apart.

Finally, we demonstrate that the application of shaped pulses also enables the detection of NMR spectra with high frequency resolution. NMR spectroscopy is an important test case for our method because very high frequency resolutions combined with MHz detection frequencies are typically required.

Specifically, we detect the NMR signal of ^{13}C nuclei located in close proximity to the NV center [89, 138, 139]. Figure 5.5(b) shows the observed spectrum (points) for a sequence with $N = 320$ control pulses together with a theoretical model (lines). Because the response of the sensor spin is no longer described by the classical description of Eq. (5.2), we perform density matrix simulations of the NV- ^{13}C system to calculate the $p(t, \tau)$ response curve. The simulations require knowledge of the parallel and perpendicular hyperfine coupling constants a_{\parallel} and a_{\perp} , respectively, which we determine in separate high-resolution correlation spectroscopy measurements [77]. Two simulations are shown with Figure 5.5(b): A first curve (dashed line) plots the expected response from the single ^{13}C nuclear spin. The second curve (solid line) reflects a simulation that includes three additional, more weakly coupled ^{13}C nuclei. The example of Figure 5.5(b) clearly shows the advantage of a high sampling resolution for detecting NMR spectra.

5.7 Conclusion and outlook

To conclude, we have presented a simple method for greatly increasing the timing resolution of dynamical decoupling sequences. Using sequences with up to 10,000

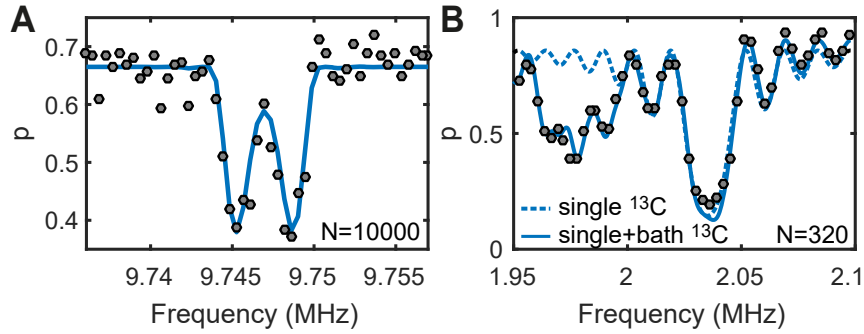


FIGURE 5.5: **Applications of pulse shaping for high-resolution spectroscopy.** (a) Spectrum of two AC test signals separated by 3 kHz. Both signals can be clearly distinguished. (b) NMR spectrum of ^{13}C nuclei located in close proximity to the NV center sensor spin. Dashed line is the theoretical response to a single ^{13}C nucleus with hyperfine coupling parameters $a_{\parallel} = 2\pi \times 114(1)$ kHz and $a_{\perp} = 2\pi \times 62(1)$ kHz. Solid line includes three additional, more weakly coupled ^{13}C bath spins. Frequency is $1/(2\tau)$.

coherent, cosine-square-shaped control pulses, we were able to improve the effective timing resolution of the interpulse delay by more than 3 orders of magnitude, with time increments as small as 0.6 ps. The resulting high frequency resolution has been demonstrated by sensing AC magnetic fields and NMR signals from individual carbon nuclear spins.

The advantage of our technique is that it simple to implement, robust, and generally applicable. Although a slightly finer timing resolution could possibly be realized by specifically optimized pulse shapes, such as those available through quantum optimum control [134], these methods typically require extensive computation and pulse calibration. Pulse shaping provides a simple means to further push the boundaries in frequency resolution and sensitivity in quantum sensing applications and can also be applied to other physical implementations, such as other solid state defect spins, trapped ultracold atoms and ions, or superconducting qubits.

Three-dimensional localization spectroscopy of individual nuclear spins with sub-Angstrom resolution

Summary

In this chapter we report on precise localization spectroscopy experiments of individual ^{13}C nuclear spins near the central electronic sensor spin in a diamond chip. By detecting the nuclear free precession signals in rapidly switchable external magnetic fields, we retrieve the three-dimensional spatial coordinates of the nuclear spins with sub-Angstrom resolution and for distances beyond 10 Å. We further show that the Fermi contact contribution can be constrained by measuring the nuclear g-factor enhancement. The presented method will be useful for mapping the atomic-scale structure of single molecules, an ambitious yet important goal of nanoscale nuclear magnetic resonance spectroscopy.

Parts of this chapter have been published as:

J. Zopes, K. S. Cujia, K. Sasaki, J. M. Boss, K. M. Itoh, C. L. Degen, *Three-dimensional localization spectroscopy of individual nuclear spins with sub-Angstrom resolution*, *Nature Communications* **9**, 4678 (2018)

6.1 Introduction

One of the visionary goals of nanoscale quantum metrology with NV centers is the structural imaging of individual molecules, for example proteins, that are attached to the surface of a diamond chip [65]. By adapting and extending measurement techniques from nuclear magnetic resonance (NMR) spectroscopy, the long-term perspective is to reconstruct the chemical species and three-dimensional location of the constituent atoms with sub-Angstrom resolution [53, 140]. In contrast to established structural imaging techniques like X-ray crystallography, cryo-electron tomography or conventional NMR, which average over large numbers of target molecules, only a

single copy of a molecule is required. Conformational differences between individual molecules could thus be directly obtained, possibly bringing new insights about their structure and function.

In recent years, first experiments that address the spatial mapping of nuclear and electron spins with NV based quantum sensors have been devised. One possibility is to map the position into a spectrum, as it is done in magnetic resonance imaging. For nanometer-scale imaging, this requires introducing a nanomagnet [63, 96, 141]. Another approach is to exploit the magnetic gradient of the NV center's electron spin itself, whose dipole field shifts the resonances of nearby nuclear spins as a function of distance and internuclear angle. Refinements in quantum spectroscopic techniques have allowed the detection of up to 8 individual nuclear spins [35, 89] as well as of spin pairs [88, 142, 143] for distances of up to $\sim 30 \text{ \AA}$ [100, 138]. Due to the azimuthal symmetry of the dipolar interaction, however, these measurements can only reveal the radial distance r and polar angle θ of the inter-spin vector $\vec{r} = (r, \theta, \phi)$, but are unable to provide the azimuth ϕ required for reconstructing three-dimensional nuclear coordinates. One possibility for retrieving ϕ is to change the direction of the static external field [138], however, this method leads to a mixing of the NV center's spin levels which suppresses the ODMR signal [107] and shortens the coherence time [144]. Other proposed methods include position-dependent polarization transfer [145] or combinations of microwave and radio-frequency fields [57, 146, 147].

Here, we demonstrate three-dimensional localization of individual, distant nuclear spins with sub-Angstrom resolution. To retrieve the missing angle ϕ , we combine a dynamic tilt of the quantization axes using a high-bandwidth microcoil with high resolution correlation spectroscopy [77, 90]. Our method provides the advantage that manipulation and optical readout of the electronic spin can be carried out in an aligned external bias field. This ensures best performance of the optical readout and the highest magnetic field sensitivity and spectral resolution of the sensor.

6.2 Theoretical description of the method

We consider a nuclear spin $I = 1/2$ located in the vicinity of a central electronic spin $S = 1$ with two isolated spin projections $m_S = \{0, -1\}$. The nuclear spin experiences two types of magnetic field, a homogeneous external bias field B_0 (aligned with the quantization axis \vec{e}_z of the electronic spin), and the local dipole field of the electronic spin. Because the electronic spin precesses at a much higher frequency than the nuclear spin, the latter only feels the static component of the electronic field, and we can use the secular approximation to obtain the nuclear free precession frequencies,

$$f_{m_S} = \frac{1}{2\pi} \|\! - \gamma_n \vec{B}_{\text{tot}}\| = \frac{1}{2\pi} \|\! - \gamma_n B_0 \vec{e}_z + m_S \vec{A}_z(\vec{r})\|. \quad (6.1)$$

Here, γ_n is the nuclear gyromagnetic ratio and

$$\begin{aligned} \vec{A}_z(\vec{r}) &= \underline{\underline{\mathbf{A}}}(\vec{r}) \cdot \vec{e}_z = (A_{xz}, A_{yz}, A_{zz}) \\ &= (a_{\perp} \cos(\phi), a_{\perp} \sin(\phi), a_{\parallel}) \end{aligned} \quad (6.2)$$

is the secular hyperfine vector of the hyperfine tensor $\underline{\underline{\mathbf{A}}}(\vec{r})$ that gives rise to the hyperfine magnetic field $m_S \vec{A}_z(\vec{r}) / \gamma_n$ (see Fig. 6.1 (b)).

To obtain information about the distance vector \vec{r} , a standard approach is to measure the parallel and transverse components of the hyperfine vector, $a_{\parallel} = A_{zz}$ and

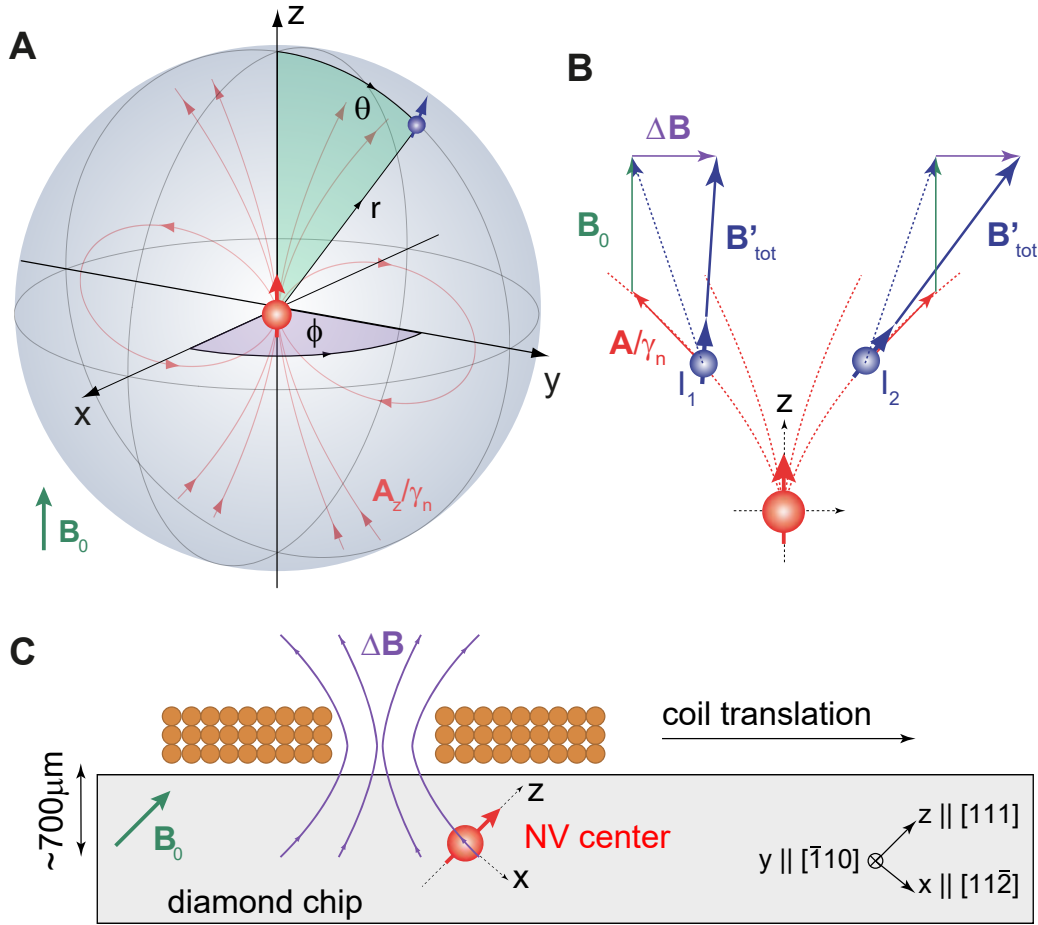


FIGURE 6.1: **Coordinate systems for spins and magnetic fields.** (a) Reference frame of the central nitrogen-vacancy (NV) sensor spin (red) with a nuclear spin (blue) located at the three-dimensional position $\vec{r} = (r, \theta, \phi)$. The quantization axis of the NV center defines the z -axis. The hyperfine field of the NV spin (red field lines) provides the magnetic field gradient for imaging. (b) Sketch of two nuclear spins I_1 and I_2 experiencing the same hyperfine interaction (red) [Eq. (6.2)]. Application of a transverse field $\Delta\vec{B}$ (purple) reduces (I_1) or increases (I_2) the total magnetic field \vec{B}'_{tot} (blue) experienced by the nuclear spins depending on the ϕ angle, allowing us to discriminate the nuclear locations. B_0 is the static external field (green). (c) Geometry of the experimental setup in the laboratory frame of reference. A small solenoid on top of the diamond chip provides a rapidly switchable magnetic field $\Delta\vec{B}$.

To change the vector orientation of $\Delta\vec{B}$, we translate the coil over the diamond.

$a_{\perp} = (A_{xz}^2 + A_{yz}^2)^{1/2}$, and to relate them to the field of a point dipole (see also chapter 3),

$$a_{\parallel} = \frac{\mu_0 \gamma_e \gamma_n \hbar}{4\pi r^3} (3 \cos^2 \theta - 1) + a_{\text{iso}}, \quad (6.3)$$

$$a_{\perp} = \frac{\mu_0 \gamma_e \gamma_n \hbar}{4\pi r^3} 3 \sin \theta \cos \theta, \quad (6.4)$$

where $\mu_0 = 4\pi \cdot 10^{-7} \text{ T m A}^{-1}$ is the vacuum permeability, $\hbar = 1.054 \cdot 10^{-34} \text{ J s}$ is the reduced Planck constant, $|\gamma_e| = 2\pi \cdot 28 \text{ GHz T}^{-1}$ is the electron gyromagnetic ratio, and where we have included a Fermi contact term a_{iso} (set to zero for now) for later discussion. Experimentally, the parallel projection a_{\parallel} can be inferred from the

precession frequencies f_{m_S} using Eq. (6.1), and the transverse projection a_{\perp} can be determined by driving a nuclear Rabi rotation via the hyperfine field of the central spin and measuring the rotation frequency [77]. Once a_{\parallel} and a_{\perp} are known, Eqs. (6.3,6.4) can be used to extract the distance r and polar angle θ of the distance vector $\vec{r} = (r, \theta, \phi)$. Due to the rotational symmetry of the hyperfine interaction, however, knowledge of a_{\parallel} and a_{\perp} is insufficient for determining the azimuth ϕ .

To break the rotational symmetry and recover ϕ , we apply a small transverse magnetic field $\Delta\vec{B}$ during the free precession of the nuclear spin. Application of a transverse field tilts the quantization axes of the nuclear and electronic spins. The tilting modifies the hyperfine coupling parameters a_{\parallel} and a_{\perp} depending on the angle between $\Delta\vec{B}$ and \vec{A}_z , which in turn shifts the nuclear precession frequencies f_{m_S} . To second order in perturbation theory, the m_S -dependent precession frequencies are given by [148]

$$f_{m_S} = \frac{1}{2\pi} \|\gamma_n \vec{B}'_{\text{tot}}\| = \frac{1}{2\pi} \|\gamma_n B_0 \vec{e}_z - \gamma_n (1 + \alpha(m_S)) \Delta\vec{B} + m_S \vec{A}_z(\vec{r})\|, \quad (6.5)$$

where $\alpha(m_S)$ is a small enhancement of the nuclear g -factor. The enhancement results from non-secular terms in the Hamiltonian that arise due to the tilting of the electronic quantization axis, and is given by [148]

$$\alpha(m_S) \approx (3|m_S| - 2) \frac{\gamma_e}{\gamma_n D} \begin{pmatrix} A_{xx} & A_{xy} & A_{xz} \\ A_{yx} & A_{yy} & A_{yz} \\ 0 & 0 & 0 \end{pmatrix}. \quad (6.6)$$

Here $D = 2\pi \times 2.87$ GHz is the ground-state zero-field splitting of the NV center. By measuring the shifted frequencies f_{m_S} and comparing them to the theoretical model of Eqs. (6.5,6.6), we can then determine the relative ϕ angle between the hyperfine vector and $\Delta\vec{B}$.

6.3 Results

We experimentally demonstrate three-dimensional localization spectroscopy of four $^{13}\text{C}_{1-4}$ nuclei adjacent to three distinct NV centers. NV₁ is coupled to two ^{13}C spins, while NV₂ and NV₃ are each coupled to a single ^{13}C spin. For read-out and control of the NV center spin, we use a custom-built confocal microscope that includes a coplanar waveguide and a cylindrical permanent magnet for providing an external bias field of $B_0 \sim 10$ mT applied along the NV center axis \vec{e}_z . Precise alignment of the bias field is crucial for our experiments and is better than 0.3° (Methods).

To dynamically tilt the external field we implement a multi-turn solenoid above the diamond surface (see Fig. 6.1 (d)). The coil produces ~ 2.5 mT field for 600 mA of applied current and has a rise time of ~ 2 μs . We calibrate the vector magnetic field of the coil with an absolute uncertainty of less than 15 μT in all three spatial components using two other nearby NV centers with different crystallographic orientations (Ref. [149] and Methods).

6.3.1 Mapping of r and θ

We begin our 3D mapping procedure by measuring the parallel and perpendicular hyperfine coupling constants using conventional correlation spectroscopy [77] with no coil field applied, $\Delta\vec{B} = 0$ (Fig. 6.2). The parallel coupling a_{\parallel} is determined from a free precession experiment (sequence ① in Fig. 6.2) yielding the frequencies f_0 and

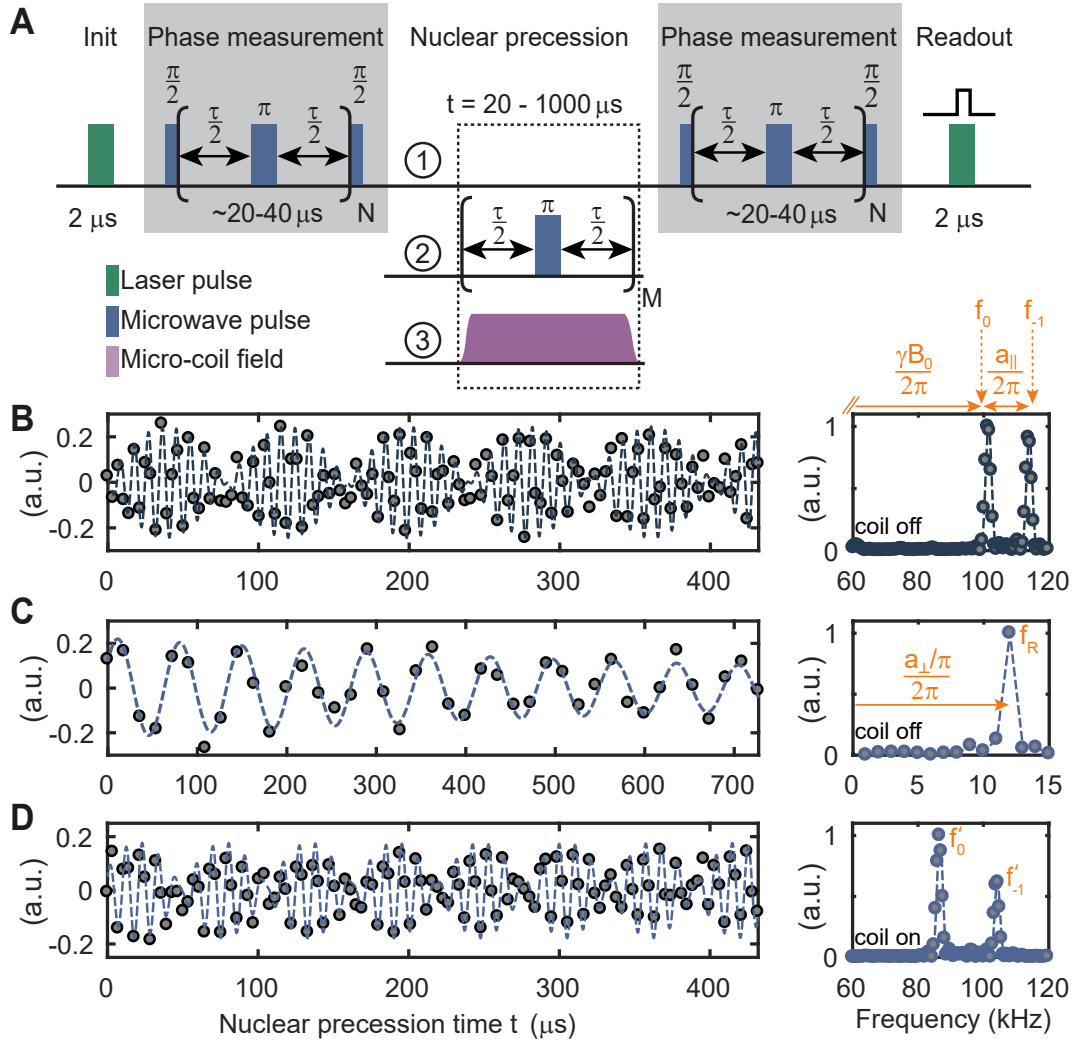


FIGURE 6.2: **Implementation of three-dimensional localization spectroscopy.** (a) Correlation spectroscopy protocol. By correlating two phase measurements we trace out the precession of the target nuclear spin(s) under different NMR sequences. Phase measurements are implemented by a Carr-Purcell-Meiboom-Gill (CPMG) train of microwave π pulses (blue) applied to the central electronic spin, where $\tau \approx [2(f_0 + f_{-1})]^{-1}$. Laser pulses (green) are used to polarize and read out the electronic spin. Repetitions are $N = 4 - 8$ and $M = t/\tau$. (b) Free precession signal of the nuclear spin as a function of time t , using sequence ①. Right panel shows the corresponding power spectrum. The two frequencies f_0 and f_{-1} are approximately equal to $\gamma_n B_0 / (2\pi)$ and $(\gamma_n B_0 + a_{\parallel}) / (2\pi)$, respectively, see text. (c) Application of periodic π pulses on the NV center during t (sequence ②) causes a Rabi nutation of the nuclear spin, whose oscillation frequency f_R is approximately equal to $(a_{\perp} / \pi) / (2\pi)$. (d) Activation of a transverse microcoil field $\Delta \vec{B}$ during the nuclear precession (sequence ③) leads to shifted frequencies f'_0 and f'_{-1} . All measurements were conducted on $^{13}\text{C}_1$. Extracted frequencies are listed in Table 6.1.

f_{-1} (Fig. 6.2 (b)). The coupling constant is then approximately given by $a_{\parallel} / (2\pi) \approx f_{-1} - f_0$. The transverse coupling a_{\perp} is obtained by driving a nuclear Rabi oscillation via the NV spin, using sequence ②, and recording the oscillation frequency f_R , where $a_{\perp} / (2\pi) \approx \pi f_R$ (Fig. 6.2 (c)). Because the Zeeman and hyperfine couplings are of similar magnitude, these relations are not exact and proper transformation must be applied to retrieve the exact coupling constants a_{\parallel} and a_{\perp} (Ref. [77] and Methods).

Quantity	Value	Reference
f_0, f_{-1}	101.7(1), 114.2(1) kHz	Fig. 6.2 (b)
f_R	14.4(1) kHz	Fig. 6.2 (c)
f'_0, f'_{-1}	88.3(3), 103.2(2) kHz	Fig. 6.2 (d)
\vec{B}_0	(0.028, -0.056, 9.502) mT	Ref. [150]
$\Delta\vec{B}$	(-1.715, 0.614, -1.547) mT	Ref. [150]

TABLE 6.1: **Data base of measured precession frequencies and calibrated external magnetic fields used to determine the 3D position of $^{13}\text{C}_1$.** Five further measurements of (f'_0, f'_{-1}) were made to improve the localization accuracy (data given in Ref. [150]). Vector magnetic fields refer to the NV coordinate system defined in Fig. 6.1.

Once the hyperfine parameters are known, we can calculate the radial distance $r = 8.58(1) \text{ \AA}$ and the polar angle $\theta = 52.8(1)^\circ$ of the nuclear spin by inverting the point-dipole formulas (6.3,6.4). The measurement uncertainties in r and θ are very small because correlation spectroscopy provides high precision estimates of both a_{\parallel} and a_{\perp} .

6.3.2 Mapping of ϕ

In a second step, we repeat the free precession measurement with the coil field turned on (sequence ③), yielding a new pair of frequency values f'_0, f'_{-1} (Fig. 6.2 (d)). We then retrieve ϕ by computing theoretical values for $f_0^{(\text{th})}, f_{-1}^{(\text{th})}$ based on Eq. (6.5) and the calibrated fields in Table 6.1, and minimizing the cost function

$$\zeta(\phi) = [f'_{-1} - f'_0] - [f_{-1}^{(\text{th})}(\phi) - f_0^{(\text{th})}(\phi)]. \quad (6.7)$$

with respect to ϕ . To cancel residual shifts in the static magnetic field and improve the precision of the estimates, we compare the frequency difference between m_S states rather than the absolute precession frequencies.

In Fig. 6.2 (a), we plot $|\zeta(\phi)|$ for three different coil positions and opposite coil currents for $^{13}\text{C}_1$. We use several coil positions because a single measurement has two symmetric solutions for ϕ , and also because several measurements improve the overall accuracy of the method. The best estimate $\phi = 239(2)^\circ$ is then given by the least squares minimum of the cost functions (dash-dotted line in Fig. 6.2 (a)). To obtain a confidence interval for ϕ , we calculate a statistical uncertainty for each measurement by Monte Carlo error propagation taking the calibration uncertainties in \vec{B}_0 and $\Delta\vec{B}$, as well as the measurement uncertainties in the observed precession frequencies into account. Values for all investigated ^{13}C nuclei are collected in Supplementary Tables 2-9 in [150].

6.3.3 Fermi contact interaction

Thus far we have assumed that the central electronic spin generates the field of a perfect point dipole. Previous experimental work [92, 148] and density functional theory (DFT) simulations [68, 151], however, suggest that the electronic wave function extends several Angstrom into the diamond host lattice. The finite extent of the spin density leads to two deviations from the point dipole model: modified hyperfine coupling constants A_{ij} , and a non-zero Fermi contact term a_{iso} . In the remainder of this study we estimate the systematic uncertainty to the localization of the nuclear spins due to deviations from the point dipole model.

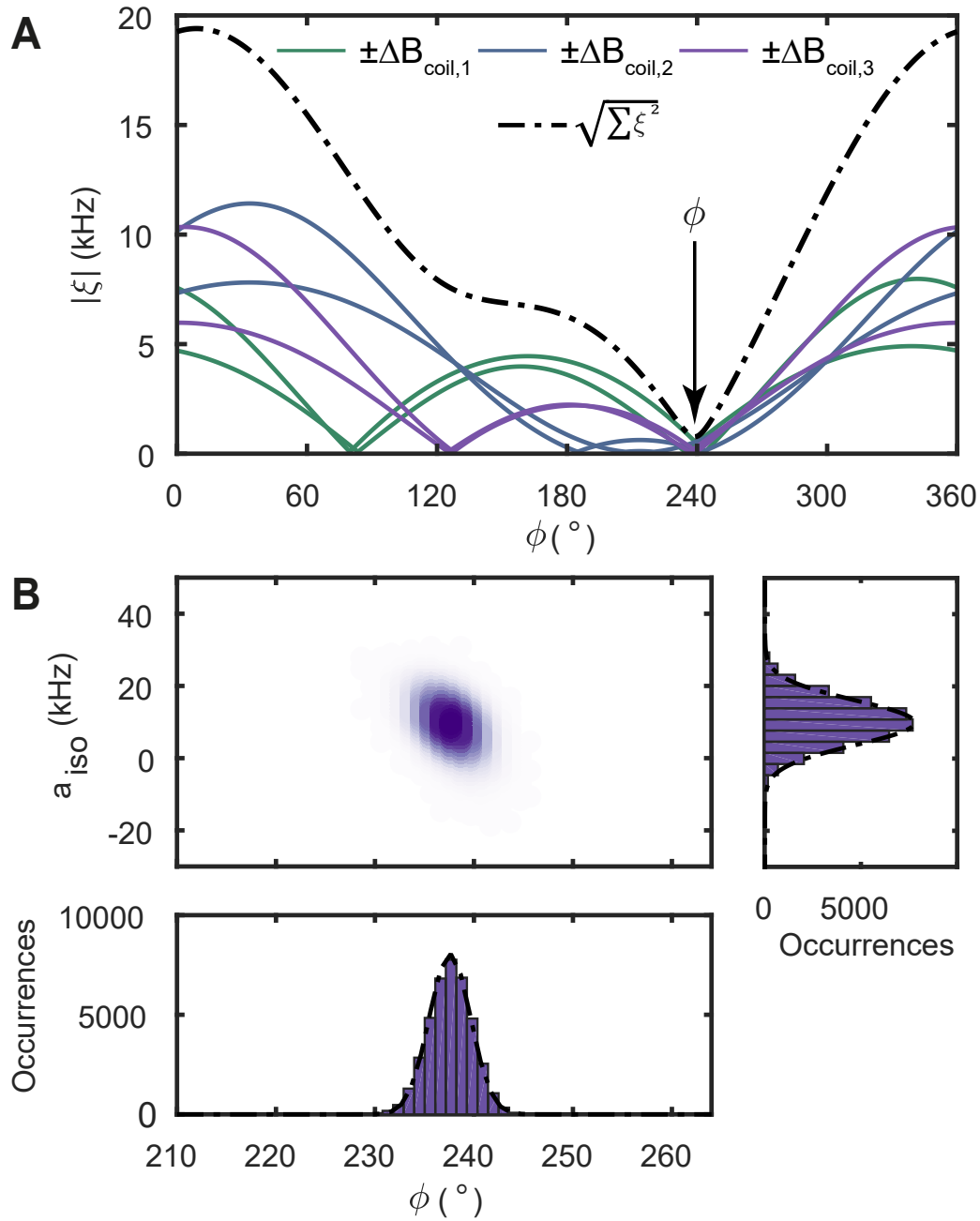


FIGURE 6.3: **Determination of azimuth angle ϕ and Fermi contact contribution a_{iso} for $^{13}\text{C}_1$.** (a) Cost function $|\xi(\phi)|$ between observed and predicted precession frequencies, as defined in Eq. (6.7). Here $a_{\text{iso}} = 0$. Six measurements are shown for three spatial coil positions (solid curves) and opposite polarities of the coil current. The estimate for ϕ is given by the minimum of the squared cost functions $\sum |\xi(\phi)|^2$ of the six measurements (dash-dotted curve). (b) Scatter plot of maximum likelihood estimates of ϕ and a_{iso} obtained by Monte Carlo error propagation. The plot is generated from $4 \cdot 10^4$ scatter points, where each point is the result of minimizing $\sum |\xi(\phi, a_{\text{iso}})|^2$ for a different Monte Carlo sampling. Histograms for ϕ (bottom) and a_{iso} (right) are obtained by integrating the 2D scatter plot along the vertical or horizontal direction, respectively. Corresponding plots for $^{13}\text{C}_{2-4}$ are given in Ref. [150].

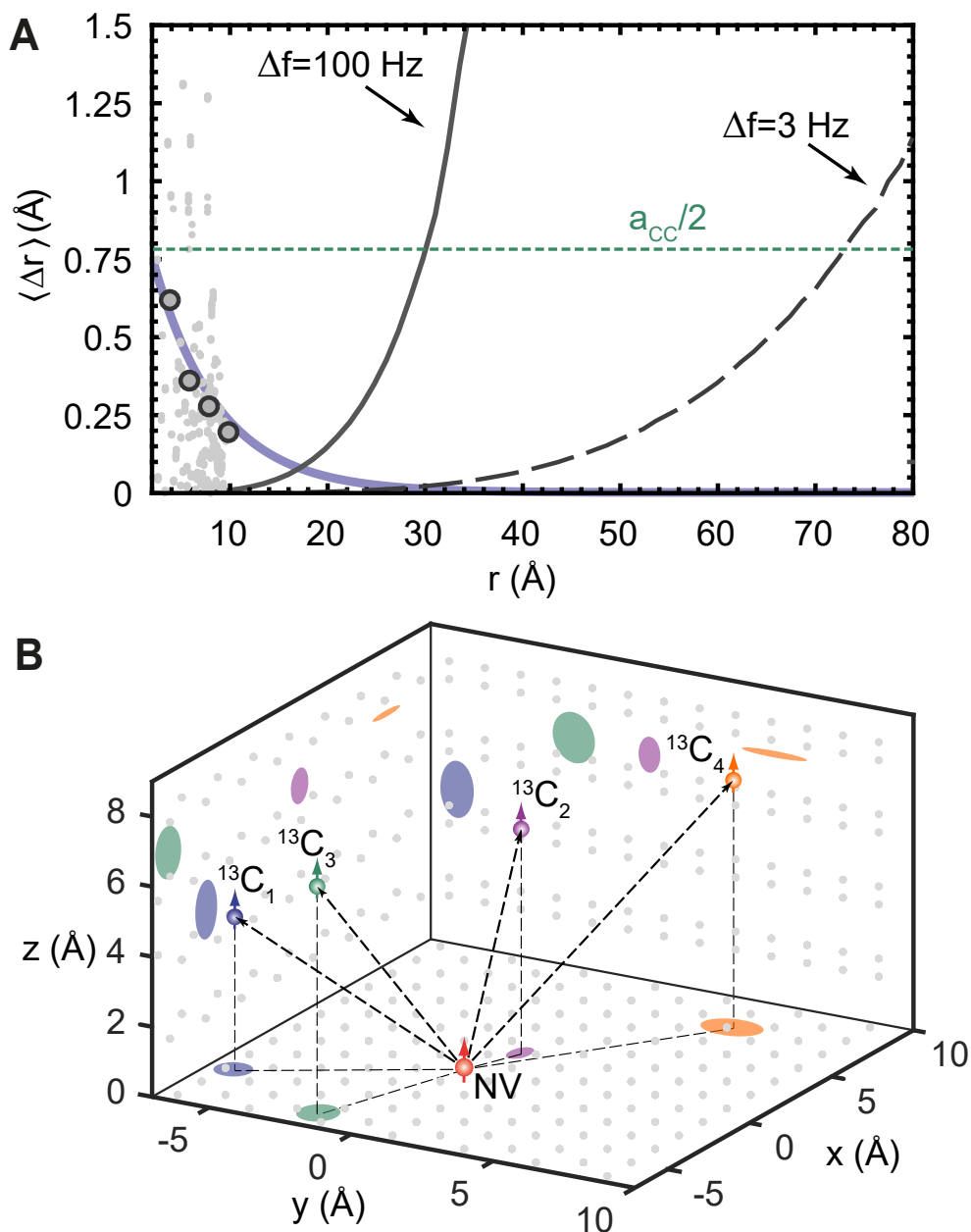


FIGURE 6.4: **Three-dimensional localization of four ^{13}C nuclear spins.** (a) Average localization uncertainty $\langle \Delta r \rangle$ as a function of radial distance r to the central spin. Gray dots represent the systematic error of the point-dipole approximation (see text), extracted for all lattice sites reported in the DFT calculation of Ref. [151]. Blue curve is an exponential fit to the median values (gray circles) of the gray dots in intervals of 2 \AA . Black curves show the uncertainty of the frequency measurement, assuming a precision of 100 Hz (this study) and of 3 Hz [72, 73, 88]. Dashed horizontal line is one-half the diamond C-C bond length. (b) Reconstructed locations of the four distant nuclear spins $^{13}\text{C}_{1-4}$. Shaded regions mark the 2σ -confidence area of the localization projected onto (xy, yz, xz) -planes of the coordinate system. Gray points represent carbon lattice positions projected onto the same planes. The origin is set to the expected center of gravity of the spin density at 2.29 \AA from the nitrogen nucleus on the N-V symmetry axis [68, 151]. Due to the inversion symmetry of the hyperfine interaction, our method cannot distinguish between sites in the upper and lower hemisphere; all ^{13}C are therefore plotted in the upper hemisphere.

Atom	Experimental values					
	a_{\parallel}/kHz	a_{\perp}/kHz	$a_{\text{iso}}/\text{kHz}$	$r/\text{\AA}$	$\theta/^{\circ}$	$\phi/^{\circ}$
$^{13}\text{C}_1$	3.1(1)	44.5(1)	9(8)	8.3(2)	58(4)	238(2)
$^{13}\text{C}_2$	119.0(1)	65.9(1)	19(15)	6.8(3)	19(3)	20(5)
$^{13}\text{C}_3$	18.5(1)	41.4(2)	3(4)	8.9(1)	43(4)	197(4)
$^{13}\text{C}_4$	1.9(1)	19.2(1)	— ^c	11.47(1)	51.8(2)	34(4)

TABLE 6.2: **Measured hyperfine couplings and inferred 3D locations of ^{13}C nuclei measured on three NV centers.** Errors are one standard deviation and represent the confidence interval from the Monte Carlo error propagation according to Fig. 6.2 (b).

Atom	Lattice sites ^a	DFT values [151]					
		a_{\parallel}/kHz	a_{\perp}/kHz	$a_{\text{iso}}/\text{kHz}$	$r_{\text{DFT}}/\text{\AA}$	$\theta_{\text{DFT}}/^{\circ}$	$\phi_{\text{DFT}}/^{\circ}$
$^{13}\text{C}_1$	447	1.1	43.1	3.9	8.6	60 ^b	240
$^{13}\text{C}_2$	25	100.4	64.8	-2.4	6.3	24 ^b	30
$^{13}\text{C}_3$	47	15.9	37.8	1.7	9.2	45 ^b	195
$^{13}\text{C}_4$				— ^d			

TABLE 6.3: **DFT values of ^{13}C nuclei that best fit to the detected nuclear spins.** DFT values are for the lattice site(s) whose calculated hyperfine couplings best match the experimental data. ^aRef. [151] does not specify the ϕ angle, therefore, three symmetric sites are compatible with our data. ^bDue to the inversion symmetry of the hyperfine interaction, our method cannot distinguish between sites in the upper and lower hemisphere; the table therefore lists $\min(\theta_{\text{DFT}}, 180^{\circ} - \theta_{\text{DFT}})$. ^cConstrained to $a_{\text{iso}} = 0$. ^dNo DFT data available.

We first consider the influence of the Fermi contact interaction, which arises from a non-vanishing NV spin density at the location of the nuclear spin. The Fermi contact interaction adds an isotropic term to the hyperfine coupling tensor, $\mathbf{A} + a_{\text{iso}}\mathbf{1}$, which modifies the diagonal elements A_{xx} , A_{yy} and A_{zz} . DFT simulations [68, 151] indicate that a_{iso} can exceed 100 kHz even for nuclear spins beyond 7 Å. It is therefore important to experimentally constrain the size of a_{iso} .

To determine a_{iso} , one might consider measuring the contact contribution to the parallel hyperfine parameter a_{\parallel} , which is equal to A_{zz} . This approach, however, fails because a measurement of a_{\parallel} cannot distinguish between dipolar and contact contributions. Instead, we here exploit the fact that the gyromagnetic ratio enhancement α depends on A_{xx} and A_{yy} , and hence a_{iso} . To quantify the Fermi contact coupling we include a_{iso} as an additional free parameter in the cost function (6.7). By minimizing $\xi(\phi, a_{\text{iso}})$ as a joint function of ϕ and a_{iso} and generating a scatter density using Monte Carlo error propagation, we obtain maximum likelihood estimates and confidence intervals for both parameters (Fig. 6.2 (b)). The resulting contact coupling and azimuth for nuclear spin $^{13}\text{C}_1$ are $a_{\text{iso}}/(2\pi) = 9(8)$ kHz and $\phi = 238(2)^{\circ}$, respectively; data for $^{13}\text{C}_{2-4}$ are collected in Table 6.2. Because the gyromagnetic ratio enhancement α is only a second-order effect, our estimate is poor, but it still allows us constraining the size of a_{iso} . By subtracting the Fermi contact contribution from a_{\parallel} , we further obtain refined values for the radial distance and polar angle, $r = 8.3(2)$ Å and $\theta = 58(4)^{\circ}$. Note that introducing a_{iso} as a free parameter increases the uncertainties in the refined r and θ , because the error in a_{iso} is large. This leads to disproportionate errors for distant nuclei where a_{iso} is small. Once nuclei are beyond a certain threshold distance, which we set to $r = 10$ Å in Table 6.2, it therefore becomes more accurate to constrain $a_{\text{iso}} = 0$ and apply the simple point dipole model.

6.3.4 Extended electronic wave function

The second systematic error in the position estimate results from the finite size of the NV center's electronic wave function. Once the extent of the wave function becomes comparable to \bar{r} , the anisotropic hyperfine coupling constants A_{ij} are no longer described by a point dipole, but require integrating a geometric factor over the sensor spin density [68]. While we cannot capture this effect experimentally, we can estimate the localization uncertainty from DFT simulations of the NV electron spin density. Following Ref. [151], we convert the calculated DFT hyperfine parameters of 510 individual lattice sites to (r, θ) positions using the point-dipole formula (6.3.6.4), and compute the difference to the DFT input parameters $(r_{\text{DFT}}, \theta_{\text{DFT}})$. For the conversion we use the experimental constraint of the contact interaction and subtract it prior to conversion. Here, we used the exact theory value of the contact term, which means that we slightly overestimate the precision of the experimental constraint. The result is plotted in Fig. 6.4 (a). We find that the difference $\langle \Delta r \rangle = r - r_{\text{DFT}}$ decreases roughly exponentially with distance, and falls below 0.2 \AA when $r > 10 \text{ \AA}$ (grey dots and curve). If we do not subtract the contact term the difference $\langle \Delta r \rangle = r - r_{\text{DFT}}$ still decreases roughly exponentially, but is approximately twice as large.

6.3.5 Conclusion

Fig. 6.4 (b) summarizes our study by plotting the reconstructed locations for all four carbon atoms in a combined 3D chart. The shaded regions represent the confidence areas of the localization, according to Table 6.2, projected onto the Cartesian coordinate planes. We note that the DFT simulations are in good agreement with our experimental results. The accuracy of our present experiments is limited by deviations from the point-dipole model, which dominate for small r (see Fig. 6.4 (a)). For larger $r \gtrsim 1 \text{ nm}$, this systematic uncertainty becomes negligible, and the localization imprecision is eventually dictated by the NMR frequency measurement. In the present study, which probed isolated ^{13}C nuclei with a narrow intrinsic line-width, the frequency precision was limited by the accuracy of our detection protocol to $\sim 100 \text{ Hz}$. This corresponds to a radial localization error of $\sim 0.75 \text{ \AA}$ at a distance of $r = 3 \text{ nm}$ (solid black line in Fig. 6.4 (a)). Improving the frequency precision to 3 Hz [88, 152] would extend this distance to $r \sim 7 \text{ nm}$ (dashed black line).

6.3.6 Outlook

Our work demonstrates a basic strategy for mapping spatial positions of single nuclei in 3D with high precision. Extending these experiments to single molecules outside a diamond chip poses a number of additional challenges, and overcoming them will require the combination of several strategies. To isolate single molecules, they can be embedded in a spin-free matrix layer deposited on the diamond surface [153] or immobilized by a linker chemistry [154]. Nuclear dipole interactions can be suppressed using homo- and heteronuclear decoupling [100], taking advantage of the existing micro-coil. Line-widths and spectral complexity can be further reduced by polarizing the constituent nuclei, and by spin dilution and isotope labeling of molecules [155]. Alternatively, measurements of inter-spin couplings will allow constraining the structure and size of molecules [132]. To sensitively detect very weakly coupled nuclei in distant molecules, spin precession can be recorded by repetitive weak measurements [99, 156]. Further improvement of sensitivity is possible by optimizing the optical detection efficiency compared to our present setup

[157], and possibly by cryogenic operation [88]. How well these strategies will work we do not know at present, but we believe that the prospect of a general single-molecule MRI technique, which will have many applications in structural biology and chemical analytics, provides sufficient motivation to warrant these efforts.

Three-dimensional nuclear spin positioning using coherent radio-frequency control

Summary

Distance measurements via the dipolar interaction are fundamental to the application of nuclear magnetic resonance (NMR) to molecular structure determination, but they provide information on only the absolute distance r and polar angle θ between spins. In this chapter, we present a protocol to also retrieve the azimuth angle ϕ . Our method relies on measuring the nuclear precession phase after the application of a control pulse with a calibrated external radio-frequency coil. We experimentally demonstrate three-dimensional positioning of individual ^{13}C nuclear spins in a diamond host crystal relative to the central electronic spin of a single nitrogen-vacancy center. The ability to pinpoint three-dimensional nuclear locations is central for realizing a nanoscale NMR technique that can image the structure of single molecules with atomic resolution.

Parts of this chapter have been published as:

J. Zopes, K. Herb, K. S. Cujia, C. L. Degen, *Three-Dimensional Nuclear Spin Positioning Using Coherent Radio-Frequency Control*, Phys. Rev. Lett. **121**, 170801 (2018)

7.1 Introduction

Nuclear magnetic resonance (NMR) and electron paramagnetic resonance (EPR) spectroscopy are among the most important analytical methods in structural biology and the chemical sciences. By combining local chemical information of atoms [158] with pair-wise distance constraints [159, 160], it becomes possible to reconstruct three-dimensional structures or structural changes of proteins and other biomolecules. While conventional NMR typically analyzes large ensembles of molecules, considerable effort has recently been expended on advancing NMR detection to the level of individual molecules [161–163]. If successfully extended to the atomic scale, NMR could enable direct imaging of three-dimensional molecular structures, with many applications in structural biology and the nanosciences. A promising platform for

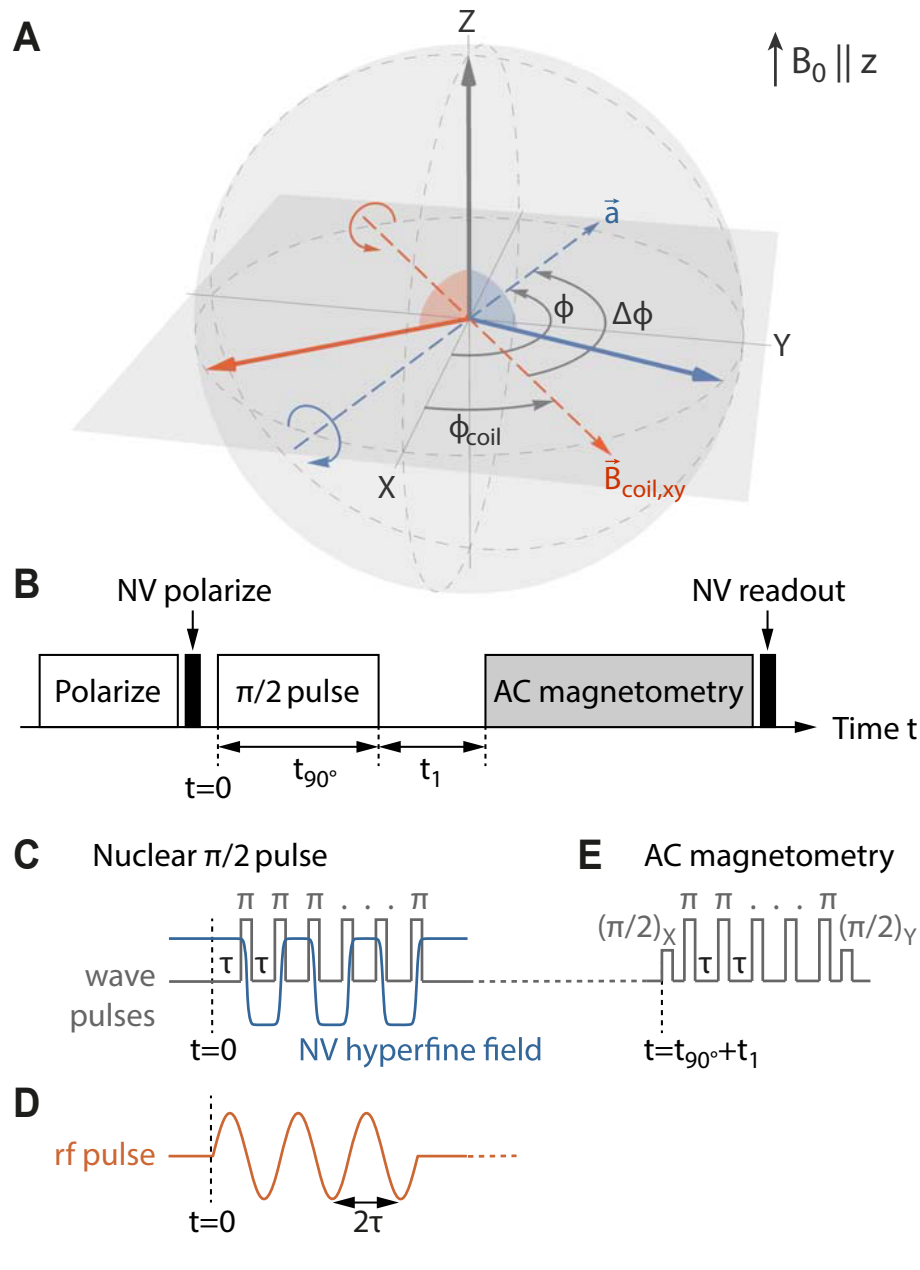


FIGURE 7.1: **Measurement principle for azimuthal positioning with coherent radio-frequency pulses.** (a) Bloch-sphere schematic of a nuclear spin before (grey arrow) and after (colored arrows) application of a $\pi/2$ rotation. The rotation is either mediated by the hyperfine interaction (blue-dashed axis) or a radio-frequency pulse generated by an external micro-coil (orange-dashed axis). The different azimuth angles of the rotation axes are translated into a phase difference $\Delta\phi$ of the nuclear spin precession, thereby linking the known orientation of the coil field to the *a priori* unknown azimuth orientation of the inter-spin vector. (b) Pulse sequence used to measure the phase of the nuclear spin precession. The nuclear $\pi/2$ pulse is implemented either (c) by a modulation of the NV center's hyperfine field using periodic microwave π pulses or (d) by driving with an external rf coil. The modulation frequency $1/(2\tau)$ is matched to the resonance of the nuclear spin. (e) AC magnetometry is implemented by a Carr-Purcell-Meiboom-Gill sequence of microwave pulses. The sequence maps the nuclear component $\langle \hat{I}_{\vec{a}} \rangle$ that is parallel to the hyperfine axis $\vec{a} \propto (\cos \phi, \sin \phi)$ onto the optically detectable polarization state of the NV center. To register the nuclear precession we sample $\langle \hat{I}_{\vec{a}} \rangle$ for a series of waiting times t_1 .

this task are diamond chips containing near-surface nitrogen-vacancy (NV) centers whose electronic spins can be exploited as sensitive local NMR probes [75, 80].

Structural imaging of single molecules involves determining the three-dimensional coordinates and elemental species of the constituent nuclei. In NV-NMR, information on the spatial position can be gained from the dipolar part of the hyperfine interaction between the nuclei and the central electronic spin [89, 138, 139]. Because of the axial symmetry of the dipolar interaction, however, only the absolute distance r and the polar (inter-spin) angle θ can be inferred from a NMR spectroscopy measurement. Although the axial symmetry can be broken by a static [138] or dynamic [150] transverse magnetic field, determination of the azimuth angle ϕ , required for reconstructing the full three-dimensional distance vector $\vec{r} = (r, \theta, \phi)$, has remained challenging [145–147].

In this Chapter, we demonstrate a second, simple and precise method for retrieving the azimuth ϕ of the inter-spin vector, allowing us to perform full three-dimensional nuclear distance measurements. Our technique relies on measuring the nuclear precession phase after application of a radio-frequency (rf) pulse by an external micro-coil. A similar concept has recently been proposed in conjunction with position-dependent polarization transfer [145]. Spatial rf-phase shifts further are a recognized issue in medical MRI [164]. We determine ϕ at low and high magnetic fields, and for polarized as well as unpolarized nuclear spins. We exemplify our method by mapping the three-dimensional locations of ^{13}C nuclei for distances up to 11 Å and angular uncertainties below 4° .

7.2 Theory

Our scheme for measuring the azimuth angle is introduced in Fig. 7.1 (a)-(d): starting from a polarized nuclear state, we perform a $\pi/2$ rotation of the nuclear spin. The rotation is generated either by modulating the hyperfine field of the NV center using microwave pulses (Fig. 7.1 (c)), or by applying a rf pulse with an external coil (Fig. 7.1 (d)). Subsequently, we let the nuclear spin precess in the equatorial plane of the Bloch sphere and detect the frequency and phase of the precession by an AC magnetometry measurement with the NV center [125, 126, 165] (Fig. 7.1 (e)).

Crucially, the starting phase of the nuclear precession at $t_1 = 0$ is set by the axis of the $\pi/2$ rotation, which is determined by the spatial direction of the rf field in the laboratory frame of reference. When driving the nuclear rotation via the hyperfine interaction, the rf field direction is given by \vec{A}_z/γ_n , where $\vec{A}_z = (a_\perp \cos \phi, a_\perp \sin \phi, a_\parallel)$ is the secular part of the hyperfine tensor, a_\parallel and a_\perp are the parallel and transverse hyperfine coupling parameters [77, 145], and γ_n is the nuclear gyromagnetic ratio (Fig. 7.1 (a), blue). Conversely, if the external coil is used to generate the rf field, the rotation axis is given by the in-plane component of the coil field \vec{B}_{coil} (Fig. 7.1 (a), red). By comparing the phases of the precession signals, we directly obtain the relative angle $\Delta\phi$ between the unknown orientation of the hyperfine vector ϕ and the calibrated orientation ϕ_{coil} of the external coil field.

7.3 Experimental method

We experimentally determine the ϕ angles of three ^{13}C nuclear spins from three different NV centers in two single-crystal diamond chips [166]. We optically polarize and read out the NV spin by short laser pulses ($\sim 2 \mu\text{s}$) and detect the fluorescence intensity in a confocal microscope arrangement. Microwave pulses at $\sim 2.5 \text{ GHz}$ are

used to actuate the $m_S = 0 \leftrightarrow m_S = -1$ electronic spin transition. To polarize the nuclear spins, we transfer polarization from the optically aligned NV center by swapping the electronic state onto the nuclear spin using two conditional rotations [86, 166]. AC magnetometry is performed by a periodic sequence of microwave π pulses with XY8 phase cycling [167] enclosed by two $\pi/2$ pulses that are phase-shifted by 90° [74, 165]. We use a permanent magnet to apply bias fields of $B_0 \sim 10$ mT and 200 mT for low field and high field experiments, respectively, aligned to within 1° of the NV quantization axis.

The key component of our experiment is the external rf coil, whose field orientation serves as the spatial reference for the ϕ angle measurement. Two generations of micro-coils are used: the first coil has a 3-dB-bandwidth of 77 MHz (deduced from the step response recorded with the NV center) and is used for low field experiments. The second coil reaches a bandwidth of 1.72 MHz. Both rf coils produce fields of ~ 5 mT/A and are operated with currents of up to 1 A. Crucial for our experiments is a precise knowledge of the direction and temporal shape of the coil magnetic field. We determine the three-dimensional vector of the coil magnetic field \vec{B}_{coil} using two other nearby NV centers with different crystallographic orientations with an uncertainty of less than $15 \mu\text{T}$ in all three spatial components [149, 150]. We align our (x, y, z) laboratory reference frame to the $([1\bar{1}2], [\bar{1}10], [111])$ crystallographic axes of the single crystal diamond chips (up to an inversion symmetry about the origin). To calibrate the dynamic response of the coil, we perform *in situ* measurements of the rf field using time-resolved optically-detected magnetic resonance (ODMR) spectroscopy (Fig. 7.2 (a),(e)) [166]. We acquire ODMR spectra in snapshots of 400 ns (a) or 100 ns (e) over the duration of the rf pulse, and determine the pulse profile by fitting the peak positions of the resonance curves.

7.4 Results

7.4.1 Flip and evolve method

Low-field measurements

In Fig. 7.2 (c),(d), we show a first set of measurements for nuclear spin $^{13}\text{C}_1$ carried out at low magnetic field, $B_0 \sim 10$ mT. The hyperfine coupling parameters of this nuclear spin are $(a_{\parallel}, a_{\perp}) = 2\pi \times (18.5(1) \text{ kHz}, 41.4(2) \text{ kHz})$, calibrated by a separate correlation spectroscopy measurement [77]. Fig. 7.2 (c) shows the reference measurement of the nuclear spin precession after application of the $\pi/2$ pulse using the hyperfine field. Fig. 7.2 (d) plots the corresponding precession signal after applying the $\pi/2$ rotation with the rf coil. We observe a clear phase shift $\Delta\phi$ between the two signals, indicating that the hyperfine field \vec{A}_z/γ_n and the coil field \vec{B}_{coil} point in different spatial directions. We verify that the phase shift changes if we vary the direction of \vec{B}_{coil} by moving the rf coil to a different position (green data in Fig. 7.2 (d)).

For ideal rf pulses and exact timings, the observed phase shift $\Delta\phi$ corresponds to the difference $\phi - \phi_{\text{coil}}$ between the azimuth angles of the hyperfine and coil magnetic fields, allowing us to directly deduce ϕ . However, due to the limited bandwidth of the rf circuit and the finite length of feed lines, the actual rf pulses tend to be delayed and distorted, leading to a phase offset. In addition, the AC magnetometry measurement is very sensitive to timing errors and resonance offsets in the microwave modulation, causing additional uncertainty in the phase measurement.

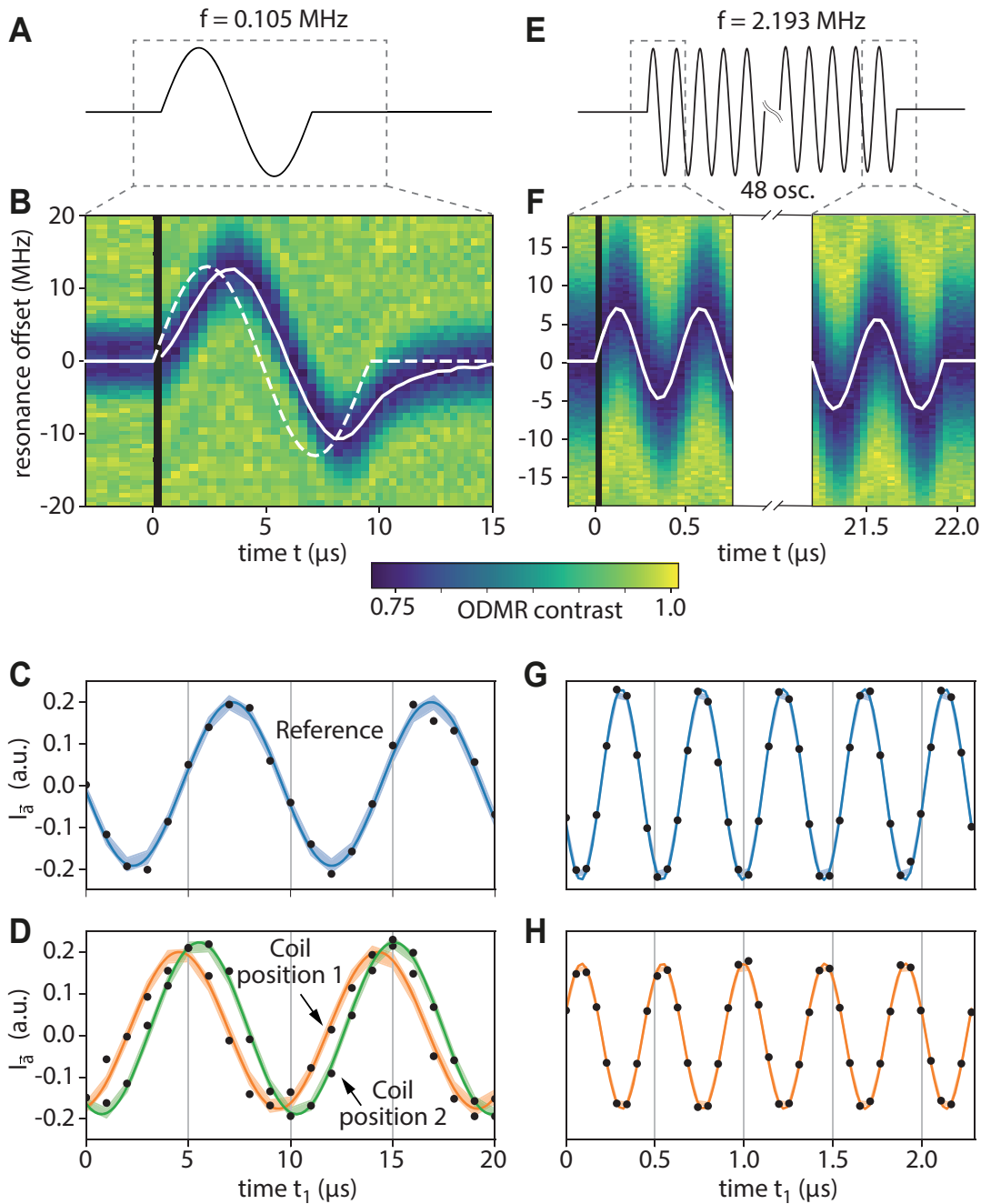


FIGURE 7.2: **Azimuthal positioning with coherent radio-frequency pulses.** (a-d) Precision measurement of the azimuth angle of $^{13}\text{C}_1$ at low magnetic field, $B_0 = 9.600(8)$ mT. (a) Waveform of the pulse sent to the rf coil. (b) ODMR spectra (vertical axis) of the rf coil magnetic field recorded in time steps of 400 ns (horizontal axis). The black vertical line marks the start time $t = 0$ of the rf pulse. The white solid line connects the resonance positions determined by Lorentzian fits. For comparison, we also plot the input waveform from (a) (white dashed line). (c,d) Nuclear precession signal measured as a function of t_1 . Dots show the experimental data. Colored lines represent density matrix simulations (best fit) discussed in the text. Shaded areas specify 2σ confidence intervals of the fits. Panel (c) shows the reference measurement (sequence of Fig. 7.1 (c)) and panel (d) measurements for two different coil positions (sequence of Fig. 7.1 (d)). (e-h) Same experiment performed on $^{13}\text{C}_3$ at high magnetic field, $B_0 = 204.902(9)$ mT.

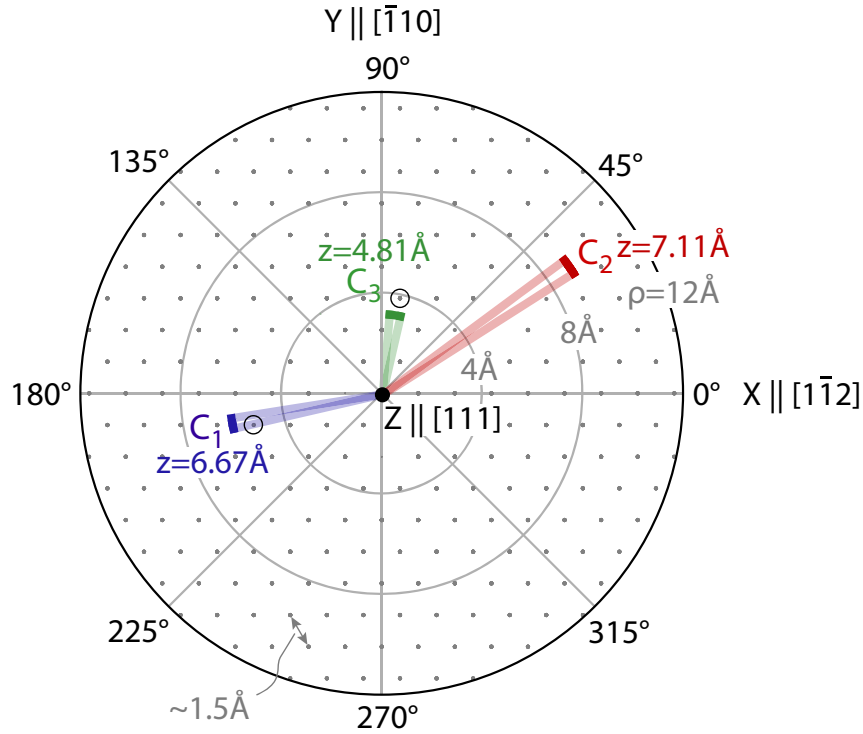


FIGURE 7.3: **Polar plot of the reconstructed nuclear spin positions in the xy -plane of the laboratory frame.** Shaded regions mark the uncertainty in ϕ of the respective nuclear spin. Radial distances $\rho = r \sin \theta$ and vertical heights $z = r |\cos \theta|$ of the nuclear sites are determined from the parallel and perpendicular hyperfine parameters by inverting the point-dipole formula [150]. The measurement uncertainties in z and ρ , neglecting deviations from the point-dipole model [68, 150, 151], are less than 0.02 \AA for all nuclei. Grey points represent the lattice sites of diamond. $^{13}\text{C}_1$ and $^{13}\text{C}_3$ are in good agreement with sites C47 and C390 (black circles) of a recent density functional theory (DFT) simulation [151] ($^{13}\text{C}_2$ is not part of the simulation). The offset between experimental and best-fitting DFT locations is due to the extended NV wave function that limits the point-dipole approximation [150]. The through-space distance of $^{13}\text{C}_2$ is $r = 11.5 \text{ \AA}$.

To compensate for these issues, we determine ϕ by fitting the experimental data with a Levenberg-Marquardt algorithm using a density matrix simulation [166, 168] as fit function and ϕ as fit parameter. We propagate the two-spin density matrix through the full sequence shown in Fig. 7.1 (b) using piece-wise constant Hamiltonians for the nuclear spin propagation, taking the calibrated vector field and temporal shape of Fig. 7.2 (a) as well as the hyperfine parameters (a_{\parallel}, a_{\perp}) as inputs. By calculating the nuclear spin evolution in the laboratory frame of reference, the simulation captures the Bloch-Siegert shift [169] and the z -component of the rf field. In addition, we directly retrieve the absolute laboratory frame azimuth ϕ rather than the relative $\Delta\phi$ between \vec{A}_z and \vec{B}_{coil} .

We start the analysis by fitting the simulation to the reference measurement (Fig. 7.2 (c)), which allows us to determine B_0 with an uncertainty smaller than $10 \mu\text{T}$. As B_0 defines the nuclear precession frequency, this calibration is of paramount importance for a precise estimate of ϕ . Afterwards we determine ϕ with a second fit to the measurements with the rf pulse (Fig. 7.2 (d)) while keeping B_0 fixed. All fit results are shown by solid lines in Fig. 7.2 (c),(d). We find an azimuth location of $\phi = 191 \pm 2^\circ$.

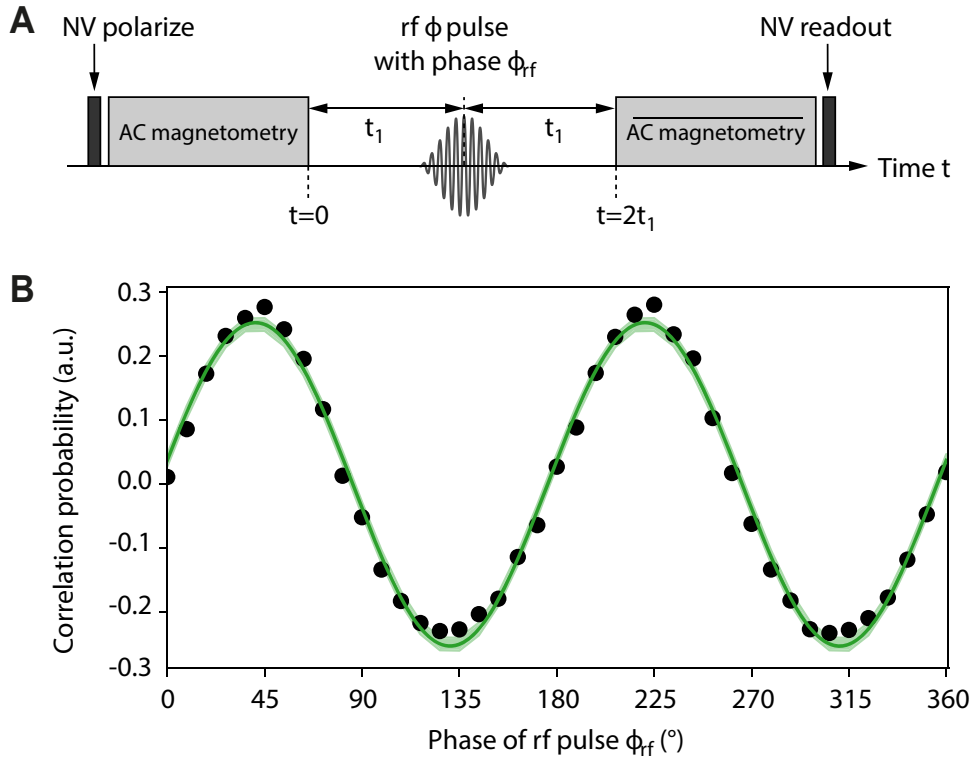


FIGURE 7.4: **Measurement of the hyperfine ϕ angle by a nuclear spin echo.** (a) Pulse sequence of the experiment: The free evolution time of a correlation spectroscopy sequence is interspersed with a π pulse generated by the rf coil. A cosine-square envelope [78] is used to suppress pulse transients, and the pulse is selective to the nuclear spin transition associated with the electronic $m_S = 0$ state. The correlation spectroscopy sequence is implemented by two AC magnetometry blocks as in Fig. 7.1 (e); the bar on the second block indicates that the sequence is reversed. (b) Spin echo modulation detected on $^{13}\text{C}_3$. Black dots show the data and the green line shows the density matrix simulation (best fit with ϕ as free parameter). The 2σ confidence intervals of the fit are indicated by shaded areas. The evolution time is $2t_1 = 31.36 \mu\text{s}$.

We have previously determined the three-dimensional coordinates of the same nuclear spin using a different positioning method [150], where $\phi = 197 \pm 4^\circ$, in good agreement with the present result. The accuracy of our experiment is presently limited by the calibration uncertainty of the coil field angle ($\sim 1^\circ$) and by the statistical fit error of the precession phase ($\sim 1^\circ$). The uncertainty due to misalignment of B_0 is below 1° [166]. Additional sources of uncertainty, like an influence of the local chemical environment, are not included in the analysis, but are expected to be insignificant for our study. The estimated three-dimensional location for this ($^{13}\text{C}_1$) and another nuclear spin ($^{13}\text{C}_2$; $(a_{||}, a_{\perp}) = 2\pi \times (1.9(1) \text{ kHz}, 19.2(1) \text{ kHz})$) are shown in Fig. 7.3.

High-field measurements

Next, we demonstrate that our azimuth positioning technique can be readily extended to high magnetic fields. High bias fields are desirable in NMR because of a better peak separation and a simplified interpretation of spectra. In addition, in NV-NMR, more efficient dynamical decoupling control and repetitive readout schemes become possible at higher fields [170]. In Fig. 7.2 (e)-(h) we show measurements

carried out at ~ 200 mT on a third nuclear spin ($^{13}\text{C}_3$) with hyperfine coupling parameters $(a_{\parallel}, a_{\perp}) = 2\pi \times (98.4 \text{ kHz}, 138.4 \text{ kHz})$. Here, we find $\phi = 81 \pm 4^\circ$. The three-dimensional location of $^{13}\text{C}_3$ is also indicated in Fig. 7.3.

The ϕ uncertainty at high magnetic field is larger than at low field because of timing errors. At 200 mT, the nuclear Larmor period is only ~ 460 ns, such that 1 ns of timing uncertainty causes a phase uncertainty of about 0.8° . For the rf pulse in Fig. 7.2 (e), we find a phase delay of $12 \pm 3^\circ$, corresponding to an overall timing uncertainty of the ODMR calibration of ~ 4 ns. Although the measured phase delay is in good agreement with the value predicted from the electrical characteristics of the rf circuit ($\sim 11^\circ$), it already introduces the largest error to the ϕ measurement. For future experiments carried out in the high bias fields of superconducting magnets [55] a precise calibration of control fields will therefore become even more critical.

7.4.2 Nuclear echo method

Finally, we discuss a complementary scheme for reconstructing the azimuth angle that does not require pre-polarization of nuclear spins. Instead of recording the nuclear precession signal as a function of t_1 , we intersperse a correlation spectroscopy sequence [77, 90] with a central rf π pulse to generate a nuclear spin echo at a fixed time $t = 2t_1$ (Fig. 7.4 (a)). By varying the pulse phase ϕ_{rf} from $0 - 360^\circ$, we modulate the amplitude of the spin echo, leading to an oscillatory signal $\propto \cos(2\phi_{\text{rf}} - 2\phi)$. We then determine ϕ from the phase offset of the oscillation. Fig. 7.4 (b) shows a spin echo oscillation for $^{13}\text{C}_3$ measured at a bias field of $204.9(1)$ mT. The compatible angles are $\{88 \pm 4^\circ, 268 \pm 4^\circ\}$, in good agreement with the result from Fig. 7.2 (h). Note that the echo method is afflicted by a 180° ambiguity in the angle measurement, because the echo oscillation repeats with ϕ_{rf} modulo π . Although the ambiguity could possibly be resolved by applying concomitant rf and microwave rotations or by introducing dc field pulses [150], it is unlikely to restrict future experiments on single molecules where relative, rather than absolute, positions are important. In addition, single-molecule NMR experiments can exploit internuclear interactions to further constrain the nuclear positions.

7.4.3 Density matrix simulations and estimation of ϕ

Density matrix simulations of the spin system

We performed density matrix simulations for all measurements and extracted the nuclear azimuthal location ϕ using non-linear least squares fitting [171]. We used the Quantum Toolbox in Python (QuTiP, [168]) software package to set up spin operators and compute the time-evolution propagators. We propagate the initial density matrix $\rho = |0\rangle\langle 0| \otimes I_e/2$ using time-independent Hamiltonians through the full measurement sequence, including the nuclear polarization step. Here $|0\rangle\langle 0|$ is the projector on the $m_s = 0$ state of the NV center and I_e is the nuclear spin identity. All timings are taken from the pulse file that was uploaded to the arbitrary waveform generators (AWG) controlling the experiments. Further input parameters are the parallel and perpendicular hyperfine parameters $(a_{\parallel}, a_{\perp})$, calibrated by conventional correlation spectroscopy [77], as well as the magnetic vector orientation and temporal shape of the coil rf pulse.

We reconstruct the azimuthal angle ϕ in two consecutive steps from the measurements: First, we determine the precession frequency of the nuclear spin. The precession frequency is a critical parameter in our experiments, because uncertainty in the frequency directly translates into an uncertainty in the detected phases and thereby

to an uncertainty in the azimuthal position ϕ . We estimate the nuclear precession frequency using the reference measurement traces, which were acquired after rotating the nuclear spin via the hyperfine interaction. The most precise estimate of the precession frequency can be obtained by simulating the dynamics of the nuclear-electron spin system to include the coherent evolution of the nuclear spin starting from the rotation with the NV center until the read-out of the NV center. The total evolution or interrogation time in our experiments is typically $20 - 40 \mu\text{s}$ long and therefore the precession frequency of the nuclear spin can be determined very precisely.

Extraction of the nuclear precession frequency

We fit the simulation to the reference measurement with the magnitude of the external bias field B_0 as a free parameter to adjust the precession frequency. Here, the bias field is assumed to be aligned with the symmetry axis of the NV center. A discussion of the effect of tilted magnetic fields follows in Section 7.4.4. We fit the simulated time trace to the experimental data with a non-linear least-squares optimization. Apart from the bias field B_0 we only allow for an amplitude scaling factor (accounting for non-ideal nuclear polarization, *e.g.*, due to relaxation) plus a constant offset as additional free parameters of the fit. Using this procedure, we determine B_0 with an uncertainty smaller than $\delta B_0 = 10 \mu\text{T}$, which corresponds to an uncertainty of the nuclear precession frequency of $\sim 100 \text{ Hz}$.

Extraction of the azimuthal position

Afterwards, we determine the azimuthal position of the nuclear spin using the nuclear precession trace after a rotation with the micro-coil. Again, we simulate the dynamics of the spin system by propagating the density matrix with B_0 now fixed. The temporal shape of the coil pulse, as determined by the 2D spectroscopy, and the vector field of the coil are added as input parameters to the simulation. The evolution of the nuclear spin during the rf-pulse is approximated by piecewise constant propagators during which the Hamiltonian is time-independent. We operate in the non-rotating reference frame of the nuclear spin, hence counter-rotating terms leading, *e.g.*, to the Bloch-Siegert shift are also captured by the simulation. Again we use a non-linear least squares optimization procedure to fit the simulated time trace to the experimental data. The free parameters are the nuclear azimuthal position ϕ and an offset and an amplitude scaling factor.

7.4.4 Effect of tilted magnetic bias fields on the accuracy in estimating $\vec{r} = (r, \theta, \phi)$

As discussed before, we have carefully aligned the magnetic bias field B_0 to the quantization axis of the NV center with a resulting tilt smaller than 1° . Here, we discuss the influence of the residual tilt on the accuracy in estimating the nuclear position.

We performed a detailed analysis of the positioning accuracy by making use of the density matrix simulations (Section 7.4.3) to perform a Monte Carlo sampling of the distribution of the estimates (r, θ, ϕ) . As an example, we consider nuclear spin $^{13}\text{C}_3$, whose three-dimensional position was determined in a magnetic field of $B_0 = 204.902(9) \text{ mT}$. All other nuclear spins were positioned in a significantly smaller magnetic field of $9.600(8) \text{ mT}$, where the alignment of the magnetic field can be performed much more precisely using auxiliary calibration NV centers, as

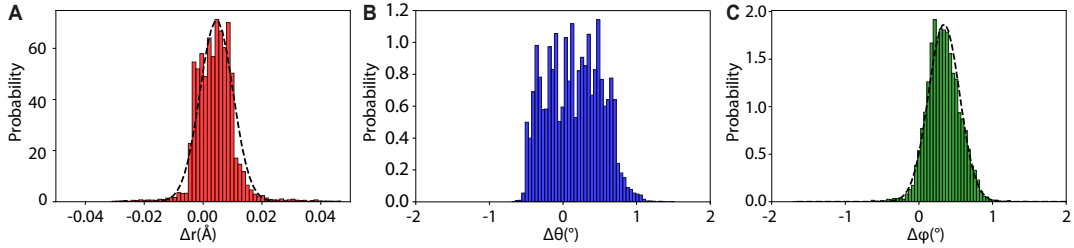


FIGURE 7.5: **Nuclear positioning uncertainty due to tilted bias fields for $^{13}\text{C}_3$.** (a) Histogram of the distribution of deviations in the estimated radial distance Δr from the actual distance r . The histogram contains 10949 samples of a Monte Carlo simulation described in the text. (b) Histogram of the deviation of θ obtained from the same Monte Carlo simulation as in (a) and with the same sample size. (c) Histogram of the deviation in ϕ . The average tilt in the Monte Carlo simulation generating the distribution was set to $\sim 1^\circ$.

described in [150]. Hence, the positioning uncertainty due to tilted magnetic fields is significantly smaller in low magnetic field (approximately one order of magnitude) and $^{13}\text{C}_3$ serves as a worst-case estimate.

The error estimation protocol follows a two-step process: First, we generate artificial measurement data with a random field tilt and a given nuclear position (r, θ, ϕ) . In a second step, we use the procedures described before to estimate $(\tilde{r}, \tilde{\theta}, \tilde{\phi})$. Finally, we compare the resulting values to the input coordinates. In each iteration of this Monte Carlo (MC) simulation we add random transverse magnetic field components which were drawn from a normal distribution with mean zero and standard deviation $\sigma = 1.4$ mT. This corresponds to tilts of $\sim 1^\circ$. In the resulting tilted magnetic field we simulated each step of the three-dimensional positioning protocol. First, we simulated the outcome of correlation spectroscopy experiments [77] to infer $(\omega_L, a_{\parallel}, a_{\perp})$. From these parameters, we directly obtain the estimates of (r, θ) of the nuclear spin location by inverting the relations for $(a_{\parallel}, a_{\perp})$ [150]. Due to the tilt of the magnetic field the hyperfine coupling parameters are slightly modified, which leads to a distribution of (r, θ) which depends on (B_x, B_y) . These distributions are shown as histograms in Fig. 7.5 (a),(b), respectively. The resulting variations in r and θ amounts to ~ 0.01 and $\sim 0.5^\circ$, respectively. For the histograms we generated 19140 Monte Carlo samples. Afterwards, we post-selected $N = 10949$ samples for which the deviation between nuclear precession frequency, obtained from the simulated correlation spectroscopy, and the one predicted by the EPR frequency (by diagonalizing the Hamiltonian) is smaller than $2\pi \times 1$ kHz. This condition was enforced in all experiments.

Subsequently, we simulate the azimuthal imaging protocol as discussed before. The interpulse spacing τ of the multipulse sequences used for the AC magnetometry was adjusted based on the result of the correlation spectroscopy. The outcome of the simulation, *i.e.*, the precession trace of the nuclear spin is analyzed by the non-linear fitting procedure (see Section 7.4.3), in the same manner as the experimental traces. The resulting distribution of $\Delta\phi$ is shown in Fig. 7.5 (c). We find that the variation in $\Delta\phi$ amounts to $\sim 0.3^\circ$. The distributions of $(\Delta r, \Delta\theta, \Delta\phi)$ are not exactly centered at zero because of the gyromagnetic ratio enhancement of the nuclear spin resulting from the transverse magnetic fields [148].

7.5 Conclusion

In conclusion, we have introduced a simple method for measuring the inter-spin azimuth ϕ , enabling us to perform three-dimensional distance measurements on single nuclear spins. We demonstrate the potential of our technique by mapping the 3D location of individual ^{13}C nuclei in diamond with a precision sufficient for assigning discrete lattice sites. Future experiments will apply 3D distance measurements to molecules deposited on the surface of dedicated diamond NMR sensor chips [54, 76, 80, 172] and provide an avenue to analyze the structure and conformation of single molecules with atomic resolution [173].

Reconstruction-free quantum sensing of arbitrary waveforms

Summary

We present a protocol for directly detecting time-dependent magnetic field waveforms with a quantum two-level system. Our method is based on a differential refocusing of segments of the waveform using spin echoes. The sequence can be repeated to increase the sensitivity to small signals. The frequency bandwidth is intrinsically limited by the duration of the refocusing pulses. We demonstrate detection of arbitrary waveforms with ~ 20 ns time resolution and $\sim 4 \mu\text{T} / \sqrt{\text{Hz}}$ field sensitivity using the electronic spin of a single nitrogen-vacancy center in diamond.

This chapter has been published as:

J. Zopes and C. L. Degen, *Reconstruction-free quantum sensing of arbitrary waveforms*, arXiv:1906.09176 (2019).

8.1 Introduction

Well-controlled two-level quantum systems with long coherence times have proven useful for precision sensing [19, 22] of various physical quantities including temperature [38], pressure [39], or electric [40] and magnetic fields [78, 136]. By devising suitable coherent control sequences, such as dynamical decoupling [174], quantum sensing has been extended to time-varying signals. In particular, coherent control schemes have allowed the recording of frequency spectra [74, 95, 127] and lock-in measurements of harmonic test signals [125].

A more general task is the recording of arbitrary waveform signals, in analogy to the oscilloscope in electronic test and measurement. In this case, conventional dynamical decoupling sequences are no longer the method of choice as the sensor output is non-trivially connected to the input waveform signal, requiring alternative sensing approaches. For slowly varying signals, the transition frequency of the sensor can be tracked in real time [175], permitting detection of arbitrary waveforms in a single shot. By using a large ensemble of quantum sensors detection bandwidths of up to ~ 1 MHz have been demonstrated [176, 177], with applications in MRI tomograph stabilization [176], neural signaling [178, 179], or magnetoencephalography [180].

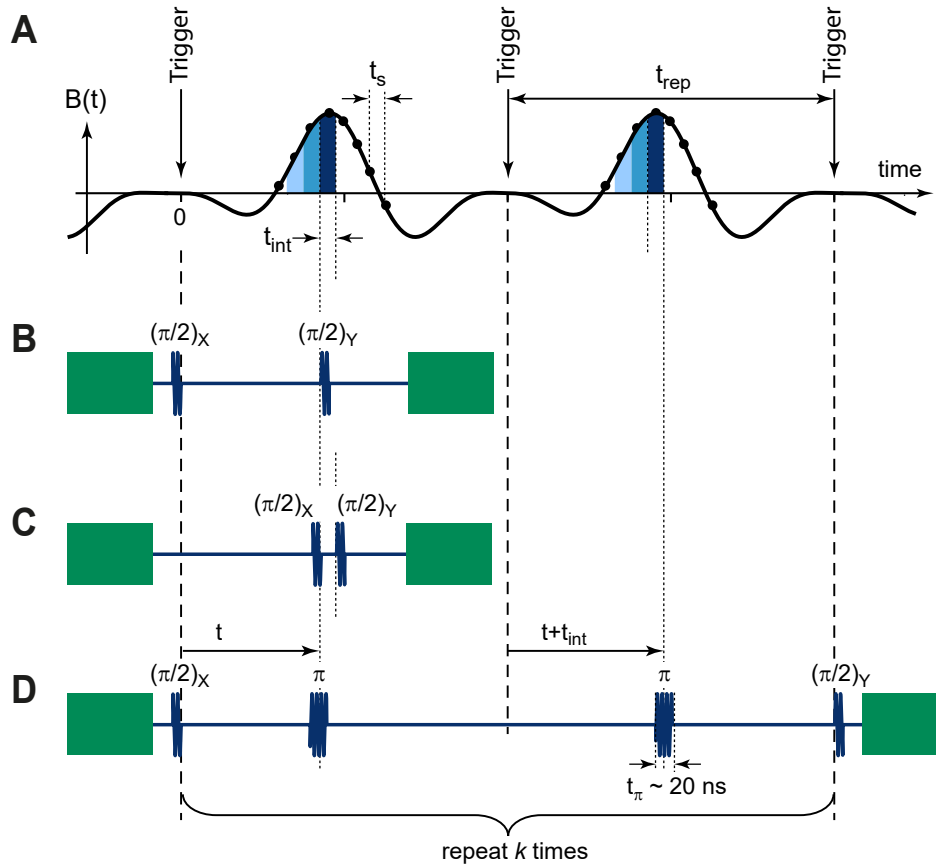


FIGURE 8.1: **Schemes for equivalent-time waveform sampling by a quantum sensor.** (a) Schematic of a repetitive arbitrary waveform $B(t)$. t is the time relative to the preceding trigger and t_{rep} is the repetition time. Dots indicate the waveform sampling and t_s is the sampling time. (b) Standard integrative Ramsey detection of the waveform. The sensor acquired phase is proportional to the integral of the waveform between 0 and t . Signals are detected by stepping t in increments of t_s . Microwave pulses are shown in dark blue. Labels indicate the pulse angles and subscripts the pulse phases. Laser arm and readout pulses are shown in green. (c) Small interval Ramsey detection of the waveform. (d) Differential detection of the waveform by spin echoes. t_{int} is the differential integration time and t_π is the π pulse duration. The differential protocol can be repeated k times to linearly increase the accumulated phase.

For rapidly changing signals the waveform can no longer be tracked, and a general waveform cannot be recorded in a single shot. However, if a waveform is repetitive or can be re-triggered, multiple passages of the waveform can be combined to reconstruct the full waveform signal. This method, known as equivalent-time sampling, is routinely implemented in digital oscilloscopes to capture signals at effective sampling rates that are much higher than the rate of analog-to-digital conversion.

In quantum sensing, one possibility is to record a series of time-resolved spectra that cover the duration of the waveform [57]. This method, however, is limited to strong signals because the spectral resolution inversely scales with the time resolution. Other approaches include pulsed Ramsey detection [62], Walsh dynamical decoupling [181, 182], and Haar wavelet sampling [183], discussed below. These methods use coherent control of the sensor to achieve competitive sensitivities, but require some form of waveform reconstruction.

8.2 Waveform quantum sensing protocols

In this Chapter we experimentally demonstrate a simple quantum sensing sequence for directly recording time-dependent magnetic fields with no need for signal reconstruction. Our method uses a spin echo to differentially detect short segments of the waveform, and achieves simultaneous high magnetic field sensitivity and high time resolution. The only constraints are that the waveform can be triggered twice within the coherence time of the sensor, and that the signal amplitude remains within the excitation bandwidth of qubit control pulses. Possible applications include the *in situ* calibration of miniature radio-frequency transmitters [57, 147], activity mapping in integrated circuits [184], detection of pulsed photocurrents [185], and magnetic switching in thin films [186].

To motivate our measurement protocol we first inspect the interferometric Ramsey method, which has been a standard method for early quantum sensing of waveforms [62]. In a Ramsey experiment a superposition state, prepared by a first $\pi/2$ pulse, evolves during a sensing time t and acquires a phase factor $\phi(t)$ that is proportional to the transition frequency ω_0 between ground and excited states (see Fig. 8.1(b)). For a spin sensor, where ω_0 is proportional to the component of the magnetic field along the spin's quantization axis, the acquired phase is

$$\phi(t) = \int_0^t \gamma_e B(t') dt'. \quad (8.1)$$

Here, $B(t)$ is the time-dependent magnetic field that we aim to measure and γ_e is the gyromagnetic ratio of the spin. To extract the phase, $\phi(t)$ is typically converted into a population difference $p(t)$ by a second $\pi/2$ pulse,

$$p(t) = \frac{1}{2}(1 + \sin(\phi(t))) \stackrel{\phi \ll 1}{\approx} \frac{1}{2}(1 + \phi(t)). \quad (8.2)$$

followed by a projective readout of the sensor and signal averaging [22]. By measuring $p(t)$ as a function of t , one thus effectively measures the integral of the magnetic field in the interval $[0, t]$. Using a numerical derivative the magnetic field can subsequently be reconstructed [62]. However, this reconstruction greatly increases noise due to the derivative [187] and often requires phase unwrapping.

A more direct method that avoids numerical processing is the sampling of the waveform in small intervals t_{int} and to build up the waveform by stepping t . The simplest approach is use a Ramsey sequence with a very short integration time t_{int} (Fig. 8.1(c)). In this case the sensor phase $\phi(t)$ encodes the field in the time interval $[t, t + t_{\text{int}}]$,

$$\phi(t) = \int_t^{t+t_{\text{int}}} \gamma_e B(t') dt' \approx \gamma_e B(t) t_{\text{int}}, \quad (8.3)$$

without the need for numerical post-processing. Thanks to the short t_{int} one can often take advantage of the linear approximation ($\sin \phi \approx \phi$) in Eq. (8.2). The short t_{int} , however, impairs sensitivity because $\phi \propto t_{\text{int}}$.

To maintain adequate sensitivity even for short t_{int} we introduce a detection protocol that accumulates phase from several consecutive waveform passages. Our scheme requires that the repetition time is short, $t_{\text{rep}} \ll T_2$, where T_2 is the sensor's coherence time, which is often the case for fast waveform signals. Our protocol is shown in Fig. 8.1(d): By inserting two π pulses at times t and $t + t_{\text{int}}$ relative to two consecutive waveform triggers, we selectively acquire phase from the time interval

$[t, t + t_{\text{int}}]$ while canceling all other phase accumulation. A similar scheme of partial phase cancellation has been implemented with digital Walsh filters [182] and Haar functions [183] via a sequence of π rotations. The linear recombination of sensor outputs in such waveform sampling, however, is prone to introducing errors, especially for rapidly varying signals whose detection requires many π pulses [181]. In our scheme, the π rotations effectively act as an *in situ* derivative to the phase integral (Eq. 8.1), bypassing the need for a later numerical differentiation or reconstruction. To further amplify the signal, the basic two- π -pulse block can be repeated k times to accumulate phase from $2k$ waveform passages, up to a limit set by $2kt_{\text{rep}} \leq T_2$. The amplified signal is (in linear approximation)

$$p(t) \approx 0.5 + 2k\gamma_e B(t)t_{\text{int}}, \quad (8.4)$$

and when converted to units of magnetic field,

$$B(t) \approx \frac{p(t) - 0.5}{2k\gamma_e t_{\text{int}}}. \quad (8.5)$$

8.3 Experimental realization

We experimentally demonstrate arbitrary waveform sampling using the electronic spin of a single nitrogen-vacancy (NV) center in a diamond single crystal. The NV spin is initialized and read out using $\sim 2 \mu\text{s}$ green laser pulses and a single-photon-counting module [136]. Microwave control pulses are generated by an arbitrary waveform generator (AWG), amplified to reach Rabi frequencies of $\sim 25 \text{ MHz}$, and applied to the NV center via a coplanar waveguide (CPW) structure [78]. Test magnetic waveforms are generated by a second function generator operated in burst mode and triggered by the AWG. The test signals are delivered to the NV center either by injecting them into the common CPW using a bias-T [73] or by an auxiliary nearby microcoil [57, 150]. The setup is operated in a magnetic bias field of 43 mT (aligned with the N-V crystal direction) to isolate the $\{m_s = 0, m_s = -1\}$ manifold of the $S = 1$ NV spin, and to achieve preferential alignment of the intrinsic nitrogen nuclear spin (here the spin 1/2 of the ^{15}N isotope) [81]. The latter is not required for our scheme, but helps reducing microwave pulse errors.

8.4 Detection of a magnetic square waveform pulse

We begin our study by recording a simple, 270-ns-long square waveform (Fig. 8.2). We record the waveform both using the standard integrative Ramsey scheme [Fig. 8.1(b)] and our differential sampling technique [Fig. 8.1(d)]. For the Ramsey scheme, we reconstruct the magnetic waveform by a numerical differentiation of the raw signal (black data in Fig. 8.2(a)) via the central difference quotient of the smoothed signal [188]. The reconstructed waveform is shown in blue. For our differential detection scheme, we directly plot the signal output without any further data processing (Fig. 8.2(b)). Clearly, the differential sampling method is able to faithfully reproduce the square pulse and is not affected by the noise amplification of the Ramsey scheme.

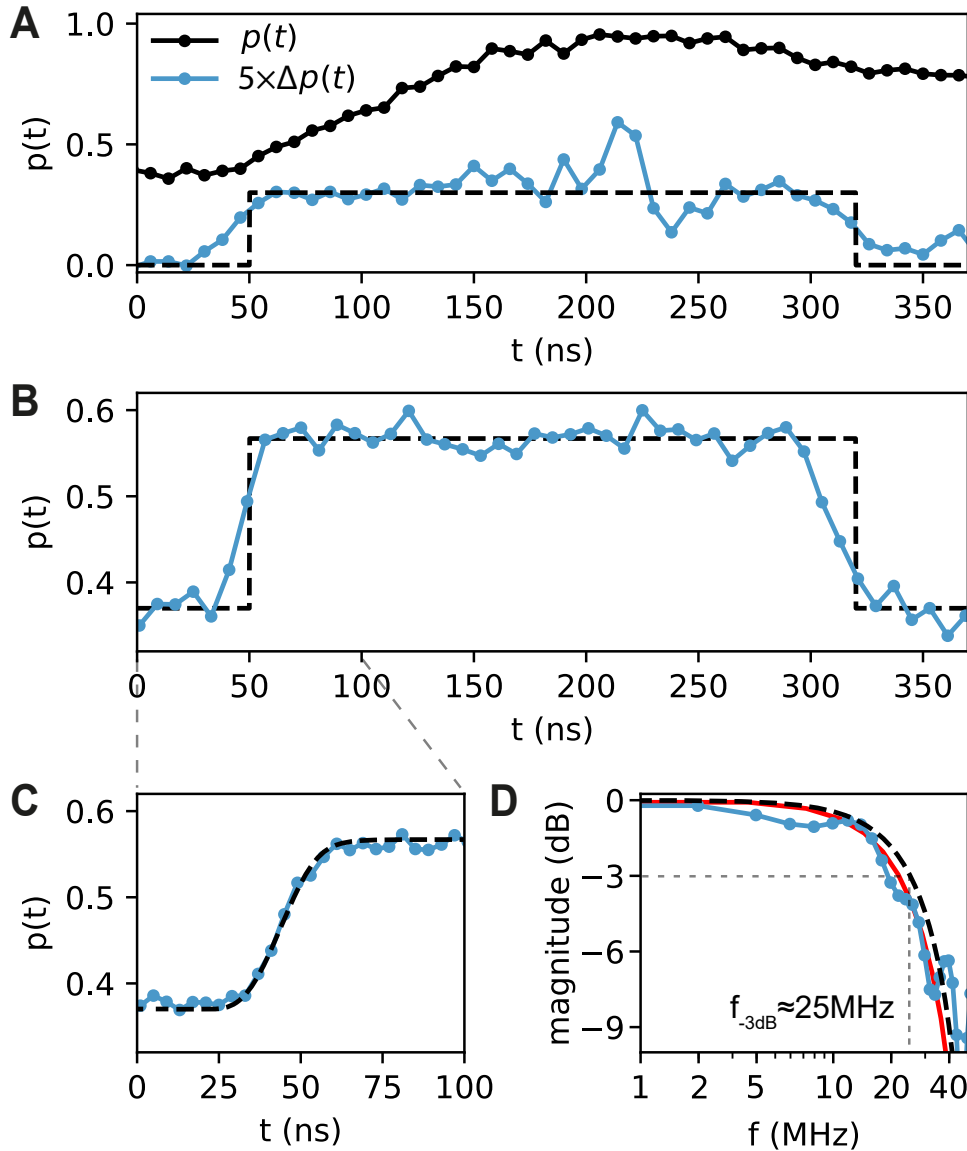


FIGURE 8.2: **Pulse detection and time resolution.** (a) Sensor response to a square-wave magnetic signal (dashed curve) recorded using the standard integrative Ramsey method [protocol of Fig. 8.1(b)]. The raw data are shown in black and the reconstructed waveform is shown in blue. The waveform is reconstructed by applying a 4-point moving average to the raw data and calculating the difference Δp between adjacent points. The dwell time is $t_s = 8$ ns and the total averaging time is 1 hour. (b) Sensor response (raw signal) to the same waveform signal recorded using the differential spin echo technique [protocol of Fig. 8.1(d) using $k = 2$]. The total averaging time is 15 min. (c) High resolution sampling ($t_s = 4$ ns) of the rising edge of the square pulse waveform. The blue points are measured data. The dashed black line is the expected step response for π -pulse and integration lengths of $t_{\text{int}} = t_\pi = 20$ ns. (d) Magnitude plot of the corresponding sensor transfer function. Blue dots are the data and the black dashed curve is the Fourier transform of a Hann window of duration $2t_\pi = 40$ ns. The red curve additionally takes the finite response time of the test signal circuit (~ 8 ns) into account.

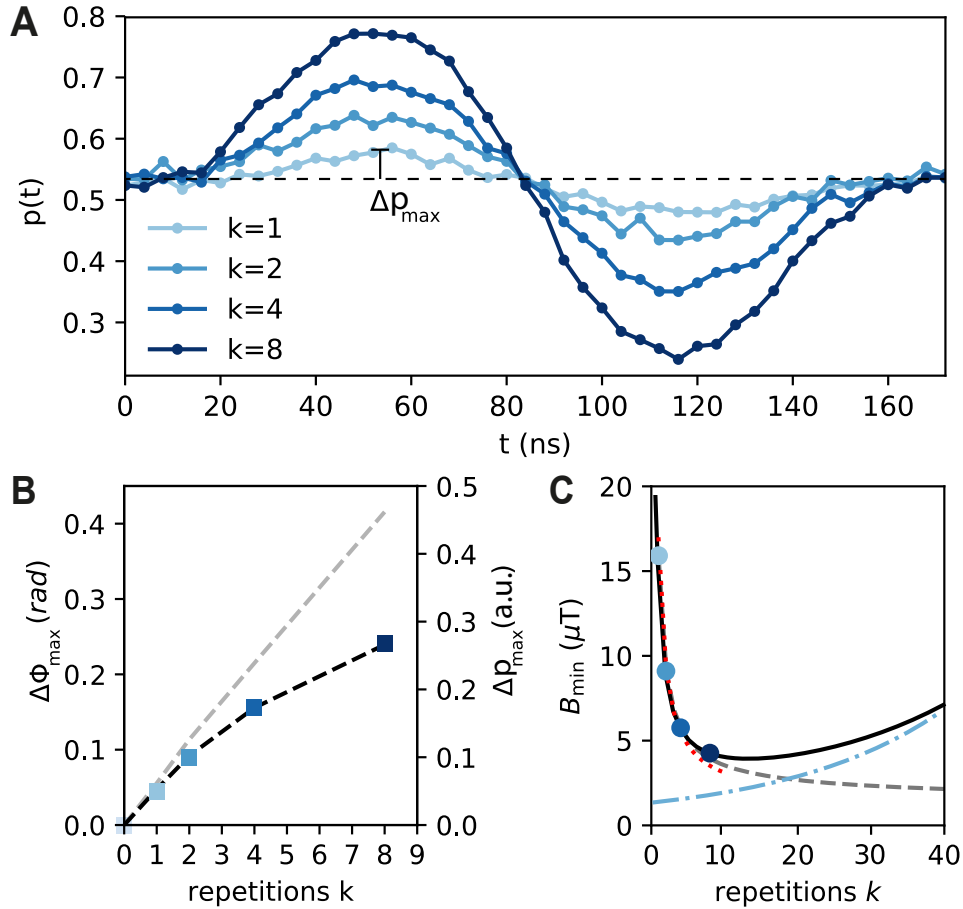


FIGURE 8.3: **Increased sensitivity by integrating $2k$ waveform passages.** (a) Sensor output $p(t)$ for $k = 1, 2, 4$ and 8 repetitions of the two- π -pulse unit (see Fig. 8.1(c)), for a sine waveform of amplitude $10 \mu\text{T}$ and frequency $f = 4 \text{ MHz}$. The integration time and π -pulse duration are $t_{\text{int}} = t_{\pi} = 20 \text{ ns}$ and the repetition time is $t_{\text{rep}} = 344 \text{ ns}$. (b) Peak output signal Δp_{\max} as a function of k (colored squares). The gray dashed line shows a linear scaling that would be expected in the absence of sensor decoherence. The black dash-dotted line takes decoherence into account ($T_2 = 14 \mu\text{s}$). (c) Minimum detectable magnetic field B_{\min} per unit time as defined by Eq. (8.6) (black curve). Colored dots represent the data from (a). The dashed, dash-dotted and dotted curves are explained in the text.

8.5 Time resolution of waveform sensing

To characterize the time resolution of the method, we record the rising edge of the pulse with fine sampling $t_s = 4 \text{ ns}$ (Fig. 8.2(c)). We find a 10-90% step response time of $\tau \sim 20 \text{ ns}$. The response time is approximately given by $\tau \approx \max(t_{\pi}, t_{\text{int}})$, since the finite pulse duration and the integration time both act as moving average filters. While t_{int} can be deliberately adjusted, t_{π} is determined by the Rabi frequency of the system and sets a hard limit to the response time.

In Fig. 8.2(d) we show the corresponding frequency transfer function $G(\omega)$ of the sensor, *i.e.*, the Fourier transform of the unit impulse response obtained from the step response. In our experiments, where $t_{\text{int}} = t_{\pi}$, the unit impulse response of the sensor is approximately given by a Hann function with characteristic length $2t_{\pi}$ (see appendix C). The Bode plot indicates a -3dB sensor bandwidth $f_{-3\text{dB}} \approx 25 \text{ MHz}$, with good agreement between theory and experiments. This bandwidth could be

slightly increased, up to ~ 40 MHz (see appendix C), by choosing shorter integration times $t_{\text{int}} \ll t_{\pi}$; however, the short integration time comes with the penalty of vanishing sensitivity.

8.6 Signal gain by repetitive acquisition

In a next step, we investigate the signal gain possible by accumulating phase from $2k$ consecutive waveform passages. Fig. 8.3(a) plots the sensor response from a weak sinusoidal test signal recorded with $k = 1, 2, 4$ and 8 . Clearly, a much larger oscilloscope response results for higher k values. To estimate the signal gain, we plot the peak sensor signal Δp_{max} (indicated in (a)) as a function of k , see Fig. 8.3(b). At small k values the increase of Δp_{max} is proportional to k , as expected, while at larger k decoherence of the sensor attenuates the signal. By correcting for sensor decoherence, we can recover the almost exact linear scaling of the signal phase $\Delta\phi_{\text{max}}$ with k (dashed line in (b)).

To quantify the overall sensitivity in the presence of decoherence and sensor readout overhead, we calculate a minimum detectable field B_{min} , defined as the input field that gives unity signal-to-noise ratio for a one-second integration time. B_{min} is given by [22],

$$B_{\text{min}} = \frac{\sqrt{t_{\text{m}} + 2kt_{\text{rep}}e^{-\frac{2kt_{\text{rep}}}{T_2}}}}{2\gamma_e k C t_{\text{int}}}, \quad (8.6)$$

where $t_{\text{m}} = 3 \mu\text{s}$ is the arm/readout duration (see Fig. 8.1(c)), $T_2 \sim 14 \mu\text{s}$ is the coherence time, and $C \sim 0.02$ is a dimensionless number that quantifies the quantum readout efficiency [22]. In Fig. 8.3(c) we plot B_{min} as a function of k . We find that $B_{\text{min}} \propto k^{-1}$ for short durations $kt_{\text{rep}} < t_{\text{m}}$, that is, the benefit of repeating the sequence is largest for small k and high repetition rates (dotted curve). Once $kt_{\text{rep}} > t_{\text{m}}$ the scaling reduces to $B_{\text{min}} \propto k^{-0.5}$ because the linear phase accumulation now competes with standard signal averaging (dashed curve). For large kt_{rep} that exceed the sensor coherence time T_2 the efficiency of the method rapidly deteriorates (dash-dotted curve).

8.7 Detection of a complex test waveform

We complete our study by demonstrating detection of a complex test waveform (Fig. 8.4). The waveform contains the sum of several Fourier components with the analytical expression for $B(t)$ given in the figure caption. In Fig. 8.4(a) we show the experimentally measured waveform (light blue points) together with the input waveform (dashed black line) in the same plot. The experimental waveform consists of $N = 280$ data points sampled at $t_s = 4$ ns horizontal resolution. Clearly, the experimental waveform agrees very well with the applied input. The experimental data are plotted without any data processing, demonstrating that our differential sampling method directly reproduces the waveform signal. Fig. 8.4 (b) further presents the corresponding power spectra of the input waveform (black dashed line) and the recorded sensor output (light blue points). Although the signal lies within the analog bandwidth of the sensor (~ 25 MHz), some attenuation is observed at higher frequencies. If desired, inverse filtering techniques could be applied to compensate the high-frequency roll-off of the sensor.

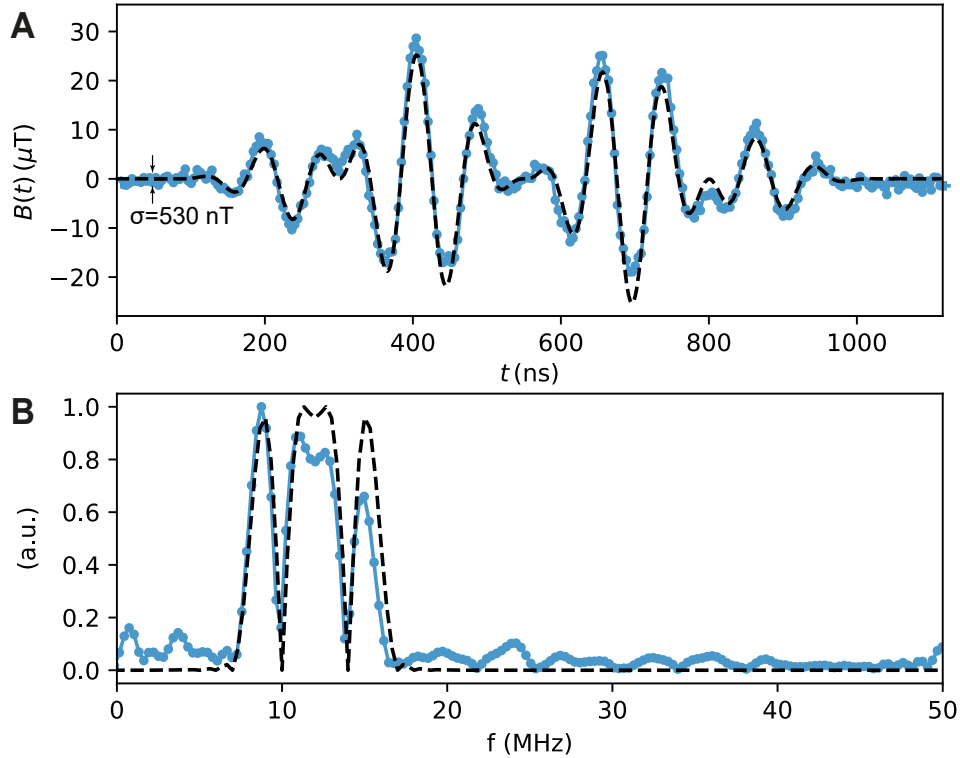


FIGURE 8.4: **Example of arbitrary waveform detection.** (a) Input waveform (dashed line) and recorded waveform data (blue dots) for a complex waveform given by $B(t) = B \sin^2(\omega t/2) [\sin(12\omega t) \cos(\omega t) \sin^2(\omega t)]$, with $B = 81.87 \text{ } \mu\text{T}$ and $\omega = 2\pi \times 1 \text{ MHz}$. The waveform is sampled using $N = 280$ data points and $t_s = 4 \text{ ns}$. Further parameters are $t_{\text{int}} = t_\pi = 20 \text{ ns}$, $t_{\text{rep}} = 1400 \text{ ns}$ and $k = 4$. The total experimental time is 60 h corresponding to $\sim 1.44 \times 10^{10}$ waveform triggers. The baseline noise is $\sigma \approx 530 \text{ nT-rms}$. (b) Normalized power spectra of the input waveform (black dashed line) and the detected waveform (light blue connected points). Fourier components at higher frequencies are slightly attenuated due to the limited bandwidth of the sensing sequence.

8.8 Limitations and possible remedies

Before concluding, we point out a few limitations and possible remedies of the differential waveform sampling technique. First, our scheme is only applicable to waveforms that can be triggered twice within the sensors T_2 time. While T_2 could be extended to some extent by adding dynamical decoupling π pulses to our protocol, very long repetition times cannot be covered, and will require resorting to, *e.g.*, the inefficient small-interval Ramsey technique (Fig. 8.1(c)). Second, the maximum peak-to-peak signal amplitude is limited by the excitation bandwidth of π pulses to $(\gamma_e t_\pi)^{-1}$, here $\sim 2 \text{ mT}$. Only relatively weak fields can therefore be detected with our method. To cover strong signals, time-resolved spectroscopy techniques are available [57]. Third, when accumulating signal over many passages k , the phase may exceed the sensor's linear range (see Eq. 8.1). In this situation, the relative phase of the second $\pi/2$ pulse could be cycled [189] to recover a linear response.

8.9 Conclusion and Outlook

In summary, we have presented a quantum sensing method for direct detection of arbitrary waveforms in the time domain using equivalent time sampling. Our method does not require any waveform reconstruction, allowing, for example, to sample arbitrary segments from a longer waveform. In addition, our protocol can be repeated to coherently accumulate phase from many waveform cycles to improve sensitivity. The analog bandwidth of our scheme is fundamentally limited by the Rabi frequency of the sensor, which sets the minimum π pulse duration t_π . In the present work, we demonstrate a time resolution of $t_\pi \sim 20$ ns using a Rabi frequency of ~ 25 MHz. To achieve better time resolution, the Rabi frequency could be increased by more than an order of magnitude by miniaturizing the coplanar waveguide [108, 190]. The highest demonstrated Rabi frequencies are 200 – 500 MHz for NV centers, corresponding to $t_\pi = 1 - 2.5$ ns [108, 190]. At this time resolution it may become feasible to study the photoresponse in materials [185] or the switching in thin film magnetic memory devices [186].

Conclusion and Outlook

In this thesis, we presented novel magnetometry protocols for spin-based quantum sensors. We experimentally realized these protocols using the NV center in diamond. All experiments were performed on single-crystal diamonds with individual, near-surface NV centers at room temperature.

Nanoscale magnetic resonance imaging

The main focus of this work, with results presented in Chapters 5, 6 and 7, was the detection of nuclear spins in the vicinity of the NV center: We developed two imaging methods to determine the three-dimensional distance vector of individual nuclear spins relative to the NV sensor. Both methods used a novel micro-coil placed in close vicinity to the diamond surface to actively manipulate nuclear spins. The first method (presented in Chapter 6) records nuclear precession in dynamically tilted external magnetic bias fields. The second method (presented in Chapter 7) uses coherent radio-frequency control to extract the nuclear location. Both imaging protocols were used to retrieve the nuclear coordinates for distances up to $\sim 12 \text{ \AA}$ and, in combination with DFT data, allowed us to constrain the position of the nuclei to individual sites in the diamond lattice. The main contribution to the uncertainty in the nuclear coordinates comes from the extent of the NV spin density. In future experiments, probing more distant spins, this uncertainty will be reduced and only spectroscopic resolution will limit the imaging accuracy.

At this point many promising research directions can be explored with the final goal of elucidating the structure of a small molecule. The most important experimental challenges that need to be overcome on the way to this goal are:

- **Increasing sensitivity:** To date the field sensitivity of the NV center suffices to detect individual nuclei at distances of up to 3 nm [138]. To improve the sensitivity the coherence properties of shallow NV centers have to be enhanced by proper surface preparation. Further, the collection efficiency of the photons emitted by the NV center have to be increased by etching optimized waveguide structures into the diamond chips. Finally, new spectroscopy techniques optimized for weakly-coupled spins have to be applied [99].
- **Enhancing spectral resolution:** The spectral resolution of the hyperfine spectroscopy techniques employed in this work is limited by the sensor spin lifetime T_1 . Recently, spectroscopy techniques have been developed in our group and elsewhere, which permit signal detection with spectral resolutions beyond

the sensor lifetime limit [74, 95, 99, 152]. For imaging of distant, very weakly coupled nuclear spins these spectroscopy methods can be combined with the positioning techniques described in this work. In addition, the inter-spin coupling between nuclei in the molecule will lead to broad, complex spectra that could be simplified by homo-nuclear decoupling techniques [100].

- Detection of inter-spin couplings between nuclei: Apart from spectral broadening couplings between nuclei also provide structural information. Controlled detection of the inter-spin couplings can be used to constrain possible structural properties of spin clusters [88].
- Sample surface preparation: Structure determination experiments on molecules critically require proper fixation and preparation of the molecules on the diamond surface. In our group first attempts to prepare organic, spin-labeled molecules in a thin polymer matrix have been conducted and signatures of the spin-labels were detected with double resonance techniques [102]. However, limited stability of the molecules has been observed, possibly due to the optical illumination. One possible remedy would be to perform experiments at low temperature and vacuum conditions where spin-labeled samples were found to be stable [191]. At room temperature the next experiments can also be performed on nuclear spins, *e.g.*, ^1H spins, under the condition that sufficient sensitivity is achieved.

Detection of arbitrary magnetic signals

The differential spin echo sequence presented in Chapter 8 addresses the problem of detecting an arbitrary magnetic field waveform with a two-level system. The novel protocol enables reconstruction-free measurements of magnetic signals, if the signal can be triggered repetitively. Our new sensing technique effectively turns the NV center into a "quantum oscilloscope" with many potential applications: Although the demonstration experiments performed in this thesis only detect artificial test waveforms, the presented method is promising for the magnetic and electrical characterization of nano-structures (including, for example, magnetic switching [186], IC activity mapping [184] or photo-response measurements [185]). For this purpose the protocol has recently been implemented on one of the scanning NV magnetometers in our group [192]. In future experiments several extensions and improvements of the differential spin echo technique can be envisioned:

- Enhancing time resolution: In the current experiments the time resolution of the sensing sequence was limited to ~ 20 ns due to the duration of the refocusing pulses. In future experiments a higher time resolution is desirable to detect the rapid dynamics of magnetization switching in next-generation memory devices or to perform photo-response measurements. The most promising approach to improve the time resolution is to reduce the distance of the NV centers to the microwave stripline as demonstrated in [108, 190]. In initial test experiments performed in our group a scanning tip was positioned in close vicinity of a microwave source and Rabi frequencies of up to ~ 150 MHz have been observed, which would translate to a time resolution of ~ 3.3 ns [192].
- Vector magnetometry: In principle, the differential spin echo technique can be applied to an ensemble of NV centers with different crystallographic orientations. From the magnetometry signal of at least three of the orientations it is

possible to reconstruct the time-dependent vector field at the position of the ensemble of NV centers.

Product operator calculations

Here, we derive a useful relation for two-spin product operators that in chapter 3 allows us to simplify the computation of the action of pulse sequences. We start with an arbitrary product state of a two-spin system $\rho = S_b \otimes I_n$ and apply the transformation $U = e^{-i\alpha(S_a \otimes I_m)}$:

$$\rho' = U\rho U^\dagger = e^{-i\alpha(S_a \otimes I_m)} \rho e^{i\alpha(S_a \otimes I_m)} = e^{-i\alpha(S_a \otimes I_m)} (S_b \otimes I_n) e^{i\alpha(S_a \otimes I_m)}. \quad (\text{A.1})$$

In the following discussion the operators S and I are assumed to describe the NV electron spin (S), reduced to a two-level system, and a nuclear spin (I), respectively. We now use Euler's formula for operators A which obey $A^2 = \mathbb{1}$ (fulfilled for Pauli matrices):

$$e^{i\theta A} = \cos(\theta)\mathbb{1} + i \sin(\theta)A. \quad (\text{A.2})$$

Applying this identity to U and U^\dagger , we obtain:

$$\rho' = [\cos(\alpha/4)\mathbb{1} - i \sin(\alpha/4)(2S_a \otimes 2I_m)] (S_b \otimes I_n) [\cos(\alpha/4)\mathbb{1} + i \sin(\alpha/4)(2S_a \otimes 2I_m)] \quad (\text{A.3})$$

We now multiply out the right part of the equation and use the mixed-product property $(A \otimes B)(C \otimes D) = (AC) \otimes (BD)$:

$$\rho' = [\cos(\alpha/4)\mathbb{1} - i \sin(\alpha/4)(2S_a \otimes 2I_m)] [\cos(\alpha/4)(S_b \otimes I_n) + 4i \sin(\alpha/4)(S_b S_a) \otimes (I_n I_m)] \quad (\text{A.4})$$

Now we additionally multiply out the left part of the equation to obtain:

$$\begin{aligned} \rho' = & \cos(\alpha/4)^2 (S_b \otimes I_n) + 4i \cos(\alpha/4) \sin(\alpha/4) (S_b S_a) \otimes (I_n I_m) \\ & - 4i \cos(\alpha/4) \sin(\alpha/4) (S_a S_b) \otimes (I_m I_n) + 16 \sin(\alpha/4)^2 (S_a S_b S_a) \otimes (I_m I_n I_m). \end{aligned} \quad (\text{A.5})$$

In chapter 3, we will compute the effect of parts of a given pulse sequence on two-spin systems using the relation that we have just derived. We will in particular discuss the most important NMR spectroscopy techniques that provide the basis for the nuclear spin imaging experiments discussed in Chapter 6 and 7.

Nuclear precession in tilted magnetic fields

Here, we derive the shift in the hyperfine coupling constants due to a tilted external quantization field in second-order perturbation theory and obtain equation 6.6 in chapter 6. The derivation follows the description in [193].

B.0.1 Definition of Hamilton operators

We consider the following Hamilton operator of a coupled spin-system consisting of the sensor spin ($S = 1$) and a single nuclear spin ($I = 1/2$):

$$H = DS_z^2 - \gamma_e \vec{B}_0 \cdot \vec{S} - \gamma_n \vec{B}_0 \cdot \vec{I} - \vec{I} \cdot (\mathbf{A}) \cdot \vec{S} \quad (\text{B.1})$$

and separate it into a pseudo-secular term (H_0) and the perturbation (V):

$$H_0 = DS_z^2 - \gamma_e B_z S_z - \gamma_n \vec{B}_0 \cdot \vec{I} - \vec{I} \vec{A}_z \cdot S_z \quad (\text{B.2})$$

$$V = -\gamma_e (B_x S_x + B_y S_y) + (I_x A_{xx} + I_y A_{yx} + I_z A_{zx}) S_x + (I_x A_{xy} + I_y A_{yy} + I_z A_{zy}) S_y \quad (\text{B.3})$$

$$= -\gamma_e (B_x S_x + B_y S_y) + (\vec{A}_x \vec{I}) S_x + (\vec{A}_y \vec{I}) S_y, \quad (\text{B.4})$$

where we defined $\vec{A}_x = (A_{xx}, A_{yx}, A_{zx})$ and $\vec{A}_y = (A_{xy}, A_{yy}, A_{zy})$. We further denote the six eigenstates of H_0 as $|\psi_i\rangle = |-1, \{\downarrow, \uparrow\}\rangle, |0, \{\downarrow, \uparrow\}\rangle, |1, \{\downarrow, \uparrow\}\rangle$.

B.0.2 Perturbation theory up to second order and for $D \gg B_z$

Here, we only calculate the correction of the energy eigenvalues due to V and do not construct the perturbed eigenstates. The theoretical background is described in the literature [193]. We first note, that the first-order perturbative correction of the energy eigenstates is given by $E_i^{(1)} = \langle \psi_i | V | \psi_i \rangle$. This expression vanishes for all six eigenstates of H_0 , because $\langle \psi_i | S_x | \psi_i \rangle = 0$ and $\langle \psi_i | S_y | \psi_i \rangle = 0$, as the eigenstates $|\psi_i\rangle$ of H_0 are eigenstates of S_z .

The second-order correction of the eigenstates of H_0 due to V is given by:

$$E_i^{(2)} = \langle \psi_i | V Q \frac{1}{E_i^{(0)} - H_0} Q V | \psi_i \rangle, \quad (\text{B.5})$$

with $Q = \mathbf{1} - |\tau_i\rangle\langle\tau_i|$. First, we now consider the correction to the state $\psi_i = |0, \{\downarrow, \uparrow\}\rangle$. To simplify the calculation, we drop the nuclear quantum state in the notation and work with the electronic eigenstates only: $|0\rangle$. Due to the completeness of Hilbert space, we may write:

$$Q = \mathbf{1} - |0\rangle\langle 0| = |-1\rangle\langle -1| + |1\rangle\langle 1|, \quad (\text{B.6})$$

which gives the following correction of the $m_s = 0$ state:

$$E_0^{(2)} = \frac{\langle 0|V|-1\rangle\langle -1|V|0\rangle}{E_0^{(0)} - E_{-1}^{(0)}} + \frac{\langle 0|V|1\rangle\langle 1|V|0\rangle}{E_0^{(0)} - E_1^{(0)}}, \quad (\text{B.7})$$

with $E_0^{(0)} - E_{-1}^{(0)} = -D \pm \gamma_e B_z$. Further, we use the following relations of spin-1 operators to simplify the expression given above:

$$\langle 1|S_x|0\rangle = \frac{1}{\sqrt{2}} \quad \langle 1|S_y|0\rangle = \frac{-1}{\sqrt{2}i} \quad \langle -1|S_x|0\rangle = \frac{1}{\sqrt{2}} \quad \langle -1|S_y|0\rangle = \frac{1}{\sqrt{2}i}. \quad (\text{B.8})$$

Using these expressions we obtain:

$$\langle 0|V|-1\rangle = -\frac{1}{\sqrt{2}}(\gamma_e(B_x - iB_y) + (\vec{A}_x - i\vec{A}_y) \cdot \vec{I}) \quad (\text{B.9})$$

$$\langle 0|V|1\rangle = -\frac{1}{\sqrt{2}}(\gamma_e(B_x + iB_y) + (\vec{A}_x + i\vec{A}_y) \cdot \vec{I}) \quad (\text{B.10})$$

We now consider $\langle 0|V|-1\rangle\langle -1|V|0\rangle$ and keep only terms that are at least linear in $\gamma_e B_x, \gamma_e B_y$, as $\gamma_e B_x, \gamma_e B_y \gg A_{ij}$:

$$\langle 0|V|-1\rangle\langle -1|V|0\rangle = -\frac{1}{2}(\gamma_e^2 B_x^2 + \gamma_e^2 B_y^2 + 2\gamma_e B_x(\vec{A}_x + \vec{A}_y) \cdot \vec{I} + 2\gamma_e B_y(\vec{A}_x + \vec{A}_y) \cdot \vec{I}), \quad (\text{B.11})$$

and note that:

$$\langle 0|V|1\rangle\langle 1|V|0\rangle = \langle 0|V|-1\rangle\langle -1|V|0\rangle. \quad (\text{B.12})$$

Inserting these expressions into equation B.7 and approximating $-D \pm \gamma_e B_z \approx -D$, we obtain:

$$E_0^{(2)} = \frac{\gamma_e^2 B_x^2 + \gamma_e^2 B_y^2 + 2\gamma_e B_x(\vec{A}_x + \vec{A}_y) \cdot \vec{I} + 2\gamma_e B_y(\vec{A}_x + \vec{A}_y) \cdot \vec{I}}{D} \quad (\text{B.13})$$

$$= \frac{\gamma_e B_x}{D} \gamma_e B_x + \frac{\gamma_e B_y}{D} \gamma_e B_y + \frac{2\gamma_e B_x(\vec{A}_x + \vec{A}_y) \cdot \vec{I} + 2\gamma_e B_y(\vec{A}_x + \vec{A}_y) \cdot \vec{I}}{D} \quad (\text{B.14})$$

The first two terms correspond to the energy shift of the NV electron spin, due to the perpendicular field and the third term corresponds to the enhancement formula for the gyromagnetic ratio of the nuclear spin.

For the $m_s = \pm 1$ - state, we obtain for the correction of the energy eigenstates:

$$E_{\pm 1}^{(2)} = \frac{\langle \pm 1|V|0\rangle\langle 0|V|\pm 1\rangle}{E_{\pm 1}^{(0)} - E_0^{(0)}}. \quad (\text{B.15})$$

as a consequence, we obtain in this case $E_0^{(2)} = -2 \cdot E_{\pm 1}^{(2)}$. Finally, we give the generalized formula (for any of the m_s -states) for the enhanced gyromagnetic ratio of the nuclear spin, as given in chapter 6 in 6.6:

$$\alpha(m_s) = (3|m_s| - 2) \frac{\gamma_e}{\gamma_n D} \begin{pmatrix} A_{xx} & A_{xy} & A_{xz} \\ A_{yx} & A_{yy} & A_{yz} \\ 0 & 0 & 0 \end{pmatrix}. \quad (\text{B.16})$$



Sensitivity and transfer function of the differential echo sequence

C.1 Transfer function and response time

We derive the expression for rise time τ and the transfer function shown by a dashed line in Fig. 8.2(d). The probability function p of the sensor in the small signal limit $\phi \ll 1$ is according to Eq. (2) of the main text given by

$$p \approx \frac{1}{2}(1 + \phi). \quad (8.2)$$

The total phase accumulated over one cycle of the differential echo sequence is given by

$$\phi(t) = \int_0^{2t_{\text{rep}}} \gamma_e B(t') M(t, t') dt', \quad (C.1)$$

where t_{rep} is the repetition time of the waveform and $M(t, t')$ is the modulation function [22] of the sensing sequence, defined below. Because the waveform function is repetitive, $B(t' + t_{\text{rep}}) = B(t')$, we can rewrite Eq. (C.1) as

$$\phi(t) = \int_0^{t_{\text{rep}}} \gamma_e B(t') [M_1(t, t') + M_2(t, t')] dt', \quad (C.2)$$

where $M_1(t, t')$ and $M_2(t, t')$ are the modulation functions of the two differential spin echo segments, which both have a duration of t_{rep} . In the case of ideal, short π pulses the modulation functions are given by step functions,

$$M_1(t, t') = \begin{cases} +1 & : t' \leq t \\ -1 & : t' > t, \end{cases} \quad (C.3)$$

$$M_2(t, t') = \begin{cases} -1 & : t' \leq t + t_{\text{int}} \\ +1 & : t' > t + t_{\text{int}}, \end{cases} \quad (C.4)$$

In the case of finite pulse durations, the modulation functions are no longer abrupt step functions, but rather described by the Rabi nutation formula where the value of M is proportional to the z-projection of the qubit. For square π pulses of

duration t_π , the modulation functions are given by

$$M_1(t') = \begin{cases} -1 & : t' \leq t - t_\pi/2 \\ +\sin\left(\frac{[t'-t]}{t_\pi/\pi}\right) & : t - t_\pi/2 < t' \leq t + t_\pi/2 \\ +1 & : t' > t + t_\pi/2, \end{cases} \quad (\text{C.5})$$

$$M_2(t') = \begin{cases} 1 & : t' \leq t + t_{\text{int}} - \frac{t_\pi}{2} \\ -\sin\left(\frac{[t'-t-t_{\text{int}}]}{t_\pi/\pi}\right) & : t + t_{\text{int}} - \frac{t_\pi}{2} < t' \leq t + t_{\text{int}} + \frac{t_\pi}{2} \\ -1 & : t' > t + t_{\text{int}} + \frac{t_\pi}{2}. \end{cases} \quad (\text{C.6})$$

For the general case where $t_{\text{int}} \neq t_\pi$ we estimate the response time τ through a set of numerical simulations of Eqs. (C.1-C.6). We compute the acquired sensor phase for varying t_{int} and t_π for a ideal step input waveform and determine the response time of the sensor output for each pair (t_π, t_{int}) . We find that the response time approximately follows

$$\tau \approx \frac{2}{\pi} \sqrt{t_\pi^2 + \frac{\pi}{2} t_{\text{int}}^2}. \quad (\text{C.7})$$

For the case where $t_{\text{int}} = t_\pi$, the transfer function can be computed analytically. The sum $M \equiv M_1(t, t') + M_2(t, t')$ of the two modulation functions is given by

$$M(t, t') = \begin{cases} 1 + \cos\left(\frac{\pi[t'-t-t_\pi/2]}{t_\pi}\right) & : t - \frac{t_\pi}{2} < t' \leq t + \frac{3t_\pi}{2} \\ 0 & : \text{otherwise} \end{cases} \quad (\text{C.8})$$

The function $M(t, t')$ is equivalent to a Hann function of characteristic duration $2t_\pi$ that is centered at $t' = t + t_\pi/2$. The transfer function of the sensing sequence is thus given by the Fourier transform of the Hann function.

C.2 Sensitivity Analysis

We analyze the sensitivity of the differential echo sequence and compare it with the sensitivity of the Walsh method presented in Ref. [182] and the time-resolved Ramsey method described by Fig. 8.2(c). According to Ref. [183], the Haar wavelet sensing method provides the same sensitivity as the Walsh method.

The reconstructed field $B(t)$ at time t using N measured Walsh coefficients \hat{B}_m is given by [182]:

$$B(t) = \sum_{m=0}^{N-1} \hat{B}_m w_m(t/t_{\text{rep}}). \quad (\text{C.9})$$

Here, $w_m(t/t_{\text{rep}})$ is the m -th Walsh function, which oscillates between ± 1 in the interval $[0, t_{\text{rep}}]$. The minimum resolvable Walsh coefficient per unit time is given by an expression analogous to Eq. (8.6):

$$\hat{B}_{\text{min}} = \frac{\sqrt{t_m + t_{\text{rep}}} \exp(t_{\text{rep}}/T_2)}{\gamma_e C t_{\text{rep}}}. \quad (\text{C.10})$$

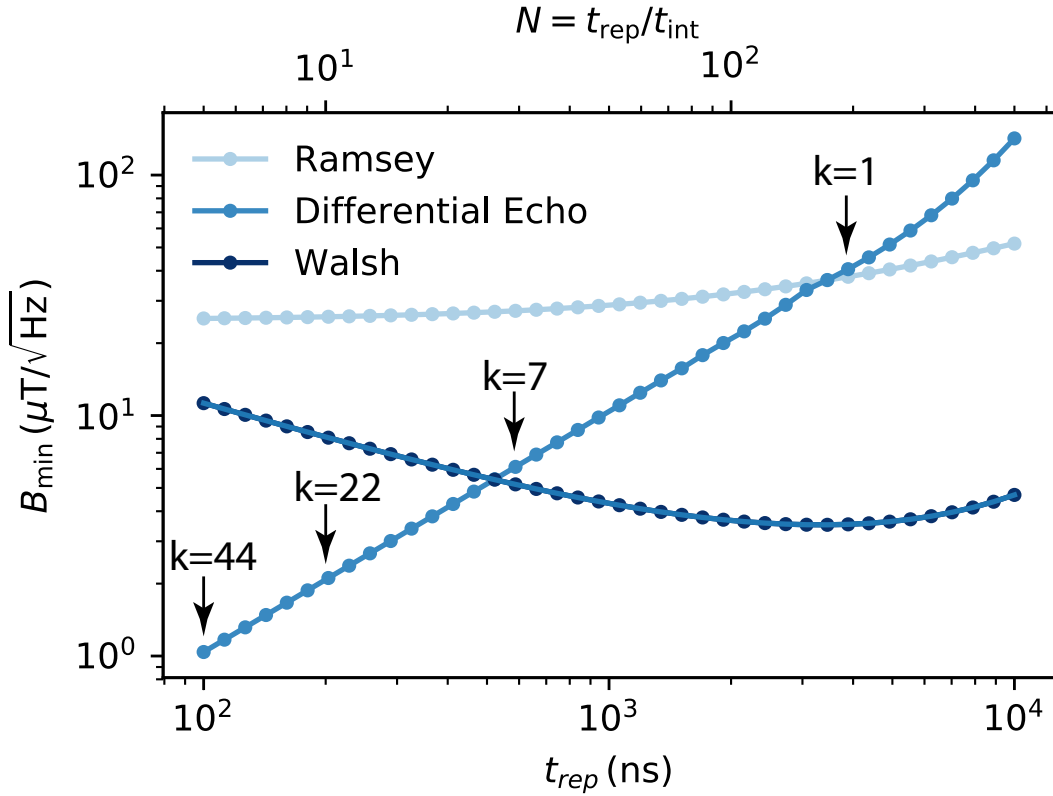


FIGURE C.1: **Minimum detectable field per unit time for different waveform sensing methods.** We plot the minimum detectable field as a function of the waveform duration t_{rep} . We use parameters typical for our experiment, $t_m = 3 \mu\text{s}$, $T_2^* = 1.5 \mu\text{s}$, $T_2 = 14 \mu\text{s}$ and $t_{\text{int}} = 20 \mu\text{s}$. For each t_{rep} , the number of waveform samples is set to $N = t_{\text{rep}}/t_{\text{int}}$ and the repetition factor k of the differential echo sequence is adjusted for optimum sensitivity according to Fig. 8.3(c).

Consequently, the minimum resolvable field at time t , according to error propagation, is given by:

$$\begin{aligned}
 B_{\text{min,Walsh}} &= \sqrt{\sum_{m=0}^{N-1} \hat{B}_{\text{min}}^2} = \sqrt{N} \hat{B}_{\text{min}} \\
 &= \frac{\sqrt{N} \sqrt{t_m + t_{\text{rep}}} \exp(t_{\text{rep}}/T_2)}{\gamma_e C t_{\text{rep}}}.
 \end{aligned} \tag{C.11}$$

This expression can be compared to the minimum resolvable field for the differential echo method, Eq. (8.6):

$$B_{\text{min,Diff}} = \frac{\sqrt{t_m + 2kt_{\text{rep}}} \exp(2kt_{\text{rep}}/T_2)}{\gamma_e C 2kt_{\text{int}}}. \tag{8.6}$$

Finally, for the time-resolved Ramsey method (Fig. 8.1c), the minimum detectable field is given by:

$$B_{\text{min,Ramsey}} = \frac{\sqrt{t_m + t_{\text{rep}}} \exp(t_{\text{int}}/T_2^*)}{\gamma_e C t_{\text{int}}}. \tag{C.12}$$

Note that to build up the full N -point waveform, a total of N measurements are needed for all methods. For the differential echo and Ramsey methods, the waveform is measured point-by-point in the time domain. For the Walsh method, N Walsh coefficients must be measured.

To get an idea of the relative sensitivities of the three methods, we compare the errors for waveform parameters set by $N = t_{\text{rep}}/t_{\text{int}}$ and $k = T_2/(4t_{\text{rep}})$, and disregard dephasing and decoherence. For the differential echo method we find:

$$B_{\text{min,Diff}} \approx \begin{cases} \frac{\sqrt{N}}{k} \left[\frac{T_2}{t_m} \right]^{1/2} B_{\text{min,Walsh}} & \text{for } t_{\text{rep}} \ll t_m, \\ \sqrt{\frac{N}{k}} B_{\text{min,Walsh}} & \text{for } t_{\text{rep}} \gg t_m. \end{cases} \quad (\text{C.13})$$

For the Ramsey method we find:

$$B_{\text{min,Ramsey}} \approx \sqrt{N} B_{\text{min,Walsh}} \quad (\text{C.14})$$

We find that the error of the differential echo sequence is lowest for small N and large k , *i.e.*, for short waveforms and long coherence times.

In Fig. C.1, we plot the minimum detectable field per unit time as function of the duration of the waveform t_{rep} for the parameters used in our experiments. We find that for short waveforms ($t_{\text{rep}} < 400$ ns, as in Figs. 8.2,8.3) the differential echo technique provides the highest sensitivity. For longer waveforms ($t_{\text{rep}} > 1$ μ s, as in Fig. 8.4) the Walsh method is superior in sensitivity. The sensitivity of the time-resolved Ramsey sequence is inferior to both sensing methods for the waveform durations considered in this work.

Bibliography

- [1] M. Planck. “Ueber das Gesetz der Energieverteilung im Normalspectrum”. In: *Annalen der Physik* 309 (1901), pp. 553–563. DOI: [10.1002/andp.19013090310](https://doi.org/10.1002/andp.19013090310).
- [2] A. Einstein. “Über einen die Erzeugung und Verwandlung des Lichtes betreffenden heuristischen Gesichtspunkt”. In: *Annalen der Physik* 322 (1905), pp. 132–148. DOI: [10.1002/andp.19053220607](https://doi.org/10.1002/andp.19053220607).
- [3] N. Bohr. “On the Constitutions of Atoms and Molecules. Pt. I.” In: *Philosophical Magazine* 26 (Dec. 1913), pp. 1–25. DOI: [10.1080/14786441308634955](https://doi.org/10.1080/14786441308634955).
- [4] W. Heisenberg. “Über quantentheoretische Umdeutung kinematischer und mechanischer Beziehungen”. In: *Zeitschrift f. Physik* 33 (19225), pp. 879–893.
- [5] E. Schrödinger. “Quantisierung als Eigenwertproblem”. In: *Annalen der Physik* 384 (1926), pp. 361–376. DOI: [10.1002/andp.19263840404](https://doi.org/10.1002/andp.19263840404).
- [6] Alain Aspect, Jean Dalibard, and Gérard Roger. “Experimental Test of Bell’s Inequalities Using Time-Varying Analyzers”. In: *Phys. Rev. Lett.* 49 (25 1982), pp. 1804–1807. DOI: [10.1103/PhysRevLett.49.1804](https://doi.org/10.1103/PhysRevLett.49.1804). URL: <https://link.aps.org/doi/10.1103/PhysRevLett.49.1804>.
- [7] Alain Aspect, Philippe Grangier, and Gérard Roger. “Experimental Realization of Einstein-Podolsky-Rosen-Bohm Gedankenexperiment: A New Violation of Bell’s Inequalities”. In: *Phys. Rev. Lett.* 49 (2 1982), pp. 91–94. DOI: [10.1103/PhysRevLett.49.91](https://doi.org/10.1103/PhysRevLett.49.91). URL: <https://link.aps.org/doi/10.1103/PhysRevLett.49.91>.
- [8] Gregor Weihs et al. “Violation of Bell’s Inequality under Strict Einstein Locality Conditions”. In: *Phys. Rev. Lett.* 81 (23 1998), pp. 5039–5043. DOI: [10.1103/PhysRevLett.81.5039](https://doi.org/10.1103/PhysRevLett.81.5039). URL: <https://link.aps.org/doi/10.1103/PhysRevLett.81.5039>.
- [9] Vincent Jacques et al. “Experimental Realization of Wheeler’s Delayed-Choice Gedanken Experiment”. In: *Science* 315.5814 (Feb. 2007), p. 966. DOI: [10.1126/science.1136303](https://doi.org/10.1126/science.1136303). URL: <http://science.sciencemag.org/content/315/5814/966.abstract>.
- [10] B. Hensen et al. “Loophole-free bell inequality violation using electron spins separated by 1.3 kilometres”. In: *Nature* 526 (2015). DOI: [10.1038/nature15759](https://doi.org/10.1038/nature15759). URL: <http://dx.doi.org/10.1038/nature15759>.
- [11] D. P. Divincenzo. “The physical implementation of quantum computation”. In: *Fortschritte der Physik* 48 (2000), pp. 771–783. URL: [http://dx.doi.org/10.1002/1521-3978\(200009\)48:9/11<771::AID-PROP771>3.0.CO;2-E](http://dx.doi.org/10.1002/1521-3978(200009)48:9/11<771::AID-PROP771>3.0.CO;2-E).
- [12] L. M. K. Vandersypen et al. “Experimental realization of shor’s quantum factoring algorithm using nuclear magnetic resonance”. In: *Nature* 414 (2001), pp. 883–887. DOI: [10.1038/414883a](https://doi.org/10.1038/414883a). URL: <http://dx.doi.org/10.1038/414883a>.

- [13] John Preskill. “Quantum Computing in the NISQ era and beyond”. In: *Quantum* 2 (Aug. 2018), p. 79. ISSN: 2521-327X. DOI: [10.22331/q-2018-08-06-79](https://doi.org/10.22331/q-2018-08-06-79). URL: <https://doi.org/10.22331/q-2018-08-06-79>.
- [14] Charles H. Bennett et al. “Experimental quantum cryptography”. In: *Journal of Cryptology* 5.1 (1992), pp. 3–28. ISSN: 1432-1378. DOI: [10.1007/BF00191318](https://doi.org/10.1007/BF00191318). URL: <https://doi.org/10.1007/BF00191318>.
- [15] H. J. Kimble. “The quantum internet”. In: *Nature* 453 (June 2008), 1023 EP –. URL: <https://doi.org/10.1038/nature07127>.
- [16] Juan Yin et al. “Satellite-based entanglement distribution over 1200 kilometers”. In: *Science* 356.6343 (2017), pp. 1140–1144. ISSN: 0036-8075. DOI: [10.1126/science.aan3211](https://doi.org/10.1126/science.aan3211). eprint: <https://science.sciencemag.org/content/356/6343/1140.full.pdf>. URL: <https://science.sciencemag.org/content/356/6343/1140>.
- [17] V. Giovannetti, S. Lloyd, and L. Maccone. “Quantum-enhanced measurements: beating the standard quantum limit”. In: *Science* 306 (2004), p. 1330. DOI: [10.1126/science.1104149](https://doi.org/10.1126/science.1104149).
- [18] V. Giovannetti, S. Lloyd, and L. Maccone. “Quantum metrology”. In: *Phys. Rev. Lett.* 96 (2006), p. 010401. DOI: [10.1103/PhysRevLett.96.010401](https://doi.org/10.1103/PhysRevLett.96.010401).
- [19] D. Budker and M. Romalis. “Optical magnetometry”. In: *Nat. Phys.* 3, 227 (2007), p. 227. DOI: [10.1038/nphys566](https://doi.org/10.1038/nphys566). URL: <http://dx.doi.org/10.1038/nphys566>.
- [20] G. Balasubramanian et al. “Nanoscale imaging magnetometry with diamond spins under ambient conditions”. In: *Nature* 455, 648 (2008), p. 648. DOI: [10.1038/nature07278](https://doi.org/10.1038/nature07278). URL: <http://dx.doi.org/10.1038/nature07278>.
- [21] V. Giovannetti, S. Lloyd, and L. Maccone. “Advances in quantum metrology”. In: *Nature Photonics* 5 (2011), pp. 222–229. DOI: [10.1038/NPHOTON.2011.35](https://doi.org/10.1038/NPHOTON.2011.35).
- [22] C. Degen, F. Reinhard, and P. Cappellaro. “Quantum sensing”. In: *Rev. Mod. Phys.* 89 (2017), p. 035002. DOI: [10.1103/RevModPhys.89.035002](https://doi.org/10.1103/RevModPhys.89.035002). URL: <https://link.aps.org/doi/10.1103/RevModPhys.89.035002>.
- [23] P. Shor. “Polynomial-Time Algorithms for Prime Factorization and Discrete Logarithms on a Quantum Computer”. In: *SIAM Journal on Computing* 26.5 (1997), pp. 1484–1509. DOI: [10.1137/S0097539795293172](https://doi.org/10.1137/S0097539795293172). eprint: <https://doi.org/10.1137/S0097539795293172>. URL: <https://doi.org/10.1137/S0097539795293172>.
- [24] J. R. Maze et al. “Nanoscale magnetic sensing with an individual electronic spin in diamond”. In: *Nature* 455, 644 (2008), p. 644. DOI: [10.1038/nature07279](https://doi.org/10.1038/nature07279). URL: <http://dx.doi.org/10.1038/nature07279>.
- [25] C. L. Degen. “Scanning magnetic field microscope with a diamond single-spin sensor”. In: *Appl. Phys. Lett.* 92, 243111 (2008), p. 243111. DOI: [10.1063/1.2943282](https://doi.org/10.1063/1.2943282). URL: <http://dx.doi.org/10.1063/1.2943282>.
- [26] T. Haberle et al. “Nanoscale nuclear magnetic imaging with chemical contrast”. In: *Nature Nano.* 10 (2015), pp. 125–128. DOI: [10.1038/nnano.2014.299](https://doi.org/10.1038/nnano.2014.299). URL: <http://dx.doi.org/10.1038/nnano.2014.299>.
- [27] A. Laraoui et al. “Imaging thermal conductivity with nanoscale resolution using a scanning spin probe”. In: *Nat. Commun.* 6 (2015), p. 8954. DOI: [10.1038/ncomms9954](https://doi.org/10.1038/ncomms9954).

- [28] K. Chang et al. "Nanoscale imaging of current density with a single-spin magnetometer". In: *Nano Letters* 17 (2017), p. 2367. DOI: [10.1021/acs.nanolett.6b05304](https://doi.org/10.1021/acs.nanolett.6b05304).
- [29] B. J. Bloom et al. "An optical lattice clock with accuracy and stability at the 1e-18 level". In: *Nature* 506 (2014), pp. 71–75. DOI: [10.1038/nature12941](https://doi.org/10.1038/nature12941). URL: <http://dx.doi.org/10.1038/nature12941>.
- [30] T. L. Nicholson et al. "Systematic evaluation of an atomic clock at 2×10^{-18} total uncertainty". In: *Nature Communications* 6 (2015), p. 6896. DOI: [10.1038/ncomms7896](https://doi.org/10.1038/ncomms7896).
- [31] S. A. Diddams et al. "An Optical Clock Based on a Single Trapped $^{199}\text{Hg}^+$ Ion". In: *Science* 293.5531 (2001), pp. 825–828. ISSN: 0036-8075. DOI: [10.1126/science.1061171](https://doi.org/10.1126/science.1061171). eprint: <https://science.sciencemag.org/content/293/5531/825.full.pdf>. URL: <https://science.sciencemag.org/content/293/5531/825>.
- [32] T. Rosenband et al. "Frequency ratio of Al^+ and Hg^+ single-ion optical clocks; Metrology at the 17th decimal place". In: *Science* 319 (2008), pp. 1808–1812. DOI: [10.1126/science.1154622](https://doi.org/10.1126/science.1154622).
- [33] N. Huntemann et al. "Single-Ion Atomic Clock with 3×10^{-18} Systematic Uncertainty". In: *Phys. Rev. Lett.* 116 (6 2016), p. 063001. DOI: [10.1103/PhysRevLett.116.063001](https://doi.org/10.1103/PhysRevLett.116.063001). URL: <https://link.aps.org/doi/10.1103/PhysRevLett.116.063001>.
- [34] M. Kastner. "Artificial Atoms". In: *Physics Today* 46.1 (1993), p. 24.
- [35] R. Schirhagl et al. "Nitrogen-vacancy centers in diamond: Nanoscale sensors for physics and biology". In: *Annu. Rev. Phys. Chem.* 65 (2014), p. 83. DOI: [10.1146/annurev-physchem-040513-103659](https://doi.org/10.1146/annurev-physchem-040513-103659). URL: <http://dx.doi.org/10.1146/annurev-physchem-040513-103659>.
- [36] L. Rondin et al. "Magnetometry with nitrogen-vacancy defects in diamond". In: *Rep. Prog. Phys.* 77 (2014), p. 056503. DOI: [10.1088/0034-4885/77/5/056503](https://doi.org/10.1088/0034-4885/77/5/056503).
- [37] J. Meijer et al. "Generation of single color centers by focused nitrogen implantation". In: *Appl. Phys. Lett.* 87 (2005), p. 261909. DOI: [10.1063/1.2103389](https://doi.org/10.1063/1.2103389).
- [38] G. Kucsko et al. "Nanometre-scale thermometry in a living cell". In: *Nature* 500 (2013), pp. 54–58. DOI: [10.1038/nature12373](https://doi.org/10.1038/nature12373). URL: <http://dx.doi.org/10.1038/nature12373>.
- [39] M. W. Doherty et al. "The nitrogen-vacancy colour centre in diamond". In: *Physics Reports* 528 (2013), pp. 1–45. URL: <http://www.sciencedirect.com/science/article/pii/S0370157313000562>.
- [40] F. Dolde et al. "Electric-field sensing using single diamond spins". In: *Nat. Phys.* 7 (2011), pp. 459–463. DOI: [10.1038/NPHYS1969](https://doi.org/10.1038/NPHYS1969).
- [41] P. Zeeman. *Ueber einen Einfluss der Magnetisierung auf die Natur des von einer Substanz emittirten Lichtes*. Verhandlungen der Physikalischen Gesellschaft zu Berlin, 1896.
- [42] B. M. Chernobrod and G. P. Berman. "Spin microscope based on optically detected magnetic resonance". In: *J. Appl. Phys.* 97, 014903 (2005), p. 014903. DOI: [10.1063/1.1829373](https://doi.org/10.1063/1.1829373). URL: <http://dx.doi.org/10.1063/1.1829373>.

- [43] G. P. Berman et al. "Measurement of single electron and nuclear spin states based on optically detected magnetic resonance". In: *J. Phys.: Conf. Ser.* 38, 167 (2006), p. 167. DOI: [10.1088/1742-6596/38/1/040](https://doi.org/10.1088/1742-6596/38/1/040). URL: <http://dx.doi.org/10.1088/1742-6596/38/1/040>.
- [44] L. Rondin et al. "Nanoscale magnetic field mapping with a single spin scanning probe magnetometer". In: *Appl. Phys. Lett.* 100 (2012), p. 153118. DOI: [10.1063/1.3703128](https://doi.org/10.1063/1.3703128).
- [45] P. Maletinsky et al. "A robust scanning diamond sensor for nanoscale imaging with single nitrogen-vacancy centres". In: *Nat. Nanotechnol.* 7 (2012), pp. 320–324. DOI: [10.1038/NNANO.2012.50](https://doi.org/10.1038/NNANO.2012.50).
- [46] J. P. Tetienne et al. "Nanoscale imaging and control of domain-wall hopping with a nitrogen-vacancy center microscope". In: *Science* 344 (2014), pp. 1366–1369. DOI: [10.1126/science.1250113](https://doi.org/10.1126/science.1250113).
- [47] J. P. Tetienne et al. "The nature of domain walls in ultrathin ferromagnets revealed by scanning nanomagnetometry". In: *Nat. Commun.* 6 (2015), p. 6733. DOI: [10.1038/ncomms7733](https://doi.org/10.1038/ncomms7733).
- [48] L. Thiel et al. "Quantitative nanoscale vortex imaging using a cryogenic quantum". In: *Nat. Nanotechnol.* 11 (2016), p. 677. DOI: [10.1038/NNANO.2016.63](https://doi.org/10.1038/NNANO.2016.63).
- [49] M. Pelliccione et al. "Scanned probe imaging of nanoscale magnetism at cryogenic temperatures". In: *Nat. Nanotechnol.* 11 (2016), pp. 700–705. DOI: [10.1038/NNANO.2016.68](https://doi.org/10.1038/NNANO.2016.68).
- [50] I. Gross et al. "Real-space imaging of non-collinear antiferromagnetic order with a single-spin magnetometer". In: *Nature* 549 (2017), p. 252. DOI: [10.1038/nature23656](https://doi.org/10.1038/nature23656).
- [51] J. P. Tetienne et al. "Quantum imaging of current flow in graphene". In: *arXiv:1609.09208* (2016). URL: <https://arxiv.org/abs/1609.09208>.
- [52] F. Casola, T. Van der Sar, and A. Yacoby. "Probing condensed matter physics with magnetometry based on nitrogen-vacancy centres in diamond". In: *Nat. Rev. Mat.* 3 (2018), p. 17088. DOI: [10.1038/natrevmats.2017.88](https://doi.org/10.1038/natrevmats.2017.88).
- [53] A. Ajoy et al. "Atomic-scale nuclear spin imaging using quantum-assisted sensors in diamond". In: *Phys. Rev. X* 5 (2015), p. 011001. DOI: [10.1103/PhysRevX.5.011001](https://doi.org/10.1103/PhysRevX.5.011001).
- [54] I. Lovchinsky et al. "Nuclear magnetic resonance detection and spectroscopy of single proteins using quantum logic". In: *Science* 351 (2016), p. 836. DOI: [10.1126/science.aad8022](https://doi.org/10.1126/science.aad8022). URL: <http://science.sciencemag.org/content/351/6275/836.abstract>.
- [55] N. Aslam et al. "Nanoscale nuclear magnetic resonance with chemical resolution". In: *Science* 357 (2017). DOI: [10.1126/science.aam8697](https://doi.org/10.1126/science.aam8697).
- [56] Andrew Horsley et al. "Microwave Device Characterization Using a Wide-field Diamond Microscope". In: *Phys. Rev. Applied* 10 (4 2018), p. 044039. DOI: [10.1103/PhysRevApplied.10.044039](https://doi.org/10.1103/PhysRevApplied.10.044039). URL: <https://link.aps.org/doi/10.1103/PhysRevApplied.10.044039>.
- [57] J. Zopes et al. "Three-Dimensional Nuclear Spin Positioning Using Coherent Radio-Frequency Control". In: *Phys. Rev. Lett.* 121 (17 2018), p. 170801. DOI: [10.1103/PhysRevLett.121.170801](https://doi.org/10.1103/PhysRevLett.121.170801). URL: <https://link.aps.org/doi/10.1103/PhysRevLett.121.170801>.

- [58] A. Gruber et al. "Scanning Confocal Optical Microscopy and Magnetic Resonance on Single Defect Centers". In: *Science* 276, 2012 (1997), p. 2012. DOI: [10.1126/science.276.5321.2012](https://doi.org/10.1126/science.276.5321.2012). URL: <http://dx.doi.org/10.1126/science.276.5321.2012>.
- [59] J H N Loubser and J A van Wyk. "Electron spin resonance in the study of diamond". In: 41.8 (1978), pp. 1201–1248. DOI: [10.1088/0034-4885/41/8/002](https://doi.org/10.1088/0034-4885/41/8/002). URL: <http://dx.doi.org/10.1088/0034-4885/41/8/002>.
- [60] F. Jelezko et al. "Observation of coherent oscillations in a single electron spin". In: *Phys. Rev. Lett.* 92 (2004), p. 076401. DOI: [10.1103/PhysRevLett.92.076401](https://doi.org/10.1103/PhysRevLett.92.076401).
- [61] F. Jelezko et al. "Observation of coherent oscillation of a single nuclear spin and realization of a two-qubit conditional quantum gate". In: *Phys. Rev. Lett.* 93 (13 2004), p. 130501. DOI: [10.1103/PhysRevLett.93.130501](https://doi.org/10.1103/PhysRevLett.93.130501). URL: <https://link.aps.org/doi/10.1103/PhysRevLett.93.130501>.
- [62] G. Balasubramanian et al. "Ultralong spin coherence time in isotopically engineered diamond". In: *Nature Materials* 8 (2009), p. 383. DOI: [10.1038/nmat2420](https://doi.org/10.1038/nmat2420). URL: <http://dx.doi.org/10.1038/nmat2420>.
- [63] C. L. Degen et al. "Nanoscale magnetic resonance imaging". In: *Proc. Nat. Acad. Sci. U.S.A.* 106 (2009), p. 1313. DOI: [10.1073/pnas.0812068106](https://doi.org/10.1073/pnas.0812068106). URL: <http://dx.doi.org/10.1073/pnas.0812068106>.
- [64] T. Staudacher et al. "Enhancing the spin properties of shallow implanted nitrogen vacancy centers in diamond by epitaxial overgrowth". In: *Appl. Phys. Lett.* 101 (2012), p. 212401. DOI: [10.1063/1.4767144](https://doi.org/10.1063/1.4767144).
- [65] F. Shi et al. "Single-protein spin resonance spectroscopy under ambient conditions". In: *Science* 347 (2015), p. 1135. DOI: [10.1126/science.aaa2253](https://doi.org/10.1126/science.aaa2253). URL: <http://science.sciencemag.org/content/347/6226/1135.abstract>.
- [66] E. Togan et al. "Quantum entanglement between an optical photon and a solid-state spin qubit". In: *Nature* 466 (Aug. 2010), 730 EP –. URL: <https://doi.org/10.1038/nature09256>.
- [67] Matthias Pfender et al. "Protecting a Diamond Quantum Memory by Charge State Control". In: *Nano Letters* 17.10 (Oct. 2017), pp. 5931–5937. DOI: [10.1021/acs.nanolett.7b01796](https://doi.org/10.1021/acs.nanolett.7b01796). URL: <https://doi.org/10.1021/acs.nanolett.7b01796>.
- [68] A. Gali, M. Fyta, and E. Kaxiras. "Ab initio supercell calculations on nitrogen-vacancy center in diamond". In: *Phys. Rev. B* 77 (2008), p. 155206. DOI: [10.1103/PhysRevB.77.155206](https://doi.org/10.1103/PhysRevB.77.155206).
- [69] S. Felton et al. "Hyperfine interaction in the ground state of the negatively charged nitrogen vacancy center in diamond". In: *Phys. Rev. B* 79 (2009), p. 075203. DOI: [10.1103/PhysRevB.79.075203](https://doi.org/10.1103/PhysRevB.79.075203). URL: <http://link.aps.org/doi/10.1103/PhysRevB.79.075203>.
- [70] Peter J. Mohr, David B. Newell, and Barry N. Taylor. "CODATA recommended values of the fundamental physical constants: 2014". In: *Rev. Mod. Phys.* 88 (3 2016), p. 035009. DOI: [10.1103/RevModPhys.88.035009](https://doi.org/10.1103/RevModPhys.88.035009). URL: <https://link.aps.org/doi/10.1103/RevModPhys.88.035009>.

- [71] G. D. Fuchs et al. "Excited-State Spectroscopy Using Single Spin Manipulation in Diamond". In: *Phys. Rev. Lett.* 101 (11 2008), p. 117601. DOI: [10.1103/PhysRevLett.101.117601](https://doi.org/10.1103/PhysRevLett.101.117601). URL: <https://link.aps.org/doi/10.1103/PhysRevLett.101.117601>.
- [72] S. Zaiser et al. "Enhancing quantum sensing sensitivity by a quantum memory". In: *Nature Communications* 7 (2016), p. 12279. DOI: [10.1038/ncomms12279](https://doi.org/10.1038/ncomms12279). URL: <http://dx.doi.org/10.1038/ncomms12279>.
- [73] T. Rosskopf et al. "A quantum spectrum analyzer enhanced by a nuclear spin memory". In: *NPJ Quantum Information* 3 (2017), p. 33. DOI: [10.1038/s41534-017-0030-6](https://doi.org/10.1038/s41534-017-0030-6). URL: <http://www.nature.com/articles/s41534-017-0030-6>.
- [74] J. M. Boss et al. "Quantum sensing with arbitrary frequency resolution". In: *Science* 356.6340 (2017), pp. 837–840. DOI: [10.1126/science.aam7009](https://doi.org/10.1126/science.aam7009).
- [75] T. Staudacher et al. "Nuclear magnetic resonance spectroscopy on a (5-nanometer)(3) sample". In: *Science* 339 (2013), pp. 561–563. DOI: [10.1126/science.1231675](https://doi.org/10.1126/science.1231675).
- [76] M. Loretz et al. "Nanoscale nuclear magnetic resonance with a 1.9-nm-deep nitrogen-vacancy sensor". In: *Appl. Phys. Lett.* 104 (2014), p. 033102. DOI: [10.1063/1.4862749](https://doi.org/10.1063/1.4862749). URL: <http://dx.doi.org/10.1063/1.4862749>.
- [77] J. M. Boss et al. "One- and two-dimensional nuclear magnetic resonance spectroscopy with a diamond quantum sensor". In: *Phys. Rev. Lett.* 116 (2016), p. 197601. DOI: [10.1103/PhysRevLett.116.197601](https://doi.org/10.1103/PhysRevLett.116.197601).
- [78] J. Zopes et al. "High resolution quantum sensing with shaped control pulses". In: *arXiv:1705.07968* (2017). URL: <https://arxiv.org/abs/1705.07968>.
- [79] T. Rosskopf. "Advanced quantum sensing using nitrogen vacancy centers in diamond". PhD thesis. ETH Zurich, 2016.
- [80] H. J. Mamin et al. "Nanoscale nuclear magnetic resonance with a nitrogen-vacancy spin sensor". In: *Science* 339 (2013), pp. 557–560. DOI: [10.1126/science.1231540](https://doi.org/10.1126/science.1231540).
- [81] V. Jacques et al. "Dynamic polarization of single nuclear spins by optical pumping of nitrogen-vacancy color centers in diamond at room temperature". In: *Phys. Rev. Lett.* 102 (2009), p. 057403. DOI: [10.1103/PhysRevLett.102.057403](https://doi.org/10.1103/PhysRevLett.102.057403).
- [82] T. Rosskopf et al. "Investigation of surface magnetic noise by shallow spins in diamond". In: *Phys. Rev. Lett.* 112 (2014), p. 147602. DOI: [10.1103/PhysRevLett.112.147602](https://doi.org/10.1103/PhysRevLett.112.147602). URL: <http://link.aps.org/doi/10.1103/PhysRevLett.112.147602>.
- [83] B. A. Myers et al. "Probing surface noise with depth-calibrated spins in diamond". In: *Phys. Rev. Lett.* 113 (2014), p. 027602. DOI: [10.1103/PhysRevLett.113.027602](https://doi.org/10.1103/PhysRevLett.113.027602). URL: <http://link.aps.org/doi/10.1103/PhysRevLett.113.027602>.
- [84] Y. Romach et al. "Spectroscopy of surface-induced noise using shallow spins in diamond". In: *Phys. Rev. Lett.* 114 (2015), p. 017601. DOI: [10.1103/PhysRevLett.114.017601](https://doi.org/10.1103/PhysRevLett.114.017601). URL: <http://link.aps.org/doi/10.1103/PhysRevLett.114.017601>.
- [85] M. Kim et al. "Decoherence of near-surface nitrogen-vacancy centers due to electric field noise". In: *Phys. Rev. Lett.* 115 (2015), p. 087602. DOI: [10.1103/PhysRevLett.115.087602](https://doi.org/10.1103/PhysRevLett.115.087602). URL: <http://link.aps.org/doi/10.1103/PhysRevLett.115.087602>.

- [86] T. H. Taminiau et al. "Universal control and error correction in multi-qubit spin registers in diamond". In: *Nature Nano.* 9 (2014), p. 171. DOI: [10.1038/nnano.2014.2](https://doi.org/10.1038/nnano.2014.2).
- [87] A. Jarmola et al. "Temperature- and magnetic-field-dependent longitudinal spin relaxation in nitrogen-vacancy ensembles in diamond". In: *Phys. Rev. Lett.* 108 (2012), p. 197601. DOI: [10.1103/PhysRevLett.108.197601](https://doi.org/10.1103/PhysRevLett.108.197601).
- [88] M. H. Abobeih et al. "One-second coherence for a single electron spin coupled to a multi-qubit nuclear-spin environment". In: *Nature Communications* 9 (2018), p. 2552. DOI: [10.1038/s41467-018-04916-z](https://doi.org/10.1038/s41467-018-04916-z). URL: <https://doi.org/10.1038/s41467-018-04916-z>.
- [89] T. H. Taminiau et al. "Detection and control of individual nuclear spins using a weakly coupled electron spin". In: *Phys. Rev. Lett.* 109 (2012), p. 137602. DOI: [10.1103/PhysRevLett.109.137602](https://doi.org/10.1103/PhysRevLett.109.137602).
- [90] A. Laraoui et al. "High-resolution correlation spectroscopy of C-13 spins near a nitrogen-vacancy centre in diamond". In: *Nature Commun.* 4 (2013), p. 1651. DOI: [10.1038/ncomms2685](https://doi.org/10.1038/ncomms2685).
- [91] C. P. Slichter. *Principles of Magnetic Resonance, 3rd edition*. Berlin: Springer, 1990.
- [92] B. Smeltzer, L. Childress, and A. Gali. "¹³C hyperfine interactions in the nitrogen-vacancy centre in diamond". In: *New Journal of Physics* 13 (2011), p. 025021. DOI: [10.1088/1367-2630/13/2/025021](https://doi.org/10.1088/1367-2630/13/2/025021). URL: <http://stacks.iop.org/1367-2630/13/i=2/a=025021>.
- [93] H. Y. Carr and E. M. Purcell. "Effects of diffusion on free precession in nuclear magnetic resonance experiments". In: *Phys. Rev.* 94 (1954), pp. 630–638. DOI: [10.1103/PhysRev.94.630](https://doi.org/10.1103/PhysRev.94.630). URL: <http://link.aps.org/doi/10.1103/PhysRev.94.630>.
- [94] M. Loretz et al. "Spurious harmonic response of multipulse quantum sensing sequences". In: *Phys. Rev. X* 5 (2015), p. 21009. DOI: [10.1103/PhysRevX.5.021009](https://doi.org/10.1103/PhysRevX.5.021009). URL: <http://dx.doi.org/10.1103/PhysRevX.5.021009>.
- [95] S. Schmitt et al. "Submillihertz magnetic spectroscopy performed with a nanoscale quantum sensor". In: *Science* 356 (2017), p. 832. DOI: [10.1126/science.aam5532](https://doi.org/10.1126/science.aam5532).
- [96] M. S. Grinolds et al. "Subnanometre resolution in three-dimensional magnetic resonance imaging of individual dark spins". In: *Nat. Nano.* 9 (2014), pp. 279–284. DOI: [10.1038/NNANO.2014.30](https://doi.org/10.1038/NNANO.2014.30).
- [97] J. M. Boss. "High-resolution magnetic field spectroscopy with nitrogen-vacancy centers in diamond". In: *Diss. ETH, in press* (2018).
- [98] K. Herb. "Active manipulation and quantum sensing of nuclear spins in diamond". MA thesis. ETH Zurich, 2018.
- [99] K. S. Cujia et al. "Watching the precession of a single nuclear spin by weak measurements". In: *arXiv:1806.08243* (2018). URL: <https://arxiv.org/abs/1806.08243>.
- [100] P. C. Maurer et al. "Room-temperature quantum bit memory exceeding one second". In: *Science* 336 (2012), pp. 1283–1286. DOI: [10.1126/science.1220513](https://doi.org/10.1126/science.1220513).
- [101] M. Loretz. "Diamond-based nanoscale nuclear magnetic resonance". In: *Diss. ETH* (2015).

- [102] N. V. Hauff. "Development of a Nanoscale Electron Spin Resonance Platform Based on a Diamond Chip". In: *Master's Thesis* (2018).
- [103] S. Pezzagna et al. "Creation efficiency of nitrogen-vacancy centres in diamond". In: *New J. Phys.* 12 (2010), p. 065017. DOI: [10.1088/1367-2630/12/6/065017](https://doi.org/10.1088/1367-2630/12/6/065017).
- [104] T. Unden et al. "Coherent control of solid state nuclear spin nano-ensembles". In: *npj Quantum Information* 4 (2018), p. 39. DOI: [10.1038/s41534-018-0089-8](https://doi.org/10.1038/s41534-018-0089-8). URL: <https://doi.org/10.1038/s41534-018-0089-8>.
- [105] H. R. Phillip and E. A. Taft. "Kramers-Kronig Analysis of Reflectance Data for Diamond". In: *Phys. Rev.* 136 (5A 1964), A1445–A1448. DOI: [10.1103/PhysRev.136.A1445](https://link.aps.org/doi/10.1103/PhysRev.136.A1445). URL: <https://link.aps.org/doi/10.1103/PhysRev.136.A1445>.
- [106] S. A. Momenzadeh et al. "Nanoengineered diamond waveguide as a robust bright platform for nanomagnetometry using shallow nitrogen vacancy centers". In: *Nano Letters* 15 (2015), pp. 165–169. DOI: [10.1021/nl503326t](https://doi.org/10.1021/nl503326t). URL: <http://dx.doi.org/10.1021/nl503326t>.
- [107] R. J. Epstein et al. "Anisotropic interactions of a single spin and dark-spin spectroscopy in diamond". In: *Nat. Phys.* 1, 94 (2005), p. 94. DOI: [10.1038/nphys141](https://doi.org/10.1038/nphys141). URL: <http://dx.doi.org/10.1038/nphys141>.
- [108] G. D. Fuchs et al. "Gigahertz dynamics of a strongly driven single quantum spin". In: *Science* 326 (2009), pp. 1520–1522. DOI: [10.1126/science.1181193](https://doi.org/10.1126/science.1181193).
- [109] S. Kolkowitz et al. "Probing Johnson noise and ballistic transport in normal metals with a single-spin qubit". In: *Science* 347 (2015), p. 1129. DOI: [10.1126/science.aaa4298](https://doi.org/10.1126/science.aaa4298). URL: <http://science.sciencemag.org/content/347/6226/1129.abstract>.
- [110] C. L. Degen. Private Communication.
- [111] Gareth A. Morris and Ray Freeman. "Enhancement of nuclear magnetic resonance signals by polarization transfer". In: *Journal of the American Chemical Society* 101.3 (1979), pp. 760–762. DOI: [10.1021/ja00497a058](https://doi.org/10.1021/ja00497a058). eprint: <https://doi.org/10.1021/ja00497a058>. URL: <https://doi.org/10.1021/ja00497a058>.
- [112] Christopher Bauer et al. "Gaussian pulses". In: *J. Magn. Res. (1969)* 58.3 (1984), pp. 442–457. ISSN: 0022-2364. DOI: [http://dx.doi.org/10.1016/0022-2364\(84\)90148-3](https://doi.org/10.1016/0022-2364(84)90148-3). URL: <http://www.sciencedirect.com/science/article/pii/0022236484901483>.
- [113] James B Murdoch, Arnold H Lent, and Margaret R Kritzer. "Computer-optimized narrowband pulses for multislice imaging". In: *Journal of Magnetic Resonance (1969)* 74.2 (1987), pp. 226–263. ISSN: 0022-2364. DOI: [http://dx.doi.org/10.1016/0022-2364\(87\)90336-2](https://doi.org/10.1016/0022-2364(87)90336-2). URL: <http://www.sciencedirect.com/science/article/pii/0022236487903362>.
- [114] J. Baum, R. Tycko, and A. Pines. "Broadband and adiabatic inversion of a two-level system by phase-modulated pulses". In: *Phys. Rev. A* 32 (1985), pp. 3435–3447. DOI: [10.1103/PhysRevA.32.3435](https://doi.org/10.1103/PhysRevA.32.3435). URL: <http://link.aps.org/doi/10.1103/PhysRevA.32.3435>.

- [115] T. Choi et al. "Optimal Quantum Control of Multimode Couplings between Trapped Ion Qubits for Scalable Entanglement". In: *Phys. Rev. Lett.* 112 (19 2014), p. 190502. DOI: [10.1103/PhysRevLett.112.190502](https://doi.org/10.1103/PhysRevLett.112.190502). URL: <https://link.aps.org/doi/10.1103/PhysRevLett.112.190502>.
- [116] N. Timoney et al. "Error-resistant single-qubit gates with trapped ions". In: *Phys. Rev. A* 77 (5 2008), p. 052334. DOI: [10.1103/PhysRevA.77.052334](https://doi.org/10.1103/PhysRevA.77.052334). URL: <https://link.aps.org/doi/10.1103/PhysRevA.77.052334>.
- [117] J. Kelly et al. "Optimal Quantum Control Using Randomized Benchmarking". In: *Phys. Rev. Lett.* 112 (24 2014), p. 240504. DOI: [10.1103/PhysRevLett.112.240504](https://doi.org/10.1103/PhysRevLett.112.240504). URL: <https://link.aps.org/doi/10.1103/PhysRevLett.112.240504>.
- [118] Takuya F. Segawa et al. "Copper ESEEM and HYSCORE through ultra-wideband chirp EPR spectroscopy". In: *The Journal of Chemical Physics* 143.4 (2015), p. 044201. DOI: [10.1063/1.4927088](https://doi.org/10.1063/1.4927088).
- [119] A. Doll and G. Jeschke. "Epr-correlated dipolar spectroscopy by q-band chirp sifter". In: *Phys. Chem. Chem. Phys.* 18 (2016), pp. 23111–23120. DOI: [10.1039/c6cp03067j](https://doi.org/10.1039/c6cp03067j).
- [120] J. M. Chow et al. "Optimized driving of superconducting artificial atoms for improved single-qubit gates". In: *Phys. Rev. A* 82 (4 2010), p. 040305. DOI: [10.1103/PhysRevA.82.040305](https://doi.org/10.1103/PhysRevA.82.040305). URL: <https://link.aps.org/doi/10.1103/PhysRevA.82.040305>.
- [121] A. W. Cross and J. M. Gambetta. "Optimized pulse shapes for a resonator-induced phase gate". In: *Phys. Rev. A* 91 (2015), p. 032325. DOI: [10.1103/PhysRevA.91.032325](https://doi.org/10.1103/PhysRevA.91.032325). URL: <https://link.aps.org/doi/10.1103/PhysRevA.91.032325>.
- [122] L. Cywinski et al. "How to enhance dephasing time in superconducting qubits". In: *Phys. Rev. B* 77 (2008), p. 174509. DOI: [10.1103/PhysRevB.77.174509](https://doi.org/10.1103/PhysRevB.77.174509). URL: <http://link.aps.org/doi/10.1103/PhysRevB.77.174509>.
- [123] G. A. Alvarez and D. Suter. "Measuring the spectrum of colored noise by dynamical decoupling". In: *Phys. Rev. Lett.* 107 (2011), p. 230501. DOI: [10.1103/PhysRevLett.107.230501](https://doi.org/10.1103/PhysRevLett.107.230501). URL: <http://link.aps.org/doi/10.1103/PhysRevLett.107.230501>.
- [124] D. Suter and G. Alvarez. "Protecting quantum information against environmental noise". In: *Rev. Mod. Phys.* 88 (4 2016), p. 041001. DOI: [10.1103/RevModPhys.88.041001](https://doi.org/10.1103/RevModPhys.88.041001). URL: <http://link.aps.org/doi/10.1103/RevModPhys.88.041001>.
- [125] S. Kotler et al. "Single-ion quantum lock-in amplifier". In: *Nature* 473 (2011), pp. 61–65. DOI: [10.1038/nature10010](https://doi.org/10.1038/nature10010).
- [126] G. De Lange et al. "Single-spin magnetometry with multipulse sensing sequences". In: *Phys. Rev. Lett.* 106 (2011), p. 080802. DOI: [10.1103/PhysRevLett.106.080802](https://doi.org/10.1103/PhysRevLett.106.080802).
- [127] J. Bylander et al. "Noise spectroscopy through dynamical decoupling with a superconducting flux qubit". In: *Nat. Phys.* 7 (2011), pp. 565–570. DOI: [10.1038/NPHYS1994](https://doi.org/10.1038/NPHYS1994).

- [128] L. M. Norris, G. A. Paz-Silva, and L. Viola. "Qubit noise spectroscopy for non-gaussian dephasing environments". In: *Phys. Rev. Lett.* 116 (2016), p. 150503. DOI: [10.1103/PhysRevLett.116.150503](https://doi.org/10.1103/PhysRevLett.116.150503). URL: <http://link.aps.org/doi/10.1103/PhysRevLett.116.150503>.
- [129] X. Qin et al. "High-time-resolution nuclear magnetic resonance with nitrogen-vacancy centers". In: *IEEE Magnetics Letters* 7 (2016), p. 6502305. DOI: [10.1109/LMAG.2016.2536661](https://doi.org/10.1109/LMAG.2016.2536661).
- [130] X. Qin et al. "An integrated device with high performance multi-function generators and time-to-digital convertors". In: *Rev. Sci. Instr.* 88 (2017), p. 014702. DOI: [10.1063/1.4973725](https://doi.org/10.1063/1.4973725).
- [131] A. Ajoy et al. "Quantum interpolation for high-resolution sensing". In: *Proc. Natl. Acad. Sci. U. S. A.* 114.9 (2017), p. 2149. DOI: [10.1073/pnas.1610835114](https://doi.org/10.1073/pnas.1610835114).
- [132] R. R. Ernst, G. Bodenhausen, and A. Wokaun. "Principles of Nuclear Magnetic Resonance in One and Two Dimensions". In: (*International Series of Monographs on Chemistry*, Clarendon Press, 1990) ().
- [133] M. Steffen, J. M. Martinis, and I. L. Chuang. "Accurate control of josephson phase qubits". In: *Phys. Rev. B* 68 (2003), p. 224518. DOI: [10.1103/PhysRevB.68.224518](https://doi.org/10.1103/PhysRevB.68.224518).
- [134] S. J. Glaser et al. "Training schrodinger's cat: Quantum optimal control". In: *European Physical Journal D* 69 (2015), p. 279. DOI: [10.1140/epjd/e2015-60464-1](https://doi.org/10.1140/epjd/e2015-60464-1).
- [135] F. Jelezko and J. Wrachtrup. "Single defect centres in diamond: A review". In: *phys. stat. sol. (a)* 203, 3207 (2006), p. 3207. DOI: [10.1002/pssa.200671403](https://doi.org/10.1002/pssa.200671403).
- [136] M. Loretz, T. Rosskopf, and C. L. Degen. "Radio-frequency magnetometry using a single electron spin". In: *Phys. Rev. Lett.* 110 (2013), p. 017602. DOI: [10.1103/PhysRevLett.110.017602](https://doi.org/10.1103/PhysRevLett.110.017602). URL: <http://link.aps.org/doi/10.1103/PhysRevLett.110.017602>.
- [137] S. Kotler et al. "Nonlinear single-spin spectrum analyzer". In: *Phys. Rev. Lett.* 110 (2013), p. 110503. DOI: [10.1103/PhysRevLett.110.110503](https://doi.org/10.1103/PhysRevLett.110.110503). URL: <http://link.aps.org/doi/10.1103/PhysRevLett.110.110503>.
- [138] N. Zhao et al. "Sensing single remote nuclear spins". In: *Nature Nano.* 7 (2012), p. 657. DOI: [10.1038/nnano.2012.152](https://doi.org/10.1038/nnano.2012.152).
- [139] S. Kolkowitz et al. "Sensing distant nuclear spins with a single electron spin". In: *Phys. Rev. Lett.* 109 (2012), p. 137601. DOI: [10.1103/PhysRevLett.109.137601](https://doi.org/10.1103/PhysRevLett.109.137601). URL: <http://link.aps.org/doi/10.1103/PhysRevLett.109.137601>.
- [140] V. S. Perunicic et al. "A quantum spin-probe molecular microscope". In: *Nat. Commun.* 7 (2016), p. 12667. DOI: [10.1038/ncomms12667](https://doi.org/10.1038/ncomms12667). URL: <http://dx.doi.org/10.1038/ncomms12667>.
- [141] A. Lazariiev and G. Balasubramanian. "A nitrogen-vacancy spin based molecular structure microscope using multiplexed projection reconstruction". In: *Scientific Reports* 5 (2015), p. 14130. DOI: [10.1038/srep14130](https://doi.org/10.1038/srep14130).
- [142] F. Shi et al. "Sensing and atomic-scale structure analysis of single nuclear-spin clusters in diamond". In: *Nature Physics* 10 (2014), pp. 21–25. DOI: [10.1038/nphys2814](https://doi.org/10.1038/nphys2814).

- [143] Andreas Reiserer et al. “Robust Quantum-Network Memory Using Decoherence-Protected Subspaces of Nuclear Spins”. In: *Phys. Rev. X* 6 (2 2016), p. 021040. DOI: [10.1103/PhysRevX.6.021040](https://doi.org/10.1103/PhysRevX.6.021040). URL: <https://link.aps.org/doi/10.1103/PhysRevX.6.021040>.
- [144] P. L. Stanwix et al. “Coherence of nitrogen-vacancy electronic spin ensembles in diamond”. In: *Phys. Rev. B* 82 (2010), p. 201201. DOI: [10.1103/PhysRevB.82.201201](https://doi.org/10.1103/PhysRevB.82.201201).
- [145] A. Laraoui, D. Pagliero, and C. A. Meriles. “Imaging nuclear spins weakly coupled to a probe paramagnetic center”. In: *Phys. Rev. B* 91 (2015), p. 205410. DOI: [10.1103/PhysRevB.91.205410](https://doi.org/10.1103/PhysRevB.91.205410). URL: <https://link.aps.org/doi/10.1103/PhysRevB.91.205410>.
- [146] Zhen-Yu Wang et al. “Positioning nuclear spins in interacting clusters for quantum technologies and bioimaging”. In: *Phys. Rev. B* 93 (17 2016), p. 174104. DOI: [10.1103/PhysRevB.93.174104](https://doi.org/10.1103/PhysRevB.93.174104). URL: <https://link.aps.org/doi/10.1103/PhysRevB.93.174104>.
- [147] K. Sasaki, K. M. Itoh, and E. Abe. “Determination of the Position of a Single Nuclear Spin from Free Nuclear Precessions Detected by a Solid-State Quantum Sensor”. In: *arXiv:1806.00177* (2018). URL: <https://arxiv.org/abs/1806.00177>.
- [148] L. Childress et al. “Coherent Dynamics of Coupled Electron and Nuclear Spin Qubits in Diamond”. In: *Science* 314, 281 (2006), p. 281. DOI: [10.1126/science.1131871](https://doi.org/10.1126/science.1131871). URL: <http://dx.doi.org/10.1126/science.1131871>.
- [149] S. Steinert et al. “High sensitivity magnetic imaging using an array of spins in diamond”. In: *Rev. Sci. Instrum.* 81 (2010), p. 43705. DOI: [10.1063/1.3385689](https://doi.org/10.1063/1.3385689). URL: <http://dx.doi.org/10.1063/1.3385689>.
- [150] J. Zopes et al. “Three-dimensional localization spectroscopy of individual nuclear spins with sub-Angstrom resolution”. In: *arXiv:1806.04883* (2018). URL: <https://arxiv.org/abs/1806.04883>.
- [151] A P Nizovtsev et al. “Non-flipping ^{13}C spins near an NV center in diamond: hyperfine and spatial characteristics by density functional theory simulation of the C 510 [NV]H 252 cluster”. In: *New Journal of Physics* 20.2 (2018), p. 023022. URL: <http://stacks.iop.org/1367-2630/20/i=2/a=023022>.
- [152] D. R. Glenn et al. “High-resolution magnetic resonance spectroscopy using a solid-state spin sensor”. In: *Nature* 555 (2018), p. 351. DOI: [10.1038/nature25781](https://doi.org/10.1038/nature25781). URL: <http://dx.doi.org/10.1038/nature25781>.
- [153] H. J. Mamin, M. H. Sherwood, and D. Rugar. “Detecting external electron spins using nitrogen-vacancy centers”. In: *Phys. Rev. B* 86 (2012), p. 195422. DOI: [10.1103/PhysRevB.86.195422](https://doi.org/10.1103/PhysRevB.86.195422).
- [154] A. O. Sushkov et al. “All-optical sensing of a single-molecule electron spin”. In: *Nano Lett.* 14 (2014), pp. 6443–6448. DOI: [10.1021/nl502988n](https://doi.org/10.1021/nl502988n). URL: <https://doi.org/10.1021/nl502988n>.
- [155] A. Loquet et al. “ ^{13}C spin dilution for simplified and complete solid-state NMR resonance assignment of insoluble biological assemblies”. In: *J. Am. Chem. Soc.* 133 (2011), pp. 4722–4725. DOI: [10.1021/ja200066s](https://doi.org/10.1021/ja200066s). URL: <https://doi.org/10.1021/ja200066s>.

- [156] T. Gefen et al. "Quantum spectroscopy of single spins assisted by a classical clock". In: *Phys. Rev. A* 98 (2018), p. 013844. DOI: [10.1103/PhysRevA.98.013844](https://doi.org/10.1103/PhysRevA.98.013844). URL: <https://link.aps.org/doi/10.1103/PhysRevA.98.013844>.
- [157] N. H. Wan et al. "Efficient extraction of light from a nitrogen-vacancy center in a diamond parabolic reflector". In: *arXiv:1711.01704* (2017). URL: <https://arxiv.org/abs/1711.01704>.
- [158] L. H. Meyer, A. Saika, and H. S. Gutowsky. "Electron distribution in molecules. III. The proton magnetic spectra of simple organic groups". In: *J. Am. Chem. Soc.* 75 (1953), pp. 4567–4573. DOI: [10.1021/ja01114a053](https://doi.org/10.1021/ja01114a053). URL: <https://doi.org/10.1021/ja01114a053>.
- [159] P. Hodgkinson and L. Emsley. "The accuracy of distance measurements in solid-state NMR". In: *J. Magn. Res.* 139 (1999), pp. 46–59. URL: <http://www.sciencedirect.com/science/article/pii/S1090780799917597>.
- [160] G. Jeschke. "Deer distance measurements on proteins". In: *Annu. Rev. Phys. Chem.* 63 (2012), pp. 419–446. DOI: [0.1146/annurev-physchem-032511-143716](https://doi.org/10.1146/annurev-physchem-032511-143716). URL: <https://doi.org/10.1146/annurev-physchem-032511-143716>.
- [161] M. Poggio and C. L. Degen. "Force-detected nuclear magnetic resonance: Recent advances and future challenges". In: *Nanotechnology* 21 (2010), p. 342001. DOI: [10.1088/0957-4484/21/34/342001](https://doi.org/10.1088/0957-4484/21/34/342001). URL: <http://dx.doi.org/10.1088/0957-4484/21/34/342001>.
- [162] J. Wrachtrup and A. Finkler. "Single spin magnetic resonance". In: *J. Magn. Reson.* 269 (2016), pp. 225–236. DOI: [10.1016/j.jmr.2016.06.017](https://doi.org/10.1016/j.jmr.2016.06.017).
- [163] I. Schwartz et al. "Blueprint for nanoscale NMR". In: *arXiv:1706.07134* (2017). URL: <https://arxiv.org/abs/1706.07134>.
- [164] E. R. McVeigh, M. J. Bronskill, and R. M. Henkelman. "Phase and sensitivity of receiver coils in magnetic resonance imaging". In: *Medical Physics* 13 (1986), pp. 806–814. DOI: [doi:10.1118/1.595967](https://doi.org/10.1118/1.595967). URL: <https://doi.org/10.1118/1.595967>.
- [165] J. M. Taylor et al. "High-sensitivity diamond magnetometer with nanoscale resolution". In: *Nat. Phys.* 4, 810 (2008), p. 810. DOI: [10.1038/nphys1075](https://doi.org/10.1038/nphys1075). URL: <http://dx.doi.org/10.1038/nphys1075>.
- [166] In: *See Supplemental Material accompanying this manuscript* ().
- [167] T. Gullion, D. B. Baker, and M. S. Conradi. "New, compensated Carr-Purcell sequences". In: *J. Magn. Res.* 89 (1990), pp. 479–484. URL: <http://www.sciencedirect.com/science/article/pii/0022236490903313>.
- [168] J.R. Johansson, P.D. Nation, and Franco Nori. "QuTiP 2: A Python framework for the dynamics of open quantum systems". In: *Computer Physics Communications* 184.4 (2013), pp. 1234–1240. ISSN: 0010-4655. DOI: <https://doi.org/10.1016/j.cpc.2012.11.019>.
- [169] A. Abragam. "Principles of Nuclear Magnetism". In: (*Oxford University Press, Oxford, 1961*) ().
- [170] P. Neumann et al. "Single-shot readout of a single nuclear spin". In: *Science* 329 (2010), pp. 542–544. DOI: [10.1126/science.1189075](https://doi.org/10.1126/science.1189075).
- [171] Matthew Newville et al. *LMFIT: Non-Linear Least-Square Minimization and Curve-Fitting for Python*. Sept. 2014. DOI: [10.5281/zenodo.11813](https://doi.org/10.5281/zenodo.11813). URL: <https://doi.org/10.5281/zenodo.11813>.

- [172] K. Ohashi et al. "Negatively charged nitrogen-vacancy centers in a 5 nm thin 12C diamond film". In: *Nano Letters* 13 (2013), pp. 4733–4738. DOI: [10.1021/nl402286v](https://doi.org/10.1021/nl402286v). URL: <http://dx.doi.org/10.1021/nl402286v>.
- [173] J. A. Sidles. "Spin microscopy's heritage achievements and prospects". In: *Proc. Natl. Acad. Sci. USA* 106 (2009), p. 2477. DOI: [10.1073/pnas.0813322106](https://doi.org/10.1073/pnas.0813322106). URL: <http://www.pnas.org/content/106/8/2477.abstract>.
- [174] G. de Lange et al. "Universal dynamical decoupling of a single solid-state spin from a spin bath". In: *Science* 330 (2010), pp. 60–63. DOI: [10.1126/science.1192739](https://doi.org/10.1126/science.1192739).
- [175] R. S. Schoenfeld and W. Harneit. "Real time magnetic field sensing and imaging using a single spin in diamond". In: *Phys. Rev. Lett.* 106 (2011), p. 030802. DOI: [10.1103/PhysRevLett.106.030802](https://doi.org/10.1103/PhysRevLett.106.030802). URL: <http://link.aps.org/doi/10.1103/PhysRevLett.106.030802>.
- [176] N. De Zanche et al. "NMR probes for measuring magnetic fields and field dynamics in MR systems". In: *Magn. Reson. Med.* 60 (2008), pp. 176–186. DOI: [10.1002/mrm.21624](https://doi.org/10.1002/mrm.21624).
- [177] Chang S. Shin et al. "Room-temperature operation of a radiofrequency diamond magnetometer near the shot-noise limit". In: *Journal of Applied Physics* 112.12 (2012), p. 124519. DOI: [10.1063/1.4771924](https://doi.org/10.1063/1.4771924). URL: <https://doi.org/10.1063/1.4771924>.
- [178] K. Jensen et al. "Non-invasive detection of animal nerve impulses with an atomic magnetometer operating near quantum limited sensitivity". In: *Scientific Reports* 6 (2016), p. 29638. DOI: [10.1038/srep29638](https://doi.org/10.1038/srep29638). URL: <https://doi.org/10.1038/srep29638>.
- [179] John F. Barry et al. "Optical magnetic detection of single-neuron action potentials using quantum defects in diamond". In: *Proceedings of the National Academy of Sciences* (2016). ISSN: 0027-8424. DOI: [10.1073/pnas.1601513113](https://doi.org/10.1073/pnas.1601513113). eprint: <https://www.pnas.org/content/early/2016/11/21/1601513113.full.pdf>. URL: <https://www.pnas.org/content/early/2016/11/21/1601513113>.
- [180] H. Xia et al. "Magnetoencephalography with an atomic magnetometer". In: *Appl. Phys. Lett.* 89 (2006), p. 211104. DOI: [10.1063/1.2392722](https://doi.org/10.1063/1.2392722). URL: <https://doi.org/10.1063/1.2392722>.
- [181] Easwar Magesan et al. "Reconstructing the profile of time-varying magnetic fields with quantum sensors". In: *Phys. Rev. A* 88 (3 2013), p. 032107. DOI: [10.1103/PhysRevA.88.032107](https://doi.org/10.1103/PhysRevA.88.032107). URL: <https://link.aps.org/doi/10.1103/PhysRevA.88.032107>.
- [182] A. Cooper et al. "Time-resolved magnetic sensing with electronic spins in diamond". In: *Nat. Commun.* 5 (2014), p. 3141. DOI: [10.1038/ncomms4141](https://doi.org/10.1038/ncomms4141). URL: <http://dx.doi.org/10.1038/ncomms4141>.
- [183] N. Xu et al. "Wavelet-based fast time-resolved magnetic sensing with electronic spins in diamond". In: *Phys. Rev. B* 93 (2016), p. 161117. DOI: [10.1103/PhysRevB.93.161117](https://doi.org/10.1103/PhysRevB.93.161117). URL: <https://link.aps.org/doi/10.1103/PhysRevB.93.161117>.
- [184] A. Nowodzinski et al. "Nitrogen-vacancy centers in diamond for current imaging at the redistributive layer level of integrated circuits". In: *Microelectron. Reliab.* 55 (2015), p. 1549. DOI: [10.1016/j.microrel.2015.06.069](https://doi.org/10.1016/j.microrel.2015.06.069). URL: <http://dx.doi.org/10.1016/j.microrel.2015.06.069>.

- [185] B. B. Zhou et al. "Spatiotemporal Mapping of Photocurrent in a Monolayer Semiconductor Using a Diamond Quantum Sensor". In: *arXiv:1903.09287* (2019). URL: <https://arxiv.org/abs/1903.09287>.
- [186] Manuel Baumgartner et al. "Spatially and time-resolved magnetization dynamics driven by spin-orbit torques". In: *Nature Nanotechnology* 12 (Aug. 2017), 980 EP -. URL: <https://doi.org/10.1038/nnano.2017.151>.
- [187] Ian Knowles and Robert J. Renka. "Methods for numerical differentiation of noisy data". In: *Electron. J. Differ. Eq.* 21 (2014), pp. 235–246.
- [188] Charles Jordan. *Calculus of Finite Differences: Third Edition*. American Mathematical Society, 2017. ISBN: 1470441004.
- [189] Helena S. Knowles, Dhiren M. Kara, and Mete Atatüre. "Demonstration of a Coherent Electronic Spin Cluster in Diamond". In: *Phys. Rev. Lett.* 117 (10 2016), p. 100802. DOI: 10.1103/PhysRevLett.117.100802. URL: <https://link.aps.org/doi/10.1103/PhysRevLett.117.100802>.
- [190] Fei Kong et al. "Nanoscale zero-field electron spin resonance spectroscopy". In: *Nature Communications* 9.1 (2018), p. 1563. DOI: 10.1038/s41467-018-03969-4. URL: <https://doi.org/10.1038/s41467-018-03969-4>.
- [191] Lukas Schlipf et al. "A molecular quantum spin network controlled by a single qubit". In: *Science Advances* 3.8 (2017). DOI: 10.1126/sciadv.1701116. eprint: <https://advances.sciencemag.org/content/3/8/e1701116.full.pdf>. URL: <https://advances.sciencemag.org/content/3/8/e1701116>.
- [192] P. Welter and M. S. Wörnle. Private Communication.
- [193] J. Maze. "Quantum manipulation of nitrogen-vacancy centers in diamond: From basic properties to applications". In: *Ph.D. thesis, Harvard University* (2010). URL: <http://www.fis.puc.cl/~jmaze/MazeHUThesis.pdf>.

List of Figures

1.1	Long-term vision for nanoscale magnetic resonance imaging with a single NV sensor.	2
2.1	Electronic structure of the NV center.	6
2.2	Quantum states of the NV center.	7
2.3	Optically detected magnetic resonance	9
2.4	Ramsey and Spin echo detection sequences.	12
2.5	Coherent control of the m_S states of the NV center.	18
2.6	Distribution of coherence times for shallow NV centers.	19
3.1	Coupling of the NV center to ^{13}C nuclear spins in the diamond host.	22
3.2	Dynamical decoupling spectroscopy with XY8 phase cycling.	25
3.3	Detection of NMR signals with dynamical decoupling spectroscopy.	28
3.4	Nuclear spin evolution during dynamical decoupling.	31
3.5	Polarization and state tomography of individual nuclear spins.	34
3.6	Correlation spectroscopy applied to a single nuclear spin.	39
4.1	Layer structure of isotopically-purified diamond samples hosting NV centers.	45
4.2	Confocal microscopy of individual NV centers.	46
4.3	Control electronics of the experimental setup.	47
4.4	Time-resolved photon counting.	48
4.5	Definition of the laboratory and NV center coordinate systems.	50
4.6	Magnetic bias field source and field stability.	52
4.7	Numerical optimization of the coil geometry.	53
4.8	Schematic of the central part of the experimental setup used in this work.	55
4.9	Characterization of the planar, radio-frequency coil.	56
5.1	Pulse shaping for dynamical decoupling spectroscopy.	61
5.2	Demonstration of high time-resolution with shaped pulses	62
5.3	Sensor response for increasing number of shaped pulses.	63
5.4	Numerical comparison between ideal and non-ideal as well as shaped and non-shaped control pulses.	65
5.5	Applications of pulse shaping for high-resolution spectroscopy.	66
6.1	Coordinate systems for spins and magnetic fields.	69
6.2	Implementation of three-dimensional localization spectroscopy.	71
6.3	Determination of azimuth angle ϕ and Fermi contact contribution a_{iso} for $^{13}\text{C}_1$	73
6.4	Three-dimensional localization of four ^{13}C nuclear spins.	74

7.1	Measurement principle for azimuthal positioning with coherent radio-frequency pulses.	80
7.2	Azimuthal positioning with coherent radio-frequency pulses.	83
7.3	Polar plot of the reconstructed nuclear spin positions in the xy -plane of the laboratory frame.	84
7.4	Measurement of the hyperfine ϕ angle by a nuclear spin echo.	85
7.5	Nuclear positioning uncertainty due to tilted bias fields.	88
8.1	Schemes for waveform sampling.	92
8.2	Pulse detection and time resolution.	95
8.3	Increased sensitivity by integrating $2k$ waveform passages.	96
8.4	Example of arbitrary waveform detection.	98
C.1	Minimum detectable field per unit time for different waveform sensing methods.	113

List of Tables

2.1	Data base of physical properties of the NV^- defect	14
3.1	Summary of NV-NMR methods used in this work	24
4.1	Geometry, magnetic and electrical design properties of the planar coil used in this work.	54
6.1	Data base of measured precession frequencies and calibrated external magnetic fields used to determine the 3D position of $^{13}C_1$	72
6.2	Measured hyperfine couplings and inferred 3D locations of ^{13}C nuclei measured on three NV centers.	75
6.3	DFT values of ^{13}C nuclei that best fit to the detected nuclear spins.	75

Danksagung

Die vergangenen vier Jahre haben mir viel Freude bereitet. Zum Abschluss dieser Arbeit möchte ich mich bei den folgenden Personen bedanken:

- Bei Christian Degen möchte ich mich für seine umfangreiche Betreuung bedanken. Ich bin sehr froh, dass ich in Deiner Arbeitsgruppe die Doktorarbeit durchführen durfte. Sowohl wissenschaftlich, aber auch menschlich warst Du ein hervorragender Betreuer.
- Ich danke Andreas Vaterlaus für die Bereitschaft das Korreferat für diese Arbeit zu übernehmen.
- Ich danke allen ehemaligen und aktuellen PhD-Studenten des NV-NMR Teams, Tobias Rosskopf, Jens Boss und Kristian Cujia für die gemeinsamen Diskussionen und Eure Unterstützung. Ich habe sehr viel von jedem von Euch gelernt.
- Kevin Chang hat mir viel über Diamantfabrikation beigebracht und hat mir den Neustart in Zürich sehr erleichtert.
- Kento Sasaki, Nils Hauff und Konstantin Herb haben im Laufe der Jahre als Master- oder Gaststudenten sehr signifikant zu den Experimenten beigetragen. Mir hat die Zusammenarbeit mit Euch viel Freude bereitet.
- Martin Wörnle und Pol Welter danke ich für die Diskussionen über das Zeitauflösungsprojekt und Takuya Segawa für Diskussionen über Spinphysik und EPR.
- Allen aktuellen und ehemaligen Büronachbarn im HPF-F8 danke ich für die angenehme Arbeitsatmosphäre: Alexander Eichler, Urs Grob, Luca Lorenzelli, Takuya Segawa, Martin Heritier, Nils Hauff, Rui Tian und Jingwen Li.
- Ich danke Takuya, Nils, Konstantin und Christian für das Korrekturlesen der vorliegenden Arbeit.
- Jan Rhensius danke ich für die gemeinsame Organisation der ETH-Studienwoche.
- Julia Tamborini und Christa Leumann danke ich für Ihre Hilfe bei organisatorischen Angelegenheiten. Unserem ehemaligen Techniker Christoph Keck danke ich für seine Unterstützung bei technischen Problemen.
- Allen weiteren Mitgliedern der Arbeitsgruppe danke ich für die entspannte, gute Arbeitsatmosphäre.
- Ich danke allen sportbegeisterten Mitgliedern an der ETH für das gemeinsame Schwimmen, Radfahren und Laufen: Christopher Mittag, Matija Karalic, Fabian Göbel, Kevin Chang, Jens Boss, Nils Hauff, David Hälgl, Thomas Gisler, Luca Lorenzelli, Kristian Cujia, Michael Loretz, Marius Palm und Janine Kipfer.

Curriculum Vitae

Jonathan Zopes

Personal details

Born on January 26, 1989, in Cologne (West-Germany)

Current address: Paul-Feyerabend-Hof 1

8049 Zürich

Switzerland

Email: jzopes@phys.ethz.ch

Education

July 2008 General qualification for university entrance (Abitur)

2009-2012 Bachelor studies in physics at University of Bonn

2012-2014 Master studies in physics at University of Bonn

2015-2019 Ph.D. student in physics at ETH Zürich

Awards

2012-2014 M.Sc. scholarship funded by the German Excellence Initiative

2011 Bachelor award at University of Bonn

2008 Abitur prize of the German Mathematical Society

Publications

1. J. Zopes and C. L. Degen, *Reconstruction-free quantum sensing of arbitrary waveforms*, arXiv:1906.09176 (2019).
2. K. S. Cujia, J. M. Boss, K. Herb, J. Zopes, and C. L. Degen, *Watching the precession of a single nuclear spin by weak measurements*, *Nature* **571**, 230-233 (2019).
3. J. Zopes, K. S. Cujia, K. Sasaki, J. M. Boss, K. M. Itoh, and C. L. Degen, *Three-dimensional localization spectroscopy of individual nuclear spins with sub-Angstrom resolution*, *Nature Communications* **9**, 4678 (2018).
4. J. Zopes, K. Herb, K. S. Cujia, and C. L. Degen, *Three-dimensional nuclear spin positioning using coherent radio-frequency control*, *Phys. Rev. Lett.* **121**, 170801 (2018).
5. T. Unden, N. Tomek, T. Weggler, F. Frank, P. London, J. Zopes, C. L. Degen, N. Raatz, J. Meijer, H. Watanabe, K. M. Itoh, M. B. Plenio, B. Naydenov, and F. Jelezko, *Coherent control of solid state nuclear spin nano-ensembles*, *npj Quantum Information* **4**, 39 (2018).
6. C. Robens, S. Brakhane, W. Alt, D. Meschede, J. Zopes and A. Alberti, *Fast, high-precision optical polarization synthesizer for ultracold-atom experiments*, *Phys. Rev. Applied* **9**, 034016 (2018).
7. J. Zopes, K. Sasaki, K. S. Cujia, J. M. Boss, K. Chang, T.F. Segawa, K.M. Itoh and C.L. Degen, *High-resolution quantum sensing with shaped control pulses*, *Phys. Rev. Lett.* **119**, 260501 (2017).
8. J.M. Boss*, K.S. Cujia*, J. Zopes and C.L. Degen, *Quantum sensing with arbitrary frequency resolution*, *Science* **356**, 837 (2017).
9. T. Rosskopf, J. Zopes, J. M. Boss, C. L. Degen, *A quantum spectrum analyzer enhanced by a nuclear spin memory*, *npj Quantum Information* **3**, 33 (2017).
10. C. Robens*, J. Zopes*, W. Alt, S. Brakhane, D. Meschede and A. Alberti, *Low-entropy states of neutral atoms in polarization-synthesized optical lattices*, *Phys. Rev. Lett.* **118**, 065302 (2017).

* denotes equal contributions.